UNIVERSITY OF SOUTHAMPTON

FACULTY OF NATURAL AND ENVIRONMENTAL SCIENCES

Ocean and Earth Sciences

Go with the flow: Timescales of biogeochemical and ecological ocean connectivity

by

Josie Robinson-Parker

Thesis for the degree of Doctor of Philosophy

October 2017

UNIVERSITY OF SOUTHAMPTON

ABSTRACT

FACULTY OF NATURAL AND ENVIRONMENTAL SCIENCES

Ocean and Earth Sciences

Doctor of Philosophy

GO WITH THE FLOW: TIMESCALES OF BIOGEOCHEMICAL AND ECOLOGICAL OCEAN CONNECTIVITY

by Josie Robinson-Parker

Ocean circulation can govern relationships between physical, biogeochemical and ecological processes and determines the connectivity between regions. As such, a variety of oceanographic problems can be addressed using a Lagrangian modelling approach. This thesis utilises velocity output from a high resolution ocean general circulation model and a Lagrangian particle tracking programme to address three topics: the global-scale efficiency of regional geoengineering by iron fertilisation; the role of natural iron fertilisation in phytoplankton blooms; and the connectivity of Marine Protected Areas (MPAs) to upstream anthropogenic impacts.

Artificial ocean iron fertilization (OIF) enhances phytoplankton productivity and is being explored as a means of sequestering anthropogenic carbon within the deep ocean for an extended period (e.g., the Intergovernmental Panel on Climate Change's standard 100 year time horizon). This study assessed the impact of deep circulation on sequestered carbon in the Southern Ocean, a high-nutrient low-chlorophyll region known to be iron stressed. The Lagrangian particle tracking approach was employed to analyze water mass trajectories over a 100 year simulation. By the end of the experiment, for a sequestration depth of 1000 m, 66% of the carbon had been re–exposed

to the atmosphere, taking an average of 37.8 years. These results emphasized that successful OIF is dependent on the physical circulation, as well as the biogeochemistry.

Following on from the long–term impact of the wider Southern Ocean circulation, the local circulation around three Southern Ocean islands was considered. In exception to the typically High Nutrient, Low Chlorophyll conditions of the Southern Ocean, phytoplankton blooms occur annually downstream of the Kerguelen Plateau, Crozet Islands, and South Georgia, fertilized by iron-rich shelf waters. The Lagrangian particle tracking approach was used to investigate if advection could explain the inter–annual variability observed in the blooms in satellite ocean colour data. The results suggest that advection can explain the extent of each island's annual bloom, but only the inter–annual variability of the Crozet bloom, therefore suggesting that other factors, such as silicate limitation or the timing of mixed layer deepening, may also determine the inter–annual variability of the downstream blooms.

Finally, the method was applied to assess the remoteness of four MPAs: Pitcairn, South Georgia, Ascension, and the British Indian Ocean Territory (BIOT), which were established to conserve important ecosystems. However, MPAs may be at risk of 'upstream' human activity, such as marine pollution. Thus, improved understanding of exactly where upstream is, and on what timescale it is connected, is important for monitoring and future planning of MPAs. By reverse Lagrangian particle tracking, circulation 'connectivity footprints' are produced for each MPA, revealing on annual timescales, that Pitcairn was not connected with land, whereas there was increasing connectivity for waters reaching South Georgia, Ascension, and BIOT. Such footprints are an inherent property of all MPAs, and need to be considered for all current and future MPAs.

Contents

List of Figures

List of Tables

Declaration of Authorship

I, Josie Robinson-Parker , declare that the thesis entitled *Go with the flow: Timescales of biogeochemical and ecological ocean connectivity* and the work presented in the thesis are both my own, and have been generated by me as the result of my own original research. I confirm that:

1. this work was done wholly or mainly while in candidature for a research degree at this University;
2. where any part of this thesis has previously been submitted for a degree or any other qualification at this University or any other institution, this has been clearly stated;
3. where I have consulted the published work of others, this is always clearly attributed;
4. where I have quoted from the work of others, the source is always given. With the exception of such quotations, this thesis is entirely my own work;
5. I have acknowledged all main sources of help;
6. where the thesis is based on work done by myself jointly with others, I have made clear exactly what was done by others and what I have contributed myself;
7. parts of this work have been published as: (Robinson et al., 2014), (Robinson et al., 2016) and (Robinson et al., 2017)

Signed:.....

Date:.....

Acknowledgements

I dedicate this thesis to my husband, Duncan Robinson-Parker. Thank you for encouraging me to undertake this feat, and for being behind me all the way.

Thanks to my three most excellent supervisors, Katya Popova, Andrew Yool and Meric Srokosz, who not only made this thesis possible they also made it incredibly enjoyable. Thank you Katya for starting me on this path during my masters degree all those years ago. I have learned so much from you, lessons that will last a lifetime. Thank you Andrew for always having the time to help and talk (and laugh) with me, and for trying to teach me the value of pedantry. I felt fortunate to have an office next to yours, where the door was always open. Meric, I thank you for your guidance and compassion. At times I have felt like one of your own, I thank you from my heart. I thank you all for our weekly meetings, which were both highly amusing and also invaluable in the making of this thesis. I already miss working with you all, thank you for what has been a wonderful journey, I could not have had better supervision.

I would like to thank Adrian New for taking an interest in this work, and for his timely and insightful comments as Panel Chair. I also thank the wider MSM group at NOCS, who collectively provided a supportive environment in which to undertake a PhD. There was always someone who could and would help. I particularly thank Andrew Coward and Jeff Blundell, for their guidance with the NEMO model, UNIX systems and Ariane code. I am grateful to Bruno Blanke and Nicolas Grima for creating the Ariane code, and for making it freely available. I am also grateful to the National Environmental Research Council, who provided funding for my studentship.

Thanks to my 256/16 office mates, particularly Maike Sonnewald and Ed Butler, for the Matlab help and also the laughs. Our conversations were always a pleasure, whether on gin or bird watching, and at times provided much needed light relief.

Thanks also to all the PhDs down corridor 256, who frequently let me invade their office and distract them from their work for a long chat. I would like to thank my non-academic friends, from Crofton and Bristol, who reminded me that there was another world outside of academia to enjoy.

Finally, thank you to my family for the endless love and support throughout my life. It was my parents who first formed my character that has enabled me to benefit so greatly from the excellent people mentioned here, I am who I am today because of the people who undertook this journey with me. Thank you all.

Chapter 1

Introduction

"Everything is everywhere, but, the environment selects" (Baas Becking, 1934)

1.1 Introduction

A ubiquitous aspect of the world's oceans is the continuous movement of water masses. The circulation of the ocean determines the connectivity between regions and can govern relationships between physical, biogeochemical and ecological processes. As such, a variety of problems in marine science can be addressed by studying the dispersal of "fluid parcels" in the ocean. In fluid dynamics, a fluid parcel is described as a very small volume of fluid, identifiable throughout its dynamic history while moving through a flow field (Batchelor, 1973). To study ocean circulation, floats have been deployed in the real ocean, such as the Argo program (`http://www.argo.ucsd.edu`), and in The Global Drifter Program (`http://www.aoml.noaa.gov/phod/dac/index.php`). However, the number of these observational data sets is limited, both in spatio-temporal frequency and across the depth domain. Consequently data resolution in certain parts of the oceans, and depth horizons, is low or even non–existent.

Given the importance of ocean circulation in distributing physical, biogeochemical, biological and other properties throughout the world's ocean and the lack of advection observations, modelling the dispersal of fluid particles can be used to fill in the gaps, which can be referred to as a Lagrangian approach. This approach is a long–standing and well proven method of studying the motion of the ocean, having being used since the early 1980s to study a variety of topics (Woods and Onken, 1982; Davis, 1983). Today, Lagrangian simulations are used to study advection, dispersion and retention. It can also be used in a broad range of oceanographic applications, from the fate of pollutants to the pathways of water masses in the global ocean. This thesis exploits the latest modelling tools to study a number of problems in which ocean advection plays

an important role. The principal tool used in this thesis is Lagrangian particle tracking combined with a high resolution general ocean circulation model. This enables a number of issues to be tackled that could not be addressed by observational means alone. In addition, this thesis shows how a Lagrangian modelling approach allows problems to be addressed on timescales from sub–seasonal to centennial, and on space scales from regional to global. The topics to be tackled in this thesis are described in Section 1.3, but first an introduction to the Lagrangian approach, and its oceanographic uses is given.

1.2 Ocean connectivity

The Oxford English Dictionary's definition of connectivity is "the characteristic or degree, of being connected (in various senses)". In oceanography, the term is principally used to describe the mechanistic spread of biological populations. It is also commonly used to describe the relatedness between ocean basins through circulation. The physical connectivity of the ocean currents plays a key role in determining the biological connectivity between many populations and ecosystems. This is via direct transport of individuals and the distribution of physical (namely heat) and biogeochemical properties, such as nutrients (nitrogen, phosphorous, silica and iron) and carbon.

Piecuch and Rynearson (2012) used Lagrangian observations (World Ocean Circulation Experiment Surface Velocity Program) to calculate probability distribution functions of fluid displacement. This probabilistic framework was demonstrated by quantifying the likelihood and timescales of dispersal of marine organisms in the Azores via the

Gulf Stream. This approach is a novel technique to derive Lagrangian statistics from drifter observations, but it is limited by the availability of drifter data sets. Lagrangian numerical modelling is an increasingly popular approach among physical and biological oceanographers seeking to better understand the influence of circulation connectivity.

The advantage of a modelling approach is that all spatial and temporal scales can be investigated limited only by computational resources, which are continually being upgraded. This allows us to address an important feature of Lagrangian studies, namely the concept that connectivity is a three-dimensional problem (Defne et al., 2016). The spatial extent of circulation connectivity is determined by a given temporal scale (e.g. length of time, 1 month - 1 year) and in some instances the period of time (e.g. January vs. June or 2001 vs. 2010) can also be significant. Lagrangian modelling allows the sensitivity of the flow or connectivity to temporal changes to be explored and appreciated.

With improving computing capabilities comes the increasing sophistication of Lagrangian modelling studies. Paris et al. (2013) developed a "Connectivity Modelling System" which can apply either abiotic or biotic behavioural characteristics to individual particles, along with impressive multi-scale nesting capabilities of independent, overlapping data to maximize resolution. This system allows users to tailor experiments to specific applications with a fine degree of detail.

With or without multi-functioning particles, a Lagrangian particle tracking approach is a powerful methodology. A basic approach of particle tracking within a modelled circulation field can give insight into a wide range of oceanographic topics. The variability

of major and minor currents, the distribution of biogeochemical properties, population and ecosystem connectivity, the spread of invasive species and of marine diseases, and the transport and fate of atmospheric dust, coastal sediments and pollutants are all examples of phenomena that can be investigated using a particle-tracking framework. This section will discuss a selection of these phenomena, but first a brief discussion on Lagrangian versus Eulerian methodologies.

1.2.1 Lagrangian versus Eulerian

There are two standard methods to characterize fluid flow: Lagrangian and Eulerian. A Eulerian approach describes a flow field using fixed coordinates at which a flow property is recorded at a given time. In a Eulerian description, the flow properties of a specific particle, or "fluid parcel", are not known. Instead, the flow passing the fixed coordinates (locations of interest) is given at a particular time. Collectively, these coordinates can define a field of any property, such as velocity, pressure or temperature. In a Lagrangian definition, individual fluid parcels are "tracked", so that their positions (and any other property of interest, e.g. velocity, temperature, etc.) are described as a function of time. The fluid parcel's movement within the flow field is defined by the flow properties which change with location and over time. To create a flow field using a Lagrangian method many fluid parcels would need to be tracked. Typically, fluid flow is a continuum and therefore the Eulerian description is usually preferred in fluid mechanics as a more efficient method (Zhang and Chen, 2007).

However, in oceanography, specifically in diagnosing the real world circulation, both methods have their advantages and disadvantages. Eulerian observations in the ocean

are collected using instrumented moorings, which are typically placed along coasts or across ocean basins in arrays. Moorings can collect data down to the sea floor at their fixed location. They are present in all oceans but have a particularly high density across the tropics. The Ocean Sustained Interdisciplinary Time series Environment observation System, known as OceanSITES (`http://www.oceansites.org/index.html`), is a network of moorings in the open ocean that has been coordinating global observations since 1999. This global network collects high time resolution data and provides long time series, but only at given locations (coordinates within the Eulerian field).

Lagrangian observations are provided by floats, which drift with the ocean currents collecting data in transit. The Array for Real–Time Geostrophic Oceanography (ARGO) programme (`http://www.argo.net/index.html`) is an international collection of profiling floats which can currently descend to depths of 2000 m (deep ARGO floats now being developed and deployed) and drift with the currents over 10–day cycles. As of June 2017, there are 3834 operational floats in the ocean providing real–time data (`http://www.jcommops.org/board?t=Argo`). For moored arrays (the Eulerian method) the location determines the use or applications of the data, meaning that regions of the ocean that do not have moored arrays, such as vast parts of the Southern Ocean, cannot be studied. For drifters (the Lagrangian method) the location is not fixed meaning that, theoretically at least, they could collect data from the entire ocean. In reality, this is dependant on the number of drifters and often the density of drifters can be low, typically one per 3° x 3° box. Additionally, collecting regular repeat measurements from drifters is not possible, rather the chances of a repeat measurement occurring is probabilistic. Nevertheless, the uses of Lagrangian and Eulerian

observations are far–reaching, providing that the choice of data and analysis is appropriate for the problem.

Where Lagrangian or Eulerian observations are lacking, the same methods can be applied to study a simulated ocean. Using velocity from a ocean general circulation model, Blanke and Raynaud (1997) used Eulerian diagnostics to evaluate the meridional, vertical and zonal mass fluxes of the Pacific Equatorial Undercurrent. However, Lagrangian calculations were necessary to accurately diagnose the mass transfers between various sections of the Pacific Equatorial Undercurrent. Although a combined approach was necessary to answer the questions raised in Blanke and Raynaud (1997), in some case, a Lagrangian approach can first be used to inform a Eulerian methodology. In studying the Agulhas leakage (the transfer of warm salty water from the Indian to the Atlantic Ocean (Rhs et al., 2013)), van Sebille et al. (2010) found from a comparison between Eulerian and Lagrangian methods that mixing in the region complicated the Eulerian measurement of the magnitude of leakage. The complication arose from not being able to define the fraction of flow that is related to other sources (Boebel et al., 2003; You et al., 2003). Another real–world problem for Eulerian measurements is the physical boundaries that determine the study site. As mentioned previously, Eulerian measurements can be taken for a region between two coasts using arrays, such as in the Mozambique Channel (Ridderinkhof et al., 2010), and in the straits of the Indonesian Archipelago (Gordon et al., 1999). However in the Agulhas region, the section between South Africa and Antarctica is dominated by the eastward flowing Antarctic Circumpolar Current which distorts the signal across the whole basin (Ganachaud and Wunsch, 2000; van Sebille et al., 2010). Given these issues, van Sebille et al. (2010) determined the magnitude of Agulhas leakage from the transport carried

by numerical Lagrangian floats, to optimise the location of a Eulerian array.

In a different, but fundamentally similar field, Zhang and Chen (2007) compared the Eulerian and Lagrangian modelling methods for predicting particle transport in air. They found that in a steady state, the Eulerian method was superior as it was computationally more efficient. However in a unsteady state, or to study an unknown parameter or process, the Lagrangian method performs better (Zhang and Chen, 2007). Many of the processes that occur within the world's ocean remain unknown and consequently it can be appropriate to apply only Lagrangian methodologies. As mentioned previously, van Sebille et al. (2010) is an example study of a purely Lagrangian study which focused on characterising the Agulhas leakage. That study used the Lagrangian methodology to understand the fundamental circulation of an unknown region, but the method can also be used in a more applied manner. Thompson and Youngs (2013) used a Lagrangian methodology to look at circulation pathways through Drake Passage, and then used that information to understand the dynamics of elevated chlorophyll within the Scotia Sea. Similarly, chapters 3, 4 and 5 of this thesis will use a Lagrangian methodology within a Eulerian framework to study three different processes. The following sections detail some further example studies of research using a Lagrangian methodology to study oceanographic problems.

1.2.2 Circulation pathways

The most direct application of a Lagrangian modelling methodology is to determine circulation pathways or water mass movements. Ocean circulation is driven by a combination of various mechanical and density forcings. Mechanically, the primary driver

is the wind which transfers momentum into the ocean as it blows across the surface. Modifications to the density of sea water are also an important driver of ocean circulation, which are controlled by temperature and salinity variations. Temperature and salinity variation is affected by heat and freshwater exchange with the atmosphere. The pattern of flow, from regional to global, is determined by the rotation and topography of the earth (Williams and Follows, 2011).

On a global scale, these forcings result in the meridional overturning circulation (MOC), which operates on the order of decades to centuries. The MOC is a system of surface and deep ocean currents which traverses all ocean basins, and transports vast quantities of heat, carbon and nutrients. This system connects the surface ocean to the deep interior at regions of water mass modification. A water mass' density can be altered by evaporation or in the formation of sea ice which increases the salinity and by a lowering of the temperature as the water moves away from the equator towards the poles. An increase in salinity and a decrease in temperature of a water mass results in a density increase which causes the water mass to sink (Stommel, 1958; Schmitz, 1995). As water mass sinks in some areas, inevitably it must upwell in others, exposing the deep interior of the ocean to the surface. A principal route through which water upwells from the deep ocean is via wind–driven Ekman transport and isopycnal mixing of water masses by mesoscale eddies, a large proportion of which occurs in the Southern Ocean (Sloyan and Rintoul, 2001; Naveira Garabato et al., 2007; Naveira Garabato, 2009).

The intricacies of this global scale circulation are still being debated today (Sarmiento and Gruber, 2006) as it is vital that we understand this system and the impact it

has in the ocean, in order to predict the response to a changing climate (Wu et al., 2012; Popova et al., 2016; van Gennip et al., 2016). A Lagrangian methodology can be used to establish water mass pathways (such as in the examples given in the previous section) and also can be used in the diagnosis of water mass transformations and mixing by eddies. By comparing the results from a regional ocean model and Lagrangian analyses with in situ observations, (Rimaud et al., 2012) were able to describe the properties and dynamics of Antarctic Intermediate Water (AAIW) in the Cape Basin. This was achieved by identifying Lagrangian particles which maintained the AAIW characteristic salinity and density profile (verified by observations) throughout a Regional Ocean Model Simulation.

Smaller scale features can collectively play an equally important role in marine ecosystems and carbon cycling. Therefore, Lagrangian methods are often used to improve our understanding of these circulation features. Using a sub–mesoscale–resolving model (1/80° horizontal resolution) with Lagrangian particle tracking, Rosso et al. (2014) assessed the degree of vertical transport around the Kerguelen Plateau. The simulation showed that vertical exchange can occur rapidly and from a great depth, which further explains the mechanisms of iron supply in the typically iron depleted Southern Ocean. In addition to nutrient supply, sub–mesoscale features can impact phytoplankton blooms by creating localised areas of stratification and alleviating light limitation in the surface mixed layer. This was studied using Lagrangian particles to represent phytoplankton within the vertically turbulent mixed layer and by recording the light exposure throughout the simulation Brody et al. (2016).

Beyond diagnosing sub–mesoscale features, currents, or even the circulation system of

a basin, Lagrangian methodologies are now being used to diagnose global scale circulation pathways. Jonsson and Watson (2016) used a Lagrangian modelling approach and network theory to calculate timescales of global surface–ocean connectivity. They found that the shortest connectivity timescale between two randomly selected patches of the ocean was on average less than a decade. Chapter 3 of this thesis uses a similar modelling approach, but is focussed on the timescales of connectivity between the deep Southern Ocean and the upper ocean.

Building upon the diagnosis of circulation features and pathways, a Lagrangian methodology can also be used to study oceanographic properties which are advected within the circulation. A Lagrangian approach is the ideal technique to aid in the understanding of the impact of advection. The next section will discuss a range of properties for which advection plays an important role in their distribution.

1.2.3 Oceanographic properties

The previous section discussed studies which used Lagrangian methods to define circulation pathways and features. Determining the circulation gives us a first order understanding of the distribution of fundamental ocean properties, such as heat and nutrients. The distribution and availability of nutrients in turn govern primary productivity, which itself leaves a characteristic imprint on the distribution and cycles of nutrients and carbon. Biogeochemical relationships between nutrients cycles and biology, and also the role of the physical oceanography, are all intrinsically linked so that it is not possible to fully understand one without knowing the other. But before we can fully appreciate the interconnections between the physics, chemistry and biology

of the oceans, we first need to understand a set of fundamental concepts.

The previous section discussed how the ocean circulates in response to atmospheric and density forcing. Another fundamental concept of the ocean is that primary production turns inorganic nutrients into organic matter. Phytoplankton are primary producers, of which all species need the same basic elemental composition: H, C, N, O and P (Redfield, 1958; Arrigo, 2005). They need these nutrients so that they can photosynthesise, the energy from which is used to create organic matter. When the phytoplankton die most of the organic matter is recycled at the surface, but some is exported to the deep via gravity induced sinking. This process is known as the biological pump (Longhurst and Harrison, 1989; Ducklow et al., 2001). Without it, the nutrient distribution throughout the water column would be uniform similar to that of salinity, due to the ocean circulation.

In reality, the distribution is highly variable depending on a regions nutrient supply, biological pump efficiency and light availability. In simple terms, at the surface physical processes increase the concentration of nutrients via upwelling, whereas the biological pump decreases the concentration. This is reversed in the deep ocean where the biological pump acts to increase the nutrient concentration via remineralisation of organic matter, and the physical processes reduces them via upwelling f(Sarmiento and Gruber, 2006). Popova et al. (2013) used a particle tracking method to look at the nutrient supply supporting the subsurface Chl–a maxima in the Arctic Ocean. They estimated that 20% of primary production in the typically oligotrophic Arctic Ocean is supported by horizontal advection of nutrient–rich Pacific and Atlantic inflow water,

which can reach the deep Arctic Ocean on a timescale of about 5 years.

In addition to the previously discussed macro nutrients, primary production requires a number of other elements to function, such as the trace metal iron. Phytoplankton need only a tiny amount of iron but it is essential for light harvesting and nitrogen–fixing. The oceanic iron cycle is highly dynamic, with dissolved iron having a very low solubility, which results in it being rapidly scavenged from the water column and locked away in seafloor sediments (Boyd and Ellwood, 2010). With such a dynamic cycle, understanding how it operates and interacts with other cycles is difficult to untangle, but it is now recognised to be an integral component of the oceans biogeochemistry, regulating the magnitude and dynamics of ocean primary productivity (Jickells et al., 2005; Tagliabue et al., 2017).

Given the importance of iron, much work has gone into furthering our understanding of its cycle. One particular topic has received much research attention, iron limitation (Martin et al., 1990). The Sub-Arctic Pacific, tropical Pacific, and Southern Ocean are areas in which relatively high nitrate and phosphate concentrations persist all year, yet chlorophyll concentrations remain low. These areas are referred to as High Nutrient, Low Chlorophyll (HNLC) regions. The prevailing view is that primary production is limited by the low availability of dissolved iron in the surface waters of these regions. A high proportion of iron in the ocean comes from the atmospheric transport of iron–rich dust, and from sediments in coastal regions (Johnson et al., 1999; Jickells et al., 2005). In the typically deep oceans of HNLC regions, far from continental dust sources (Gao et al., 2013), it has been shown that phytoplankton blooms can be stimulated by

adding dissolved iron to the surface water (Martin and Fitzwater, 1988; de Baar, 2005).

There is strong support for the iron limitation theory, but there are also other factors which will impact chlorophyll concentrations in HNLC regions, such as efficient grazing by zooplankton (e.g. copepods) and also light limitation due to deep mixed layers (Banse, 1996). Lagrangian studies have been used to try and tease apart the specific role iron plays in ocean biogeochemistry. d'Ovidio et al. (2015) used satellite derived Eulerian and Lagrangian water origin maps to understand the bloom dynamics around the Kerguelen Plateau. This was then validated using the trajectories of drifters released during the KEOPS2 project. Collectively, this approach provides important insights into the timing and pathways of iron supply. Similarly, Sanial et al. (2014) used three independent methods to look at the phytoplankton blooms downstream of the Crozet Islands. Altimetric Lagrangian surface currents were derived to estimate the timescales of the surface water transport between the island sediments and the offshore bloom site.

Chapter 4 of this thesis also uses Lagrangian particles to represent iron from Southern Ocean islands sediments, comparing the trajectories with satellite ocean colour data. The chapter aims to test the hypothesis that lateral advection can explain the inter–annual variability observed in the island's downstream phytoplankton blooms.

1.2.4 Population connectivity

Thus far, we have focused on connectivity in terms of physical circulation, such as the connectivity between ocean basins. Physical connectivity plays a fundamental role in ecology through the exchange of individuals among geographically separated subpopulations that collectively comprise a metapopulation. For most benthic marine species with multiple life cycle stages, this exchange occurs during the earliest life history stage (spore, egg, or larva). Metapopulation is the term used to describe a highly dynamic "population of populations" (Levins, 1970) existing in a balance between extinction and re–colonization, which affect demographic persistence, the co–existence of interacting species, and evolution (Hastings and Harrison, 1994). A key process in determining the dynamics of a metapopulation, is the population connectivity. Advection can influence local and connected community structure, genetic diversity, and also the resiliency of populations to human exploitation (Botsford et al., 2001; Cowen et al., 2007).

It is important to note that a Lagrangian approach can be misleading in studying population connectivity. Cowen et al. (2000) used Eulerian and Lagrangian flow models, coupled with linear mortality estimates to assess rates of larval dispersal. They found that physical dispersal alone in a simple advective model (two–dimensional advection–diffusion) may overestimate larval exchange rates. This is due to the models not taking into account the effect of retention of locally spawned larvae. There are also other characteristics of biology which add extra layers of complexity to modelling of dispersal, such as the postflexion–stage in fish larvae which allows them to descend in the water column, and along–trajectory mortality (Fuchs et al., 2007). The living behaviours

of biology must be factored into modelling efforts to predict population connectivity accurately, especially if those efforts are being used to inform management decisions in relation to Marine Protected Areas (MPAs) or fisheries.

Having acknowledged the limitations of Lagrangian methodologies in studying population connectivity, ultimately, understanding the biophysical processes that determine metapopulation patterns requires integrated interdisciplinary approaches, for which high–resolution Lagrangian modelling is a powerful tool. For example, Lagrangian modelling is ideal for diagnosing the timescales of dispersal, which is critically important in understanding population connectivity (Cowen and Sponaugle, 2009; Fossette et al., 2012).

Determining the dispersal of planktonic larvae is difficult to quantify due to their small size and the vast and complex fluid environment they occupy. Consequently, there is a lack of empirical data on population connectivity, which hinders modelling efforts through lack of verification (Cowen et al., 2007). At the larger scale individual level, sea turtles are a well studied example of a species greatly influenced by advection. Juvenile turtles are dispersed by ocean surface currents, and there is evidence to suggest that this passive dispersal stage is formative to future life stages. Using a Lagrangian approach, Scott et al. (2014) compared juvenile drift scenarios with satellite–tracked adult sea turtle migrations. They found a strong relation between the two patterns implying that adult migration is influenced by the their early life cycle stage spent drifting within ocean currents.

However, prevailing currents are not the only factor that can determine dispersal patterns. Monzon-Arguello et al. (2012) used both modelled Lagrangian trajectories and drifting buoys, alongside storm track data to explain the presence of Cape Verde hatchlings in the Bay of Biscay. General circulation patterns alone do not explain the dispersal patterns found in the turtle hatchlings. Instead their results show that storm–forcing may result in novel dispersal or migration patterns.

At the ecosystem level, the west Antarctic Peninsula and South Georgia provide an example of two separate ecosystems each with their own characteristic differences in seasonality and species composition, yet a fundamental similarity in ecosystem structure and function. This is despite the ecosystems having major physical differences due to their difference in latitude. In comparing the two ecosystems, Murphy et al. (2013) found that both regions fit within a broader Southern Ocean ecosystem continuum. The differences between them are driven by differences in the sea ice and biogeochemical conditions. But a generic Southern Ocean food web model is maintained by the underpinning connectivity of advective flows (namely the Antarctic Circumpolar Current) and biological transfers, and flows of material and movements of organisms.

On a wider scale still, Treml et al. (2007) used a Eulerian advection–diffusion approach with graph theory (patterns in spatial connections) to look at the connectivity between reefs throughout the Tropical Pacific. They found the scale of coral larvae dispersal to be on the order of 50–150 km, along major ocean currents and through island chains. This approach allowed them to diagnose upstream and downstream connections of populations. Determining which populations are upstream or downstream of another are

an important factor in understanding the wider metapopulation. A region that produces individuals that are dispersed to another region, can be described as a "source", whereas the receiving region would be considered a "sink". Figueira (2009) developed a spatially explicit source–sink metapopulation model, to determine the relative importance of dispersal versus demography (variable habitat quality which affects local production) in identifying a region as either a source or sink. The model uncovered a highly complex relationship between demography and connectivity, which involves a framework of multiple parameters suggesting that dispersal ability alone does not define a regions source or sink status within a metapopulation.

It is imperative that we do understand the mechanisms behind source and sinks within a metapopulation if we are to be able to predict their resilience to increasing anthropogenic pressures, and provide effective conservation (Hutchings, 2000; Doney et al., 2014). Indeed, understanding the relationships between all biophysical factors that contribute to population connectivity is critical to the successful implementation of management strategies and conservation (Roberts, 1997; Mills et al., 2013). Spatial management, such as MPAs, are a growingly popular management technique designed to conserve biodiversity and sustain fisheries (Christie and White, 2007). However, the true effectiveness of this strategy is yet to be proven (Jameson et al., 2002). This is most likely because too many MPAs are set up in the wrong places or with unrealistic expectations (Sale et al., 2005). A new approach is to use modelling in the design stage of MPAs. However currently, the majority of these models focus primarily on questions concerning fishery management rather than population dynamics (Gerber et al., 2003). Nevertheless, the need for a holistic approach to management and conservation strategies has been identified, and knowledge gaps about what constitutes an effective

MPA are starting to be filled in (Sale et al., 2005; Jones et al., 2007).

One aspect of the connectivity of MPAs that has received comparatively little research attention is the possible negative impacts of upstream connectivity. Upstream connectivity can determine an MPA's exposure to pollution. For instance, it is a known issue that coastal MPAs, within close proximity to populated land, are at risk of pollution and other human impacts (Partelow et al., 2015), but it is unclear whether these same risks apply to open sea MPAs as a consequence of oceanic circulation. Chapter 5 of this thesis aims to tackle this question, by using a Lagrangian approach to identify upstream water sources to four MPAs. A key part of this analysis is to assess the vulnerability of the MPAs to upstream sources of pollution, a global problem which is growing.

1.2.5 Marine pollution

Ocean circulation will transport anything that occurs naturally within the ocean, and also anything that is added to it by humans. Marine pollution, such as agricultural run-off, radionuclides, untreated sewage, oil, plastics and other debris, is a growing global problem (Derraik, 2002; Shahidul Islam and Tanaka, 2004; Michael Beman et al., 2005; Abbriano et al., 2011; Rossi et al., 2013). It has been estimated that in 2010, 275 million metric tons of plastic waste was generated in 192 coastal countries, of which 4.8–12.7 million metric tons entered the ocean (approximately 1.8–4.6%) (Jambeck et al., 2015).

Via advection, marine pollution is now spread throughout the world's oceans, from the Arctic to Antarctica, with marine habitats worldwide being contaminated with man-made debris (Derraik, 2002; Katsanevakis, 2008; Barnes et al., 2009). The impact of marine pollution can be devastating, such as eutrophication, entanglement in or ingestion of marine debris, the subsequent absorption of toxins (namely, polychlorinated biphenyls), and even the transportation of "invader species" on floating debris (Shahidul Islam and Tanaka, 2004; Gregory, 2009; Wright et al., 2013; Gall and Thompson, 2015).

In addition to the direct ecological impacts on marine ecosystems, marine pollution can also adversely impact human activities. The loss of fish stock to large debris, namely discarded fishing equipment, is a significant problem. In crustacean fisheries alone, it was estimated that the removal of 9% of derelict pots and traps could equate to an annual increase of landings worth US $831 million (Scheld et al., 2016). There are also potential risks associated with the consumption of marine sourced foods which have been contaminated with pollutants. Van Cauwenberghe and Janssen (2014) found micro–plastics in the soft tissues of commercially grown bivalves, and estimated that European shellfish consumers could be exposed to 11,000 micro–plastic particles per year.

The issue of marine pollution has been considered since the controversies surrounding the dumping of radioactive waste in the late 1950's. Scientific concern for the welfare of the ocean arising from anthropogenic pressures gathered momentum in the 1970's (Cousteau, 1971; Nations, 1972). However, the health of the ocean continues to

decline (Rogers and Laffoley, 2013). More recently, marine pollution has gained notoriety with the mainstream public through media interest in so called "garbage patches". These garbage patches are accumulation zones that occur due to the convergence of the surface flow in the five great ocean gyres. Lagrangian methodologies were used to understand the formation of the garbage patches, such as Wakata and Sugimori (1990) and Kubota (1994) who used Lagrangian simulations to explain the mechanisms by which debris accumulates in the North Pacific.

More recently, sophisticated Lagrangian methodologies and high resolution global ocean simulations are being used to further our understanding of these accumulation zones in the subtropical latitudes of the major ocean basins. Lebreton et al. (2012) developed a methodology to describe the accumulation of floating marine debris, which can be continuously updated and adapted to assess the changing worldwide production and disposal of waste. van Sebille et al. (2012) combined a Lagrangian modelling methodology with drifter observations, the results from which suggest there may even be a sixth accumulation zone currently undetected in the Barents Sea. Additionally, using a global Lagrangian methodology they were able to describe the differences between the accumulation mechanisms of each site. This gave further insight into the degree of connectivity between basins, suggesting that on centennial timescales the different basins are much better connected than previously thought.

Once accumulated in these garbage patches, the debris can be trapped for decades or much longer. This is because a large proportion of the debris which makes up the patch is plastic. Plastics are produced as many different varieties of polymers, and

from macro to micro in size. The key characteristic which makes plastic so commercially popular is also the reason why they are so harmful and wide spread in the ocean: their durability (Cole et al., 2011). In a review of the plastic problem, Moore (2008) calculated that between 1960 and 2000, the world production of plastic increased 25–fold, while recovery of the material remained below 5%. It was also estimated that marine pollution is made up of 60–80% of plastic, and as high as 90–95% plastic in some regions of the world.

With an alarming amount of plastic entering the ocean, and the known detrimental impacts on ecosystems and wildlife (Gregory, 2009) knowing how the plastic spreads from source is important. Using over 10,000 surface drifters (released during the Surface Velocity and Global Drifter Programs) Maximenko et al. (2012) developed a statistical model to determine the potential spread of marine debris. This allowed them to construct a global map showing the origin of drifters which ended up in accumulation zones. Determining the distribution of plastic in the ocean is an important step towards understanding the impacts of the pollution, however we are missing vital information about the quantity of plastic currently in the ocean. An estimate for micro–plastic was given at 93 – 236 thousand metric tons, which is only approximately 1% of global plastic waste estimated to enter the ocean in the year 2010 (van Sebille et al., 2015). The reason for this wide ranging, and likely under–estimate is partly due to fundamental knowledge gaps in the sources, transformations and fates of micro–plastics in the ocean.

Though we do not yet fully understand the scale of the problem of plastics in the ocean, it is apparent that action must be taken to remedy the issue. There is evidence to suggest that micro-plastics are accumulating in the deep sediments (Van Cauwenberghe

et al., 2013), from which it is irretrievable. Before it reaches the sediments, there is the possibility of removing plastics whilst at the surface. Sherman and van Sebille (2016) used a Lagrangian method to determine the optimum location to deploy "plastic collectors". Their approach suggested a different location, to the previously considered best location. It was thought that the region of highest plastic density would be the optimum location for plastic collectors to remove the most amount of plastic. However the results of the Lagrangian study showed that a region with the highest plastic flux would "catch" more floating plastic.

Plastic pollution is an ongoing problem, with more and more waste ending up in the ocean on a daily basis. Oil spills occur rarely, but when there is an incident it is devastating (Abbriano et al., 2011). One of the most public and notorious spills was the Exxon Valdez oil tanker spill in 1989, which emitted 41.6 million litres of oil, and had a dramatic impact on Alaskan wildlife (Atlas and Hazen, 2011). The incident killed more than 30,000 birds of 90 different species in just over 4 months (Piatt et al., 1990). Over 25 years on since the disaster, and the effect on the marine environment is still being felt, through the persistence of toxic sub–surface oil and chronic exposure resulting in delayed population reductions and cascades of indirect effects (Peterson et al., 2003).

The threat of oil spills is not solely limited to shipping incidents, there can also be rare but catastrophic spills from oil wells, the most infamous recently being the Deepwater Horizon Oil Spill in 2010. Over 87 days, 779 million litres flowed across the Gulf of Mexico region (Atlas and Hazen, 2011). For oil spill incidents, the effect of advection is to worsen the problem, spreading the oil far and wide from source. It was found that 2113 km of shoreline had been contaminated with oil after the spill (Nixon et al.,

2016), with 847 km still contaminated one year after despite concerted clean up efforts (Michel et al., 2013).

In the aftermath of a disaster, response time is key to limiting the damage. Lagrangian methodologies are frequently used to track the spread of the plume and predict what regions are likely to be affected. These studies, such as Liu et al. (2011, 2014), Camilli et al. (2010), and Paris et al. (2012), are able to take into account seasonal variations in the circulation, circulation at different depths, and also the amount of oil emitted. They can be used to mobilise a rapid response, but are also valuable several months after the incident to help direct the clean up operation and also predict which habitats are likely to have been affected.

1.3 Overview

Having surveyed several studies which use a Lagrangian approach and discussed various oceanic processes and issues, this thesis now moves on to applying the approach to three problems. This thesis aims to increase understanding of the impacts of advection specifically on: long–term carbon sequestration at depth, natural iron fertilisation around Southern Ocean islands, and the connectivity between MPAs and land. This thesis is structured in the following way:

- Chapter 2 is on the methodology in which a description of the main tools used throughout the thesis can be found, namely the Ocean General Circulation

Model, and the Lagrangian particle tracking tool. Additionally, it includes a section on how to setup a Lagrangian experiment

- Chapter 3 looks at the long–term fate of carbon sequestered in the deep Southern Ocean
- Chapter 4 focusses on the role of advection in natural iron fertilisation around three islands in the Southern Ocean
- Chapter 5 aims to determine the degree of connectivity between four MPAs and potential detrimental human impacts associated with land
- Chapter 6 is the final chapter, which provides a summary of the research and concluding remarks. It briefly explores alternative approaches to the studies within this thesis and suggests potential future work
- Supplementary material for Chapters 2, 3, 4 and 5 can be found in Appendix A, B, C, and D, respectively

Chapters 3, 4 and 5 are all published manuscripts, each of which can be found in Appendix E (Appendix E.1, E.4, and E.5, respectively). Additionally, an extra paper looking at the Madagascar phytoplankton bloom was co-authored with M A Srokosz alongside the thesis, utilising a similar methodology to the one applied in Chaper 4. The paper can be found in Appendix E.3. Finally, an article for the NERC Planet Earth magazine was written about the work of Chapter 3, which can be found in Appendix E.2.

Chapter 2

Methodology

"Work, work, work, work, work" (Rihanna, 2016)

This chapter will describe the main tools used throughout this thesis, namely the Nucleus for European Modelling of the Ocean (NEMO) model and the Ariane Lagrangian particle tracking package. This section will briefly describe some key features of the NEMO model, full details are described in Madec and the NEMO team (2008) (`www.nemo-ocean.eu`). Each research chapter has a chapter relevant methodology section, detailing any additional tools or data used in the analysis and also the experiment design details.

2.1 NEMO

NEMO is a ocean general circulation model (OGCM) which solves the Primitive Equations on a discrete grid. It is a framework of ocean related engines, such as the physical component, Océan PArallélisé (OPA) which contains ocean dynamics and thermodynamics, and the sea–ice component Louvain la Neuve Ice Model (LIM2), which accounts for ice dynamics, brine inclusions and subgrid-scale thickness variations. The model has a quasi–isotropic tripolar grid (regular Mercator grid in the Southern Hemisphere) which becomes finer in resolution towards the poles known as the NEMO ocean configuration (ORCA), based on Madec and Imbard (1996). NEMO's equations are solved on an orthogonal curvilinear coordinate system. The Primitive Equations consist of the Navier–Stokes equations along with the equation of state (Jackett and McDougall, 1995). NEMO is a z-level model using the three–dimensional Arakawa C–grid (Arakawa, 1972). NEMO exists in many configurations. The descriptions given here describe the configuration used in this thesis.

The model is forced by 6 hourly winds, daily heat fluxes, and monthly precipitation fields using DFS4.1 surface forcing (Brodeau et al., 2010). The data is saved as successive 5 or 30–day means. In this thesis two ORCA-configurations are used: ORCA025 and ORCA0083. These differ in horizontal resolution, where the value of the resolution is given by the resolution at the equator expressed in degrees, 1/4° and 1/12° respectively. ORCA025 and ORCA0083 have a similar grid, with gradually decreasing cell volumes moving away from the equator. In both configurations, the surface layer is allowed to vary in a non–linear free surface scheme. They have 75 vertical layers, concentrated towards the surface, which vary smoothly with depth (increasing from 1 m thickness at the surface to 200 m at abyssal depths). Both resolutions have partial bottom cells, to help smooth the bathymetry. This avoids abrupt step changes in bathymetry, which is significant for shallow slope regions (Madec and the NEMO team, 2008). The bathymetry file for ORCA025 was created by interpolating the 1° NEMO bathymetry file on to the 1/4° grid. Bernard et al. (2006) describe how it was derived from the ETOPO2v2 dataset (1/30° resolution) (Amante and Eakins, 2009), which involved smoothing it to avoid numerical noise. The ORCA0083 bathymetry is made up of ETOPO1 data (1/60° resolution) (Amante and Eakins, 2009) in the deep ocean, and GEBCO08 data (available at `http://www.gebco.net/data_and_products/gridded_bathymetry_data/`) in shallow areas, the formation of which was described in Bourdalle Badie et al. (2012).

Chapter 3 used ORCA025 velocity data (1/4° resolution) saved as successive 30–day means. At the time of the work, the ORCA0083 data were not available, but the ORCA025 data were the appropriate choice regardless given the global scale experiment and century long run time. The following Chapters, 4 and 5, used ORCA0083

velocity data (1/12° resolution) saved as successive 5–day means. This resolution was based on the study sites, which in both Chapters were small islands. As the experiments were over short times scales (from 1–10 years) and focused on specific ocean regions, local circulation patterns and mesoscale features were more important than a global scale, century long experiment. The advantage in using ORCA0083, rather than ORCA025, is that the higher degree resolution is eddy–resolving, whereas ORCA025 is only eddy-permitting. Representation of eddies (lateral turbulence) within the model depends on whether the mesoscale feature is smaller or greater than the grid–spacing.

The NEMO model performance around the Canary Islands was assessed by Duchez et al. (2014), whilst investigating the variability in the Atlantic Meridional Overturning Circulation (AMOC). Focusing on the Florida Straits transport calculated using observational data from the RAPID–WATCH/MOCHA array project, Duchez et al. (2014) assessed the three NEMO simulations at different resolutions: 1°, 1/4° and 1/12°. They found that the seasonal cycle of the AMOC is in good agreement between RAPID and NEMO, with the 1/12° simulation being closest to the observational dataset.

The three different resolution NEMO simulations were also assessed by Quartly et al. (2013) focusing on the eddies in the Mozambique Channel. Previously, it was thought that flow through the channel was dominated by the western boundary current (WBC), however it is now described as a series of large poleward–propagating anticyclonic eddies. They found that the 1° resolution simulation produced a slow WBC in the channel, the 1/4° simulation produced a more intense WBC, and the 1/12° simulation produced a "a chaotic conglomerate of eddies". They also explored additional differences between configurations, specifically the lateral boundary condition, finding that

using free–slip boundary conditions, in place of no–slip, improved the realism of the Mozambique Channel flow markedly.

Marzocchi et al. (2015) compared the North Atlantic subpolar circulation in the 1/4° and 1/12° resolution models. Model output is validated against a range of observational datasets, such as volume transport across five sections calculated from cruise data, absolute geostrophic velocities derived from satellite altimetry and the UK Met Office Hadley Centre observational dataset ENSEMBLES (sea surface temperature and sea surface salinity). Specifically, the 1/12° resolution model was quantitatively validated which showed several improvements from the equivalent lower resolution versions of the model. Inevitably, the study also highlighted some processes that the model was failing to accurately represent. Overall, the 1/12° resolution model was found to realistically reproduce the shape of the Subpolar Gyre, the position of the North Atlantic Current, and the Gulf Stream separation. In the following chapters, parts of the validation performed by Marzocchi et al. (2015) are replicated for each study site. Namely, a qualitative comparison between the modelled surface velocity and surface velocities derived from satellite altimetry.

2.2 Ariane

Ariane is a program which was designed for the offline calculation of three dimension Lagrangian particle trajectories in a given velocity field of an OGCM, and was developed by Bruno Blanke and Nicolas Grima (Blanke and Raynaud, 1997) at the

Laboratoire de Physique des Ocans (LPO, Brest, France). A combined Eulerian-Lagrangian methodology allows for the diagnosis of physical pathways and the dynamics and distributions of tracers along trajectories. The code is freely available online at `www-connexe.univ-brest.fr/lpo/Ariane/`. The version used throughout this thesis is Ariane–v2.2.0 (2008), with a few code adaptations by J. R. Blundell and E. E. Popova to improve reliability, such as removing particles "trapped" on land.

The algorithm uses three dimensional velocities (U, V, W) on a Arakawa C–grid (Arakawa, 1972) (ideal to calculate vector quantities across grid faces) to calculate streamline trajectories, which can be used to describe Lagrangian circulation dynamics simulated by a OGCM. The physical model equations of an OGCM are discretized, which is ideal for the analytical calculation of successive streamline segments over a time–sampled velocity field. Figure 2.1 **A** is a schematic representation of a single trajectory within a three–dimensional grid. Using archived velocity data from a volume conserving OGCM, a streamline trajectory can be calculated by assigning a "particle" with an infinitesimal fraction of the incoming transport. Assuming a linear progression of each velocity component along its corresponding direction, elementary relations describe the trajectory along the three axes, as depicted in Figure 2.1 **B**. The non–divergence of the velocity field ensures continuous trajectories within this cell. To calculate the position and time that a particle exits a grid cell, potential "crossing times" for each direction are evaluated independently, with the minimum of these estimates representing the actual final position on the exit side. This method for computing trajectories is both fast and accurate, by only calculating positions on the edge of individual grid cells. It is important to note that the streamline trajectories calculated by Ariane are only driven by advection and turbulent diffusion is

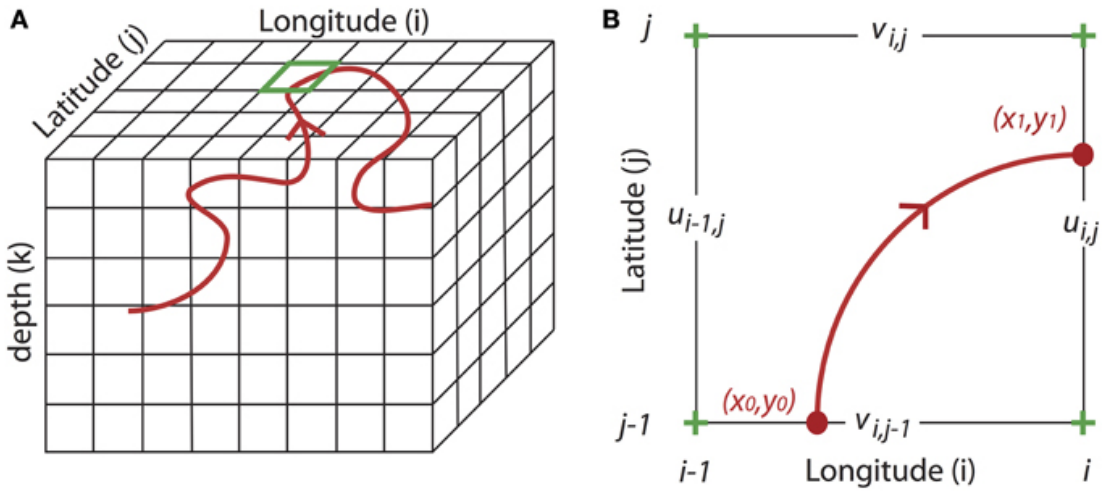

Figure 2.1: Figure taken from Chenillat et al. (2015), their Figure 1. Panel **A**: Lagrangian trajectory (red line) driven by a Eulerian velocity field (u,v,w) in a three-dimensional grid model. Panel **B**: Lagrangian computations within a grid cell (highlighted green in Panel **A**) in the horizontal plane.

ignored. Nevertheless, by injecting a velocity field with hundreds of thousands of Ariane particles, this efficient Lagrangian integration scheme makes it possible to perform water–mass tracing experiments within simulated oceans (Blanke and Raynaud, 1997; Blanke et al., 1999).

2.3 Ariane experiment configuration

Each Ariane experiment must have a separate directory, including a namelist file (detailing various parameters of the experiment and OGCM), an initial position text file (where the particles are to be released from), and a symbolic link pointing to the Ariane code. This section details the basic steps that are necessary to setup a namelist file and also how to create an initial position text file.

2.3.1 Configuring the namelist file

The namelist allows users to define variables in the code. This includes information about the OGCM data (space and time dimensions of the velocity files), information about the particles in the experiment (number and time parameters), and any additional parameters of the experiment, such as temperature and salinity tracers, which can also be used in the analysis when available. Ariane allows for a broad range of parameters to be altered to tailor each experiment to specific problems. An example namelist file used for an experiment within this thesis can be found in Appendix A. The steps listed below detail the main parameters frequently altered for different experiments. Most parameters, such as the model grid details, only needed to be inputted once so will not be described here.

1. Decide if your analysis will include the use of temperature and salinity data. Set *key_alltracers* to *True* to include extra data, or *False* not to include it. To calculate extra data throughout a trajectory significantly lengthens the experiment run time. Temperature and salinity trajectory analysis was not included in this thesis.

2. Lagrangian integrations can be calculated either forward or backward in simulation time. Set *forback* to either *forward* (such as in Chapters 3 and 4) or *backward* (Chapter 5).

3. *nmax* is the maximum number of particles in the experiment, rounded up to the nearest thousand particles.

4. Velocity data time sample is given in *ntfic*, i.e. for ORCA0083 velocity data saved as successive 5–day means, *ntfic* would equal 5 (assuming tunit is set to one day).

5. If a long timescale is required, such as in Chapter 3, the same velocity data can be cycled through multiple times, i.e. 10 years of velocity data can be cycled through 10 times to give a century of velocity data. The *maxcycles* parameter is used to set the desired number of cycles.

6. *frequency* determines the output frequency of trajectory positions. Throughout this thesis, this value was always set to match the velocity data time sampling (*ntfic*).

7. *nb_output* is the maximum number of trajectory positions, rounded up to the nearest hundred positions.

8. *lmt* refers to the number of velocity data files to be read by Ariane. It is important that this value is given accurately, as if this value exceeds the number of available files the experiment will fail.

9. The following sections: *ZONALCRT*, *MERIDCRT*, *VERTICRT*, *TEMPERAT*, and *SALINITY* direct Ariane to the archived velocity data. Use this section to select which model time period is to be used. The *ind0_* and *indn_* should be identical values in each section or the experiment will fail.

   (a) *ind0_* is the first velocity data input file to be read

   (b) *indn_* is the last velocity data input file to be read

   (c) Whether a forward or a backward integration, these values do not change

   (d) The difference between *ind0_* and *indn_* is the *lmt* value

Full guidance for setting up an Ariane namelist file can be found on the website (`www-connexe.univ-brest.fr/lpo/Ariane/`).

2.3.2 Create an initial position text file

Each particle of an experiment is represented by a line of five values in the text file. There must be as many lines as desired particles. The first three values are the spatial indices, x (longitude), y (latitude), and z (depth), given in model grid coordinates, i, j, and k. A particle placed on or very near to land or the ocean floor would be removed from the experiment by the Ariane code, so it is important to ensure a particle is at minimum half a grid cell away from land. If particles are placed closer to land for the purposes of the experiment (e.g. in Chapter 4), it is likely that some of the particles will have been deleted by Ariane. This is particularly important as analysis and interpretation require an accurate number of particles.

The fourth value in the initial position text file is the time index, which relates to the time boundaries given in the namelist file. This time index is where, in time, you want your first time step to begin from. One unit of the time index relates to each velocity input. That is to say, a value of 1 in the time index would begin calculating a particle trajectory from the first velocity data file read by Ariane. The length of a time step, and consequently the duration of an experiment, depends on the velocity input data. For instance, two time steps of velocity saved as 5-daily means would give a trajectory of 10 days, whereas 2 time steps of velocity saved as 30-daily means would give a 60 day long trajectory. For forward tracking experiments, the first particle release would use a time index of 1, with subsequent particle releases being initiated by increasing the time index. For a backward tracking experiment, the time index would be set to

the total number of time steps required for the desired length of the experiment. For example, to calculate a trajectory backwards for a 30 day duration using velocity input data of 5-daily means, the time index would be 6 (6 time steps x 5-daily averaged velocity = 30 days).

The fifth value of the initial position text file is used only for "quantitative" experiments, in which it refers to the volume to be conserved along the trajectory. All experiments in this thesis where "qualitative", with the fifth value always set to 1.

If the experiment was setup correctly and the code successfully ran to completion, the results are saved as ariane_trajectories_qualitative.nc. This netCDF file contains all the particle trajectory data ready for analysis.

Chapter 3

How deep is deep enough? Ocean iron fertilization and carbon sequestration in the Southern Ocean

"How deep is your love? Is it like the ocean?" (Calvin Harris and Disciples, 2015)

The content of this section was published in 2014, the reference is:

Robinson, J., E. E. Popova, A. Yool, M. Srokosz, R. S. Lampitt, and J. R. Blundell (2014), How deep is deep enough? Ocean iron fertilization and carbon sequestration in the Southern Ocean, *Geophysical Research Letters*, **41**, 2489-2495, doi:10.1002/2013gl058799.

The paper can be found in Appendix E.1.

3.1 Introduction

The Intergovernmental Panel on Climate Change 5^{th} Assessment Report (IPCC AR5) states that the climate has and is warming, unequivocally, and we can now be 95-100% certain that since the mid-20^{th} century it is primarily due to anthropogenic influence (Working Group I, 2013). Against this backdrop of increasing greenhouse gas emissions and global climate change, a number of schemes have been proposed to "geoengineer" the Earth's climate. Ocean iron fertilization (OIF) is one such scheme aimed at modifying the biogeochemical cycle of carbon in the ocean in order to increase the oceanic uptake of CO_2. OIF is intended to artificially stimulate the biological pump by exploiting the surplus macronutrients found in so-called high nutrient low chlorophyll (HNLC) regions where biological activity is restricted by the availability of the micronutrient iron (Martin, 1990). The Southern Ocean (SO) is by far the largest expanse of HNLC waters, and is iron-stressed because overlying air masses circle the Earth in a latitude band that has sparse landmass and thus supplies little iron-rich aeolian dust. Consequently, the SO has been identified as a particularly favorable location for OIF (Lampitt et al., 2008).

In the Intergovernmental Panel on Climate Change 4^{th} Assessment Report (IPCC AR4) successful iron fertilization is divided into phases, of which artificial stimulation of a surface phytoplankton bloom is only the first. For the second phase, a proportion of the particulate organic carbon (POC) produced must sink down the water column and reach the main thermocline or deeper before being remineralized. Finally, the third phase is long-term sequestration of the carbon at depth out of contact with the atmosphere. Characterizing the relevant time and space scales for sequestration is

not a wholly objective procedure (Leinen, 2008). Nonetheless, the 100 year timescale adopted in IPCC forecasting is frequently used (Oschlies et al., 2010; Rickels et al., 2010), and the typical depth of the main thermocline, 1000 m (Bindoff and Willebrand, 2007), serves as a vertical horizon clearly removed from the surface ocean and atmosphere (Passow and Carlson, 2012).

Here we investigate these spatio-temporal scales, specifically the long-term fate of carbon that reaches the deep ocean. Model simulations of the trajectories of Lagrangian particles associated with geoengineered carbon are performed to establish the fate of such material. Statistical analysis of the resulting deep ocean pathways is then used to evaluate carbon sequestration in the SO, with a particular focus on the significance of the 1000 m depth horizon and centennial timescale.

3.2 Methodology

The Nucleus for European Modelling of the Ocean (NEMO) model is an ocean general circulation model (GCM). The NEMO 1/4° resolution model has been developed with particular emphasis on realistic representation of fine-scale circulation patterns (Madec and the NEMO team, 2008), and provides an ideal platform to conduct Lagrangian particle tracking experiments. Here we use 10 years of monthly averaged circulation output from 1997-2006 that we cycle 10 times to create a 100-year simulation. The Ariane package (Blanke and Raynaud, 1997) (available online at: http://stockage.univ-brest.fr/∼grima/Ariane) is applied to the resulting 100-year NEMO velocity field to

track water parcels using point particles that are released into the modeled ocean circulation (Popova et al., 2013). These particles are intended here to represent water masses within which sinking POC, produced through the activities of surface OIF, has been remineralized to dissolved inorganic carbon. They should not be confused with actual POC particles, since their modelled behaviour (neutral buoyancy, indefinite lifespan) does not emulate that of sinking biogenic material.

To test the suitability of the 1000 m minimum depth recommendation by the IPCC AR4 (Bindoff and Willebrand, 2007; Barker and Bashmakov, 2007) for OIF, we deploy Lagrangian particles across the SO at a depth of 1000 m. Particles are placed south of the midpoint between the nitrate maxima to the south and nitrate-depleted waters to the north, which represents the northern limit of the HNLC region in the SO. The particles are spaced regularly across the model grid and, accounting for bathymetric features shallower than 1000 m, this gives a total of 24982 particles, a sufficient number to resolve SO water mass pathways. During the 100-year simulation, particle trajectories (horizontal position, depth) are recorded at monthly intervals.

The upper mixed layer (UML) of the ocean is characterized by vigorous mixing and near-homogeneous physical and biogeochemical properties and represents the volume of water in close contact with the atmosphere (Sprintall and Cronin, 2009). Here we use the base of the UML, referred to as the mixed layer depth (MLD), as the key boundary to separate failed and successful carbon sequestration, judging any Lagrangian trajectories that enter the UML as potential pathways for OIF carbon to escape back in to the atmosphere. In our analysis we specifically define our boundary, MLDX, as the modeled (local) mean annual maximum MLD rather than instantaneous MLD. The

advantage of this approach is that it uses a single horizon to determine leakage of OIF carbon, however a sensitivity analysis was performed using the maximum annual maximum depth of the MLD and also the actual monthly MLD which only minimally altered the results.

The accuracy of the model-derived MLD was examined by comparison with the MLD calculated from World Ocean Atlas (WOA) 2009 fields of temperature (Locarnini et al., 2010) and salinity (Antonov et al., 2010), using 2 criteria: a density change of 0.125 (sigma units) and a variable density change corresponding to a temperature change of 0.5°C (Monterey and Levitus, 1997), both calculated 10 m from the surface to avoid complications with ice cover. Repeating our central analysis using an observation-derived MLDX, we found that the difference between using the WOA- and NEMO-calculated MLDX to be relatively small. Therefore, and since it is consistent with NEMO's velocity field, we refer only to the NEMO-derived MLDX in the rest of this paper, which was determined using the density calculation method with a critical value of 0.01 (sigma units). Full details on the MLDX sensitivity analysis and comparison with observations, including the global and SO mean MLD, can be found in Tables 1 and 2 of the supplementary material. Additionally, Fig. 1 in the supplementary material shows the NEMO-derived mean annual maximum MLD that is used in the analysis, MLDX, referred to as *NEMO Diagnostic (Sigma, 0.01)* in Table 2.

3.3 Results

Of the 24982 Lagrangian particles that were injected into the SO at 1000 m, 66% were advected above MLDX taking an average of 37.8 (σ = 22.2) years. In Fig.3.1 each marker represents the location where a particle crossed the MLDX boundary, with the color indicating the time in years. The most significant feature of Fig.3.1 is the large-scale sequestration failure within the SO, which accounts for the majority (97%) of all leakage into the UML (average: 37.4 σ = 22.2 years to fail). The particle advection into the UML can be attributed to the Antarctic Circumpolar Current (ACC), which circulates Antarctica in an eastward direction (Rintoul, 2011). Lagrangian particles caught in the ACC are transported across MLDX as the current is forced up and over sea floor topography, predominately the Scotia Ridge Arc System and the Kerguelen Plateau. The deep dense water (containing the particles at 1000 m) is mixed with the overlying lighter water mass, gaining buoyancy and gradually transporting the particles above MLDX. In addition to advection into the UML, there is also Ekman suction occurring in the SO, which upwells the particles south of the Westerlies wind stress maximum over the axis of the ACC (Sarmiento and Gruber, 2006). This is particularly visible in the Pacific and Atlantic sectors of Fig.3.1, between the latitude bands of 55 °S - 65 °S.

The SO has a particularly energetic circulation connecting the three major ocean basins. Consequently, in our experiment the geographical extent of the particles trajectories covers the entire global ocean (See 1000 m and 2000 m Experiment Movies in supplementary material). By studying the trajectories of successfully sequestered particles it becomes apparent that there is no well-defined deep advective pathway out of the SO. Instead particle advection out of the SO is distributed relatively evenly

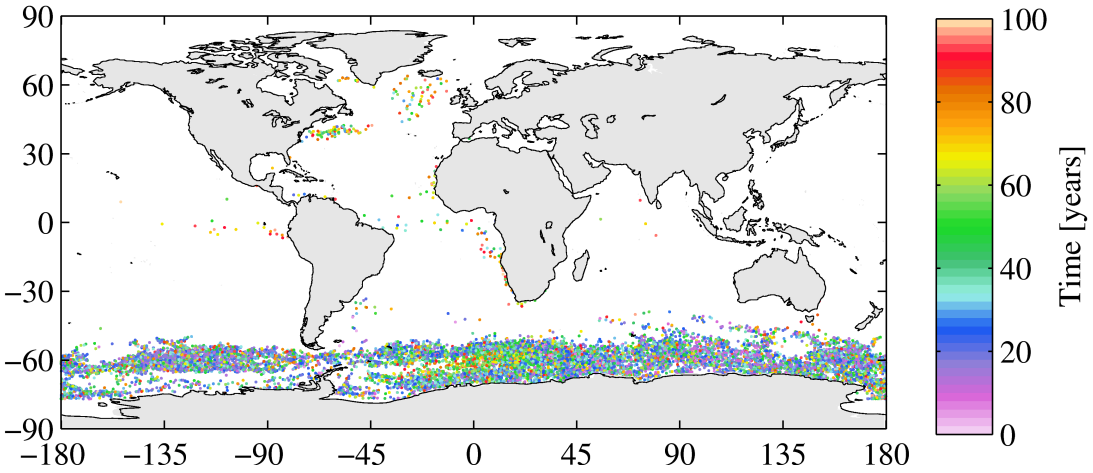

Figure 3.1: Colored markers represent locations where the Lagrangian particles enter the upper mixed layer. The color of a marker represents the time (years) it took to reach the upper mixed layer within the 100-year run.

across all longitudes, not including the western boundary currents. Fig.3.2 indicates the density of trajectories of particles that remained sequestered for the entire 100-year simulation. In Fig.3.2 the highest density of sequestered particle trajectories is within the Ross Gyre, which suggests that this location may facilitate carbon sequestration. In our model the Ross Gyre feeds Lagrangian particles into the narrow westward bound Antarctic Slope Current (ASC). Once within the ASC, particles can be entrained into Antarctic Bottom Water via deep-water formation along the slopes of the Antarctic continent (Nicholls et al., 2009).

Fig.3.3a illustrates geographical patterns in the time taken for failed particles to be advected across MLDX. The Weddell Gyre is a prominent feature within Fig.3.3a, where the time taken for particles to fail is longest in the center of the gyre, and then decreases towards its periphery. This pattern occurs because particles starting in the Weddell Gyre become trapped in its strong cyclonic motion (Williams and Follows, 2011) which prolongs upwelling to an average of 55.2 years (σ = 20.8) in the core of the gyre (experiment average: 37.8 years, σ = 22.2). Of the particles that start in

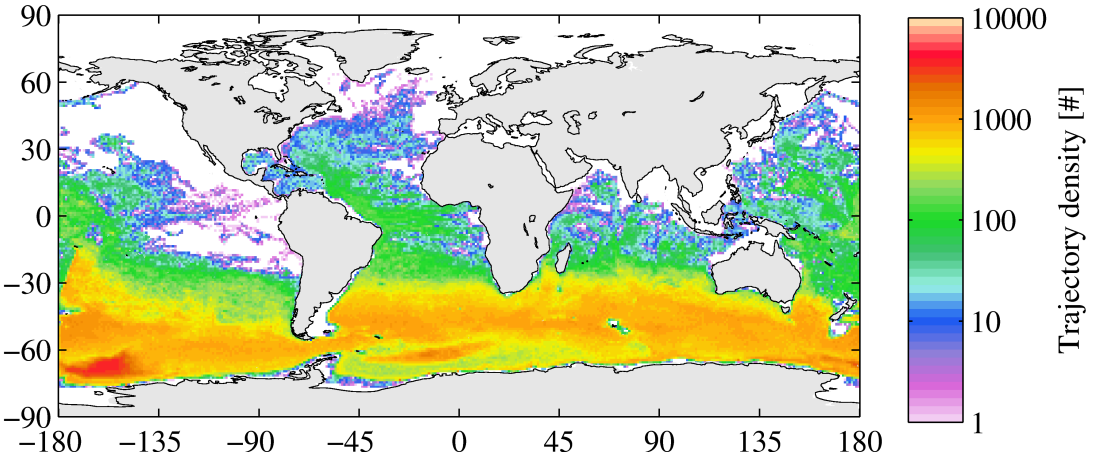

Figure 3.2: Time-integrated (0-100 years) census of successfully sequestered particles to illustrate their horizontal dispersal. Colors denote the cumulative "density" of particle trajectories based on monthly position throughout the simulation. Note that, for clarity, the color scale is shown in log units.

the Weddell Sea, 85% are advected into the UML, which is the highest failure rate of any region within the SO. The Ross Gyre is also a prominent feature in Fig.3.3a, though unlike the Weddell Gyre, this location may instead be suitable for OIF due to the connection with the ASC and consequent deep-water formation along the edge of the continental shelf.

Aside from the Weddell and Ross Gyres, there is little clustering within Fig.3.1a, which suggests that particles that start next to each other in the experiment can experience radically different fates. This high sensitivity to initial conditions may be attributed to the vigorous circulation of the SO which has a number of meandering fronts particularly between the latitude bands of 60 °S and 40 °S (Rintoul, 2011).

Based on our criterion for carbon sequestration, Fig3.3b shows the geographical distribution of sequestration efficiency, indicating how much sequestration results from particles seeded in each area. As in Fig.3.3a, the Ross Sea shows up as an area that

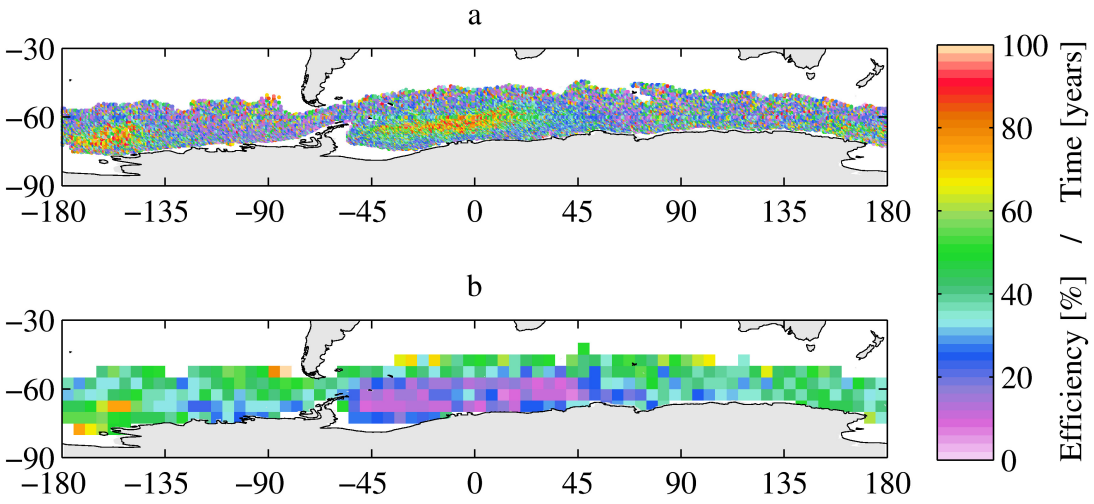

Figure 3.3: a) Markers are located at the initial positions of unsuccessful Lagrangian particles at the beginning of the 100-year simulation. The color of a marker represents the time (years) it took to reach the upper mixed layer. Particles that did not upwell during the simulation are not included in the plot. b) Efficiency of sequestration based on the criterion that a particle has to remain below the upper mixed layer to be classed as sequestered. The color of each 5 °x5 ° grid cell represents the percentage of particles initially in that cell which remain sequestered for the entire 100 year simulation. Grid cells with fewer than 10 particles have not been included in the plot.

has high rates of success, while the Weddell Sea is a mixture of areas of relatively high (center of the gyre) and low (peripheral regions) sequestration. A notable low efficiency patch in Fig.3.3b occurs at roughly 45 °E and 60 °S. Particles starting in this location become trapped in the ACC eastbound flow and consequently are lifted up and over the Kerguelen Plateau. Note that sequestration efficiency here relates to the 100-year window of our simulation, and that numerous particles ostensibly sequestered here might escape in a longer simulation.

Having studied the depth criterion (1000 m) suggested by the IPCC AR4, we conducted a sensitivity experiment that injected Lagrangian particles at a depth of 2000 m. By the end of this experiment (100 years), only 29% of the particles had breached MLDX taking an average time of 58.4 years (σ = 22.1), with 71% of the particles

remaining sequestered for the entire simulation. Further analysis revealed that, of the 29% of particles that did upwell, the vast majority (98%) were again upwelled within the SO, with an average timescale of 58.3 years (σ = 22.1).

3.4 Discussion

The SO has been repeatedly highlighted as the best area for OIF as it is the largest HNLC region on earth, with potential for large-scale OIF leading to a noticeable impact on atmospheric CO_2 concentrations (Lampitt et al., 2008). From the palaeo-record it is evident that the SO plays a key role in regulating atmospheric CO_2 content, potentially sequestrating up to 100 Pg C in the past (Kohfeld et al., 2005). Consequently, the SO has been the site of a number of iron addition experiments (Boyd et al., 2012b) which generally suggest that OIF does result in enhanced export at the time of fertilization.

Based on these experiments, this study assumes that OIF can enhance export of POC to depth and assesses the impact of ocean circulation on the efficiency of intentional OIF in the SO, specifically focusing on how much deep-sequestered carbon is brought back into contact with the atmosphere downstream of the fertilization site. In our 1000 m experiment, designed to trace the fate of the sequestered carbon for 100 years, 66% was upwelled into the UML on a mean time scale of 37.8 (σ = 22.2) years (Fig.3.2). The majority (97%) of the carbon brought back into contact with the atmosphere is upwelled within the SO, taking an average timescale of 37.4 (σ = 22.2) years. Such a "leakage" within the vicinity of the fertilization patch questions whether the SO is as

good a location for OIF as initially thought.

However, even if the carbon is leaked into the UML there is no guarantee that it would be immediately outgassed. To try and assess the robustness of the fail criteria used in the analysis, the percent failed was re-calculated, but allowing the particles 12 consecutive months in the UML without being classed as failed so long as they are re-subducted beneath MLDX within a year. This only reduced the failure rate by 4%, which suggests that advection into the UML generally results in a long stay in the mixed layer, which greatly increases the risk of outgassing. However, if the carbon is brought back to the surface one must assume so too is the Fe associated with it, however this is highly dependent on the timescales of upwelling, and whether this Fe would be bioavailable for further fertilization is non-trivial (Jiang et al., 2013).

Focusing on successful sequestration for 100 years in our experiment, Fig.3.2 illustrates the wide geographical extent of the sequestered carbon dispersed by ocean circulation. At the end of the 100 years, only 46% of the sequestered carbon initialized at 1000 m remained within the SO, with the fraction being slightly higher (56%) for the 2000 m experiment. The dispersion evident in our results demands highly sophisticated methods of observation and modelling if validation of carbon sequestration is to be carried out to an acceptable level. In any future commercialization of OIF, the fraction of the sequestered carbon which remains in the deep ocean must be properly estimated (Rickels et al., 2010). However, as Fig.3.2 illustrates, the global-scale dispersal of the majority of sequestered carbon presents serious logistical difficulties for monitoring. Furthermore, this dispersal may additionally interfere with attempts to attribute ownership and to allocate carbon credits appropriately (See 1000 m and 2000

m Experiment Movies in the supplementary material).

To date, intentional OIF has been examined in a number of modeling studies employing different criteria to quantify the efficacy of OIF (Table 3 in the supplementary material), such as the overall reduction in atmospheric CO_2 by the end of the simulation (Aumont and Bopp, 2006) or the cumulative CO_2 uptake divided by the cumulative iron addition (Sarmiento et al., 2010). These studies have effectively assessed OIF efficiency end-to-end: the impact on primary production; the impact on export of POC to the deep ocean; and the downstream return of carbon to the surface ocean. Our study is unique in that it separates out the impact of ocean circulation from other biogeochemical aspects of OIF to focus solely on phase 3 of OIF and the long-term fate of carbon that has ostensibly been sequestered to depth.

A number of studies (Aumont and Bopp, 2006; Oschlies et al., 2010; Sarmiento et al., 2010) report a high proportion of the sequestered carbon being re-exposed to the atmosphere over a long time scale, however the processes or timescales in these models were not discussed. A particular advantage of our study is the use of a much higher resolution 1/4° physical model. This provides an improved representation of important fine-scale circulation features that are not present in the coarse resolution models (2 °-3 °) previously employed for OIF studies (see Table 3 in the supplementary material). As our study highlights the importance of the circulation in determining global efficiency of OIF, this suggests that models of even higher resolution may be required for an accurate assessment of the geoengineering potential of OIF.

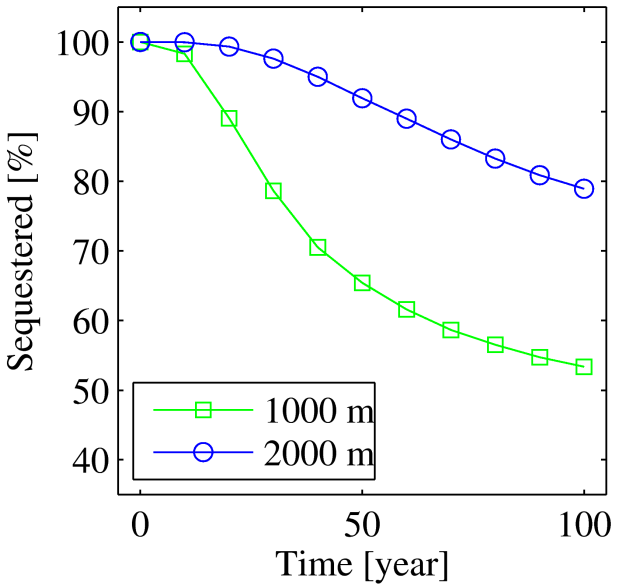

Figure 3.4: Decadal time-series showing the number of particles that remain successfully sequestered below the upper mixed layer for both the 1000 m (green line) and 2000 m (green line) experiments.

In a related study, which does discuss sequestration timescales, DeVries et al. (2012) find a biological pump sequestration efficiency over 100 years globally of about 0.3 (i.e. 30%; their Figure 3c), with higher efficiency in small regions, such as the Weddell Sea - results not dissimilar to those in this paper. However, their study does not address the question of OIF explicitly and is carried out with a steady state ocean circulation model at low resolution (2°).

Fig.3.4 compares the 1000 m and 2000 m experiments, showing a decadal time-series of the fraction of carbon remaining below the UML. Unsurprisingly, carbon exported to depths of 2000 m has a significantly higher probability of remaining sequestered for a period of 100 years than carbon exported to only 1000 m depth. As only relatively modest sequestration of carbon reaching 1000 m occurs, this would suggest that 1000 m is insufficient as an ocean-wide standard for carbon sequestration, and that deeper depth horizons are necessary to provide more reliable sequestration on a centennial

timescale, for in the SO at least. This raises the question of how difficult is it to ensure such depth of export and sequestration. de Baar et al. (2008) state that below 100-250 m, particulate matter is vigorously respired and remineralised by bacteria so that on average only 1-10% of the sinking particulates reach depths below 1000 m. Using the Martin et al. (1987) export curve we can estimate that of the sinking material from 100m, 14% makes it to 1000 m and 8% reaches 2000 m, which means that while more than 85% of the sinking flux is lost by 1000 m, the flux is decreased by less than a half between 1000 m and 2000 m. By choosing 2000 m as a reference depth, the 45% loss in exported material can be compensated by 40% gain in reducing advective leakage. This would increase the estimated efficiency of intentional OIF when the role of ocean circulation is taken into account. However, it is important to note that the Martin et al. (1987) curve is based on observations from the oligotrophic Pacific, whereas a recent experiment in a SO mesoscale eddy concluded that - in contrast - over 50% of the biomass was exported below 1000 m (Smetacek et al., 2012).

There are several caveats for our work. One is that our experiments use present-day ocean circulation and do not take into account future climate change which is widely anticipated to have a significant impact on ocean circulation and mixing. The most pronounced impact on the conclusions of this study could be the effects of a warming ocean and freshening at mid- to high-latitudes, both of which will tend to increase vertical stratification (Doney et al., 2012; Salle et al., 2013). Within the framework of our experiments, increased stratification would potentially decrease the amount of carbon re-exposed to the atmosphere and increase efficiency estimates. More generally, our work uses the ocean circulation from a single model at a single resolution. Future work involving a variety of models with varying resolutions, as well as using

circulation fields from simulations that extend into perturbed projections of the 21^{st} century ocean, may help resolve these uncertainties.

3.5 Conclusions

1. The export of sequestered carbon to a depth of 1000 m in the Southern Ocean does not guarantee its sequestration within the ocean for a period of 100 years

2. More than 66% of sequestered carbon returns into contact with the atmosphere within 100 years, with a mean timescale of 37.8 years

3. Within 100 years, carbon originally sequestered in the Southern Ocean is redistributed throughout the world ocean, with implications for monitoring

4. The chaotic nature of Antarctic Circumpolar Current flow causes sequestered carbon initially in close proximity to be unpredictably and widely dispersed to different fates

5. Sequestered carbon exported to 2000 m experiences lower leakage to the atmosphere (29%), suggesting that more stringent depth criteria may facilitate more accurate carbon credits systems

6. Considering physical transport is just as critical as biogeochemical processes when evaluating the efficiency of OIF schemes

Chapter 4

A tale of three islands: downstream natural iron fertilization in the Southern Ocean

"It was the best of times, it was the worst of times, it was the age of wisdom, ..."
(Charles Dickens, 1859)

The content of this section was published in 2016, the reference is: Robinson, J., E. E. Popova, M. A. Srokosz, and A. Yool (2016), A tale of three islands: Downstream natural iron fertilization in the Southern Ocean, *Journal of Geophysical Research: Oceans*, *121*, doi:10.1002/2015JC011319. The paper can be found in Appendix E.4.

4.1 Introduction

It is now generally accepted that iron, in conjunction with light, is a major limiting factor of primary production in the Southern Ocean, indirectly controlling the biological pump and drawdown of carbon dioxide from the atmosphere (Takahashi et al., 2009; Blain et al., 2007; Boyd et al., 2007; de Baar et al., 1995; Martin, 1990; Martin et al., 1990). However, there are exceptions to the high nutrient, low chlorophyll conditions that prevail across most of the Southern Ocean. Large phytoplankton blooms are observed downstream of continental shelf and land mass (Blain et al., 2007; Pollard et al., 2007a; Korb et al., 2008), where iron is suggested to be supplied to surface waters predominately from ocean sediments (Bakker et al., 2007; Tyrrell et al., 2005; Thomalla et al., 2011). In order to understand these important high productivity regions, we need to characterize the timescales and mechanisms that transport iron to where primary production occurs (Boyd et al., 2012a; d'Ovidio et al., 2015; Wadley et al., 2014). Here we focus on three Southern Ocean islands groups, the Kerguelen Plateau, Crozet Islands and South Georgia and Shag Rocks, outlined by black boxes in Figure 4.1a, specifically looking at the role of advection in determining the spatial extent of the downstream blooms.

Iron supply in the Southern Ocean comes from a variety of different sources including: aeolian input; brine rejection and drainage from sea ice; sediments; entrainment from the deep ocean via winter mixing, Ekman pumping, and upwelling at ocean fronts; and it is also constantly resupplied via rapid recycling of organic material (Boyd and Ellwood, 2010; Gille et al., 2014; Graham et al., 2015; Korb et al., 2008; Schallenberg et al., 2015; Tagliabue et al., 2014). A recent study by Graham et al. (2015) suggests

that coastlines, continental and island, are key sources of iron to the Southern Ocean, and also provides a comprehensive description of the behavior of iron in sediment pore waters and the mechanisms behind its flux into over–lying bottom water. Another source, recently found to be relevant to the Kerguelen Plateau, is riverine input associated with snowmelt. This source is important during spring, as there is increased rainfall and runoff, whereas freezing conditions during the winter inhibit this iron supply (van der Merwe et al., 2015). In this paper we focus on the potential for iron fertilization from island sources, primarily from sediments and run–off.

As iron is released from island sediments, internal waves and turbulence mix the iron up into surface waters which then fuels phytoplankton production (Bowie et al., 2015; Boyd, 2007; Korb et al., 2008; Park et al., 2008a). Iron that is not immediately utilized by biota or scavenged from the water column can be transported downstream of its source via lateral advection within the local circulation and also by stirring within mesoscale features (Abraham et al., 2000; d'Ovidio et al., 2015). As it advects, iron can undergo many processes and transformations as part of the complex iron cycle, which can alter both the transport and bioavailability of iron. For instance, iron can be diluted by physical mixing, it can be kept in circulation by iron–binding ligands, or there can be luxury uptake of the iron by biota and hence "internal advection" (Mongin et al., 2008). In various forms, iron can be lost from the surface by sinking or it can be retained in the surface water and then remineralized downstream of the original source and supply a new area with iron (Boyd et al., 2000; Boyd, 2007).

In order to test the hypothesis that inter–annual variability observed in the spatial extent of downstream island blooms could be explained by horizontal advection, the

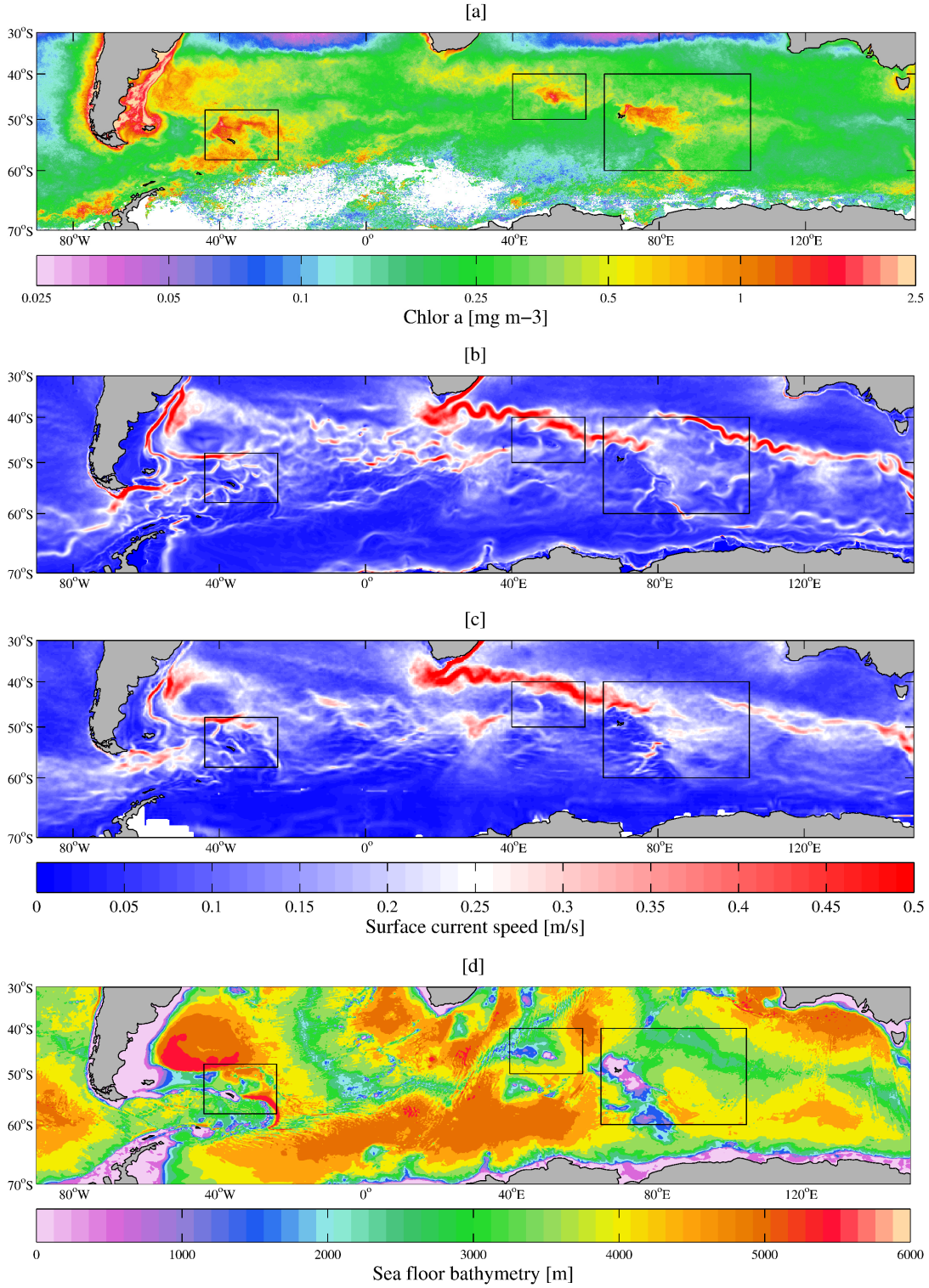

Figure 4.1: A Southern Ocean overview of satellite ocean color, satellite and modeled surface current speed, and the bathymetry in the model. Panel [a] is a decadal average, 1998 – 2007, of the chlorophyll–a concentration [mg m^{-3}] in the month of November. Panels [b] and [c] are the decadal averages (1998 – 2007) of surface current speed [m^{-s}], from the NEMO model, at 1/12°, and the Aviso data, at 1/4° resolution, respectively. Panel [d] is the Southern Ocean bathymetry within the NEMO 1/12° model, contours are in meters below the sea surface. Black boxes denote the study areas: South Georgia left, Crozet islands middle, Kerguelen right.

details of the iron cycle are not considered here. In this paper the term "iron advection" refers to any iron from island sources in a form that can be laterally transported, via either advection or stirring, and is also bioavailable at the bloom site, hence what is demonstrated in this paper is the potential for iron fertilization. To diagnose the advection around each island, Lagrangian particles were released within velocity fields from the NEMO (Nucleus for European Modelling of the Ocean) 1/12° ocean general circulation model, a resolution high enough to resolve eddies and small scale circulation patterns around the islands. In the analysis the Lagrangian trajectories, representing water mass potentially fertilized with iron, are compared against the observed bloom areas in the satellite data. Additionally, the possible causes for bloom termination will be considered for each island, utilising the model diagnostics and also World Ocean Atlas nutrient data.

4.2 Methodology

In order to assess the impact of iron that could potentially be advected downstream of Southern Ocean islands, satellite derived data (chlorophyll–a concentrations and sea surface currents) were compared with Lagrangian particle trajectories within velocity output from the NEMO 1/12° model. Here we give a brief description of each of the three study sites, the tools used, and explain the experimental design.

4.2.1 Study sites

The Kerguelen Plateau and Heard Island (southeast of the Kerguelen Island), depicted by the box on the right of Figure 4.1d (bathymetry plot), is a major bathymetry feature within the Indian Ocean sector of the Southern Ocean, extending from 46°S to 64°S at the 3000 m isobath. It forms a major barrier to the eastward flowing Antarctic Circumpolar Current (ACC), with most of the flow being deflected to the north of the plateau ($\sim$ 100 Sv), and the substantial remainder to the south (30–40 Sv), steered primarily by the topography. The circulation over the plateau between the two islands is rather stagnant, $<$5 cm $^{-s}$ on average. A major circulation feature within the region is the Polar Front (PF), which cuts between the two islands, flowing close to the southeast Kerguelen Island (Park et al., 2008b, 2014). The Kerguelen bloom occurs on decadal average during November to January, as demonstrated in Figure 4.3a., and is predominately made up of diatom species above the plateau (Blain et al., 2001). However, note that the Kerguelen bloom can persist for much longer periods, due to a concurrent resupply of essential nutrients via remineralisation and entrainment from the deep ocean during vertical mixing (Boyd, 2007).

Crozet Islands (46°S, 52°E), depicted by the central black box in Figure 4.1d, is separated from the Del Cano Rise plateau to the west by the Subantarctic Front (SAF), which is the dominant circulation feature in the area. The SAF predominately lies west to east within the ACC, but turns sharply north between the two plateaus (Crozet and Del Cano Rise), before turning eastward to the north of Crozet as it comes into contact with the Agulhas Return Current (Bakker et al., 2007; Pollard et al., 2007b). Over the plateau and to the north of the island (bounded by the SAF) is an area of Polar

Frontal Zone characterised by weak circulation (15 – 20 Sv), within which iron can accumulate during the winter months that can subsequently fuel a bloom (Planquette et al., 2007). The phytoplankton community structure of the Crozet bloom, described by Poulton et al. (2007), is made up of varying sizes of diatoms, and very small prymnesiophyte *Phaeocystis antarctica*. Biomass varies considerably near to the plateau between species, but further away from the plateau, to the northwest and east, prymnesiophyte *P.antarctica* can dominate.

South Georgia, and Shag Rocks (northwest of South Georgia), hereafter referred to collectively as South Georgia, are located to the east of Drake Passage, highlighted by the left black box in Figure 4.1d. The islands form part of the North Scotia Ridge at roughly 54°S, 37°W, directly in the path of the ACC. The PF lies north of the islands, and the Southern ACC Front flows to the south, looping anti–cyclonically around South Georgia before flowing east again (Orsi et al., 1995; Meredith et al., 2003). North of the island, enclosed by the PF and Southern ACC Front, is the South Georgia Basin, within which prolonged blooms exist throughout the growing season (Borrione and Schlitzer, 2013). This paper will focus on the South Georgia Basin bloom, but there are blooms occurring to the south and west of the islands (Ward et al., 2007), although these blooms are partly subsurface and may not be represented by satellite observations. Furthermore the region is one of the most productive regions across the entire Southern Ocean, with various sources of iron and phytoplankton (Ardelan et al., 2010; Murphy et al., 2013; Thomalla et al., 2011). Consequently, from satellite ocean color data alone, it is not possible to delineate blooms fertilised by iron from South Georgia sediments or from elsewhere within the basin (Antarctic peninsula or ice melt). The

South Georgia Basin bloom (hereafter referred to as the South Georgia bloom) is dominated by large diatom species, but is described as "patchy" over scales of 10 – 20 km, with fragmented diatom colonies occurring alongside a more invariant community of small autotrophs and heterotrophs (Atkinson et al., 2001; Korb et al., 2008).

Each of the three islands have different characteristics which determine the ecosystem that they support and its functioning, but for a generalized overview of the Southern Ocean ecosystem see Boyd (2002). These islands have been selected for this study as their blooms have been extensively explored in the field (Blain et al., 2008; Pollard et al., 2007a; Korb et al., 2008; Murphy et al., 2013), the results from which can be used to support our own analysis.

4.2.2 Satellite data

4.2.2.1 Chlorophyll observations

The ocean color data used in this study comes from the ESA Ocean Colour Climate Change Initiative. Here we use a (level 3 geographically mapped) merged and bias corrected product from the MERIS, MODIS and SeaWiFS datasets, with a horizontal resolution of up to 4 km (Storm et al., 2013). Because of the low solar elevation and sea–ice coverage in winter, data is unavailable in some areas, most visibly the Weddell Sea in Figure 4.1a, but by averaging over a month, year and decade, we can fill in many of the gaps. This study has utilized monthly chlorophyll–a (chl–a) concentrations over the period 1998 – 2007, the first decade in which we have good satellite coverage across the world. In this study, the chlorophyll data is used to represent

phytoplankton biomass, defining the island blooms.

4.2.2.2 Altimetric sea surface currents

The satellite altimeter data is produced by Ssalto/Duacs and distributed by the Archiving Validation and Interpretation of Satellite Data in Oceanography (Aviso) group, with support from CNES (`http://www.aviso.altimetry.fr/duacs/`). Here we utilize a merged dataset, from only two satellites at any one time, each having the same ground track and stable sampling which provides a homogenous time series. This along–track, delayed time data product has great stability and therefore is the ideal product for use in inter–annual comparison studies (Le Bars et al., 2014).

The along–track Absolute Dynamic Topography (ADT) is obtained by adding the Sea Level Anomaly to the Mean Dynamic Topography (Mean Sea Surface Height minus Geoid). A mapping procedure using optimal interpolation with realistic correlation functions is applied to produce ADT maps (MADT or L4 products) onto a Cartesian 1/4° x 1/4° grid (AVISO, 2014). Here we use the sea surface geostrophic velocities computed from the ADT over the period of 1998 – 2007.

4.2.3 NEMO model and Ariane Lagrangian particle tracking

The NEMO 1/12° resolution ocean general circulation model has been developed with particular emphasis on realistic representation of fine–scale circulation patterns (Madec and the NEMO team, 2008), which provides an ideal platform to conduct Lagrangian

particle–tracking experiments around the small islands of the Southern Ocean. Full details of the model run, including model setup and configuration, can be found in Marzocchi et al. (2015) as only a brief description will be given here. The model is initialized with World Ocean Atlas (WOA) 2005 climatological fields and forced with 6–hourly winds, daily heat fluxes, and monthly precipitation fields (Brodeau et al., 2010). The run begins in 1978, with output through to 2010, of which we are interested in 1998 – 2007. Model output is stored offline as successive 5 day means throughout the model run, of which the velocity fields are used for the particle tracking in this paper.

The Ariane package (Blanke and Raynaud, 1997) (available online at: `http://stockage.univ-brest.fr/~grima/Ariane`) is applied to the NEMO velocity field to track water parcels using point particles that are released into the modeled ocean circulation (cf. Popova et al. (2013) and Robinson et al. (2014), who used output from the NEMO 1/4° model). These particles are intended here to represent water masses fertilized by iron scoured from the island sediments. Further details about the Ariane package can be found in Blanke and Raynaud (1997) and Blanke et al. (1999).

An important caveat to the results is that we do not expect the NEMO 1/12° model to reproduce the detailed mesoscale flows year–by–year due to chaotic dynamics, as the mesoscale eddy field is not initialised to match that of the real world (only possible using data assimilation). Nevertheless, the model does reproduce the larger scale flow field in the vicinity of the islands, which is important for downstream advection (see Figure 4.1b and c).

4.2.4 Experiment design

In order to study the advection of iron from island sources and make a qualitative comparison with the ocean color 1998 – 2007 observations, Lagrangian particles were released monthly into the modeled circulation from around the shelf regions of each island, from January 1998 to December 2007. Particles are deployed in every other grid cell of the 1/12° model grid along the horizontal (latitudinally and longitudinally), and at each level of the NEMO grid depth domain down to a maximum depth of 180 m (30 depth levels, not equally spaced see Madec and the NEMO team (2008)), around each of the three islands (cf. Srokosz et al. (2015), who used a similar analysis for the Madagascar bloom). Figure 4.2 shows the starting positions of the particles around each of the islands. The particles had to be spaced at a high enough resolution to resolve the fine scale circulation patterns around each island, but the experiments were limited computationally, as the islands are not of a comparable area, so there could not be a particle within every model grid cell. The particles are released in both the horizontal and vertical extent, to represent iron that is scoured from the shelf sediment (down to 180 m in this experiment) and mixed upwards (Ardelan et al., 2010; Blain et al., 2001; Hewes et al., 2008; Planquette et al., 2007) as well as other island sources, such as river run–off (van der Merwe et al., 2015). Particles that are subducted deeper than 200 m, i.e. out of the euphotic zone, along their trajectory are removed from the analysis. At the horizontal and vertical grid spacing described, that results in 8240 Lagrangian particles being released each month from the Kerguelen and Heard Island, 465 particles from Crozet, and 2820 particles from South Georgia and Shag Rocks.

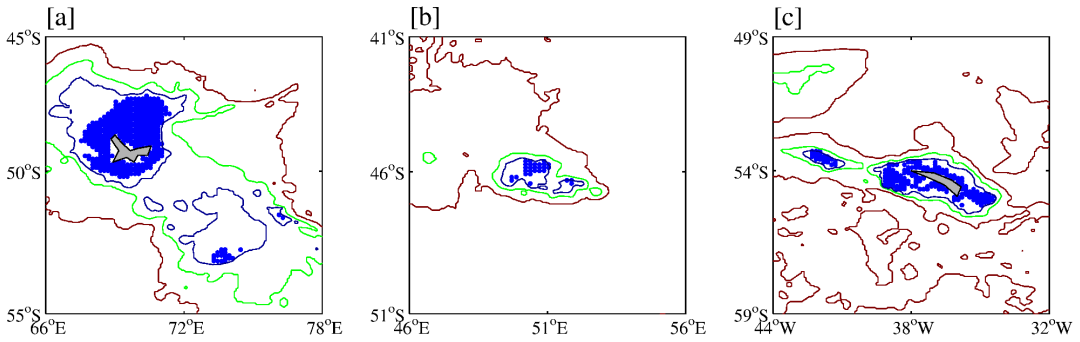

Figure 4.2: The starting positions of the Lagrangian particles around the islands. Particles are placed over shallow bathymetry (< 180 m), around Kerguelen and Heard Island, Crozet Islands, and South Georgia and Shag Rocks; plots [a], [b], and [c] respectively. In plots [a] and [c], only every other particle is plotted for clarity. The plot also includes contours of 500 m (dark blue), 1500 m (green) and 3000 m (red) isobaths. Note that the axis for each panel are not consistent.

4.2.4.1 Assumptions and limitations of method

The main assumption in this study is that surface waters in the Southern Ocean are iron limited, and that the addition of iron to an area, via horizontal advection, would initiate a bloom. However in reality, productivity can be co–limited in the Southern Ocean, with light or silicate for example, and there are also seasonal factors which control phytoplankton growth, which can vary in both time and space (Boyd, 2002).

In the analysis to follow, the advection time over a period of twelve months is discussed. Note that the residence time of bioavailable iron in surface waters is not yet fully understood, but thought to be relatively short, on the order of only weeks to months (Boyd and Ellwood, 2010; Shaked and Lis, 2012; Schallenberg et al., 2015). However, studies have also shown that iron can be transported during winter months and remain in the upper ocean to be available to stimulate blooms in the summer months (Mongin et al., 2009; d'Ovidio et al., 2015). Graham et al. (2015) postulates that this might be possible due to intense biological recycling of iron, or the long–range transport of

particulate iron, or even by currently unknown processes. For the time being these questions remain unanswered, and so for the purpose of this study all of the iron from the islands is assumed to remain available throughout the year. A further assumption is that all advective pathways have the potential to be fertilized with iron.

A caveat to this analysis is that, in using satellite ocean color data, it is not possible to detect subsurface chlorophyll maxima, which are known to exist in certain regions of the Southern Ocean (Holm-Hansen et al., 2005; Tripathy et al., 2015). Therefore we cannot use our analysis to draw any conclusions on the location or variability of known subsurface chlorophyll maxima (Ward et al., 2007), and make the distinction now that only surface blooms are considered, hereafter just referred to as blooms.

As touched upon in the introduction, the representation of iron and its transport in this method is a simplification. Ideally this study would be performed using tracers in a high–resolution, fully coupled biogeochemical model, but the computational resources required for this would be extreme. Such a study would need a coupled model at a resolution high enough to formally resolve the small–scale circulation features that occur around the islands at the center of this study. As such, the analysis presented in our results and discussion is restricted to consider only potential iron advection and consequent fertilization.

4.3 Results

4.3.1 Ocean color

Figure 4.1a is a 10 year average of satellite derived sea surface chl–a concentrations in November, over 1998 to 2007. The islands of interest are highlighted by black boxes, from which it is clear that these island blooms can be more than double the magnitude of productivity anywhere else in the Southern Ocean. Figure 4.3 is the decadal monthly averages, of surface chl–a concentration, for a single location inside, and a single location outside of the bloom sites for each island. Each location was selected arbitrarily based on persistence either inside or outside (upstream of the ACC) of the annual bloom. The latitude and longitude coordinates of each location inside the bloom are 72°E and 49°S, 52.5°E and 45.5°S, 38.5°W and 52.5°S; for Kerguelen, Crozet and South Georgia respectively. The coordinates of each location upstream of the bloom are 66°E and 48°S, 45.5°E and 46.5°S, 49.5°W and 52.5°S (cf. Park et al. (2008b) their figure 11, Pollard et al. (2009) their figure 1, and Korb et al. (2004) their figure 1, for schematic positioning of the ACC around Kerguelen, Crozet and South Georgia respectively). In this paper, a bloom is defined by chl–a concentrations higher than 0.5 mg m^{-3}, as it is consistently higher than chl–a outside of each islands typical bloom regions (Comiso et al., 1993; Moore and Abbott, 2000). Also, when 0.5 mg m^{-3} of chl–a is exceeded in Figure 4.3, it occurs on a steep gradient from one month to the next, indicating the start of a bloom. Additionally this concentration is low enough to avoid complications with double peaks in chl–a associated with South Georgia, as can be seen in Figure 4.3c. South Georgia is a region that frequently has two bloom peaks per year (Borrione and Schlitzer, 2013), however it is outside of the scope of this work to analyze peak bloom events. Therefore, in order to focus on inter–annual rather than

inter–seasonal variability, we consider the average chl–a concentration over the bloom period. The error bars in Figure 4.3 are 1 standard deviation in chl–a for each month, over the ten year period. The size of the error bars is an indication of the seasonality across the regions and annual cycles. South Georgia in particular, has large error bars which is due to the range in magnitude of annual blooms. For instance, the average chl–a for January over 1998 – 2007 is <1 mg m^{-3}, however in January of 2002, the concentration was as high as 15 mg m^{-3} (Korb and Whitehouse, 2004).

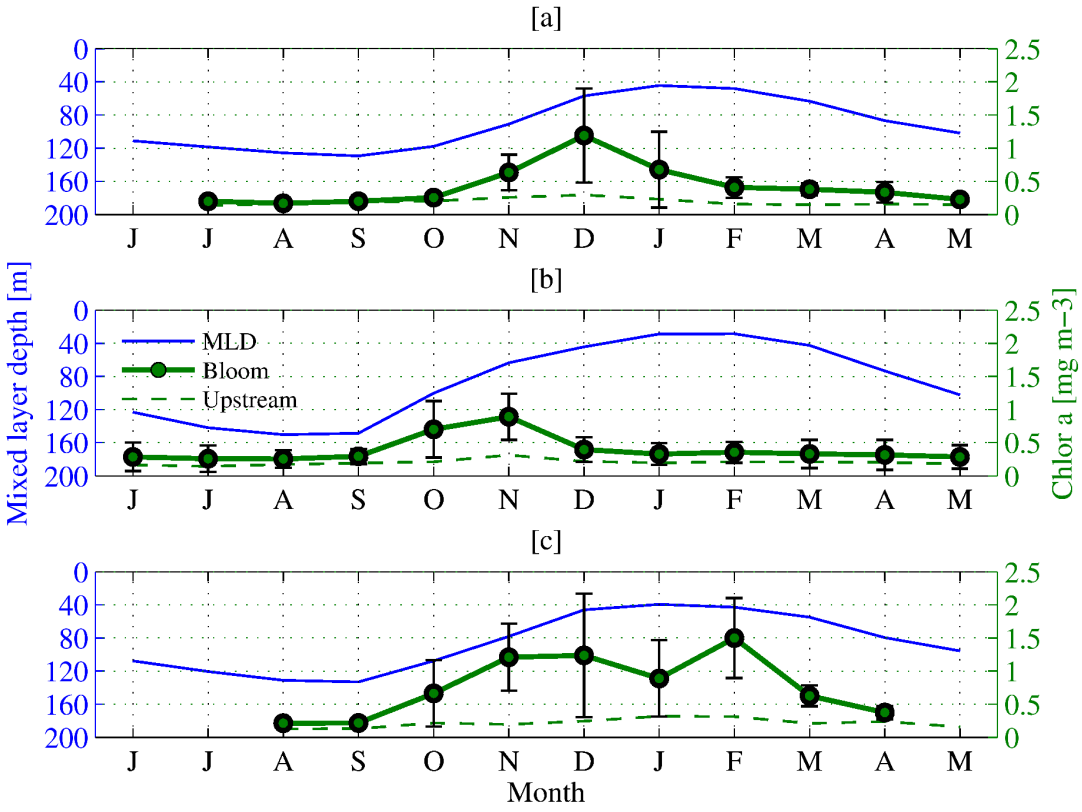

Figure 4.3: The average chlorophyll–a concentration [mg m^{-3}] (satellite ocean color) of each month over the 10 year period. Concentrations are from two locations, one inside (thick green line with markers) and one outside of the bloom region (dashed green line), for each island. The data points from inside the bloom region include error bars which are plus and minus one standard deviation in chlorophyll–a for each month, over the ten year period. The blue line represents the decadal average of the mixed layer depth of each location inside the bloom. Panels [a], [b], and [c] are Kerguelen, Crozet and South Georgia. Note the x axis, 'Month', begins from June through to May.

Figure 4.3 also includes the averaged (decadal) monthly mixed layer depth (MLD) in the 'bloom' site for each island, calculated online in the NEMO model. Comparing the bloom and MLD curves we see that the bloom is likely triggered by the onset of a shallowing mixed layer (Venables and Moore, 2010). The MLD, specifically its role in terminating the blooms, is considered in further detail in the discussion.

Figure 4.4 shows example years of a small and a large averaged bloom period (hereafter referred to as the bloom) for each island, during 1998–2007. Maximum and minimum blooms for Kerguelen occur in 2003 and 2000, Crozet is 2004 and 2001, and South Georgia is 2002 and 2006. Strikingly, Figure 4.4 demonstrates the strong inter–annual variability in both bloom magnitude and area, which may be explainable by studying the potential iron advection from the islands.

4.3.2 NEMO vs. Aviso surface current speed

The ability of the chosen model to accurately represent the circulation in the study area is critical to the quality of the results. In order to assess the performance of the NEMO 1/12° model we can compare with satellite derived sea surface currents (Aviso). The Aviso data is the geostrophic component of the velocity, whereas the NEMO model is the absolute velocity, but this should not impact a comparison between the two as they are near equal at the surface. By comparing the decadal averages of NEMO and Aviso, side by side (Fig. 4.1), we can assess the models performance.

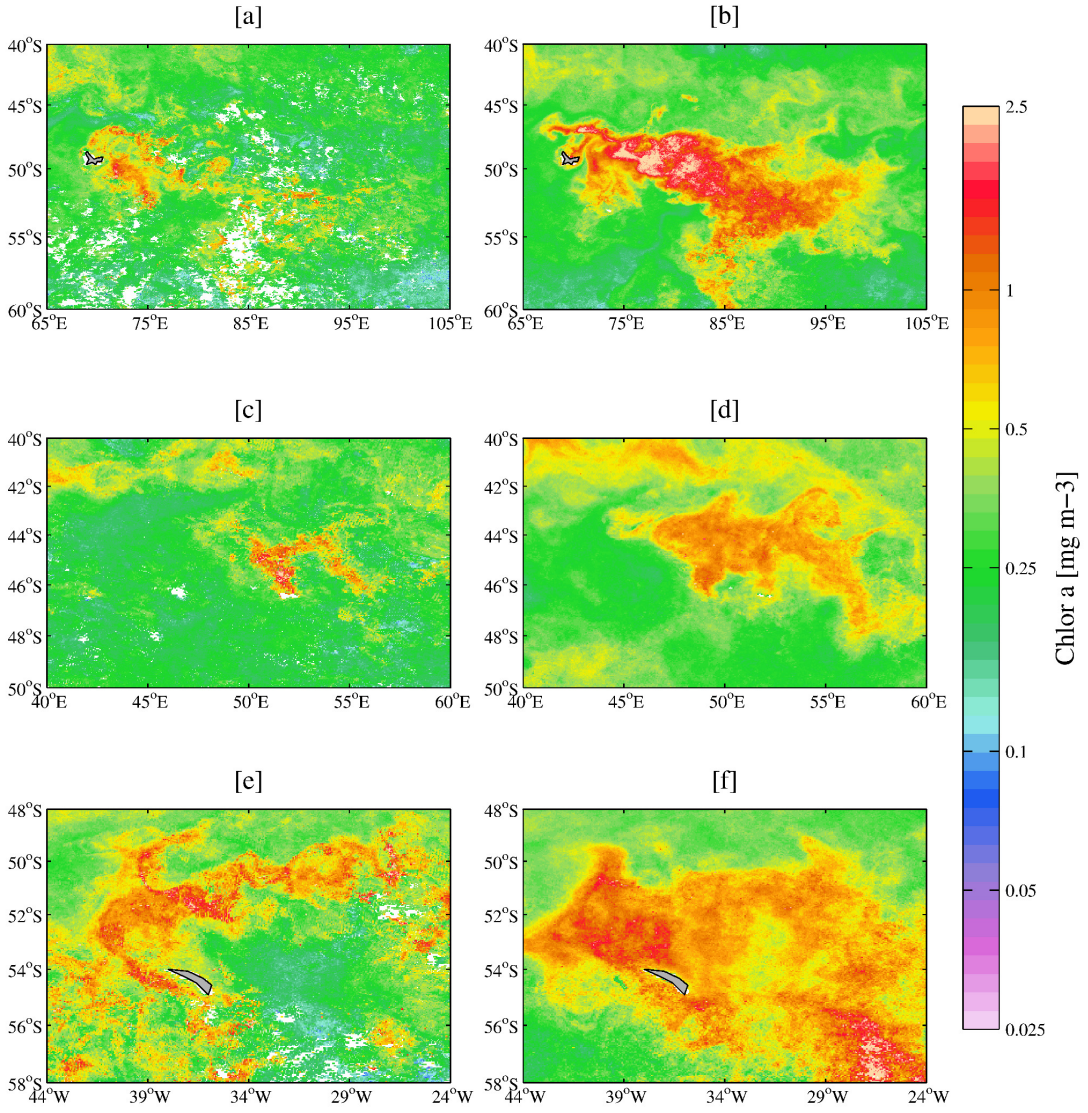

Figure 4.4: Example years of satellite ocean color plots of each island. Chlorophyll–a concentrations have been averaged over the bloom period for each year. The top row is Kerguelen (bloom period: Nov – Jan), years 2000 ([a]) and 2003 ([b]); the middle row is Crozet (bloom period: Oct – Dec), years 2001 ([c]) and 2004 ([d]); and the bottom row is South Georgia (bloom period: Oct – Apr), years 2006 ([e]) and 2002 ([f]). Panels [a], [c], and [e] are examples of a small bloom extent during the 1998 – 2007 year period, and panels [b], [d], and [f] are years with a large bloom extent.

Figure 4.1[b] and 4.1[c] are a comparison of the decadal (1998 – 2007) average ocean surface current speed, from NEMO and Aviso respectively, across the Southern Ocean. Qualitatively, the model correctly captures the major features, and also their magnitude. Fast flowing currents are stronger in the model than Aviso, and also boundaries of fast flowing currents within the modeled circulation are more defined than in the

observations. This may be due to data smoothing caused by the correlation function applied to the Aviso data or due to the model under representing sub–mesoscale features. Figures C.1.1 - C.1.3 in the supporting information show the decadal, annual and monthly averaged circulation, of both model and satellite derived velocities, for each island for illustrative purposes.

4.3.3 Advection of iron towards the bloom site

In this paper we hypothesize that the advection of iron downstream of islands allow blooms to occur in the otherwise high nutrient, low chlorophyll regime of the Southern Ocean. Here we investigate the timescales of fertilization, and the degree to which the circulation can impact inter–annual variability, during the period 1998 – 2007.

The Kerguelen bloom occurs on decadal average during November to January, as demonstrated in Figure 4.3a. For this analysis, we focus on the average surface chl–a concentration over the bloom period (November to January in Kerguelen's case) for each year, referred to as the bloom. Figure 4.5 shows the patch around Kerguelen that could potentially be fertilized with iron by the local circulation in the NEMO model. The fertilized patch is depicted by colored markers, which represent the location of trajectories in October for each year, with the different colors indicating the month in which the particles were released from the island. Strikingly, the fertilized patch is much larger than the bloom extent, represented by black contours in each annual subplot. The trajectories propagate east from the island between the latitude band of roughly 45°S – 54°S, but then spread both northward and southward in extent from roughly 77°E. However, despite the fertilized patch reaching as far north as 40°S in

Figure 4.5, we can see from the black contours that the bloom area is never north of 45°S in any of the years.

Having found that the horizontal advection of iron would be sufficient to fertilize the bloom in principle, a further question arises as to whether the bloom is terminated by the exhaustion of iron in the surface water. This question cannot be addressed directly using the NEMO 1/12° simulation, as it is not a coupled biogeochemistry model. However, if the bloom is terminated by the exhaustion of iron then a question that can be addressed is: can advection resupply iron in the period between the end of one bloom and the start of the next? As addressed by Mongin et al. (2009), and more recently by d'Ovidio et al. (2015). For Kerguelen, the location of the fertilized patch was very consistent, however there are temporal differences in the timing of advection. Nevertheless, the results show the maximum advection time for the particles to reach the furthest extents of the bloom is on the order of 5 – 6 months, suggesting that horizontal advection is sufficient to resupply the bloom area with iron, in agreement with Mongin et al. (2009) and d'Ovidio et al. (2015).

Figure 4.6, is the same as 4.5, but focusing on Crozet. The Crozet bloom occurs one month earlier than the Kerguelen bloom, on decadal average during October to December (Pollard et al., 2007a), and so the trajectories shown in Figure 4.6 represent the fertilized patch in September. Figure 4.6 suggests there is more inter–annual variability in the circulation around Crozet than Kerguelen, both spatially and temporally. In Figure 4.6, the fertilized patch tends to be north of the island and to the east, made up of particles released in June through to August (light green to orange on the color bar). This indicates that the timescale for fertilization, of water mass being within the

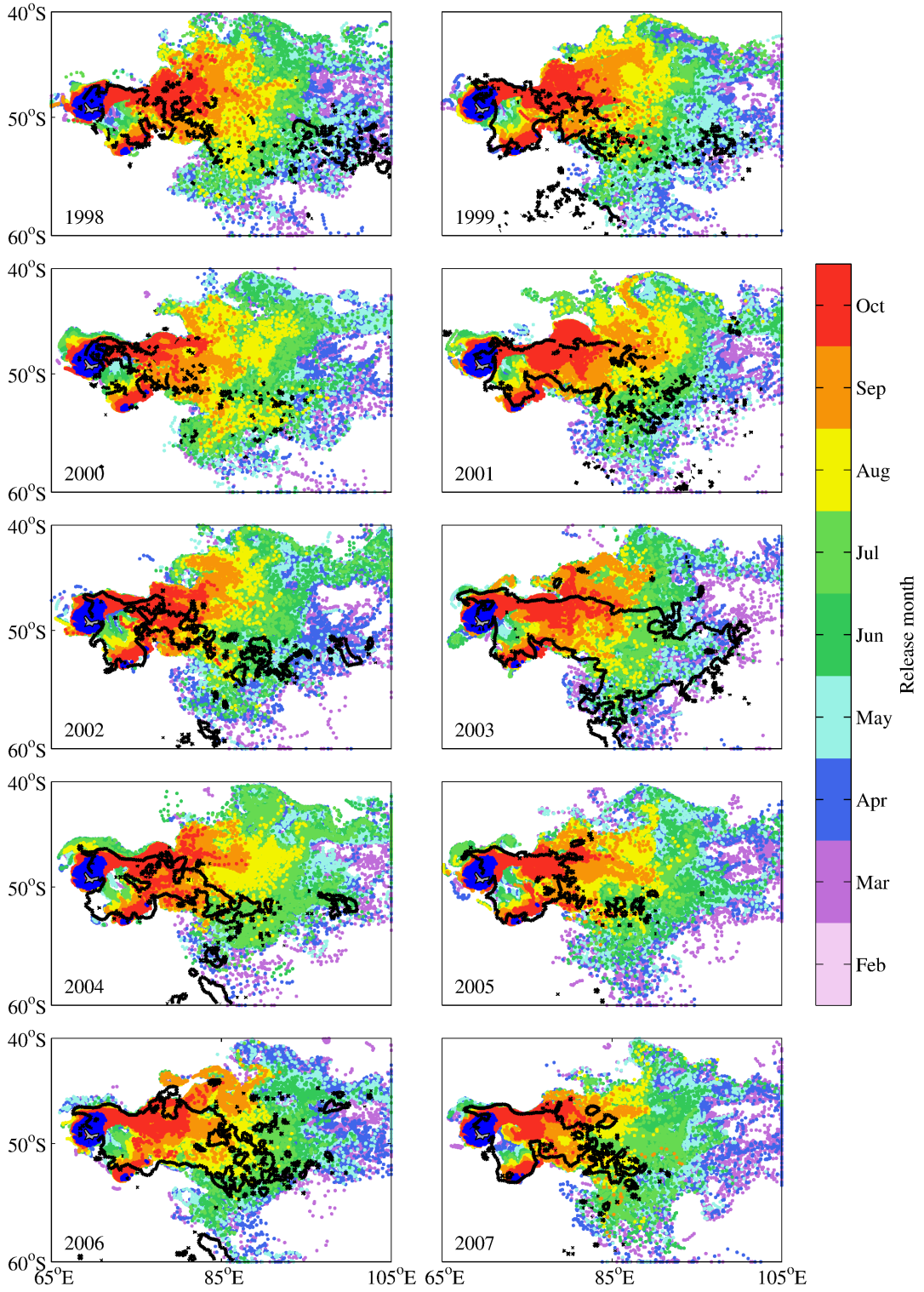

Figure 4.5: Extent of Lagrangian trajectories around Kerguelen. 8240 particles were released monthly from their starting positions, denoted in blue, however only every second particle is shown here for clarity. Particle trajectories in October (preceding the start of the bloom), are depicted by colored markers. The color of the trajectory relates to the month in which it was released as indicated by the color bar. The black contour represents the averaged bloom area, over November – January, of chlorophyll–a concentrations above 0.5 mg m^{-3}. Only trajectories that are shallower than 200m are included in this plot.

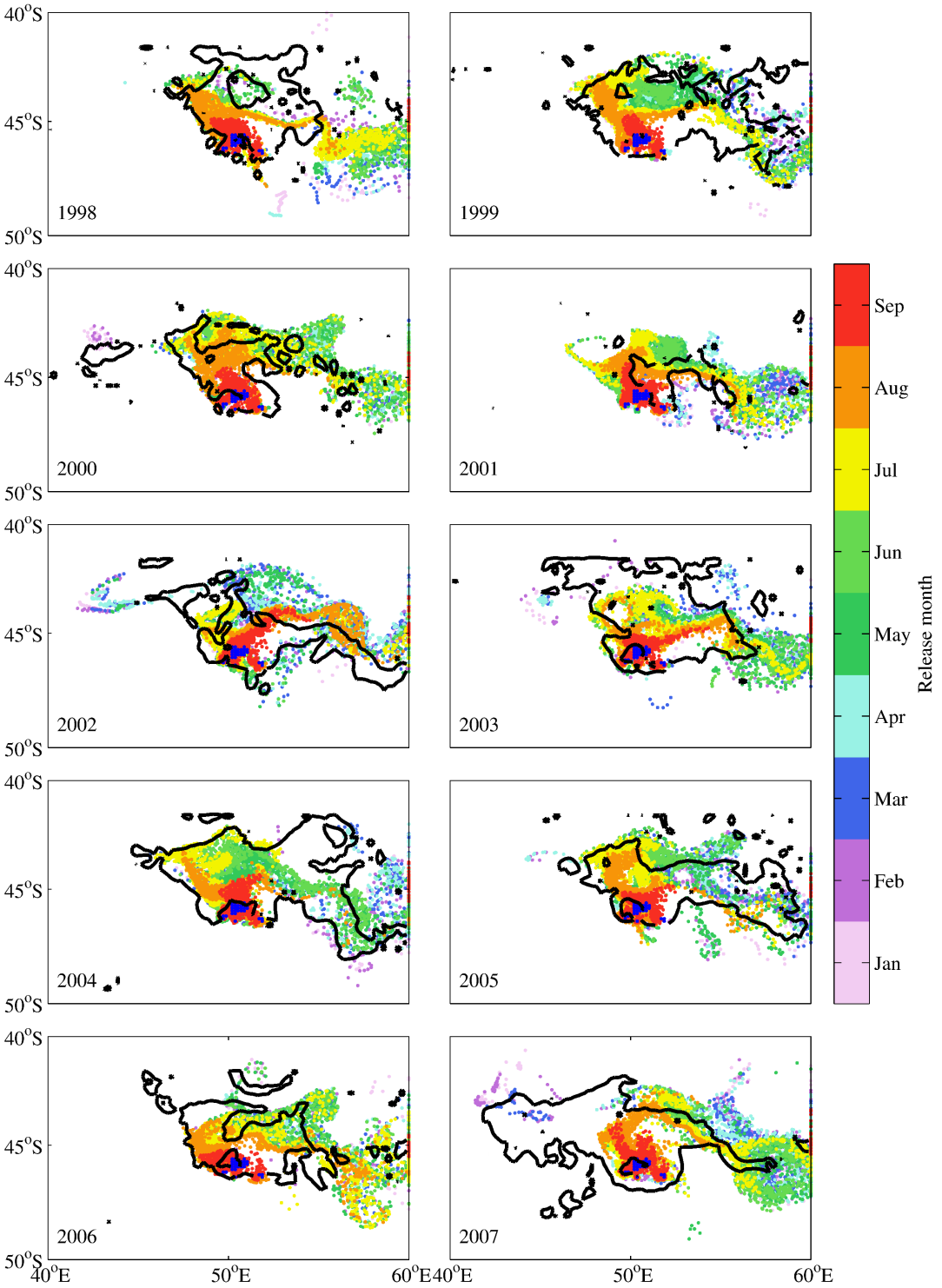

Figure 4.6: Extent of Lagrangian trajectories around Crozet. 465 particles were released monthly from their sing positions, denoted in blue, however only every second particle is shown here for clarity. Trajectories in September (preceding the start of the bloom), are depicted by colored markers. The color of the trajectory relates to the month in which it was released as indicated by the color bar. The black contour represents the averaged bloom area, over October – December, of chlorophyll–a concentrations above 0.5 mg m^{-3}. Only trajectories that are shallower than 200m are included in this plot.

immediate vicinity of Crozet (where the particles are released) to outside of the bloom area (the black contours), is on the order of 3 – 4 months, however Figure 4.6 clearly shows the inter–annual variability in this timescale. There are some years in Figure 4.6 where we see the fertilized patch extending to the west of the island, most visibly in the years 2000, 2002, 2003, and 2007. The color of the markers seen to the west of the island in some of the years show the particles were released earlier in the year, ranging from January (2000) to April (2002). Focusing on the black contours in Figure 4.6, representing chl–a concentrations above 0.5 mg m^{-3} during the bloom period, there are years in which the bloom is propagated to the west also, most clearly apparent in 2000 and 2007.

The bloom associated with South Georgia occurs on decadal average, during October to April, however South Georgia experiences the highest seasonality of all the three islands in this study. Here we discuss the South Georgia bloom, although the surrounding area is one of the most productive regions within the Southern Ocean (Ardelan et al., 2010; Young et al., 2014), so separating a bloom associated with iron only advected from South Georgia is not non–trivial. In order to address this issue, we have applied a mask to the ocean color data, to remove chl–a that was most likely fertilized from other iron sources in the region, guided by the surface chl–a climatology around South Georgia produced by Borrione and Schlitzer (2013). Figure 4.7 is again, the same as Figures 4.5 and 4.6, with the colored markers representing the particle locations in September (preceding the start of the bloom). The extent of the fertilized patch around South Georgia changes annually, although to a lesser degree than around Crozet. What does remain almost annually consistent, is the north and eastward advection of the particles (with the exception of 2006) and an associated bloom occurring

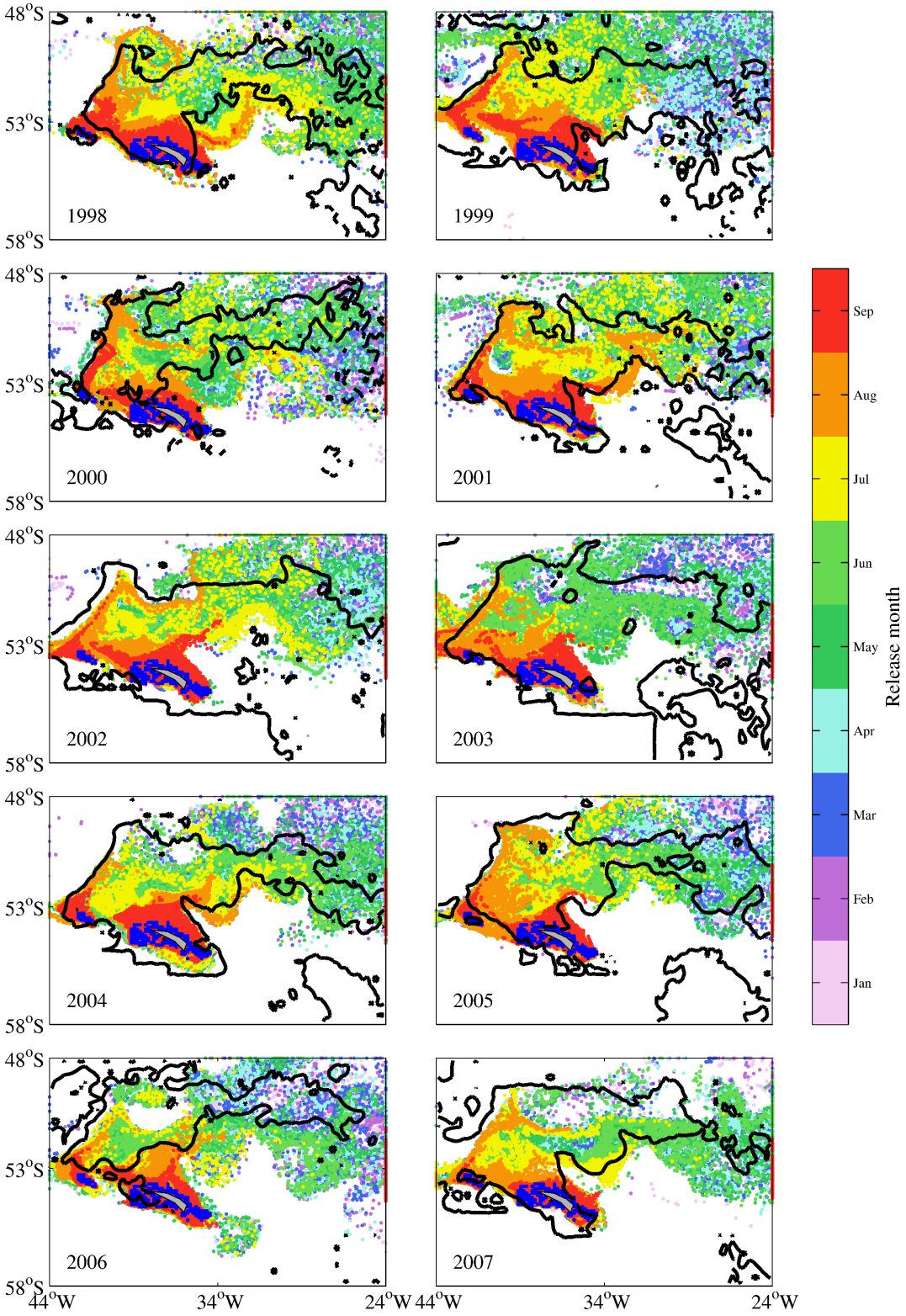

Figure 4.7: Extent of Lagrangian trajectories around South Georgia. 2820 particles were released monthly from their starting positions, denoted in blue, however only every second particle is shown here for clarity. Trajectories, in October (preceding the start of the bloom), are depicted by colored markers. The color of the trajectory relates to the month in which it was released as indicated by the colorbar. The black contour represents the averaged bloom area, over October – April, of chlorophyll–a concentrations above 0.5 mg m^{-3}. Only trajectories that are shallower than 200m are included in this plot.

within the Georgia Basin, which is just north of the island. In some of the years, most distinctly in 2004 and 2005, there is a well defined boundary edge to the trajectories on the western side of the fertilized patch. This sloping western boundary edge is also apparent in the average bloom area in almost all years (2006 being the most apparent exception). The trajectories and bloom are restricted to the east of this boundary due to the eastward flowing PF which acts as a physical barrier (Moore et al., 1999; Korb and Whitehouse, 2004). The colored markers represent the particles locations in the month of September, and therefore particles that are released at the beginning of September have only had one month to be advected, and consequently are the closest to South Georgia. Focusing just on the recently released particles, from August and September (orange and red), it is apparent that, for the majority of the years, this western boundary of both the fertilized patch and bloom area is an important route for iron to be advected away from South Georgia, flowing towards Shag Rocks and then along the PF. This circulation feature was also found by Young et al. (2011) in their higher resolution regional model, described as a unidirectional link between the two land masses (see their Figure 7).

Table 4.1 provides the size of both the annual blooms and fertilized patches around Kerguelen. As can also be seen in Figure 4.5, the fertilized patch is much larger than the bloom, and there is more variability in the bloom size than in the fertilized patch. Consequently, the annual percentage of the bloom area that is within the fertilized patch is consistently very high, with an average of 77% (st dev $\pm$6.5). As the fertilized patch is much larger than the bloom area, it would suggest that iron availability is not the only, or at least most important, factor controlling the Kerguelen bloom extent and inter–annual variability. The year 2003 had the largest bloom in our study period,

Table 4.1: Size of the annual bloom and fertilized patch around Kerguelen, and the percent of each area that is overlapped by the other. Bloom Area is the total area of the average (November to January) chl–a concentration above 0.5 mg m^{-3}; Fertilized patch is the extent of particle trajectories in October (prior to the start of the bloom); Bloom Overlap is the percent of the bloom area overlapped by the fertilized patch; Fertilized Overlap is the percent of the fertilized patch overlapped by the bloom.

Year	Bloom Area (km^2)	Fertilized patch (km^2)	Bloom Overlap (%)	Fertilized Overlap (%)
1998	674572	2731476	74	18
1999	803847	2676533	64	19
2000	339783	2693883	78	10
2001	832765	2593000	84	27
2002	613450	2621786	75	18
2003	1602173	2435464	73	48
2004	729515	2637034	72	20
2005	532218	2568354	84	17
2006	1056154	2539699	82	34
2007	640068	2358635	86	23

Table 4.2: Size of the annual bloom and fertilized patch around Crozet, and the percent of each area that is overlapped by the other. Bloom Area is the total area of the average (October to December) chl–a concentration above 0.5 mg m^{-3}; Fertilized patch is the extent of particle trajectories in September (prior to the start of the bloom); Bloom Overlap is the percent of the bloom area overlapped by the fertilized patch; Fertilized Overlap is the percent of the fertilized patch overlapped by the bloom.

Year	Bloom Area (km^2)	Fertilized patch (km^2)	Bloom Overlap (%)	Fertilized Overlap (%)
1998	223784	216357	35	36
1999	300810	251913	52	62
2000	168707	259734	59	38
2001	70586	231342	60	18
2002	195589	238834	42	34
2003	299167	232525	41	52
2004	355097	252176	48	67
2005	258354	246721	54	56
2006	209982	244683	47	40
2007	342084	282999	32	39

Table 4.3: Size of the annual bloom and fertilized patch around South Georgia, and the percent of each area that is overlapped by the other. Bloom Area is the total area of the average (October to April) chl–a concentration above 0.5 mg m^{-3}; Fertilized patch is the extent of particle trajectories in September (prior to the start of the bloom); Bloom Overlap is the percent of the bloom area overlapped by the fertilized patch; Fertilized Overlap is the percent of the fertilized patch overlapped by the bloom.

Year	Bloom Area (km^2)	Fertilized patch (km^2)	Bloom Overlap (%)	Fertilized Overlap (%)
1998	527788	801679	79	52
1999	671337	864382	70	54
2000	453359	810443	79	44
2001	560929	798532	74	52
2002	946833	704231	50	67
2003	854692	750085	56	64
2004	587281	713427	69	57
2005	626285	700466	66	59
2006	414108	703676	56	33
2007	543833	573456	61	58

in which the bloom did extend out across and to the southern edges of the fertilized patch. It is possible, that in 2003 the primary limiting factor to the Kerguelen bloom was alleviated so the bloom could extend further out into the regions of available iron. This hypothesis will be considered later in the study.

Looking at Table 4.2, the Crozet bloom is a third of the size of the Kerguelen bloom, with an average bloom size of 242,416 km^2 compared to the Kerguelen average of 782,455 km^2. Focusing on the percentage of the bloom site overlapped by the trajectories (*Fertilized patch*) for each year, there is a range of 60% – 32% overlap. This is reflected in the percentage of the fertilized patch overlapped by the bloom, ranging from 67% – 34%. Both the bloom area and fertilized patch around Crozet vary annually, and Crozet has the lowest overlap out of the three islands studied.

The average size of the South Georgia bloom over 1998 – 2007 was 618,645 km^2, smaller

than the average size of the fertilized patch at 742,038 km^2. In Table 4.3, we can see a large range in the bloom area around South Georgia across the years, the maximum being 946,833 km^2 in 2002 and the minimum being 414,108 km^2 in 2006 (see Figure 4.4). There is also a range in the size of the fertilized patch, although not as large as the range in bloom size. Focusing on the amount of overlap between the bloom and trajectories, we see that the annual bloom overlaps are generally larger than the fertilized patch overlaps (2002 and 2003 being the exceptions). This is due to the fertilized patch being larger than the bloom area for the majority of the years. However, as with the other two islands, there is a range in the annual overlaps, which can be explained by a combination of inter–annual variability in the sizes and locations of the annual blooms, and also, to differing degrees for each island, the inter–annual variability in the size and locations of the fertilized patches (Kerguelen being the most consistent, and Crozet exhibiting the most variation).

Figure 4.8 shows the overlap of the bloom (bloom period average, chl–a concentration greater than 0.5 mg m^{-3}) by the fertilized patch from each individual monthly release of particles. In the Kerguelen plot, we see a maximum range of around 10 – 25% between years, in the overlap between monthly releases of particles and the average bloom. The cause of this range is a combination of inter-annual variability in both the advection and bloom extent. In comparison with Figure 4.5 and Table 4.1, it is apparent that the highest degree of variability comes from the bloom, although the inter-seasonal variation in advection timing and consequently fertilization could also impact bloom development. Particles released in October, just prior to the start of the bloom, cover around 10 – 15% of the bloom area, with the maximum bloom coverage from releases in April – June for the majority of the years. This gives an advective

fertilization timescale of between 5 – 7 months for maximum bloom coverage. The circulation on the Kerguelen Plateau itself is known to be sluggish, certain parts even described as stagnant (Park et al., 2014). This localized slow moving water on the plateau (where particles start) may account for the low bloom overlap percentage by particles released just prior to the start of the bloom (November).

In Figure 4.8, Crozet shows less inter–annual variability than Kerguelen, of less than 10% difference between years. The most apparent difference between Crozet, and the other two islands, is that the advective fertilization timescale is much shorter, with maximum bloom overlap from particles released in June – August, which is 2 – 4 months prior to the start of the bloom (typically October). However, Crozet has the lowest bloom overlap, with a maximum of 25% from an August release in 2000. For the majority of the years, the maximum percent coverage of the bloom is below 20%.

The South Georgia plot of Figure 4.8 shows a degree of consistency in the timing of fertilization, but high variability in the bloom overlap from each monthly release, across the years. The variability in bloom overlap is on the order of 10 – 15%, and the advective fertilization timescale is roughly April – June, 4 – 6 months prior to the typical start of the bloom. The maximum percentage bloom overlap is 40%.

4.4 Discussion

Here we consider other factors that could impact the bloom, light limitation and nutrient control, before addressing our three main research questions: Can advection

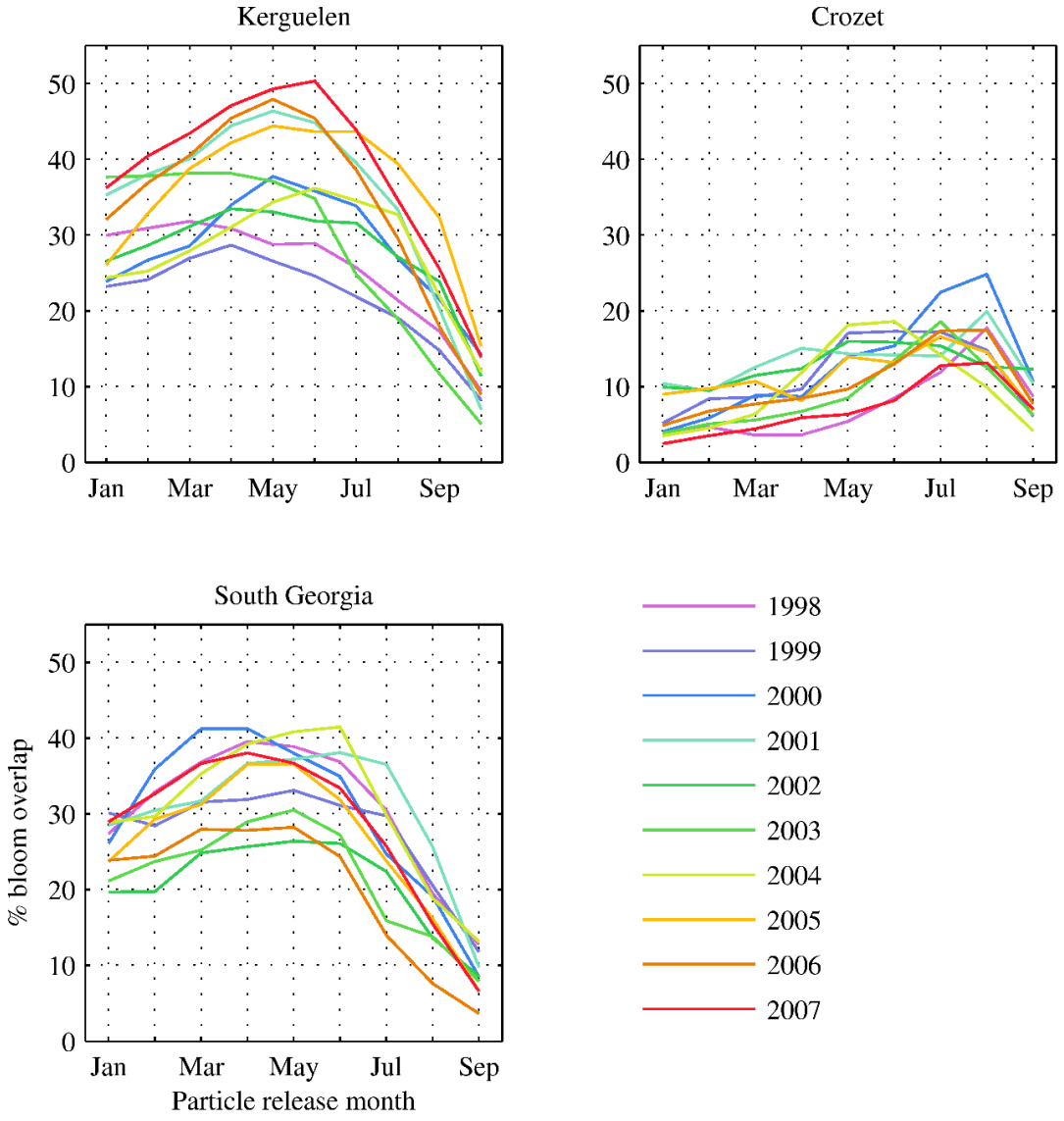

Figure 4.8: The percent of the bloom area overlapped by Lagrangian trajectories from each monthly release for each year. For each monthly release of particles, trajectories that were within the bloom area, in the month that is prior to the start of the bloom, were recorded and used to calculate the percentage area coverage of the bloom by Lagrangian trajectories. Any particles deeper than 200 m were not included. The y axis, *% bloom overlap*, indicates the percentage of the bloom area overlapped by particles from each monthly release shown on the x axis, *Particle release month*. Each colored line represents an individual year.

explain the extent of the bloom area? Can advection explain the bloom inter–annual variability? And what factors could cause bloom termination?

4.4.1 Light limitation

In addition to iron limitation in the Southern Ocean, light limitation also plays an important role in controlling productivity Wadley et al. (2014). The light levels encountered by phytoplankton cells is partly determined by the mixed layer depth (MLD), as they are vertically mixed between high surface irradiance and low subsurface irradiance (Venables and Moore (2010) – explanations and references therein). To assess the light availability around the islands during the typical bloom periods, Figure 4.9 shows the decadal average monthly depths of the mixed layer, calculated online in the NEMO model, over 1998 – 2007.

The top row of Figure 4.9, shows the MLD around Kerguelen which remains in a similar spatial pattern during the bloom period, with a distinct divide between the shallower north and deeper south. During the period 1998 – 2007, the Kerguelen bloom is constrained to the south of this divide where the MLD is deepest. The middle row shows the MLD around Crozet which exhibits the typical shallowing north to south of the MLD from winter into summer. In Figure 4.9 the bottom row is a two month decadal average of the mixed layer for the South Georgia region. Two months have been averaged together in order to capture the entire bloom period within the plot, from which we can see the typical north to south shallowing of the mixed layer from winter into summer. Both the Kerguelen and Crozet Islands blooms have typically terminated when the mixed layer is shallow enough for there still to be light available,

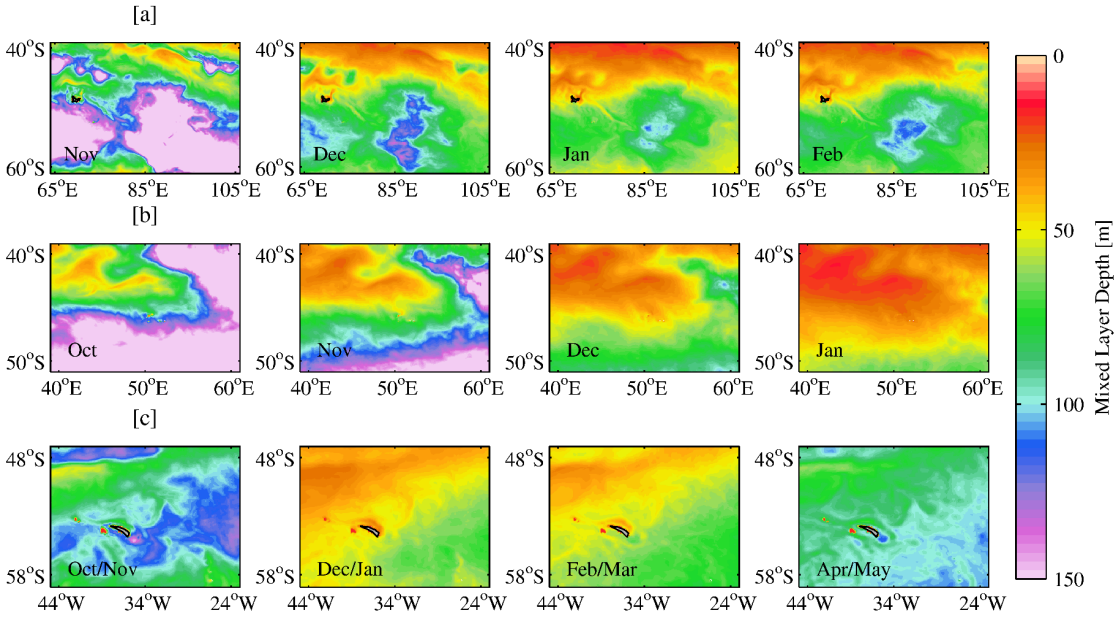

Figure 4.9: Monthly climatologies (decadal, 1998 – 2007) of the modeled mixed layer depth, calculated online by the NEMO model, around Kerguelen, Crozet and South Georgia. The color scale is m below the surface, with warm colors indicating shallow depths and cold colors representing deeper depths.

which suggests that neither bloom is terminated by light limitation (Venables et al., 2007; Venables and Moore, 2010). The South Georgia bloom, however, persists for the entire season and typically ends when the mixed layer begins to deepen in winter, strongly indicating that the bloom is terminated by diminishing light, and not by the exhaustion of iron.

4.4.2 Nutrient control

The depth of the mixed layer is also significant for the amount of nutrients being brought to the surface from the deep, such as nitrate and silicate as well as iron. World Ocean Atlas (WOA) climatologies show the concentration of nitrate to be high across much of the Southern Ocean, south of the Sub-Antarctic Front, whereas silicate concentrations decrease rapidly north of the Polar Front (Boyer, 2013). At Kerguelen,

during the recent KEOPS 2 cruise (October – November 2011) Lasbleiz et al. (2014) found higher concentrations of silicate south of the PF at roughly 72°E, close to the plateau.

One possible hypothesis is that silicate is the primary limiting factor controlling the large and highly variable Kerguelen offshore bloom (i.e. longitudinally far away from the plateau), both in spatial extent and inter–annual variability. This could explain why the bloom is contained to the south (bloom northern limit of 44°S), where a deeper MLD can mix silicate to the surface, despite the iron potentially being advected and available as far north as 40°S (see Figure 4.5). Many previous Southern Ocean iron fertilization studies, both artificial and natural, have reported the development of a large diatom bloom in the fertilized patch (Blain et al., 2001; de Baar et al., 2008; Mongin et al., 2008) and consequently, in the region of Kerguelen, depletion of silicate over the plateau (Mosseri et al., 2008). The absence of a non-diatom bloom is explained by the efficient grazing of microbial communities by copepods and salps as suggested by Banse (1996) and Smetacek et al. (2004). However, the majority of studies have been focused on the bloom above the plateau rather than further downstream, whereas the 2011 KEOPS II cruise focused mainly on the bloom located just northeast of the Kerguelen Islands above the abyssal plain. Their results suggest that the majority of diatom silica production during the bloom event is sustained by 'new' silica, supplied primarily from pre-bloom winter water and also vertical supply. As the bloom progresses, the silicon pump is strengthened by the sinking of biogenic silica, and consequently the standing stock of available silica diminishes over time. Estimates for the duration of the high productivity bloom period is on the order of 85-86 days, after which the bloom declines (Mongin et al., 2008; Closset et al., 2014). These conditions

could also be true of the far offshore bloom, which in some years extends further east than 95°S (2003, in Figure 4.5), but further in–situ observations, of both silicate concentrations and bloom composition, would be necessary to either prove or disprove this.

4.4.3 Can advection explain the extent of the bloom area?

Focussing now on the circulation around each island, we discuss if the modeled advection can explain the spatial extent of the island blooms. Our results suggest that iron advected from the Kerguelen and Heard Islands could fertilize an area which overlaps the annual bloom extent, but is actually much larger than the area of the bloom. Figure 4.10 shows that the bloom which occurs over the plateau (southeast of the Kerguelen island) is predominately fertilized by iron advected from Heard island (Zhang et al., 2008). This is in agreement with a water mass path way study on the plateau using radium isotopes during the 2005 KEOPS cruise, which also found the water mass on the plateau to have originated from Heard island (van Beek et al., 2008).

We find that the larger bloom event, which extends as far as 100°E in some years, is mostly fertilized by iron advected from Kerguelen island (see Figure 4.10), in agreement with Mongin et al. (2009) who also performed a modeled advection study on the Kerguelen bloom.

During the recent KEOPS II cruise, iron budgets were calculated focusing on blooms occurring on the plateau, and also offshore in the "plume", which show the importance of a horizontal supply of iron particularly, for the offshore bloom (Bowie et al., 2015). This separation, in the fertilization of the plateau bloom and offshore bloom, is due to the PF which occurs between the two islands, and flows close to the southern and

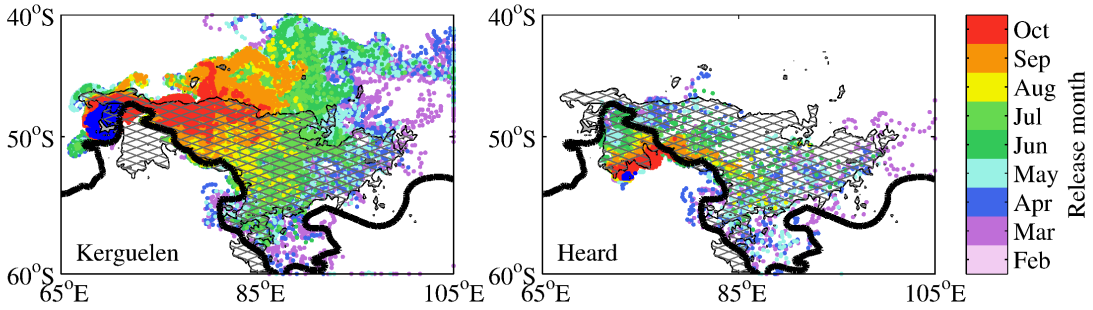

Figure 4.10: Lagrangian trajectories originating from the Kerguelen and Heard Islands in 2003. Collectively, 8240 particles were released monthly from their starting positions, denoted in blue, however only every second particle is shown here for clarity. Particle trajectories are depicted by colored markers, with the color of the marker relating to the month in which it was released as indicated by the color bar. Gray hatching represents the bloom area, averaged over November – January, where chlorophyll–a concentrations are above 0.5 mg m^{-3}. The thick black contour represents the approximate location of the Polar Front in the model for 2003. Only trajectories that are shallower than 200m are included in this plot.

eastern edge of Kerguelen. Using the definition described in Park et al. (2014), the thick black contour in Figure 4.10 represents the modeled location of the PF for the year 2003. The general position and shape of the PF is fairly consistent each year, however the modeled PF does exhibit small annual variations. In Figure 4.10, it is apparent that the extent of the Kerguelen island trajectories, and also in 2003 the bloom, is strongly bounded (in the south) by the location of the PF.

The location of the Crozet bloom was different annually, in some years propagating north west, but most frequently to the north east of the island. The fertilized patch is also predominately to the north east of Crozet, but there are exceptions in some years when small narrow currents flow north west from the island. Meridionally, both the fertilized patch and consequently bloom area occur northwards of the islands, due to the formation of a Taylor Column around the island vicinity (Popova et al., 2007). Zonally, the majority of particles are advected by water which has detrained from a

branch of the SubAntarctic Front (SAF), and are advected eastward which corresponds with the orange Argo float trajectories in Figure 5 of Pollard et al. (2007b). Lagrangian particles which are advected westward are entrained into a secondary branch from the main SAF, which flows anticyclonic around Del Cano Rise (blue drifter trajectories in Figure 5 (Pollard et al., 2007b)), before eventually turning eastward at roughly 44deg. In Figure 4.6, we see that the years in which the fertilized patch is propagated to the west (2000, 2002, 2003 and 2007), the particle trajectories are from releases earlier in the year, roughly from January to April. This is due to the water mass north of the island (but south of the SAF) being very sluggish, resulting in particle entrainment into the anticyclonic component of the SAF around Del Cano Rise, taking several months.

The model does show potential iron advection extending into all regions of the Crozet annual bloom areas, however the fertilized patch in the north west was never as large as the blooms which occurred in the north west. Read et al. (2007) found that sub–mesoscale features were important in the development and duration of the Crozet bloom, and accounted for the bloom's "patchiness". Though the physical model used in this study is at a very high resolution (1/12°), it cannot reproduce the exact eddy field behavior year–on–year, and therefore we do not expect the annual bloom to match the annual fertilized patch. Considering the stochastic nature of eddies, we believe the model to have demonstrated that the local Crozet advection is sufficient to disperse iron into all annual extents of the bloom. Furthermore, the NEMO modeled Lagrangian pathways are in general agreement with drifter data and also altimetry–based Lagrangian model results (Pollard et al., 2007b; Sanial et al., 2014).

A bloom associated specifically with iron advected from South Georgia is impossible

to delineate in this study, as the surrounding region is one of the most productive areas of the Southern Ocean (Figure. 4.1a), due to various other sources of iron e.g. the Antarctic Peninsula (Ardelan et al., 2010; Murphy et al., 2013). Advection from South Georgia is predominately northwards and then eastwards, joining with the ACC, overlapping with the annual blooms that occur in the north easterly region of South Georgia (Korb et al., 2004). There is a striking sloped western edge to both the bloom area and fertilized patch in most years, caused by the position of the PF, which is bounded by the local topography (Moore et al., 1999). Between South Georgia and the PF and ACC, the modeled advection was annually consistent and likely to fertilize the annually occurring bloom in this area.

4.4.4 Can advection explain the bloom inter–annual variability?

The area that could potentially be fertilized with iron via advection around Kerguelen annually extends into a fairly consistent spatial coverage, although there are significant inter–seasonal variations. Despite this, the fertilized patch was much larger than the bloom area in all years of the study period, suggesting that advection alone cannot explain the blooms inter–annual variability. Focussing on 2003, in Figure 4.10, we see the open ocean bloom extending as far south as 60°S between a southward and then northward deviation of the PF (creating a v–shape). However in most years, the bloom area does not closely match the fertilized patch, and in no years does the bloom propagate as far north (bloom northern limit of 44°S) as the Lagrangian particles. Assuming that the modeled spread of Lagrangian particles is correct, this would suggest that another factor is limiting the spread of the bloom into all areas of available iron, a factor which could be the predominate driver of the inter–annual variability. This

would support the theory of silicate limiting the Kerguelen bloom, but without more silicate concentration observations in the far offshore area we can only speculate.

The Crozet blooms during 1998 – 2007 show a high degree of inter–annual variability, most frequently extending far to the east, but in some years to the west and on occasion extending further north than typical. Our results find a similar degree of inter–annual variability in the modeled local circulation around Crozet, both in the timing of fertilization (i.e. the speed of advection) and the extent of the fertilized patch (i.e. size and direction of patch). Although the fertilized patch in our model does not closely match the observed blooms, our results do suggest that iron advection could predominately control the inter–annual variability seen in the Crozet bloom.

The advection of iron from South Georgia annually covers a similar region (a predominately north, then eastward flow), although there are exceptions. The timescale for fertilization is highly variable (distance travelled from the iron source out into the bloom area per month), which could have an impact on the bloom.

4.4.5 Factors controlling bloom termination

As the NEMO model offers a range of diagnostics, we can also propose possible bloom termination mechanisms for each island. In the modeled MLD data, the region surrounding Kerguelen does not clearly follow the north to south shallowing of the MLD in summer typical of the Southern Ocean (Figure 4.9a). There is a very clear divide in the depths of the mixed layer between the shallower north and deeper south at roughly

45°S – 50°S. The Kerguelen bloom is always to the south of 45°S, however in the WOA dataset there is nitrate available north of this, as well as iron according to our advection results (Figure. 4.5). Additionally, the WOA nitrate concentration is still high in February, so it is unlikely to be nitrate exhaustion that terminates the bloom. We conjecture that as the bloom is constrained to regions with a deep mixed layer, it is dependant on a deep supply of silicate as suggested by Mongin et al. (2008), and found to be the case by Closset et al. (2014) in the bloom just offshore of the plateau. There is partial evidence from the WOA that the surface silicate concentration downstream of Kerguelen is lower in February, than in the previous three months, however this is based upon very few data. Looking at data from the first KEOPS cruise, figure 1 in the supplementary material of Blain et al. (2007) shows the concentrations of both nitrate and silicate from locations inside and outside of the bloom. It shows that inside the bloom there is no silicate but there is nitrate, whereas outside the bloom there is plenty of both, suggesting silicate to be the limiting nutrient. This suggests that the sampling conducted during the KEOPS II expedition close to the plateau (Closset et al., 2014), needs to be repeated further downstream in future field work in order to determine whether the offshore bloom has similar dynamics longitudinally.

The modeled monthly MLD around the Crozet region does exhibit some inter–annual variability, but typically, shallows north to south from winter into summer, and is shallower than 50 m by the end of the Crozet bloom. However the WOA climatology suggests there is still nitrate available in January, which suggests that iron exhaustion most likely terminates the bloom. This is supported by an experiment performed on the CROZEX cruise, where the addition of iron to an area of bloom decline resulted in the stimulation of further phytoplankton growth (Moore et al., 2007).

The South Georgia bloom is the most variable in this study, varying in both timing and extent. The decadal average bloom period is from October to April, although it can last longer and also start earlier in some years. The nitrate concentration remains high throughout the bloom period, which suggests a deepening mixed layer being the limiting factor for the otherwise persistent South Georgia bloom. This is supported by Korb et al. (2008), who found evidence of a persistent supply of both macronutrients and iron, by physical processes, to the area throughout the growing season.

4.5 Conclusions

In the high nutrient, low chlorophyll Southern Ocean (Martin et al., 1990; de Baar et al., 1995; Boyd et al., 2007), blooms are observed in satellite ocean color data occurring annually downstream of Kerguelen, Crozet and the South Georgia islands. It is generally accepted that the iron limitation prevailing across the Southern Ocean is locally overcome by the horizontal advection of iron from island sources (Blain et al., 2001; Murphy et al., 2013; Sanial et al., 2014). In this study, Lagrangian particle tracking, with the NEMO 1/12° ocean general circulation model, was used to assess whether potential iron advection can explain the extent of the blooms, and also their inter–annual variability over the period 1998 – 2007. We also use the modeled circulation and diagnostic variables to consider possible causes of bloom termination for each of the islands.

We find that lateral advection downstream of the Southern Ocean islands is sufficient to fertilize all areas where annual blooms can occur. The patch fertilized by iron–rich water from Kerguelen is much larger in extent than the area of the bloom, whereas the patch fertilized around Crozet is comparable in size, taking into account inter–annual variability, to the size of the bloom. The patch of water fertilized by iron–rich South Georgia sediments also closely matches with the annual bloom, however delineating a bloom associated only with South Georgia proved problematic.

The advection around Kerguelen was consistent in spatial extent annually, however the timing of potential fertilization varied inter-seasonally across the years. This could contribute to the blooms inter-annual variability, however the results suggest that the far offshore Kerguelen bloom (in some years occurring as far east as 100°E), has another primary factor controlling its inter–annual variability, and we offer the hypothesis of silicate being the ultimate limiting factor on a diatom dominated Kerguelen bloom. This hypothesis could be tested with in–situ nutrient sampling of the area, similar to the recent KEOPS II expedition (Closset et al., 2014), or alternatively by a high–resolution coupled biogeochemical model to properly resolve the key biogeochemical and physical processes. The results suggest that the inter–annual variability seen in the Crozet bloom can be explained by variations in the advected iron supply. The fertilized patch around South Georgia was fairly consistent spatially, however it did have variations in the timing of advection from the island out to the bloom site. This potentially could account for the inter–annual variability seen in the South Georgia bloom.

In assessing the possible causes of bloom termination, we find that nutrient exhaustion is most likely to cause the Kerguelen and Crozet blooms to collapse (silica and iron, respectively). Whereas winter convection causing the mixed layer to deepen is most likely the terminating factor of the South Georgia bloom, as physical processes maintain a continual supply of macronutrients and iron to the area, these are unlikely to be limiting (Korb et al., 2008). Typically, both the Kerguelen and Crozet blooms end well before the mixed layer begins to deepen in winter, whereas the South Georgia bloom persists for the entire season until the mixed layer deepens.

Chapter 5

Far-field connectivity of the UK's four largest marine protected areas: Four of a kind?

"The game is afoot" (Arthur Conan Doyle, 1904)

The content of this chapter was submitted for publication in Earth's Future, the reference is: Robinson, J., A. L. New, E. E. Popova, M. A. Srokosz, and A. Yool (2017), Far-field connectivity of the UK's four largest marine protected areas: Four of a kind?, Earth's Future, doi:10.1002/2016ef000516. The accepted paper can be found in Appendix E.5.

5.1 Introduction

The world's oceans were once widely considered to be an inexhaustible resource, and consequently undervalued. However, it is now clear that the health of various ecosystems, and the fishery assets that they support, are deteriorating (Boehlert, 1996; Mills et al., 2013; Doney et al., 2014). Global trends in world fisheries show a marked decline since the late 1980s, with over five hundred species added to the Red List of Threatened Species of International Union for Conservation of Nature (IUCN) – the World Conservation Union (*The World Bank*, 2006; and references therein). Consequently, food security issues are mounting with vulnerable communities in developing countries worst affected (Watson and Pauly, 2001; Pauly et al., 2005; Golden et al., 2016).

In response to this danger, and the mounting threat of climate change, new marine management and novel biodiversity conservation efforts are being developed and deployed worldwide in order to curb the negative trends (Halpern et al., 2008; Day et al., 2012; Barner et al., 2015). One such management tool is Marine Protected Areas (MPAs), the definition of which varies considerably internationally, but a basic premise defined by the IUCN describes "a clearly defined geographical space, recognised, dedicated and managed, through legal or other effective means, to achieve the long–term conservation of nature with associated ecosystem services and cultural values" (*Dudley*, 2008: 60). The biodiversity, conservation and fishery goals associated with MPAs are numerous and wide ranging, including habitat and biodiversity protection, ecosystem restoration, improved or restored fishery, the maintenance of spawning stock and spillover benefits into fishing grounds (Christie and White, 2007). To validate the

IUCN definition and realise these goals, it is necessary to minimise the impact of human activities on the MPAs, primarily achieved through designating "no-take zones" to either completely stop or sustainably manage fishing in the area (Edgar et al., 2014).

An important component of the MPA framework is the areas' connectivity with its surroundings. In the marine environment connectivity plays a much more important role than on land, as in the ocean everything is connected over long timescales (Jonsson and Watson, 2016). Much work has gone into diagnosing biological outcomes of the downstream connectivity of MPAs, as it informs whether MPAs are successful in achieving conservation goals, such as seeding species in other areas, and also directs spatial management for further conservation efforts (Fogarty and Botsford, 2007; Christie et al., 2010). In order to seed species downstream, the timescale of connectivity is crucial, as the pelagic larval duration of the species needs to be equal or greater than the connectivity timescale (Cowen et al., 2007; Gawarkiewicz et al., 2007). However, both directions of connectivity are important, and one aspect of MPA connectivity which has received relatively little research attention or policy consideration, is the possible negative impact of upstream connectivity. Upstream connectivity can determine an MPAs exposure to pollution, for instance it is a known issue that coastal MPAs, within close proximity to populated land, are at risk of pollution and other human impacts (Partelow et al., 2015), but it is unclear whether these same risks apply to open sea MPAs as a consequence of oceanic circulation. Additionally, there could be an impact on the conservation efforts of the MPA if a key species in the ecosystem is being overfished upstream of the MPA (Stoner et al., 2012), or risks from alien species which may be come invasive as climate change forces species poleward (Wernberg et al., 2011; Constable et al., 2014).

In order to understand the upstream risks that an MPA is exposed to, and help MPAs achieve their conservation goals (Jameson et al., 2002), it is necessary to diagnose the origin of the water that flows into the region, and the timescales on which this occurs. In doing so, one needs to take into account seasonal and inter–annual variability of the ocean circulation. This study introduces the idea of a "connectivity footprint", by which an MPA is connected to the upstream area via ocean currents, which can be estimated using high resolution ocean circulation models. This paper examines the upstream connectivity of the UK's largest currently designated open seas MPAs, detailing the key circulation features and timescales in the results section, and then discusses the possible negative implications associated with each. First, we introduce the MPAs at the centre of this study, followed by the methodology and experiment design.

5.1.1 Study sites: Marine protected Areas

While in 2010, the United Nations set a target of protecting over 10% of the World Ocean by 2020 (Diversity, 2014), currently, however, only 2.8% is protected (IUCN and UNEP-WCMC, 2013). In view of this conservation target, in its 2015 manifesto the UK Conservative party promised to work towards preserving UK marine habitats, and outlined plans to create a "blue belt" of protected oceans around the UK's Overseas Territories (Alexander and Osborne, 2015). Since then, it has designated an additional two new large MPAs in quick succession. However, monitoring these requires constant data-gathering and evaluation, in order to provide the best protection and conservation.

In this paper, we compare four of the largest, managed, marine British Overseas Territories: Pitcairn Island Marine Reserve (henceforth Pitcairn), South Georgia & South Sandwich Islands Marine Protected Area (South Georgia), Ascension Island Ocean Sanctuary (Ascension) and Chagos British Indian Ocean Territory Marine Protected Area (BIOT). For the purpose of this paper, we avoid the international ambiguity surrounding MPA terminology (*The World Bank* 2006; see chapter 2) and will only consider the IUCN definition (*Dudley*, 2008: 60). We compare all four sites as equals, referring to them in text as MPAs, however, first we briefly introduce them here individually describing their current management as well as their general biomes and ecosystems.

Table 1 details some basic information about each of the MPAs included in this study, the locations of which can be seen in Figure 5.1, with the initial indicating each MPA. What is immediately apparent is the vast difference in size between the areas, with South Georgia being the largest and Ascension the smallest. In terms of threatened species, BIOT is the most precious habitat being home to over 80 IUCN Red List species (List, 2015), however all of the MPAs are important sanctuaries for threatened species.

Situated centrally in the South Pacific subtropics is the Pitcairn MPA, consisting of four remote islands which form part of the Polynesia/Micronesia biodiversity hotspot (Myers et al., 2000). The Pitcairn Island is of volcanic origin, and is the only inhabited island of the four, whereas Henderson Island is a raised coral island, and the islands of Oeno and Ducie are small atolls. Currently, these coral reef communities are healthy environments, largely due to their uniquely isolated location and resulting

	Pitcairn	**S. Georgia**	**Ascension**	**BIOT** [a]
Year Designated	2015 [b]	2012	2016 [c]	2010
Location	24°S, 127°W	54°S, 36°W	7°S, 14°W	6°S, 71°E
SST [d] (°C)	24.75	1.78	25.89	28.19
MPA size (km^2)	834,334 [e]	1,070,000	234,291	545,000
No-take (%)	100	2	52.6 [f]	100
Island size (km^2)	62	3755	88	60
Inhabitants (#)	56	20	1122	4000
Threatened Species [g]	37	9	53[h]	81

Table 5.1: A table of basic information on each of the MPAs in this study. Pitcairn, is known as the Pitcairn Islands Marine Reserve; S. Georgia, as South Georgia & South Sandwich Islands Marine Protected Area; Ascension, as Ascension Island Ocean Sanctuary; and BIOT, as British Indian Ocean Territory Marine Protected Area. Information from Petit and Prudent (2010) and Pelembe and Cooper (2011), unless otherwise stated in the footnotes. *SST*, refers to sea surface temperature at the *Lat/Lon* given for each MPA, which is an average of six decadal climatologies (1955-2012). *Inhabitants*, also includes temporary persons at the time of census.

[a] Status currently under dispute, see Lunn (2016) for latest update
[b] Officially designated, but not yet implemented (Alexander and Osborne, 2015)
[c] Officially designated, but not yet implemented (Foundation, 2016)
[d] Locarnini et al. (2010)
[e] Trusts (2015)
[f] Could be declared, subject to local agreement, as soon as 2017 (Foundation, 2016)
[g] IUCN Threatened species Version 2015-4 *Animals* (List, 2015)
[h] Total threatened species for the Ascension Island including Saint Helena and Tristan da Cunha

near–pristine conditions (Friedlander et al., 2014). In a bid to maintain the unspoilt nature of the Pitcairn Islands, the Exclusive Economic Zone (EEZ) surrounding Pitcairn has been designated as a marine reserve which will ban all commercial fishing in the area, but allow for the continuation of local fishing activities, once implemented. Due to the remote location of the islands', enforcing the ban will require satellite monitoring rather than the usual costly patrol boats. Once an effective monitoring and enforcement regime is established and agreed upon by the Pitcairn community, interested NGOs and the UK government, the Pitcairn marine reserve will become one of

the largest no-take areas in the world (France et al., 2015).

Parts of the most productive waters of the Southern Ocean are found within the South Georgia MPA, located in the Atlantic sector, just east of Drake Passage. The MPA includes the South Sandwich Islands, which are approximately 700 kilometres south-east of South Georgia. This diverse marine ecosystem is sustained by to the nutrient–rich cold water which upwells from the deep ocean, and supports an abundance of wildlife within its harsh polar environment (Murphy et al., 2013). Due to the nature of this inhospitable island, there are no permanent inhabitants, just temporary populations of scientists and tourists. The islands are home to several million seabirds of many different species, a number of which are on the threatened species Red List (List, 2015), and are considered to be one of the most important seabird habitats in the world. Consequently, the MPA was designated in 2012, which prohibits all bottom trawling, a ban on bottom fishing at depths less than 700 m, and no-take zones (IUCN Category 1) around areas of high benthic biodiversity, totalling 20,431 km^2. Additionally, there are seasonal restrictions on certain fisheries to protect local predators (Petit and Prudent, 2010; Collins, 2013).

The most recently designated MPA in this study is the Ascension Island, which is situated just south of the equator in the Atlantic Ocean. Ascension Island is of volcanic origin and includes a few small uninhabited islands just offshore. The islands are young, formed only 1 million years ago, and consequently have relatively poor terrestrial biodiversity. However, due to its isolated location there are many endemic species, and the marine biodiversity is high. The island is also home to one of the most

important populations of breeding Green turtles in the world, and is consequently considered to be an important habitat that needs to be preserved (Pelembe and Cooper, 2011). Ascension was designated as a marine reserve in 2016, closing just over half the area to allow research to scope the eventual boundaries of the MPA, with the intention to assigned the region a no-take area.

The BIOT MPA, also known as the Chagos Archipelago, is situated centrally within the Indian Ocean, half way between Africa and Indonesia and to the south of India. The area includes 55 coral islands spread over five atolls, of which Diego Garcia is the largest, with approximately 4000 temporary residents. The 25,000 km^2 coral reefs of BIOT are unspoilt by human activity and in great health, owing to the protected status and the pristine waters, which could act as a global benchmark for unpolluted water (Guitart et al., 2007). This unique reef system supports a rich ecosystem that includes over 80 species on the threatened species list, and is consequently judged as possessing outstanding ecological value (Sheppard et al., 2012). In order to preserve this environment, in 2010 the UK government declared the area around BIOT as the then largest no-take marine reserve in the world at 544,000 km^2. Since that time, there have been legal issues surrounding BIOT's designation as an MPA. However, efforts are being made to confirm its status and ensure the future protection of this exceptionally well–preserved marine ecosystem (Lunn, 2016).

5.2 Methodology

In order to understand the potential exposure of MPAs to pollution and other risks, here we diagnose the MPAs' connectivity through ocean circulation. Once the connectivity is defined, it is then possible to assess the level of contact with human activity, and therefore risk. The tools and data used in this analysis are described here, along with the experimental design aimed at addressing these issues.

5.2.1 Ocean GCM model and Lagrangian particle tracking

The NEMO (Nucleus for European Modelling of the Ocean) 1/12° resolution global ocean general circulation model has been developed with particular emphasis on realistic representation of fine–scale circulation patterns (Madec and the NEMO team, 2008; Marzocchi et al., 2015), which provides an ideal platform to conduct Lagrangian particle–tracking experiments. Full details of the model run, including model setup and configuration, can be found in Marzocchi et al. (2015) so only a brief description will be given here. The model is initialized with World Ocean Atlas (WOA) 2005 climatological fields and forced with realistic 6–hourly winds, daily heat fluxes, and monthly precipitation fields (Brodeau et al., 2010). The run begins in 1978, with output through to 2010, of which we are interested in 2000 – 2009. Model output is stored offline as successive 5 day means throughout the model run, of which the velocity fields are used for the particle tracking in this paper.

The Ariane package (Blanke and Raynaud, 1997) is applied to the NEMO velocity field to track 3D trajectories of water parcels using virtual particles that are released into

the modeled ocean circulation (cf. *Popova et al.*, 2013; *Robinson et al.*, 2014; *Srokosz et al.*, 2015, who use a similar methodology). These Lagrangian particles are intended here to represent water that enters within the boundaries of the MPAs. Further details about the Ariane package can be found in Blanke and Raynaud (1997) and Blanke et al. (1999).

5.2.1.1 Modelled versus observed surface currents

The ability of the chosen model to accurately represent the circulation in the study area is critical to the quality of the results. In order to qualitatively assess the performance of the NEMO 1/12° model, we compare the modelled surface velocity with the Ocean Surface Current Analysis-Real-time (OSCAR) dataset. The dataset provides global sea surface currents at 1/3° spatial resolution and a time resolution of five day averages (available at `http://www.oscar.noaa.gov/`). The OSCAR velocity field is calculated by a linear combination of geostrophic, Ekman–Stommel, and thermal–wind currents (Lagerloef et al., 1999; Johnson et al., 2007).

Figures 5.1[a] and [b] provide a comparison of the decadal (2000 – 2009) average ocean surface current speed, from OSCAR and NEMO respectively, encompassing the four MPAs. The comparison shows good agreement between observed and modelled surface currents, in terms of both the correct locations and magnitudes. The model does have known peculiarities at the equator, namely unexpected overturning cells at depth, however this is unlikely to impact the surface or near–surface circulation. Additionally, the Antarctic Circumpolar Current, is known to be weaker in the model than the real world ocean, but the main circulation features of the Southern Ocean are in the correct

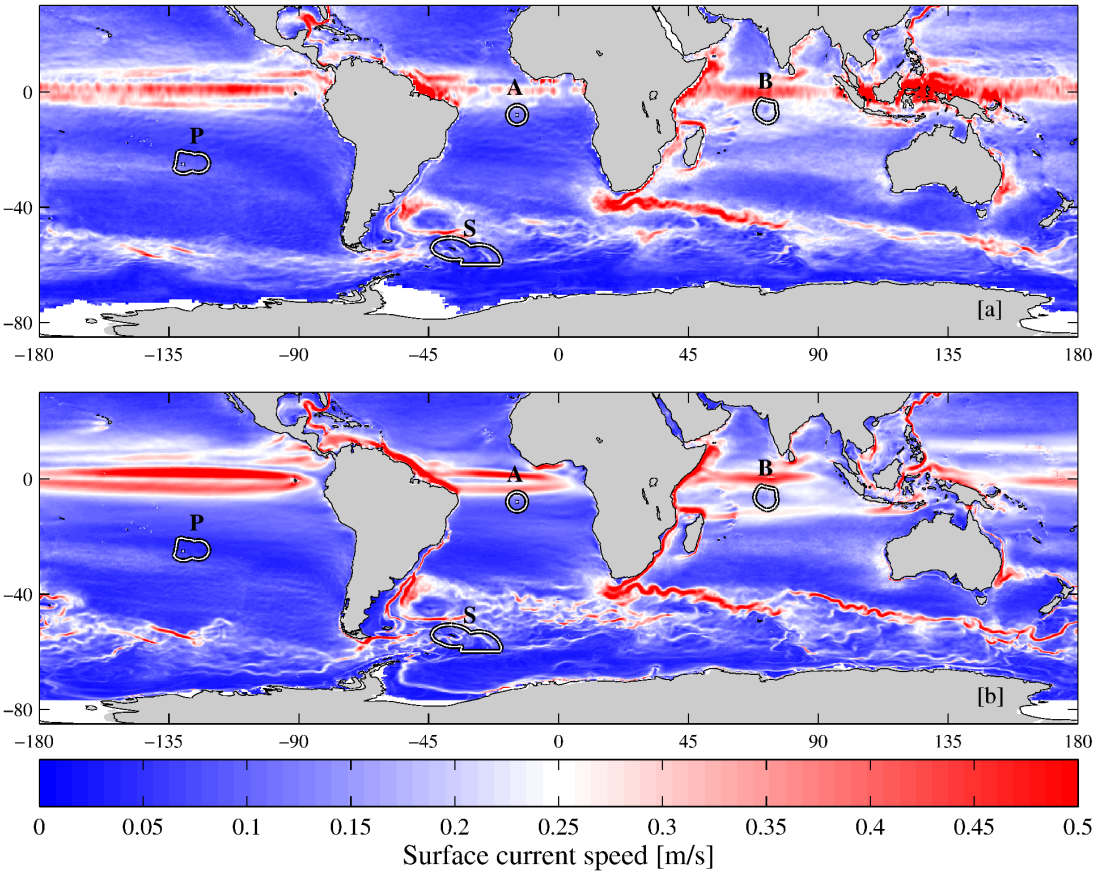

Figure 5.1: Observed and modelled decadal average, 2000 – 2009, surface current speed (m s^{-1}). The observed velocity, panel [a], is the OSCAR data set at 1/3° resolution and the modelled velocity, panel [b], is the NEMO ocean general circulation model at 1/12° resolution. The black and white contours denote the boundaries of the marine protected areas. The initials above each contour, represents: P for Pitcairn, S for South Georgia, A for Ascension, and B for BIOT.

location. There is also less small–scale variability in the model, owing to lower levels of eddy kinetic energy than the real ocean, despite the model being eddy–resolving at 1/12° resolution. Nevertheless, studies have shown the model to realistically reproduce key circulation features, such as the North Atlantic Current and the Gulf Stream separation (Marzocchi et al., 2015), and several western boundary currents (Popova et al., 2016).

Figures D.1.1 – D.1.4 in the supplementary material show the decadal, annual and

monthly averaged circulation, of both NEMO and OSCAR surface current speeds, around the region of each MPA for illustrative purposes.

5.2.2 Experiment design

In order to diagnose the source regions of the water that enters the four MPAs, Lagrangian particles were released monthly into the modeled circulation, and followed backwards in time (back tracked) during January 2000 to December 2009. Consequently, each monthly release of particles is essentially the month in which the particles arrive at the MPA. Particle positions are recorded at 5–daily time intervals, for a total of 72 time–steps with 5–day intervals, an advection period of 1 year. For the purpose of this study, we found 1 year's worth of trajectories to be sufficient in assessing connectivity, as all but one MPA was connected to land within a 12 month period (details in the results section). Particles are deployed at every 5th grid cell of the 1/12° model grid horizontally (latitudinally and longitudinally) across the MPA boundaries, and at depths of 1, 20, 40, and 60 meters. Particles were placed down to a depth of 60 meters to approximate the euphotic zone (within which most organisms reside). The final boundaries of the Ascension MPA are not yet designated, so for the purpose of this study we have used the Ascension Exclusive Economic Zone as the boundary. The particle placement was designed to be consistent in resolution across all MPAs for comparable analysis. However, the MPAs vary drastically in size (see Table 1), resulting in a different number of particles within each MPA experiment. At the horizontal and vertical grid spacing described, 1888 Lagrangian particles are released at the beginning of each month for ten years from the Pitcairn MPA, 6155 particles from South Georgia MPA, 844 particles from the Ascension MPA, and 1241 from the

BIOT MPA.

5.2.3 Population density data

In discussing the MPAs connectivity with land in the results section, exposure to risk is discussed in terms of connectivity with highly populated areas in the discussion section. The population density data used for this is the Gridded Population of the World, Version 3 (GPWv3) Future Estimates for 2015 produced by for International Earth Science Information Network et al. (2005), and can be seen in Figure 5.2. GPWv3 data provides estimated population density in persons per square km at 1/4° resolution across the globe. The data used is a projection of population density from the 2004 dataset to 2015. The 2004 dataset it produced by dividing the population count grids by the land area grid, then the values are extrapolated based on a combination of subnational growth rates from census dates and national growth rates from United Nations statistics to produce the 2015 projection. More information and the itself data is available at `http://sedac.ciesin.columbia.edu/data/set/gpw-v3-population-density-future-estimates`.

As a first-order approximation of population density effects, the 1/4° gridded population density field was extrapolated out from the land into the entire ocean grid by simple natural neighbour interpolation (using the Matlab v2013a scatteredInterpolant function). This approach does not factor in the effect of cumulative population density, i.e. where a stretch of coastline may be impacted by a significant inland population. However, restrictions in the availability of data mean that the GPWv3 dataset frequently averages population over an extended area, decreasing the significance of such

errors (albeit locally). Note that this analysis also conflates human population density with impact, when the latter may actually be a stronger function of local technology, environmental regulations and resource management.

The interpolated population density was recorded for Lagrangian particle trajectories which were within 85 km of the coast line. A distance of 85 km is used as it has been used in previous studies as the global average width of the continental shelf (Walsh, 1991; Elrod et al., 2004), within which area, the water is considered as well mixed (Nash et al. (2012), and references therein). Consequently, we assume water properties or human pollution, are evenly distributed throughout the water mass above the shelf.

5.3 Results

In order to assess the degree of exposure to pollution risk from upstream sources, we diagnose the origin of the water that enters the MPAs and the associated timescales. Across parts of the World's Oceans the circulation can shift both seasonally and inter–annually, and at varying magnitudes, which can significantly alter an MPA's connectivity. In this section, we describe the general circulation around the four MPAs, and the connectivity timescales with land. We then address the seasonal and inter-annual variability of the circulation, across a ten year period.

5.3.1 General circulation and connectivity of MPAs

Figure 5.2 includes all of the particle data, across all months and years, in the experiments. Dark red trajectories represent an advection time of one month, before reaching the MPAs and consequently are the closest to the boundaries (black contours). Dark blue trajectories represent an advection time of 12 months, and are therefore at a greater distance from the MPAs. This figure demonstrates all possible sources of water to the MPAs throughout a ten year period, including inter–annual and seasonal variability.

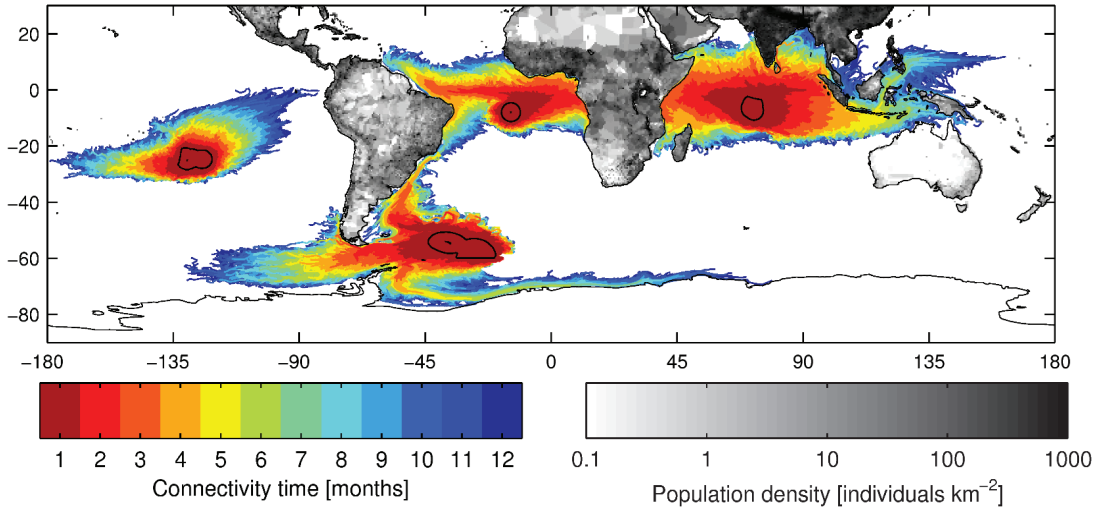

Figure 5.2: The time, in months, that it takes for ocean surface waters to reach the marine protected areas. The colored area represents the trajectories of particles which arrive at the marine protected areas, each month during 2000 – 2009. The colour of the trajectories indicate the time in months for the particles to be advected to the marine protected area, termed on the color bar as the connectivity time. The black contours represent the boundaries of the marine protected areas. The greyscale land indicates the population density, in persons per km^2 at 1/4° resolution.

What is apparent from Figure 5.2, is that all the MPA's, except Pitcairn, are connected with land within a one year timescale. As can be seen from Figure 5.1, the Pitcairn marine reserve is in an area of relatively slow surface currents. This is due to

it being positioned towards the centre of the basin–wide, anti–cyclonic South Pacific Gyre. There are two lobes of source water into the Pitcairn reserve, the main source originating from the northeast, and the second source originating from the west. To further understand the circulation pattern around Pitcairn, a ten year back tracking simulation was performed in order to identify the key circulation features that influence the Pitcairn MPA (Figure 5.3). This revealed that two major currents feed the Pitcairn MPA, namely the Pacific Equatorial Undercurrent and the Humboldt Current. Particles travelling in the undercurrent across the entire basin, are at roughly 200 m on the western side, and gradually shoal as they travel towards the east (Grenier et al., 2011). Once reaching the west coast of South America, wind–driven coastal upwelling brings all particles to the surface (Talley et al., 2011). The Humboldt Current is an eastern boundary current flowing northwards along the west coast of the South American continent (Fiedler and Talley, 2006). The northeastern lobe of source water flows from the northwest coast of South America, whereas the western source is formed of water that has spent more time circulating in the anti–clockwise current of the sub–tropical gyre. Ekman transport causes the surface water to move towards the central region of a subtropical gyre (Martinez et al., 2009), as is visible in Figure 5.2. In terms of Pitcairn's connectivity, the MPA is connected to the South American continent within a 2 year timescale (via both the Pacific Equatorial Undercurrent and the Humboldt Current), and also the Malay Archipelago within 3–4 years (via the Pacific Equatorial Undercurrent).

The South Georgia MPA has three main sources of water; the Antarctic Circumpolar Current flowing from west to east around Antarctica, a southern source from the Antarctic Slope Current, with flows east to west along the Antarctic shelf (Rintoul

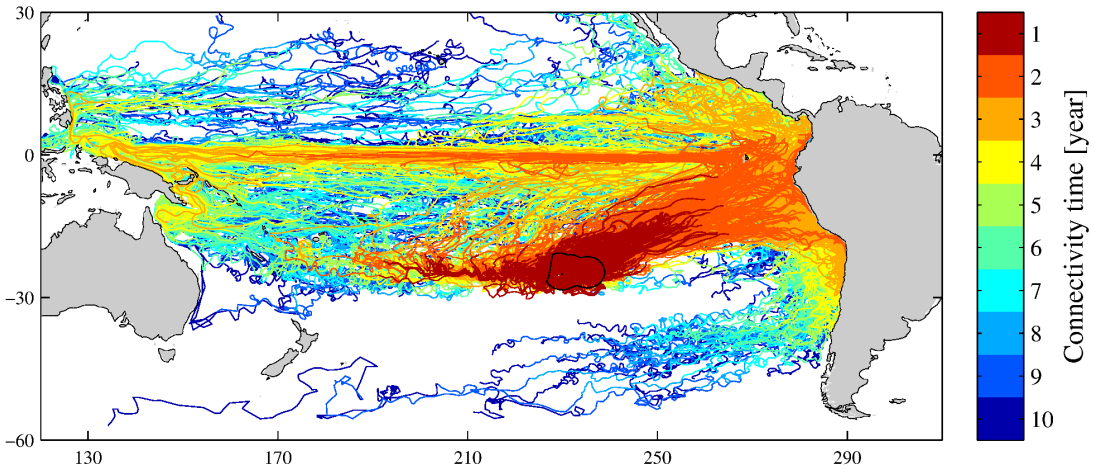

Figure 5.3: The time, in years, that it takes for ocean surface waters to reach the Pitcairn marine protected area. The colored area represents the trajectories of particles which arrive at Pitcairn, each year during 2000 – 2009. The colour of the trajectories indicate the time in years for the particles to be advected to the marine protected area, termed on the color bar as the connectivity time. The black contour represents the boundary of the Pitcairn marine protected areas

et al., 2001), and a northern source via the return flow of the Malvinas Current, and also small but frequent eddies which are shed from the Brazil Current and are associated with the Subantarctic Front (Peterson and Stramma, 1991). From these sources, we can see in Figure 5.2 that the South Georgia MPA has a connectivity timescale on the order of 3–4 months. However, in considering the exposure to human activity, the only source for the South Georgia MPA that could be significant, taking into account population density, is from the Brazil Western Boundary Current, which flows southward along the east coast of the South American continent.

The Ascension MPA is positioned just south of the equator in the mid-Atlantic. Consequently, the two main sources of water are the westward flowing South Equatorial Current and the eastward flowing North Equatorial Countercurrent. There is also an eastward flowing source, just subsurface, via the Atlantic Equatorial Undercurrent (Brandt et al., 2014). The dominant source of water to the Ascension MPA is from

the eastern side of the Atlantic, as seen in Figure 5.2. Parallel to the west coast of Africa, are two main currents each flowing in a meridional direction, which meet in a confluence region at about 15°S before turning west to become part of the South Equatorial Current. Flowing north to south is the Guinea Current and its extension the Angola Current, and flowing south to north is the Benguela Coastal Current (Lass et al., 2000). The highly seasonal eastward flowing North Equatorial Countercurrent originates from the western side of the Atlantic at roughly 5–10°N (Richardson et al., 1992). A small proportion of the North Equatorial Countercurrent is fed by the northward flowing North Brazil Current, but the majority of the countercurrent is fed by northern hemisphere waters originating in the North Equatorial Current at roughly 10°N (Goes et al., 2005). The eastward flowing North Equatorial Countercurrent is strongest in the late boreal summer into fall, with a reversal of the near–surface current in spring due to a change in the Northeast Trade winds (Richardson et al., 1992). The Atlantic Equatorial current system connects the Ascension MPA with the west coast of Africa within a time period of 2–3 months, and with the east coast of Brazil within 3–4 months.

The BIOT MPA is positioned towards the centre of the Indian Ocean, just south of the equator. In Figure 5.2, it is apparent that the BIOT MPA has various sources of water from across the entire Indian Ocean, and also from the Pacific through the Indonesia Throughflow. The circulation of the Indian Ocean is extremely complex (Wyrtki, 973b), owing in part to the geographical configuration, but primarily to the unique monsoonal wind forcing. Here we provide a brief description of the typical surface ocean circulation from the literature, focusing on key features relevant to the analysis.

The Indian Ocean is the smallest of the three major ocean basins, extending only as far north as 25°N on either side of the Indian subcontinent. The southern sector of the Indian Ocean is bounded by the Antarctic Circumpolar Current through which it is connected with the Atlantic and Pacific Oceans. There is also an important connection with the low latitude Pacific via the Indonesian Throughflow, which flows unidirectionally from the Pacific into the Indian through the Indonesian Archipelago. Once exiting the Archipelago it flows westward within the South Equatorial Current. However, annual variability is high, and an ENSO signal has been observed (Hautala et al., 2001; Sprintall et al., 2014). In the southern half of the Indian Ocean is a basin–wide subtropical gyre, which flows anti–cyclonically driven by westerly winds at high (Southern) latitudes and south-easterly trade winds at low latitudes, similar to the mean wind patterns of the Atlantic and Pacific. The South Equatorial Current flows westward across the basin throughout the year at roughly 10–16°S, with a transport of some 50–55 SV, and separates the subtropical south from the tropical and northern Indian Ocean (New et al., 2007). For parts of the year, a confluence of two currents at roughly 2–3°S along the east coast of Africa, results in the eastward flowing South Equatorial Countercurrent, which together with the South Equatorial Current, becomes the northern and southern branches of a transitory tropical cyclonic gyre (Schott and McCreary, 2001; Talley et al., 2011).

North of the South Equatorial Current, is a unique circulation regime which seasonally reverses driven by monsoonal wind forcing. The Southwest Monsoon winds peaks in July–August, and the Northeast Monsoon winds in January–Februrary, driving seasonal reversals in the ocean currents in this region (Schott and McCreary, 2001).

Greatly influenced by the reversing Southwest and Northeast Monsoons, are the two large embayments to the east and west of the Indian subcontinent, the Arabian Sea and the Bay of Bengal, respectively. During the Southwest Monsoon (winds blowing to the north–east over India) the open-ocean currents that circulate between the Arabian Sea and the Bay of Bengal flow eastward (Southwest Monsoon Current), whereas flow is westward during the Northeast Monsoon (Northeast Monsoon Current), influencing the formation of the South Equatorial Countercurrent. These monsoon currents are made up of many different branches, each forced individually by a combination of both local and remote processes. However, the Northeast Monsoon Current is notably weaker and more disorganised than the Southwest Monsoon Current, as the Southwest Monsoon winds are stronger than the Northeast Monsoon winds, and consequently the ocean response is stronger and more consistent to the Southwest Monsoon. The transition between Southwest to Northeast Monsoons, and vice versa, occurs relatively quickly during March–April and October, during which the equatorial winds are westerlies, rather than the typical trade winds (Schott and McCreary, 2001; Shankar et al., 2002; Talley et al., 2011). This brief dominance of westerlies forms the eastward flowing Wyrtki Jets, which are significantly stronger than the westward flowing South Equatorial Current during this time (Wyrtki, 1973).

For a schematic diagram of the Indian Ocean circulation and a thorough description of the entire regime, see Schott and McCreary (2001), Figures 8 and 9. For a more in–depth discussion specifically of the northern Indian Ocean monsoonal circulation, see Shankar et al. (2002).

In terms of connectivity timescales, the BIOT MPA is connected to: the east coast of

Africa within 3 months advection time; to Indonesia within 3–4 months, and via the Indonesian Throughflow, to the Malay Archipelago within 4–7 months; and to India within a range of 3–6 months. Northwards of 20°S, particle trajectories from the BIOT MPA fill the entire Indian Ocean basin, with the exception of the northern Arabian Sea.

5.3.2 Seasonal and inter–annual variability

Figure 5.4 shows all the particles from the monthly releases for each year of the experiment, indicating the density of the trajectories and the inter–annual variability for each MPA. Focusing on Pitcairn in Figure 5.4, the trajectory density "footprint" in each subplot is generally the same in each year with the two distinct lobes to the northeast and west. In some years, the particles backtrack further away from Pitcairn, such as in years 2006 and 2007, and in others the particles remain closer to the MPA boundary, such as in years 2002 and 2003. However, these variations are not large enough to enable connectivity to any coastline.

For the South Georgia MPA, the highest trajectory density is within the Antarctic Circumpolar Current, indicating this to be the dominant source current. Conversely, Figure 5.4 also shows that the lowest density of trajectories advecting towards the South Georgia MPA comes from the northern source. As with Pitcairn, the South Georgia MPA has little inter–annual variability.

Focussing next on the Ascension MPA, Figure 5.4 shows the dominant source of water to originate from the west coast of Africa, specifically the Angola Current and South

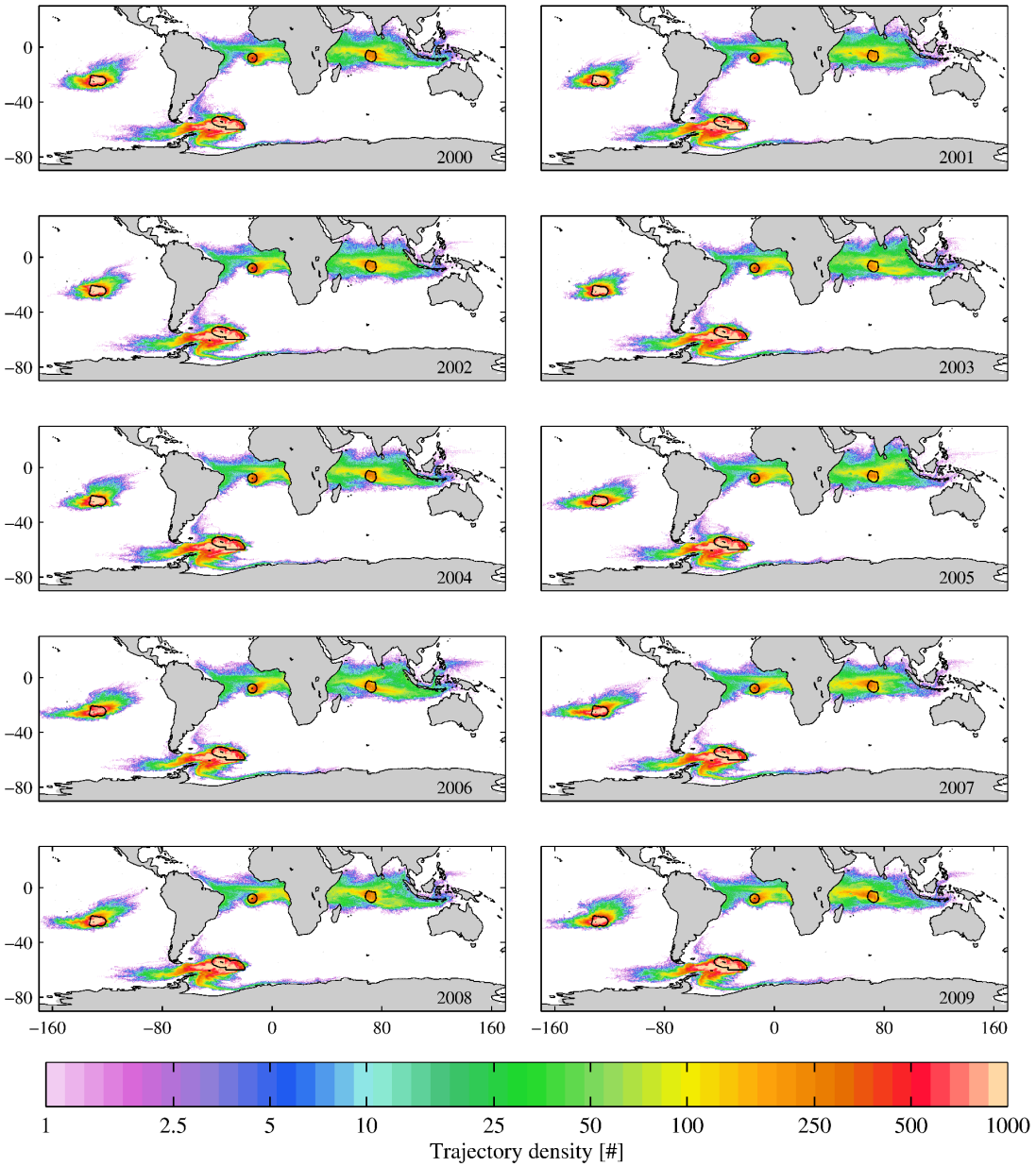

Figure 5.4: Census of particle advection towards the marine protected areas for each years trajectories. The annual plots include all the particles released monthly from the marine protected area, each with an advection time of one year. Colors denote the cumulative "density" of particle trajectories based on their 5–daily position throughout the 10–year experiment, representing the total number of trajectories that have passed through each 0.25° grid cell.

Equatorial Countercurrent. In terms of variability, the trajectory density footprint is generally the same inter–annually, whereas further analysis revealed that there can be seasonal variations due to the strength of the North Equatorial Countercurrent varying seasonally (Richardson et al., 1992).

Finally, focusing on the BIOT MPA in Figure 5.4, there are two dominant sources of surface water for the MPA, one each from the east and the west. However, there is a high degree of variability both across and within the years. In 2009, the dominant source is from the east, indicated by the logarithmic color bar. Whereas in 2003, the highest trajectory density is from the west, and in some years there is an equal amount of water originating from both the east and west. This variability has a significant impact on the connectivity times of the BIOT MPA to various continents. The BIOT MPA experiences by far the highest degree of inter–annual circulation variability out of the four MPAs in this study.

In order to examine the seasonal variability of circulation around the BIOT MPA, Figure 5.5 shows the origin of the water for each climatological month that arrives at BIOT, from which the impact of the seasonally reversing circulation is apparent. Note that the colour scale of Figure 5.5 is different to that of Figure 5.4 because a lower resolution grid was used for the BIOT monthly climatologies, which shows dominant pathways more clearly. Figure 5.5 shows that the key features that determine the source waters to the BIOT MPA are the South Equatorial Current (including the Indonesian Throughflow), the periodic Countercurrent and Wyrtki Jets, and the reversing Monsoonal Currents.

Focusing on one of the clearer features within Figure 5.5, it is apparent that the Indonesian Throughflow is an important source to the BIOT MPA of water arriving

during September–December. Meyers et al. (1995), found that flow through the Indonesian Archipelago is largest during the Boreal summer, and taking into account an appropriate time lag between water passing through the Archipelago and arriving at BIOT, agrees with Figure 5.5 where there is a high density of particles within the Indonesian Throughflow during September–December arrival months. Other than the Indonesian Throughflow, the remaining picture is unclear, due to the reversal of the northern circulation and periodic appearance of the South Equatorial Countercurrent and Wyrtki Jets. The Wyrtki Jets in particular confuse the plot as when these dominate for 3 months out of the year, they are so strong that over an annual average of surface currents, flow can appear eastward across the basin, despite the westward flowing South Equatorial Current dominating for the majority of the year (Talley et al., 2011). Furthermore, there is a time lag between the occurrence or reversal of these features, which each influence the source water to the BIOT MPA at different times of the year, and the arrival of the influenced water at the MPA. Each feature has its own associated time lag, between the initial influence on the circulation, and the waters arrival at the MPA, for instance Wyrtki Jets are extremely fast, over 100 cm s^{-1} (Talley et al., 2011), whereas the Summer Monsoon Current has been observed to flow much slower at 35 cm s^{-1} (August 1993) (Stramma et al., 1996).

The complex, seasonally transforming, circulation pattern of the Indian Ocean is neither spatially nor temporally consistent year–on–year (Shankar et al., 2002; Schott et al., 2009). This explains why Figure 5.5 does not clearly represent the monsoon driven circulation presented in Indian Ocean schematic circulation plots (such as Schott and McCreary (2001) Figures 8 and 9). As Figure 5.5 represents climatological months, the inter–annual variability smooths out the presence of any distinct features visible

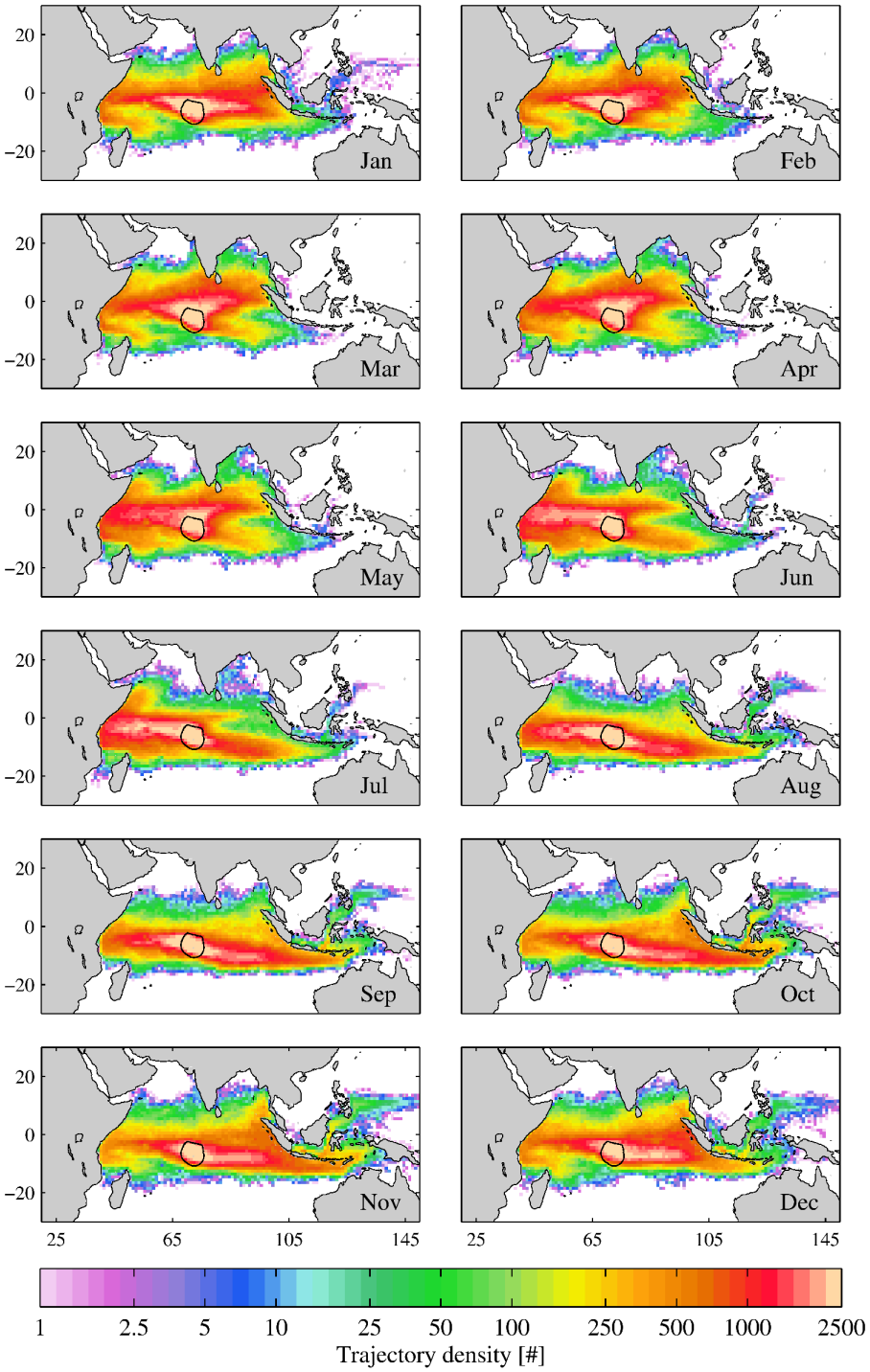

Figure 5.5: Census of particle advection towards the British Indian Ocean Territory marine protected area for each climatological month. Each plot includes the particles released in a given month for every year of the 10–year experiment, with an advection time of one year. Colors denote the cumulative "density" of particle trajectories based on their 5–daily position throughout the 10–year experiment, representing the total number of trajectories that have passed through each 1° grid cell.

in the trajectories. To provide a clearer example, and also to demonstrate the degree of inter–annual variability in addition to the seasonal variability, Figure 5.6 shows four individual experiments of particle releases, arriving at the BIOT MPA within January and July, from a selection of years within the 10–year study period. Focusing on the top two panels, the origin of the water arriving in January 2005 was dominantly from the northwest, the Bay of Bengal and Indonesia region, whereas in January 2009 the majority came from the western side of the basin. This inter–annual variability also occurs at other times of the season, as shown by the bottom two panels of water arriving at BIOT in July for two different years. In 2001, the water is predominantly from the west, whereas in 2003 there are significant sources from both the western and eastern sides of the Indian Ocean.

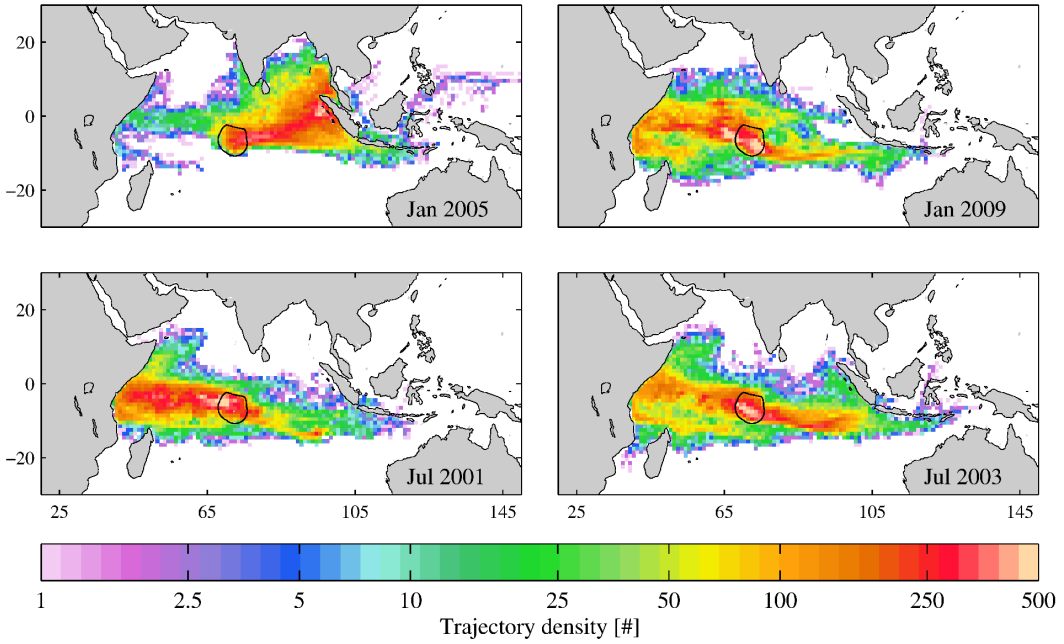

Figure 5.6: Census of particle advection towards the British Indian Ocean Territory marine protected area for four months of the experiment. The plots include the particles released in a given month for every year of the 10–year experiment, with an advection time of one year. Bottom left annotation details which month and year each plot represents. Colors denote the cumulative "density" of particle trajectories based on their 5–daily position throughout the 10–year experiment, representing the total number of trajectories that have passed through each grid cell.

These variations in the circulation can arise as direct impacts of remote external factors, as well as from the inter–annual and seasonal variability that exists in the monsoonal wind forcing. The two principal large–scale climatological features which can impact the Indian Ocean circulation, although there are several other seasonal oscillations, are the local Indian Ocean Dipole (IOD) (Saji et al., 1999), and the globally impacting El Niño/Southern Oscillation (ENSO) (Bjerknes, 1969; Diaz et al., 2001). It is outside the scope of this work to describe these features in detail, but briefly the IOD is a shift in sea surface temperatures between the western and eastern Indian Ocean sectors, with each alternately becoming warmer and then colder in an irregular oscillation, typically lasting the boreal summer and autumn (Saji et al., 1999). The ENSO is an irregularly periodical occurrence of a warm phase (El Niño), and cool phase (La Niña) in sea surface temperatures, caused by a variation in winds over the tropical eastern Pacific Ocean, affecting much of the tropics and subtropics (Schott et al., 2009). El Niño typically lasts for 9–12 months, whereas La Niña can last for 1–3 years. There is much research and evidence of the influence of these phenomena directly on the currents of the Indian Ocean (Gnanaseelan et al., 2012), indirectly via impacts on the monsoon cycle (Ashok et al., 2001; Pillai and Chowdary, 2016), and importantly on how they interact (Luo et al., 2010). For a thorough discussion on Indian Ocean circulation variability and associated climate variability, see Schott et al. (2009) and references therein.

5.4 Discussion

5.4.1 Coastal Connectivity and exposure to human activity

In Figure 5.2, it is apparent that three of the four MPAs in this study are strongly connected with land, over a one year timescale. Connectivity with land could be detrimental to the MPAs pristine condition, as land is the main source of pollution to the ocean, of which plastic makes up the most significant part (Shahidul Islam and Tanaka, 2004; Gall and Thompson, 2015). Jambeck et al. (2015) estimated that in 2010, 275 million metric tons of plastic waste was generated in 192 coastal countries, of which 4.8–12.7 million metric tons entered the ocean (approximately 1.8–4.6%). Plastics are produced as many different varieties of polymers, and from macro to micro in size, but the key characteristic which makes plastic so commercially popular is also the reason why they are so harmful and wide spread in the ocean: their durability (Cole et al., 2011; UNEP, 2016). Depending on the type of plastic, once in the ocean it can either sink to the ocean floor or be transported worldwide by surface currents (van Sebille et al., 2015). Most famously, there is a relatively high concentration of floating plastic which has accumulated in so called "garbage patches" in the five sub-tropical gyres in the Indian Ocean, North and South Atlantic, and North and South Pacific (Martinez et al., 2009; Maximenko et al., 2012; Eriksen et al., 2013). Marine plastics can have significant detrimental ecological impacts, and consequently there has been much research on the impacts of both macro and micro–plastics on biota. Direct impacts on marine species includes entanglement in macro–plastics, and ingestion of micro–plastic and subsequent absorption of toxic chemicals, namely polychlorinated biphenyls (PCBs). Indirect negative impacts can come from the trophic transfer of plastics or toxins, and also floating plastic debris transporting "invader" species (Derraik, 2002; Wright et al.,

2013; Gall and Thompson, 2015). For a thorough synthesis on the issue of marine plastics, see UNEP (2016).

Having outlined the issues surrounding marine plastics, and noting the findings of Jambeck et al. (2015), who states that population size is a significant factor in the amount of plastic litter from coastal regions, we now discuss the MPAs in this context. Using the trajectory data presented in Figure 5.2, the percentage of source water that originates from within 85 km of the coast (global average width of shelf) was calculated for each monthly experiment from each MPA, and presented in Tables D.2.1 – D.2.4 of the supplementary material. The table demonstrates the degree of seasonal and inter–annual variability discussed in the results section, but also quantifies what is apparent in Figure 5.2. On average, over a one year timescale, the Pitcairn MPA is not connected with land, whereas of the water than flows into the South Georgia MPA, a fraction of 0.02 originates from the coast, a fraction of 0.34 for Ascension, and 0.71 for BIOT (see Figure 5.7). However, in terms of plastic pollution, connectivity with land is only significant for the MPAs if the land is highly populated (Jambeck et al., 2015). In Figure 5.2, the land is filled with population density data (for International Earth Science Information Network et al., 2005), which was used to further assess source water originating from the coast. As is apparent in Figure 5.2, India, and parts of Indonesia and Africa, have the highest population density of the countries which are connected with the MPAs, most notably to BIOT. To quantify this, Tables D.2.5 – D.2.8 in the supplementary material details the maximum population density person/km^2 encountered by the source water, from each monthly experiment for each MPA (see the methodology section for how this data was interpolated on to the ocean grid). This information is significant, as even if an MPA has only a small fraction of

its source water originating from land, if the coast is relatively densely populated, then the degree of risk from pollution is higher, as is the case for the South Georgia MPA. However, the worst case scenario, is to be highly connected with densely populated coast, as is the case for the BIOT MPA. The highest population density encountered by the South Georgia source water, was 3134 person/km^2, originating from the coastal cities of the State of São Paulo; for Ascension, 5288 person/km^2, originating from the coastal region of Lagos; and for the BIOT MPA, 15,203 person/km^2, originating from the coastal region of Mumbai. We note that this approach is a simplification, assuming that a high population density equates to high levels of pollution. In reality, the situation is more complex and depends on the economic status of the coastal region which can determine factors such as the quality of waste management systems Jambeck et al. (2015). Nevertheless, we use this approach as a first–order approximation of the possible pollution risk as a consequence of coastal connectivity. We also note that a large proportion of plastics which enter the marine environment do not float, and therefore would not impact the MPAs via circulation connectivity.

5.4.1.1 Four of a kind?

Having outlined the average coastal connectivity, and maximum population density, encountered by the MPA source waters, Figure 5.7 presents this information for cross–comparison of each MPA over a one year advection period. The previous section discussed the maximum population density ever encountered by the source water, whereas the population density presented in Figure 5.7, is the average across the maximum population densities encountered for each of the 10 years.

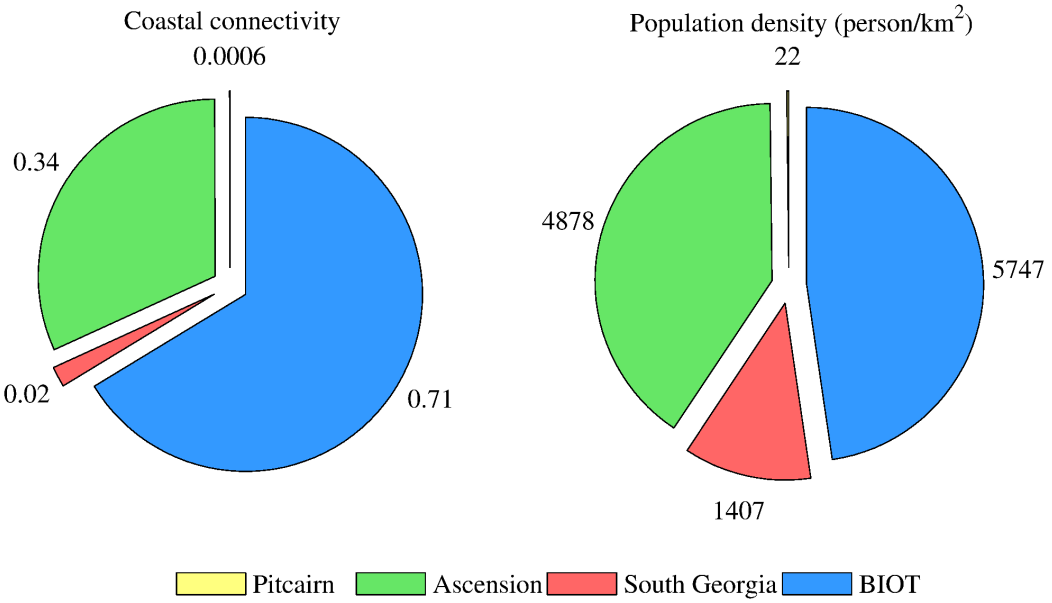

Figure 5.7: A comparison of the coastal connectivity of, and the population density encountered by, water that flows in to each MPA over a 1–year advection period. The left pie chart shows the fraction of water entering each MPA that originates from the coast. The coastal connectivity is an average across the 10–year study period, of the annual maximum fraction of water originating from the coast. The right pie chart is the highest population density, in person/km^2, encountered by water that originates from the coast and flows into the MPAs. The population density given is an average across the 10–year study period, of the annual maximum population densities encountered. The yellow segment represents the Pitcairn MPA (although the color is not visible in the chart due to it being only a tiny fraction), green represents the Ascension MPA, red represents the South Georgia MPA, and blue represents the BIOT MPA.

Focusing first on the Pitcairn MPA in Figure 5.7, it is immediately apparent that the model suggests there is no risk of coastal pollution via ocean circulation. The South Georgia MPA has a very low coastal connectivity fraction (0.02), however the coast it is connected with includes the relatively highly populated southeast coast of Brazil. Nevertheless, with such a low coastal connectivity the exposure to coastal pollution is low. The Ascension MPA, has an average annual maximum coastal connectivity of 0.34, of which the average annual maximum population density encountered is 4878 person/km^2. As such, the Ascension MPA is exposed to a significant pollution risk via ocean circulation. This is a particular threat to the islands important rookery for

the endangered green turtle (Petit and Prudent, 2010), as the juvenilles can perish by ingesting less than 1 g of marine debris (Santos et al., 2015). Finally, the BIOT MPA is the most vulnerable to coastal pollution via ocean circulation of all the MPAs in this study, as it has both the highest coastal connectivity, at 0.71, and population density encountered, at 5747 person/km^2. The BIOT MPA is comprised of 55 coral islands spread between five atolls, with more than 220 species of coral, and is currently considered to be one of the best preserved reefs in the world (Sheppard et al., 2012). However, recent research has revealed that corals are ingesting micro–plastics, which could potentially impair their health (Hall et al., 2015). The BIOT MPA corals are currently reported to be in excellent health (Sheppard et al., 2008), but with the revelation that corals are ingesting micro–plastics (Hall et al., 2015), and the results presented here showing the high degree of exposure to densely populated coastlines and consequent plastic pollution, the pristine condition of the BIOT corals may be under threat.

5.4.2 Further negative impacts of connectivity

This paper has focussed on the pollution threat from land, specifically discussing plastic, however connectivity with the coast and marine plastics are not the only issue. Many other human activities take place in the ocean, from which a variety of hazards to the marine environment can arise. Here we will briefly discuss other threats to MPAs through their connectivity, namely issues associated with shipping, oil spills, and fishing.

The industrial scale shipping of cargo, making up 90% of world trade movement (Kaluza et al., 2010), across all major ocean basins takes the risks associated with human activity out into the open ocean. In 1995, it was reported that as many as 600,000 plastic containers worldwide were being dumped at sea per day from shipping (Wace, 1995). There is also the daily disposal of onboard garbage and sewage from both commercial and tourism ships (Shahidul Islam and Tanaka, 2004). In addition to marine litter, there is the threat of oil spills, which are rare but devastating. One of the most public and notorious spills, was the Exxon Valdez oil tanker spill in 1989, which emitted 41.6 million litres of oil, and had a dramatic impact on Alaskan wildlife (Atlas and Hazen, 2011). The incident killed more than 30,000 birds of 90 different species in just over 4 months (Piatt et al., 1990). Over 25 years on since the disaster, and the effect on the marine environment is still being felt, through the persistence of toxic sub–surface oil and chronic exposure resulting in delayed population reductions and cascades of indirect effects (Peterson et al., 2003). A final known threat strongly associated with shipping, is marine bioinvasion. The two major routes by which invasive species spread, is via discharged water from ships' ballast tanks (Ruiz et al., 2000) and hull fouling (Drake and Lodge, 2007). In several parts of the world, invasive species have caused species extinction and habitat alteration (Mack et al., 2000). Kaluza et al. (2010) produced a network map of global ship movements (their Figure 1), the style of which can be overlaid with an MPAs connectivity footprint, to show which major shipping routes could potentially affect the MPAs, either through an oil spill disaster or increasing exposure to marine litter or invasive species.

The threat of oil spills is not solely limited to shipping incidents, there can also be rare but catastrophic spills from oil wells, the most famous recently being the Deepwater

Horizon Oil Spill in 2010. The oil from the spill, 779 million litres (Atlas and Hazen, 2011), was spread across the Gulf of Mexico region by ocean circulation (Liu et al., 2011), with 847 km of shoreline still contaminated one year after the spill despite clean up efforts (Michel et al., 2013). In the aftermath of this disaster, similar methods to that used here have been used to calculate the "circulation footprint" from possible oil spills, in order to reduce risk through better response and improved situational awareness (Jacobs et al., tted). This approach, in combination with the results presented here, can enable MPA managers to likewise be more aware of potential oil spill risks within their connectivity footprint, and consequently be prepared in the event of a spill.

Fishing activities have marine litter issues such as fishing tackle (Shahidul Islam and Tanaka, 2004), but more importantly, also have negative impacts on biology. Marine species can have various stages to their life cycles, which can involve larval dispersal during a pelagic stage. Dispersal via ocean currents determines the connectivity of local populations and therefore the knowledge and understanding of it is vital for conservation strategies (Mora and Sale, 2002). Unless a system is efficiently self-sustaining (retainment exceeds or equals overspill), overfishing in one region, can impact populations downstream, and consequently isolated MPA ecosystems could be vulnerable. Figueira (2009) looked at identifying "patches" as either sources or sinks within a metapopulation, in order to more effectively designate marine reserves. Knowing a location's contribution to the ecosystem, and using the MPA connectivity footprints, can help fill in the knowledge gaps of population connectivity, and aid in the spatial management of protection efforts (Sale et al., 2005).

5.4.3 Future work

In this study we have produced a one year connectivity "footprint" for each MPA, and used it to assess connectivity with land. However, as discussed in the previous section, pollution is not restricted to the coast, there are various other sources of potential hazards. The connectivity footprints produced in this study could be compared with other risk factors, such as shipping lanes, oil rigs, or fishing grounds, similar to the global human impact study by Halpern et al. (2008). Additionally, the work here focuses on a timescale of one year, but a more detailed study of the timescales of particular risks could be considered. This would fully assess the pollution threat, and or, ecological implications posed to each MPA through connectivity.

In the introduction, the implications of downstream (forward) connectivity were introduced, namely seeding species to other areas. In order to seed species downstream, the timescale of connectivity is crucial, as the pelagic larval duration of the species needs to be equal to or greater than the connectivity timescale (Cowen et al., 2007; Gawarkiewicz et al., 2007; Heath, 2008). The methodology and analysis used in this study can be performed in exactly the same way, but with forward Lagrangian particle tracking, enabling the timescales of downstream connectivity to be determined. Forward connectivity footprints, in addition to the backward connectivity footprints, would be extremely useful in the formation of networks, or ecological zones of MPAs, to protect ecological processes and areas that are necessary for the full life cycle of marine species (Halpern, 2003; Bank, 2006). Additionally, this could also be a tool to aid marine spatial planning, as there are increasing calls for the integration of MPAs with fisheries management to aid global biodiversity (Gell and Roberts, 2003; Hilborn,

2016).

One final consideration, whether considering the forward or backward circulation connectivity of MPAs, is the potential for the circulation itself to change, under the stress of climate change. Observations show that the intensity and position of western boundary currents are already changing (Wu et al., 2012; Yang et al., 2016). Also, a model projection has forecast further deviations in the circulation between the 2000–2010 and 2050–2059 decadal averages (Popova et al., 2016). In order to assess the impact such circulation changes may impose on ocean ecosystems, such as on the connectivity, nutrient pathways, and migration of species, further in-depth Lagrangian study using model future projections would be required.

5.5 Summary

- MPAs are typically established to conserve important ecosystems and protect marine species, but their success in achieving these goals requires evaluation, particularly with regard to their vulnerability to upstream impacts.

- Here we present the "connectivity footprints" of four MPAs, for a timescale of one year, using a Lagrangian particle tracking technique within a high resolution ocean general circulation model, and specifically consider their connectivity with land.

- Over a one year timescale, Pitcairn MPA is not connected with land, whereas of the water than flows into the South Georgia MPA, a fraction of 0.02 originates from the coast, a fraction of 0.34 for Ascension, and 0.71 for BIOT, with variability (both seasonal and inter–annual) found to be notably high for BIOT.

- Population density of the connected coastlines is considered in terms of exposure to pollution, specifically plastics, and identified as a coastal connectivity risk that needs to be considered in the management of MPAs.

- Further risks to MPAs, associated with open–ocean connectivity, namely shipping, oil spills and fishing, are discussed and highlight the potential use of the connectivity footprint in relation to these threats.

- We advocate connectivity footprints of MPAs should be used as a tool to improve future MPA designation, and in spatial planning of current MPA networks, and suggest future work to improve the diagnosis of connectivity footprints of MPAs.

Chapter 6

Summary and outlook

"And now, the end is near" (Sinatra, 1969)

This chapter will summarise the findings of the research, and discuss alternative methods and analysis with acquired hindsight and experience. Finally, recommendations for future work will be suggested, to follow on from what has been achieved in this thesis.

6.1 Summary of research

The first piece of research focused on the potential long–term sequestration of carbon in the deep Southern Ocean. For this study, it was assumed that ocean iron fertilisation would stimulate a bloom across the iron-stressed Southern Ocean, which consequently would trap carbon through photosynthesis into phytoplankton biomass. Secondly, it was assumed that this biomass would sink down through the water column via the biological pump to a depth of 1000 m, which literature (Intergovernmental Panel on Climate Change) had indicated would be a depth great enough to isolate the carbon from the atmosphere for a timeframe on the order of a century. The aim was to test the hypothesis that carbon below a depth of 1000 m would remain sequestered in the deep ocean for a period of 100 years. The methodology involved using the Ariane Lagrangian particle tracking tool with velocity output from the NEMO general ocean circulation model at 1/4° resolution. Ariane particles, representing water mass containing sequestered carbon, were placed at a depth of 1000 m across the Southern Ocean, and their trajectories within the NEMO circulation tracked for one hundred years. The analysis showed that 66% of the carbon was advected into the mixed layer and effectively into contact with the atmosphere in less than 100 years, with a mean timescale of 37.8 years. Significantly, it was discovered that the vast majority of the

carbon was being re-exposed to the atmosphere via advection in the Antarctic Circumpolar Current. This strongly indicates that the export of carbon to a depth of 1000 m in the Southern Ocean does not guarantee sequestration in the deep ocean for a period of 100 years. The results emphasise that successful ocean iron fertilisation and carbon sequestration require consideration of the role of circulation as well as biogeochemistry.

Having focused on the large–scale and long–term impact of water mass movement within the Southern Ocean, the next step was to consider Southern Ocean circulation on smaller scales and shorter timescales. A preliminary look at the trajectory data within the Southern Ocean over shorter timescales revealed a high degree of both seasonal and inter–annual variability in the circulation. Also, during work on the first study, it was noted that there have been numerous studies focusing on natural iron fertilisation to predict the efficacy of artificial iron fertilisation. A recurrent theme within natural iron fertilisation studies is the "island mass effect" (Gilmartin and Revelante, 1974; Bakker et al., 2007). Iron limitation of primary productivity prevails across much of the Southern Ocean but there are exceptions; in particular, the phytoplankton blooms associated with the Kerguelen Plateau, Crozet Islands and South Georgia. These blooms occur annually, fertilised by iron and nutrient–rich shelf waters that are transported downstream from the islands, a process referred to as the island mass effect. Considering the interesting dynamics across seasonal and inter–annual circulation variability, this posed interesting questions about the impact of advection on phytoplankton blooms around Southern Ocean islands. Here we use a high–resolution ($1/12^{\circ}$) ocean general circulation model and Lagrangian particle tracking to investigate whether inter–annual variability in the lateral advection of iron could explain the inter-annual variability in the spatial extent of the blooms. Comparison with ocean

colour data, 1998 to 2007, suggests that iron fertilisation via advection can explain the extent of each island's annual bloom, but only the inter-annual variability of the Crozet bloom. The area that could potentially be fertilised by iron from Kerguelen was much larger than the bloom, suggesting that there is another primary limiting factor, potentially silicate, that controls the inter-annual variability of the bloom's spatial extent. For South Georgia, there are differences in the year-to-year timing of advection and consequently fertilisation, but no clear explanation of the inter–annual variability observed in the bloom's spatial extent has been identified. The model results suggest that the Kerguelen and Crozet blooms are terminated by nutrient exhaustion, probably iron and/or silicate, whereas the deepening of the mixed layer in winter terminates the South Georgia bloom. Therefore, iron fertilisation via lateral advection alone can explain the inter–annual variability of the Crozet bloom, but not fully that of the Kerguelen and South Georgia blooms.

The second study looked at the advection of iron downstream from Southern Ocean islands, and the consequent impact on the associated phytoplankton blooms. This also revealed that South Georgia and the South Sandwich Islands' phytoplankton blooms were influenced by upstream sources of iron. This raised an interesting question as to the remoteness of these seemingly isolated islands. An important outcome of the second study, which was later employed in the third study, was "connectivity footprints". The footprints were a visualisation of the spatial extent of lateral advection from one location over a given period of time, or in other words the timescale of connectivity between locations. The final piece of research departed from the topic of iron to look at Marine Protected Areas (MPAs). MPAs were a highly relevant contemporary topic at the time of the research due to the announcement of the new Pitcairn MPA which would become

one of the largest in the world, and also one of the remotest. MPAs are established to conserve important ecosystems and protect marine species that may otherwise be threatened in the wider ocean. However, even MPAs established in remote areas are not wholly isolated from impacts from elsewhere. Upstream activities, possibly thousands of kilometres away, can influence an MPA through ocean currents, which determine the connectivity of MPAs. For example, persistent marine pollutants, such as plastics, can be transported from neighbouring shelf regions to MPAs. Also, the ecosystem may be affected if larval dispersal by ocean currents is reduced due to overfishing in a seemingly remote upstream area. Thus, improved understanding of exactly what lies upstream, and on what timescale it is connected to an MPA, is of great importance for the ongoing protection and monitoring of these key marine areas. A high–resolution ocean general circulation model ($1/12^\circ$ horizontal grid) and Lagrangian particle tracking were used to diagnose the connectivity of four of the UK's largest MPAs: Pitcairn; South Georgia & Sandwich Islands; Ascension; and the British Indian Ocean Territory (BIOT). The idea of a circulation connectivity footprint was introduced by which an MPA is connected to upstream areas. Annual connectivity footprints were calculated for each of the four MPAs, taking into account seasonal and inter–annual variability. These footprints showed that, on annual timescales, Pitcairn was not connected with land over a twelve month timescale, whereas there was increasing land connectivity for waters reaching South Georgia, Ascension and, especially, BIOT. BIOT also had a high degree of both seasonal and inter–annual variability, which drastically changed the footprint, year–on–year. Such connectivity footprints are an inherent property of all MPAs, and need to be considered when MPAs are first proposed or their viability as refuges evaluated.

These three studies collectively show the importance of ocean connectivity, across all timescales and from regional to global spatial scales. The work also highlights the significance of temporal variability and how characterising this aspect is essential to fully understand ocean connectivity. The work has shown the power and utility of Lagrangian methods in studying advection and its associated impacts, and how this can be applied to a wide range of ocean problems as demonstrated by the three disparate topics chosen in this thesis. It builds on previous work using the same Lagrangian approach, such as Blanke and Raynaud (1997) who used a combined Eulerian and Lagrangian method to study the annual mean mass balance of the Pacific Equatorial Undercurrent and van Sebille et al. (2014) who used simulated Lagrangian particles to study the inter–annual variability in Pacific–to–Indian Ocean connectivity, to name just a couple. Furthermore, an important outcome of the work is to further raise the profile of ocean sensitivity to human impacts through advective connectivity.

6.2 Alternative approaches

During the first study, analysis and optimisation of the Ariane code was undertaken. This revealed that the majority of computational resources, namely memory and time, were taken up by reading in and out the velocity data and that the number of particles in an experiment had a relatively small impact on run time and memory usage. In hindsight, the carbon sequestration experiment could have had a much higher density of particles to cover such a vast region of highly dynamic circulation. Additionally, repeat releases of particles would have given valuable information about the degree of variability in the results. For the first 10 years, particles could have been released

annually to look at annual variability and thereafter released each decade to study variability across that timeframe. The two later studies proved the high degree of variability in advection, both annually and seasonally, so an improvement to the first study would have been to have looked at decadal variability.

In the natural iron fertilisation experiment, the analysis of South Georgia and Shag Rocks was complicated by other sources of iron in the vicinity. The work could have been supplemented by including the Antarctic Peninsula in the experiment, to see how much of the downstream advection from the Peninsula influences the South Georgia region. There are many studies, both observational and simulated, which could have been used to support such an analysis.

The MPA chapter began by assessing the level of connectivity with human activity, which quickly evolved to focus on plastic marine pollution. If the analysis had been devised with marine plastics at the forefront, then the study could have been improved by using a function in the Ariane code which forces the particles to remain at the surface, analogous to floating plastic. This would have enabled the analysis to be much more focused, rather than the generalised approach that was adopted. In addition to forcing the particles to remain at the surface, an alternative Ariane code was developed by A J G Nurser that included realistic wind forcing which would have been appropriate for a floating plastic study, accounting for wind drift effects on floating material. However, this code was developed too late for the final chapter and consequently not enough time was available to test the robustness of the code, so it was not used here. Following publication of this chapter, an article about marine plastics being found on Henderson Island (part of the Pitcairn Island

group) was published `https://www.theguardian.com/environment/2017/may/15/38-million-pieces-of-plastic-waste-found-on-uninhabited-south-pacific-island?`. Had this article come out sooner, an additional experiment for Pitcairn could have been performed, with parameters set to represent floating plastic.

In addition, if more time had been available Chapter 5 would have benefitted from a more thorough investigation and understanding of the BIOT seasonal and annual variability. Many features impact the Indian Ocean circulation, but one that could have been considered with the model data is the Indian Ocean Dipole. Analysis could have been performed to first establish if the NEMO model realistically reproduces the dipole, and if so, it could have been included in the variability analysis.

6.3 Future work

To enhance the work done in this thesis and future work using the Ariane and NEMO models, a sensitivity analysis of model resolution could be undertaken. Comparison experiments could be devised, such as initially having 1 particle for every grid cell and running with the 1/4° and 1/12° resolution data. One might expect the advection in certain parts of the model domain to be similar (major ocean gyres), whereas in other locations (Arctic and Southern Oceans) the results could look significantly different. These results could be further validated by using satellite velocity data to determine which model resolution accurately reproduces the real-world circulation and in which areas. It is generally assumed that an increase in resolution equates to an increase in realism with respect to the real world ocean. However, there is research to suggest that

this is not always the case depending upon the focus of the study (Sonnewald, 2016).

To build upon the work undertaken in the carbon sequestration chapter, the same methodology and analysis could be applied in other regions that have been identified as possible ocean iron fertilisation sites, such as the equatorial and Northern Pacific (Shepherd et al., 2009). Alternatively, a global experiment could be performed to produce a global map of suitable and unsuitable locations of carbon sequestration in the deep ocean, which would produce a global version of Figure 3.3b. This is relevant for other geoengineering schemes which are based on enhanced ocean productivity but not on the micronutrient iron, such as Shoji and Jones (2001) and Yool et al. (2009).

Looking further ahead, if the climate continues to warm at the current rate there is evidence to suggest that major circulation features will shift (Wu et al., 2012; Popova et al., 2016; van Gennip et al., 2016). As has been discussed throughout this thesis, advective connectivity can have major impacts on several processes within the ocean, ranging from biological implications to the spread of pollution. A Lagrangian methodology within a Eulerian framework could be used to create global connectivity maps, showing the shortest connection routes between basins (similar to Jonsson and Watson, 2016 and Froyland et al., 2014) or showing the degree of connectivity of a basin within different timeframes (i.e. degree of connectivity to other basins within 1 year versus 10 years). This could be further expanded to look at the surface and deep ocean, to give insight into the connectivity of the overturning circulation. Once a method to determine global connectivity (looking at various factors of connectivity) has been devised, it can be applied to the NEMO forecast model, run forward until 2099 under the strong warming RCP8.5 scenario. This will provide a picture of how

global connectivity might change throughout the century under a changing climate. Connectivity, either directly or indirectly, impacts most ocean processes and therefore understanding how it might change as a result of a changing climate could be vitally important in aiding policy makers (such as MPA planners) to protect vulnerable ocean ecosystems.

6.4 Concluding remarks

This thesis has shown the power of a Lagrangian approach in addressing three key areas of oceanographic research: the global-scale efficiency of regional geoengineering by iron fertilisation; the role of natural iron fertilisation in phytoplankton blooms; and the connectivity of MPAs to upstream anthropogenic impacts. This approach is an important tool which can be applied to many other related oceanographic research problems and will continue to be so into the foreseeable future.

Appendix A

Supplementary material for Chapter 2

A.1 Example Ariane namelist file

```
&ARIANE
  key_roms       = .FALSE. ,
  key_alltracers = .FALSE.,
  key_sequential = .TRUE.,
  mode           = 'qualitative',
  forback        = 'backward',
  bin            = 'NOBIN',
  nmax           = 120000,
  tunit          = 86400.,
  ntfic          = 5,
  key_approximatesigma=.FALSE.,
/
&SEQUENTIAL
  maxcycles = 1
/
&QUALITATIVE
  delta_t   = 86400.,
  frequency = 5,
  nb_output = 200,
  mask      = .FALSE.,
/
&OPAPARAM
  imt      = 4322,
  jmt      = 3059
  kmt      = 75,
  lmt      = 144,
  key_periodic     = .TRUE.,
  key_jfold        = .TRUE.,
  pivot            = T,
  key_computew     = .FALSE.,
  key_partialsteps = .TRUE.,
  key_sigma        = .TRUE.,
  zsigma           =   2000.,
/
&ZONALCRT
  c_dir_zo     = '/noc/msm/scratch/oikos/ekp/ARIANE/REGIONS/
NEMO_0083_1980_2010/means_5d/',
  c_prefix_zo  = 'U',
  ind0_zo      = 2118,
  indn_zo      = 2262,
  maxsize_zo   = 4,
  c_suffix_zo  = '.nc',
  nc_var_zo    = 'vozocrtx',
  nc_var_eivu  = 'NONE',
  nc_att_mask_zo = 'missing_value',
/
&MERIDCRT
  c_dir_me     = '/noc/msm/scratch/oikos/ekp/ARIANE/REGIONS/
NEMO_0083_1980_2010/means_5d/',
  c_prefix_me  = 'V',
  ind0_me      = 2118,
  indn_me      = 2262,
  maxsize_me   = 4,
  c_suffix_me  = '.nc',
```

```
  nc_var_me    = 'vomecrty',
  nc_var_eivv  = 'NONE',
  nc_att_mask_me = 'missing_value',
/
&VERTICRT
  c_dir_ve     = '/noc/msm/scratch/oikos/ekp/ARIANE/REGIONS/
NEMO_0083_1980_2010/means_5d/',
  c_prefix_ve  = 'W',
  ind0_ve      = 2118,
  indn_ve      = 2262,
  maxsize_ve   = 4,
  c_suffix_ve  = '.nc',
  nc_var_ve    = 'vovecrtz',
  nc_var_eivw  = 'NONE',
  nc_att_mask_ve = 'missing_value',
/
&TEMPERAT
  c_dir_te     = '/noc/msm/scratch/oikos/ekp/ARIANE/REGIONS/
NEMO_0083_1980_2010/means_5d/',
  c_prefix_te  = 'T',
  ind0_te      = 2118,
  indn_te      = 2262,
  maxsize_te   = 4,
  c_suffix_te  = '.nc',
  nc_var_te    = 'votemper',
  nc_att_mask_te = 'missing_value',
/
&SALINITY
  c_dir_sa     = '/noc/msm/scratch/oikos/ekp/ARIANE/REGIONS/
NEMO_0083_1980_2010/means_5d/',
  c_prefix_sa  = 'T',
  ind0_sa      = 2118,
  indn_sa      = 2262,
  maxsize_sa   = 4,
  c_suffix_sa  = '.nc',
  nc_var_sa    = 'vosaline',
  nc_att_mask_sa = 'missing_value',
/
&MESH
  dir_mesh     = '/noc/users/jr5g10/ariane/
nemo0083/2009_v3.3.1_dfs5.1.1/5_day',
  fn_mesh      = 'allmeshes.nc',
  nc_var_xx_tt = 'glamt',
  nc_var_xx_uu = 'glamu',
  nc_var_yy_tt = 'gphit',
  nc_var_yy_vv = 'gphiv',
  nc_var_zz_ww = 'gdepw_0',
  nc_var_e2u   = 'e2u',
  nc_var_e1v   = 'e1v',
  nc_var_e1t   = 'e1t',
  nc_var_e2t   = 'e2t',
  nc_var_e3t   = 'e3t',
  nc_var_tmask = 'tmask',
  nc_mask_val  = 0.,
```

Appendix B

Published supplementary material for Chapter 3

B.1 Supplementary tables

Table B.1.1: Mixed Layer Depth Sensitivity Analysis: Observation-derived vs. model derived MLDX

MLD Calculation Method			Failed (%)	Ave. Time (years)	Mean Global MLD (m)	Mean SO MLD (m)
World Ocean Atlas 2009	Sigma (crit = 0.125)	Max	81	18.8	194	336
		Monthly	75	23.0	97	165
	Variable Sigma (crit = 0.5°C)	Max	68	34.6	149	193
		Monthly	65	37.2	77	98
NEMO Temperature and Salinity	Sigma (Crit = 0.125)	Max	84	21.2	269	382
		Mean	78	28.5	212	305
		Monthly	77	29.5	112	168
	Variable Sigma (crit = 0.5°C)	Max	75	31.3	220	288
		Mean	70	35.1	176	231
		Monthly	70	35.6	91	122

Table B.1.1: Mixed Layer Depth Sensitivity Analysis: Observation-derived vs. model-derived MLD. A sensitivity analysis on observation derived mixed layer depth (MLD) versus model derived MLD. The observations are from the 2009 World Ocean Atlas

data sets, using temperature and salinity (in table: World Ocean Atlas 2009), and the model used is the NEMO 1/4° simulation which produces monthly mean temperature and salinity output (NEMO Temp and Sal). The MLD's have been calculated using two methods, density (Sigma) and variable potential density (Variable sigma), with critical values of 0.125 (sigma units) and 0.5°C respectively (see section 3.2 of paper for method description). With each method of calculation, a sensitivity test using two possible climatologies and also the actual monthly MLD (Monthly) has been explored. Model output from 1997 - 2006 (same as the velocity data used in Ariane) is used to calculate the mean of each annual maximum MLD (Mean) and also the absolute maximum of each annual maximum MLD (Max). Each of these MLD's have been used as MLDX in our main analysis to calculate percent failed (Failed) and average time scale to failure (Ave. Time). Finally, of each MLD calculated and used as MLDX, the table gives the overall global mean depth of the mixed layer (Mean Global MLD) and the average depth of the mixed layer in the Southern Ocean (Mean SO MLD). The maximum difference in failure rate between monthly MLD and the maximum of the annual maximum MLD for each calculation method is 7% (NEMO data, sigma method). In regard to observation vs. model derived MLD, the last two columns reveal the model to over-estimate the depth of the mixed layer compared to observations, and consequently causes higher failure rates, but only slightly.

Table B.1.2: Mixed Layer Depth Sensitivity Analysis: Model diagnostic MLDX

MLD Calculation Method		Failed (%)	Ave. Time (years)	Mean Global MLD (m)	Mean SO MLD (m)
NEMO Diagnostic (Sigma: 0.01)	Max	69	35.6	166	221
	Mean	66	37.8	130	173
	Monthly	65	38.3	64	86
Re-calc Diagnostic MLD	Max	70	34.8	171	233
	Mean	66	37.2	130	173
	Monthly	66	37.7	63	88
Upper critical value = 0.1	Max	81	25.7	251	350
	Mean	75	30.5	199	281
	Monthly	74	31.3	104	153
Lower critical value = 0.001	Max	62	38.3	80	123
	Mean	60	39.8	67	100
	Monthly	59	40.3	35	49

Table B.1.2: Mixed Layer Depth Sensitivity Analysis: Model diagnostic MLDX sensitivity. In Table B.1.1, MLD was calculated from NEMO data using different criteria (density, variable potential density). These calculated MLDs differ from that used in our default analysis because they were calculated from 30 day mean model output of temperature and salinity rather than the diagnostic MLD calculated timestep-by-timestep by NEMO whilst online. To assess the significance of this temporal difference in calculation method, we recalculated MLD using the same criterion (sigma 0.01, 10 m reference depth) as our default analysis (in table: Diagnostic MLD) but using 30 day mean model temperature and salinity output (Re-calc Diagnostic MLD). In spite of this calculation difference, the recalculated MLD closely matched that produced online by NEMO in simulation, and the particle failure rates and times are also very similar. Next, we conducted a sensitivity analysis on the value of the sigma criterion using critical values lower (0.001; Lower Critical Value) and higher (0.1; Higher Critical Value) than the default value (0.01). These aimed to provide respectively lower and higher MLDs to estimate the sensitivity of our particle failure approach to MLD. As Table

B.1.1, Table B.1.2 lists the global and Southern Ocean average MLDs determined using these alternative criteria, together with the resulting failure rate (%) and average time to failure (years). As previously, this analysis utilized Max, Mean and Monthly MLDs. The MLDX used in the Results section of the paper is highlighted in red, the modeled mean annual maximum MLD.

Table B.1.3: Failure sensitivity analysis: Outgassing timescale variability

Max. limit in mixed layer (months)	Failed (%)
1	66
2	65
3	65
4	64
5	64
6	64
7	63
8	63
9	63
10	62
11	62
12	62

Table B.1.3: Failure sensitivity analysis: Outgassing timescale variability. A sensitivity analysis to assess the robustness of the fail criteria used in the main analysis of the paper. Repeating the main analysis (calculating the % failed) the particles were allowed to spend up to 12 months in the mixed layer without being classed as failed so long as they are resubducted beneath MLDX within the specified number of months (in table: Max limit in mixed layer). The second column (Failed) refers to the failure percentage at the end of the experiment having allowed for the defined number of months a particle can spend in the UML. Even with a maximum allowance of 12 months in the UML, this only reduces the failure rate by 4%.

Table B.1.4: Ocean Iron Fertilization Modeling Studies. The data presented in B.1.4 was extracted from papers outlined under *Authors*. The table includes details about a selection of previous ocean iron fertilization modeling studies, specifically details about the physical models used. Column *Physical Model*: The underlying physical model used in the study. Column *Resolution*: The resolution of the underlying physical model. Column *Coupled Model*: Models that were coupled to the physical model for the experiment. Column *Simulation Time*: Number of years the experiment was run for. Column *Sequestration Criteria*: Details about how the study defines sequestration success.

B.2 Supplementary figure

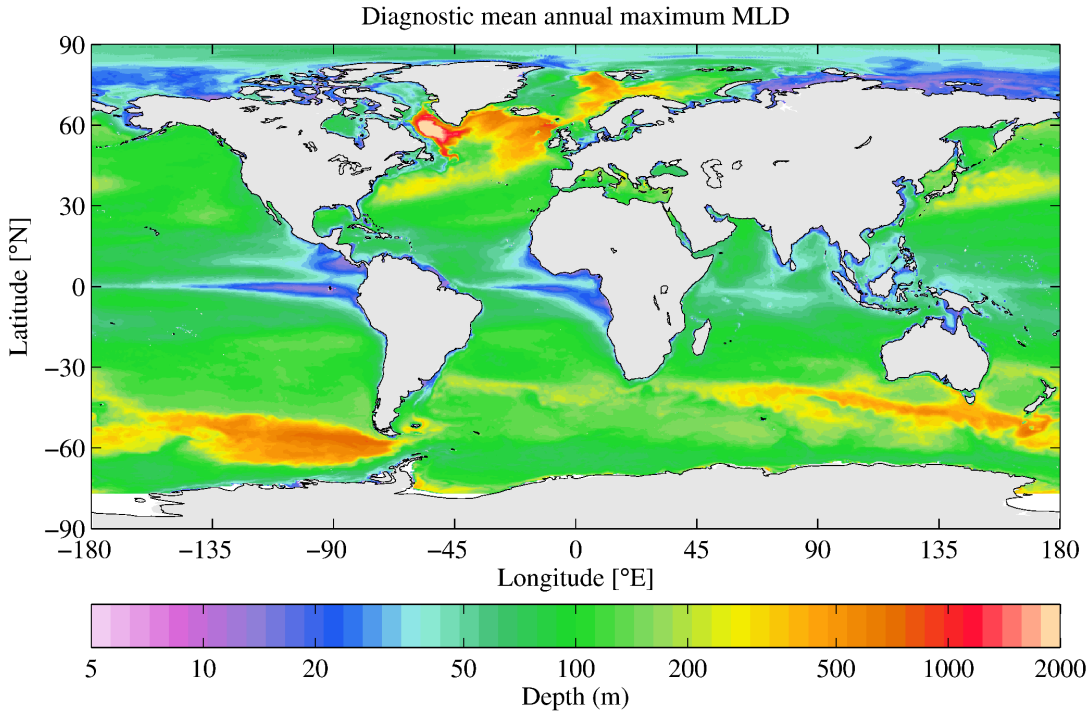

Figure B.2.1: The NEMO modeled mean annual (1997–2006) maximum MLD used in the main analysis as MLDX. The color scale is logarithmic, and represents the depth (m) of the mixed layer. This is the NEMO models diagnostic mixed layer, which was calculated using the density method with a critical value of 0.01 sigma units.

B.3 Supplementary movies

To view the movies, see Supporting Information at: `http://onlinelibrary.wiley.com/doi/10.1002/2013GL058799/full`.

Table B.1.4: Ocean Iron Fertilization Modeling Studies.

Author	Physical Model	Resolution	Coupled Model	Simulation Time	Sequestration Criteria
Oschlies et al. (2010)	University of Victoria Earth System Climate Model	1.8° latitude 3.6° longitude	Marine ecosystem model. Energy-moisture balance model of the atmosphere. Dynamic-thermodynamic sea ice component	1765 - 2300 (Fertilization began in 2011)	Air-Sea CO_2 flux at the location of fertilization and globally
Sarmiento et al. (2010)	Ocean component of the GFDL CM2.1 global coupled climate model	Horizontal resolution is 3° x 3° in the mid-latitudes and 3° x 2°/3° near the equator	GFDL TOPAZ - Biogeochemistry	100 year simulation	The cumulative atmospheric CO_2 uptake divided by the cumulative iron addition
Aumont & Bopp (2006)	ORCA2 -LIM	Horizontal resolution is 2° x 2° in the mid-latitudes and 0.5° at the equator	Dynamic-thermodynamic ice model (Louvain-La Neuve) and PISCES	100 year simulation	% increase in export
Dutkiewicz et al. (2006)	MIT ocean circulation model	2.8 ° x 2.8 °	Coupled oceanic iron, phosphorus and carbon cycles using the adjoint method	10 and 100 year for air-sea flux of CO_2	Ton of carbon sequestered per additional ton of bioavailable iron added
Gnanadesikan et al. (2003)	OCMIP model	3.75° x 4.5°	OCMIP 2 biogeochemical model	100 year simulation	Discusses advantages and caveats

Appendix C

Published supplementary material for Chapter 4

C.1 Supplementary figures

The supporting figures show the same velocity data as in Figure 4.1 [b] and [c] of the main article, but are zoomed in on the three islands studied in this paper. The supporting figures show the decadal, annual and monthly averaged velocity, from both the NEMO model and Aviso satellite data, for illustrative purposes.

Figures C.1.1 - C.1.3 show the decadal, annual and monthly averaged circulation, of both model and satellite derived velocities, for each island. The left column is the Aviso velocity and the right column is the NEMO modeled velocity, the green contour represents the 180 m isobath. The top two panels is the decadal average velocities (same as Figure 4.1 [b] and [c]), the middle two panels are the 1998 annual average,

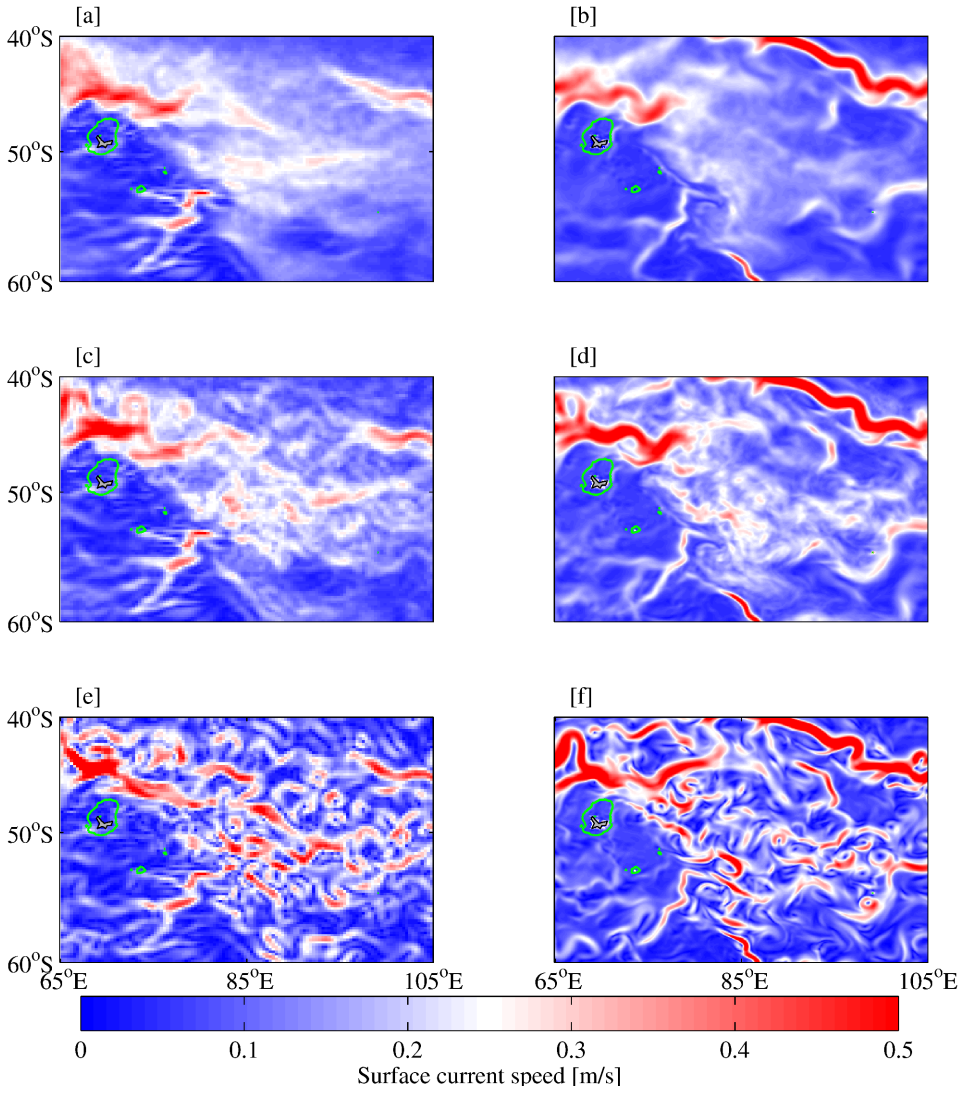

Figure C.1.1: Average surface current speed [m^{-s}] from model and satellite data around the Kerguelen Plateau. The left column is the Aviso satellite derived circulation, at 1/4° resolution, and the right column is the NEMO modeled circulation, at 1/12° resolution. The top row, [a] – [b], is the decadal average over 1998 – 2007; the middle row, [c] – [d], are the 1998 annual average; and the bottom row [e] – [f], are monthly averages of January 1998. The green contour represents the 180 m isobath.

and the bottom panels are the monthly average, January 1998.

As with the wider Southern Ocean, the model correctly captures the major features, and also their magnitude, around each islands. In Figure S1, the model does a good job at simulating the local circulation around the island, and further downstream, across

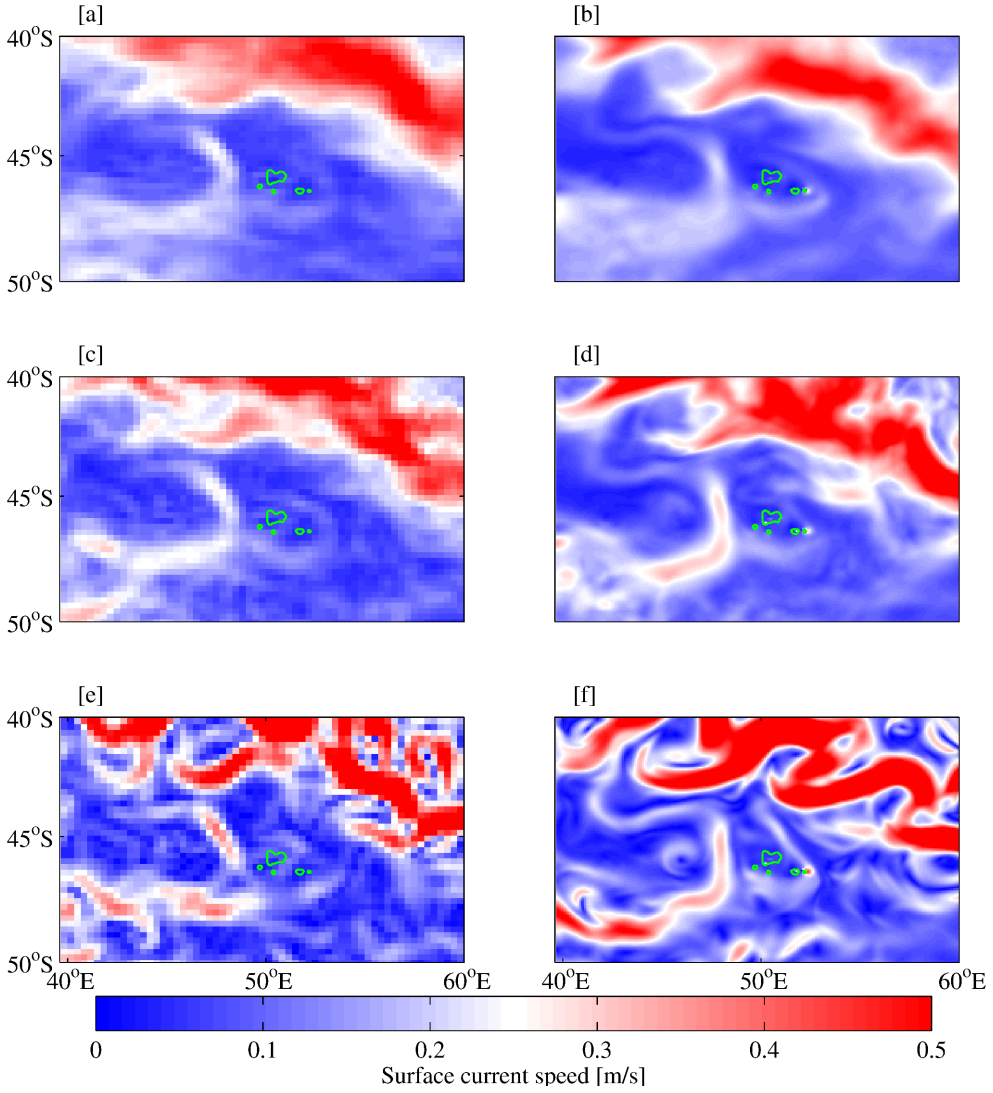

Figure C.1.2: Average surface current speed [m^{-s}] from model and satellite data around the Crozet Islands. The left column is the Aviso satellite derived circulation, at 1/4° resolution, and the right column is the NEMO modeled circulation, at 1/12° resolution. The top row, [a] – [b], is the decadal average over 1998 – 2007; the middle row, [c] – [d], are the 1998 annual average; and the bottom row [e] – [f], are monthly averages of January 1998. The green contour represents the 180 m isobath.

the three averaged periods. The only exception is the large current in the northeast region of the Kerguelen plot, which is much stronger than in the observations, however as there is no bloom occurring in this region it will not impact the results.

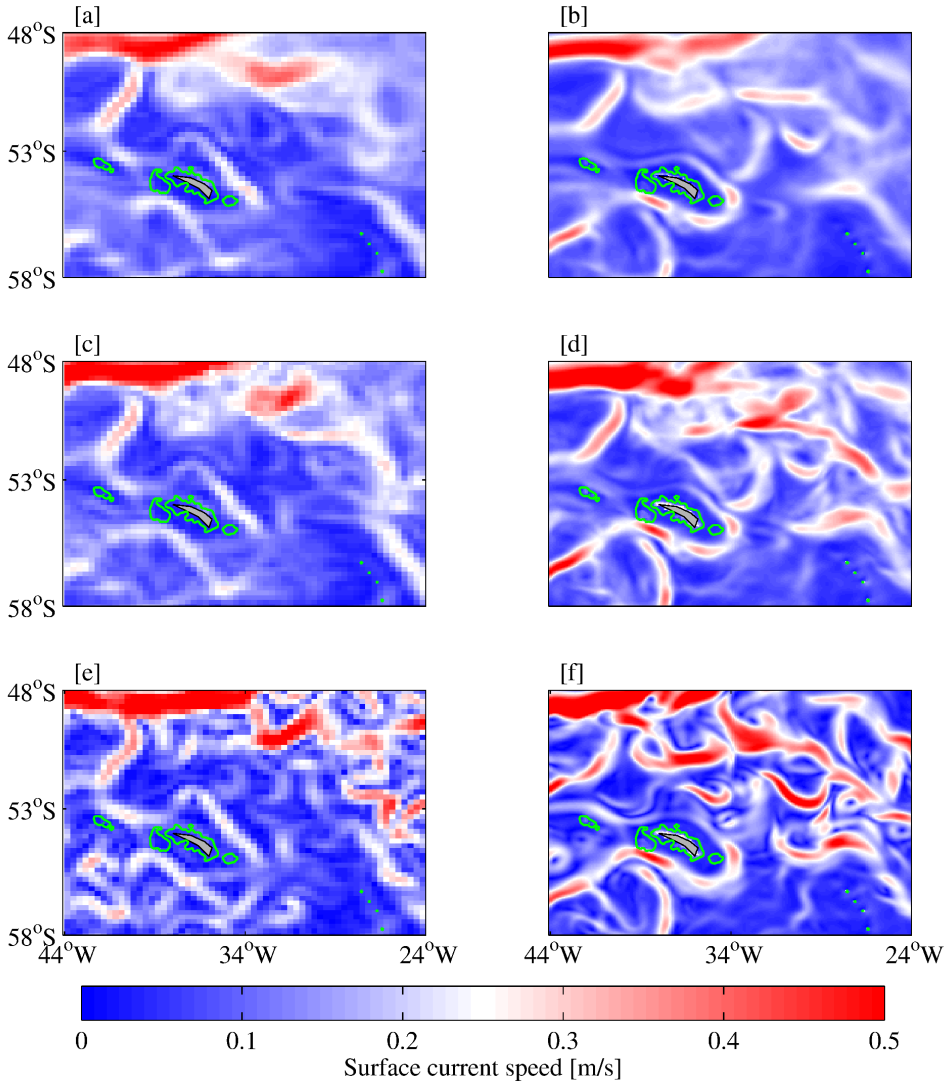

Figure C.1.3: Average surface current speed [m^{-s}] from model and satellite data around South Georgia. The left column is the Aviso satellite derived circulation, at 1/4° resolution, and the right column is the NEMO modeled circulation, at 1/12° resolution. The top row, [a] – [b], is the decadal average over 1998 – 2007; the middle row, [c] – [d], are the 1998 annual average; and the bottom row [e] – [f], are monthly averages of January 1998. The green contour represents the 180 m isobath.

Figure S2 demonstrates that the model is reproducing the Crozet Islands local circulation very well. At the highest temporal resolution, the monthly averages (bottom row), there are more noticeable variations between the model and observations. However, the meandering current in the northeast of the plot is a complex feature which the model captures in the correct location and magnitude, if not identical shape.

In Figure S3, the model simulates the local circulation around South Georgia reasonably well, however the area is highly dynamic and consequently difficult to capture exactly. Nevertheless, the model reproduces all the main features in the correct locations, and at a comparable magnitude to the observations.

Appendix D

Submitted supplementary material for Chapter 5

D.1 Supplementary figures

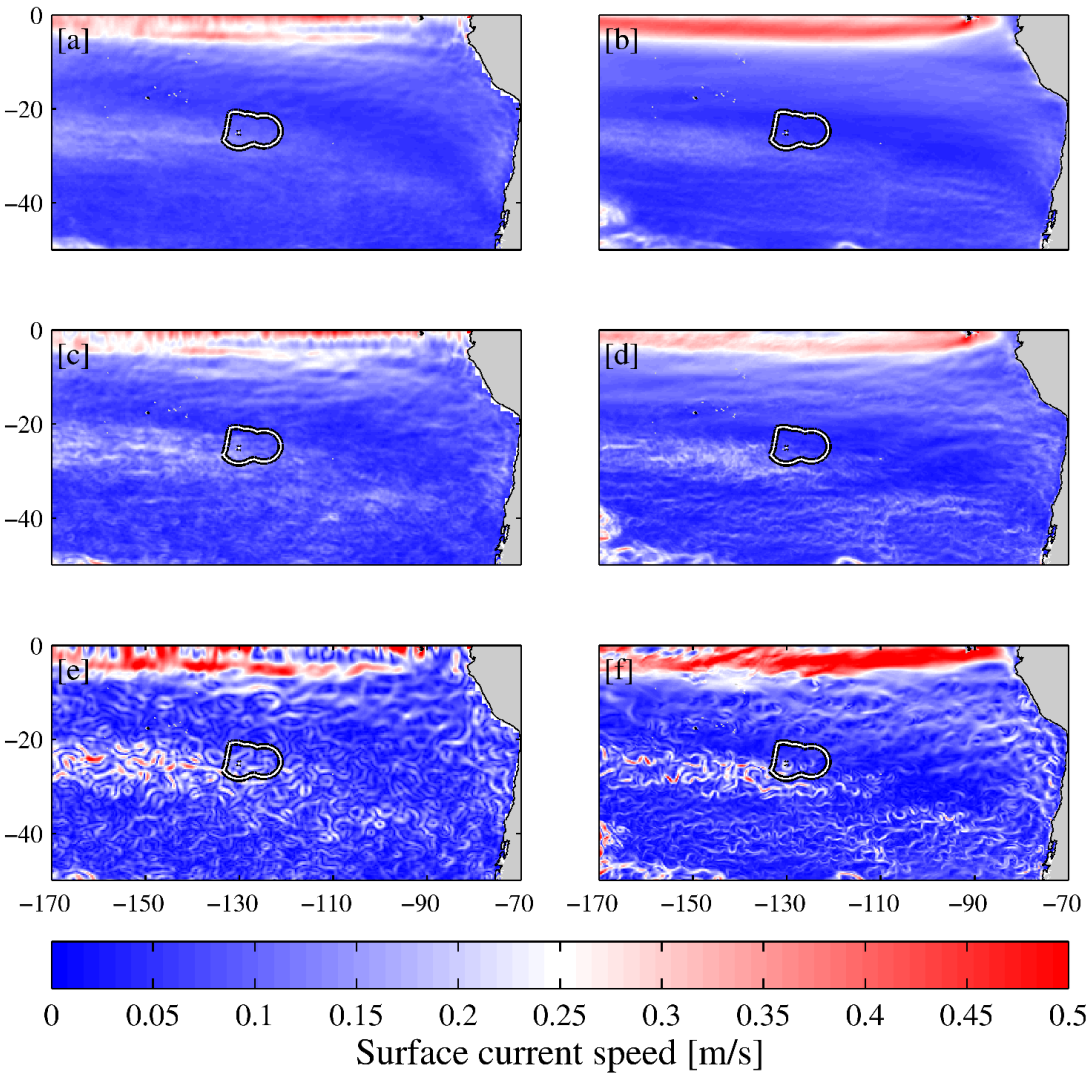

Figure D.1.1: Observed and modelled decadal, annual and monthly average surface current speed (m s^{-1}) around the Pitcairn marine protected area. The observed velocity, panels [a,c,e], is the OSCAR data set at 1/3° resolution, and the modelled velocity, panels [b,d,f], is the NEMO ocean general circulation model at 1/12° resolution. Panels [a] and [b] are the decadal average surface current speeds (2000 – 2009). Panels [c] and [d] are the annual average surface current speeds (2000). Panels [e] and [f] are monthly average surface current speeds (January, 2000). The black and white contour denotes the boundary of the Pitcairn marine protected area.

D.2 Supplementary tables

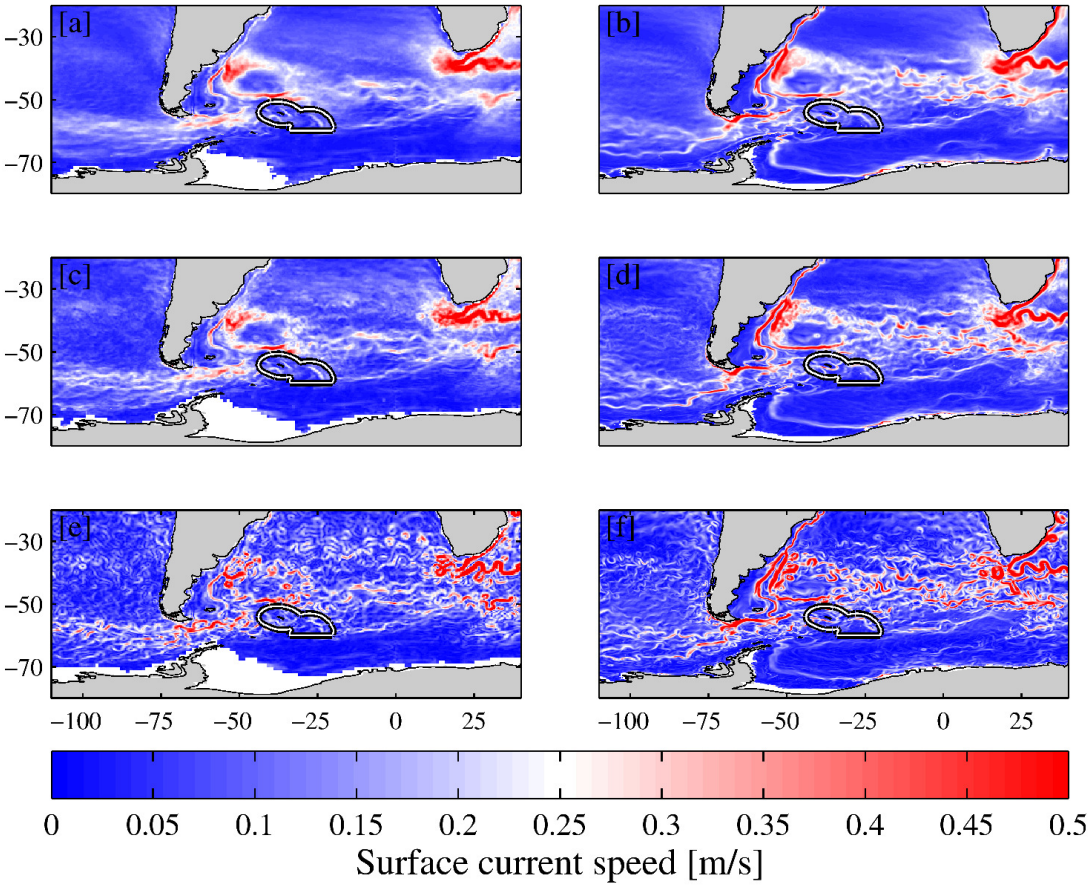

Figure D.1.2: Observed and modelled decadal, annual and monthly average surface current speed (m s^{-1}) around the South Georgia marine protected area. The observed velocity, panels [a,c,e], is the OSCAR data set at 1/3° resolution, and the modelled velocity, panels [b,d,f], is the NEMO ocean general circulation model at 1/12° resolution. Panels [a] and [b] are the decadal average surface current speeds (2000 – 2009). Panels [c] and [d] are the annual average surface current speeds (2000). Panels [e] and [f] are monthly average surface current speeds (January, 2000). The black and white contour denotes the boundary of the South Georgia marine protected area.

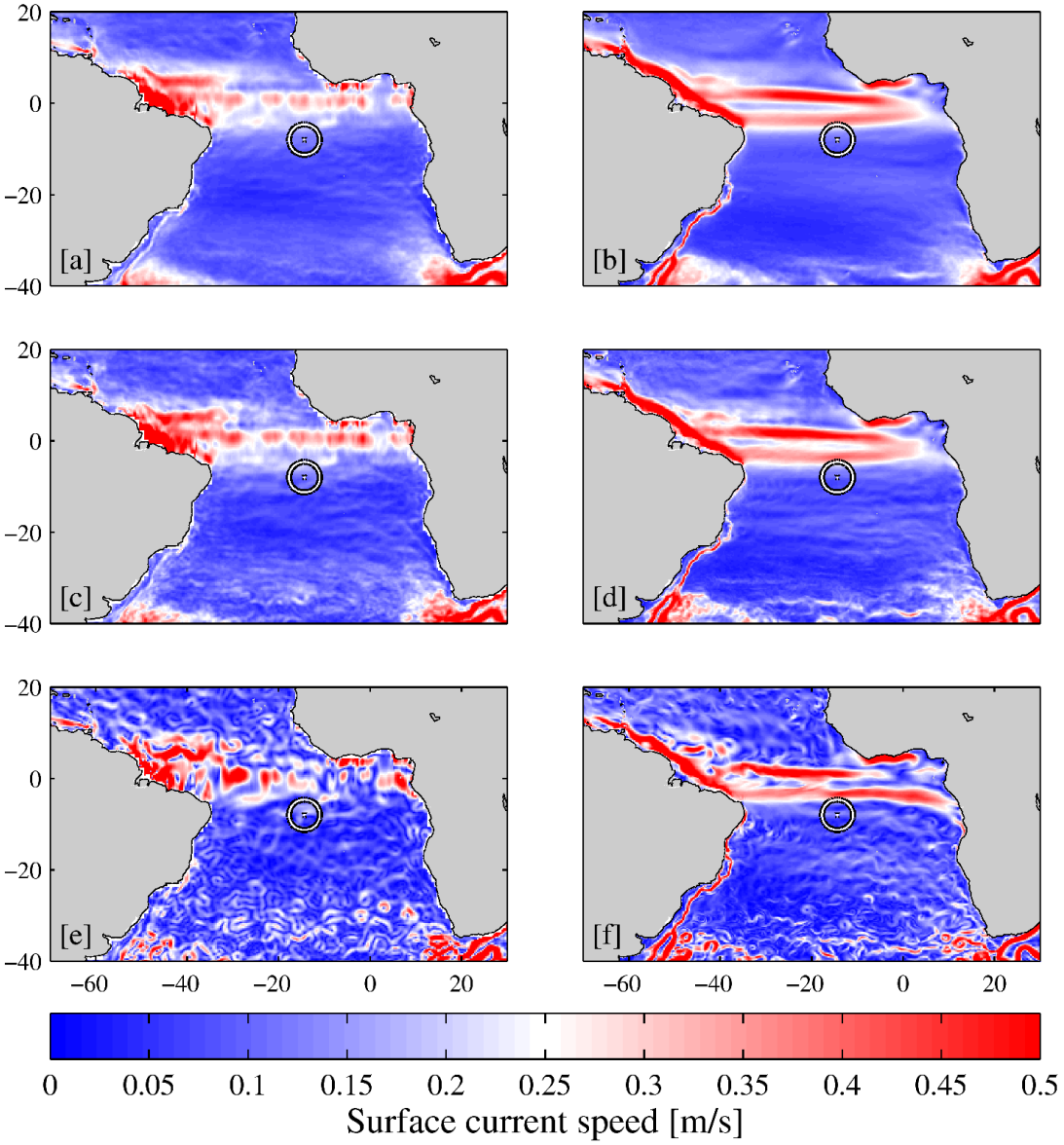

Figure D.1.3: Observed and modelled decadal, annual and monthly average surface current speed (m s^{-1}) around the Ascension marine protected area. The observed velocity, panels [a,c,e], is the OSCAR data set at 1/3° resolution, and the modelled velocity, panels [b,d,f], is the NEMO ocean general circulation model at 1/12° resolution. Panels [a] and [b] are the decadal average surface current speeds (2000 – 2009). Panels [c] and [d] are the annual average surface current speeds (2000). Panels [e] and [f] are monthly average surface current speeds (January, 2000). The black and white contour denotes the boundary of the Ascension marine protected area.

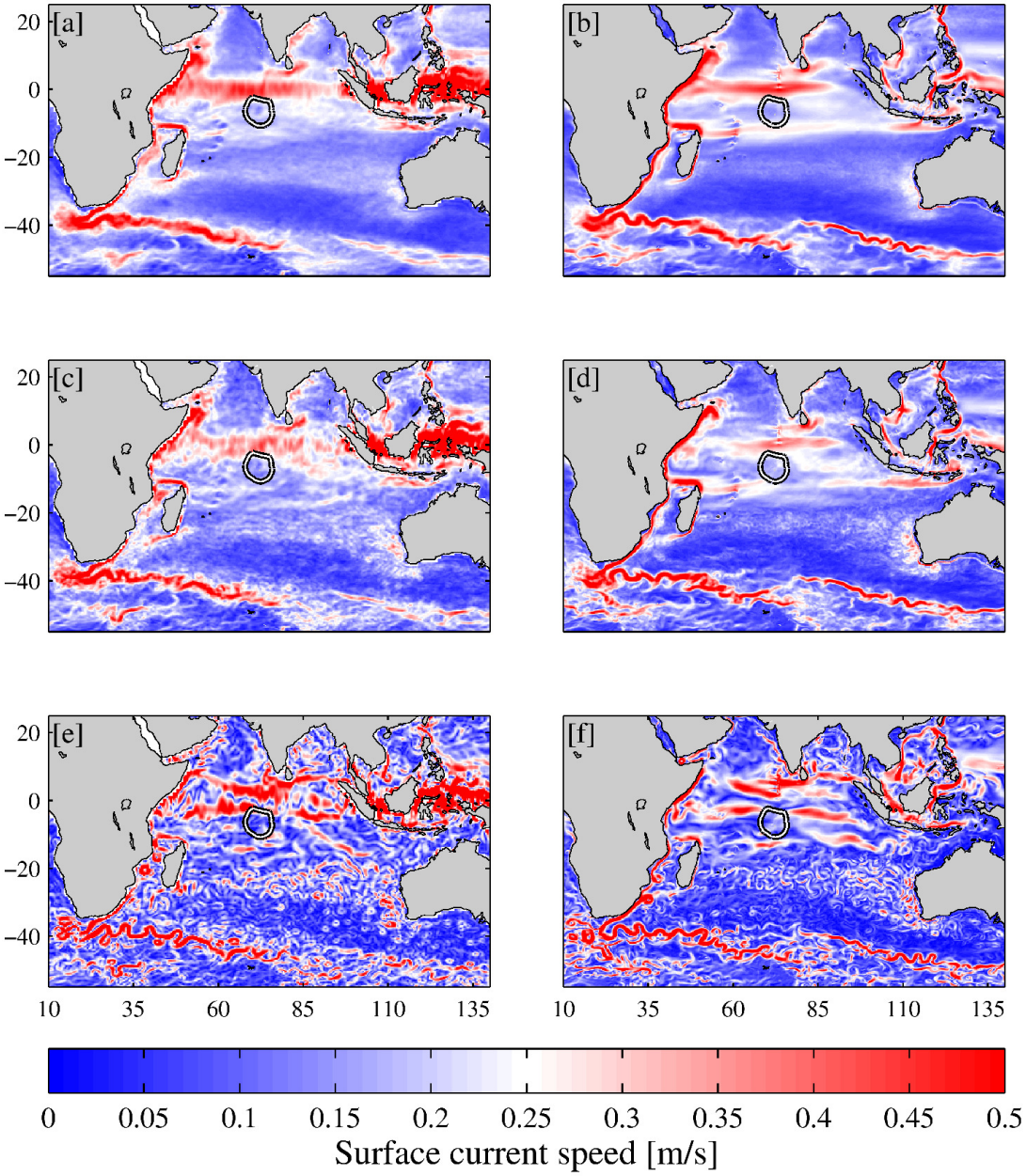

Figure D.1.4: Observed and modelled decadal, annual and monthly average surface current speed (m s^{-1}) around the BIOT marine protected area. The observed velocity, panels [a,c,e], is the OSCAR data set at 1/3° resolution, and the modelled velocity, panels [b,d,f], is the NEMO ocean general circulation model at 1/12° resolution. Panels [a] and [b] are the decadal average surface current speeds (2000 – 2009). Panels [c] and [d] are the annual average surface current speeds (2000). Panels [e] and [f] are monthly average surface current speeds (January, 2000). The black and white contour denotes the boundary of the BIOT marine protected area.

Year	**Jan**	**Feb**	**Mar**	**Apr**	**May**	**Jun**	**Jul**	**Aug**	**Sep**	**Oct**	**Nov**	**Dec**
2000	0.00	0.00	0.00	0.00	0.00	0.00	0.00	0.00	0.00	0.00	0.00	0.00
2001	0.00	0.05	0.00	0.00	0.00	0.00	0.00	0.00	0.00	0.00	0.00	0.00
2002	0.00	0.00	0.00	0.00	0.00	0.00	0.00	0.00	0.00	0.00	0.00	0.00
2003	0.05	0.16	0.00	0.00	0.00	0.00	0.00	0.00	0.00	0.00	0.00	0.00
2004	0.00	0.00	0.00	0.00	0.00	0.00	0.00	0.00	0.00	0.00	0.05	0.05
2005	0.00	0.00	0.00	0.00	0.00	0.00	0.00	0.00	0.00	0.00	0.00	0.00
2006	0.05	0.00	0.00	0.00	0.00	0.00	0.00	0.00	0.00	0.00	0.00	0.00
2007	0.00	0.00	0.00	0.00	0.00	0.00	0.00	0.00	0.00	0.00	0.00	0.21
2008	0.00	0.00	0.00	0.00	0.00	0.00	0.00	0.00	0.00	0.00	0.00	0.00
2009	0.00	0.00	0.00	0.00	0.00	0.00	0.00	0.00	0.00	0.05	0.05	0.00

Table D.2.1: Percentage of water source that originates within 85 km of land, for the Pitcairn MPA. For each monthly release, throughout the 10–year experiment, the percentage of particles which circulated within 85 km of the coast.

Year	**Jan**	**Feb**	**Mar**	**Apr**	**May**	**Jun**	**Jul**	**Aug**	**Sep**	**Oct**	**Nov**	**Dec**
2000	1.32	1.66	1.41	1.32	1.25	1.23	1.20	1.38	1.15	1.06	0.96	0.54
2001	0.81	1.06	0.99	0.97	0.86	0.47	0.47	0.67	1.07	1.28	1.14	1.45
2002	0.93	1.23	1.06	1.49	1.40	1.40	1.19	0.76	1.07	0.86	0.88	0.96
2003	0.68	0.62	0.54	0.41	0.57	0.50	0.45	0.47	0.36	0.94	0.76	1.01
2004	0.99	0.99	1.06	1.20	1.10	1.20	1.33	1.17	0.88	1.06	0.65	0.91
2005	0.94	0.93	0.99	0.99	1.56	1.92	1.66	1.15	1.53	1.64	1.14	1.38
2006	1.19	0.86	0.71	0.63	0.63	0.60	0.78	0.73	0.70	0.57	0.71	0.97
2007	0.94	0.83	0.76	1.19	1.10	1.38	1.15	1.17	1.28	1.07	1.33	1.06
2008	1.92	2.03	1.66	1.79	2.05	1.97	1.71	1.45	1.14	0.80	1.04	0.94
2009	1.01	1.09	1.25	1.06	1.35	1.41	1.40	1.67	1.51	1.40	1.40	1.48

Table D.2.2: Percentage of water source that originates within 85 km of land, for the South Georgia MPA. For each monthly release, throughout the 10–year experiment, the percentage of particles which circulated within 85 km of the coast.

Year	**Jan**	**Feb**	**Mar**	**Apr**	**May**	**Jun**	**Jul**	**Aug**	**Sep**	**Oct**	**Nov**	**Dec**
2000	21.92	24.88	22.27	21.21	18.36	22.27	19.08	15.64	14.81	11.26	12.20	17.18
2001	25.47	24.29	23.93	28.79	20.38	16.82	20.02	17.18	16.94	16.82	18.36	19.91
2002	24.05	24.41	27.61	24.53	26.30	28.91	26.30	29.50	23.70	19.19	20.50	23.58
2003	27.73	31.52	34.83	32.94	31.28	29.27	28.91	31.04	31.64	27.37	23.10	21.33
2004	34.48	30.69	30.33	34.36	35.07	37.56	33.29	31.99	29.03	21.45	21.45	23.22
2005	28.79	34.95	34.60	31.87	32.23	32.58	32.23	29.50	25.71	22.04	25.95	29.86
2006	30.92	31.64	38.03	34.24	32.58	33.65	32.94	28.55	25.00	23.93	22.63	20.38
2007	29.74	33.41	38.03	35.90	34.12	31.40	28.55	26.30	20.26	20.02	24.17	28.32
2008	26.18	29.38	30.81	32.94	29.74	32.46	34.24	32.46	32.35	28.08	26.18	27.37
2009	28.91	26.66	30.92	31.40	32.94	35.43	31.87	32.11	29.86	21.21	25.71	25.36

Table D.2.3: Percentage of water source that originates within 85 km of land, for the Ascension MPA. For each monthly release, throughout the 10–year experiment, the percentage of particles which circulated within 85 km of the coast.

Year	**Jan**	**Feb**	**Mar**	**Apr**	**May**	**Jun**	**Jul**	**Aug**	**Sep**	**Oct**	**Nov**	**Dec**
2000	34.57	35.05	62.77	67.04	64.87	67.77	62.77	50.44	48.27	58.66	43.59	34.25
2001	58.90	66.64	73.25	70.35	72.52	67.28	60.44	57.61	46.01	34.25	30.38	31.35
2002	55.36	51.41	57.13	62.85	59.55	63.17	54.47	29.33	29.33	42.63	53.02	58.42
2003	48.91	57.21	66.72	70.99	68.98	65.19	54.47	51.97	62.69	75.10	76.63	69.46
2004	52.14	49.56	56.57	65.03	71.07	67.69	56.73	42.39	53.91	70.83	68.09	54.71
2005	67.69	74.70	75.02	70.75	80.42	76.79	68.57	48.51	44.56	52.86	43.92	49.15
2006	58.74	60.76	64.30	66.48	57.05	51.57	43.92	46.90	57.86	75.10	74.94	69.54
2007	44.00	52.54	52.94	53.59	52.14	58.02	71.15	66.40	59.31	58.34	56.65	62.37
2008	48.51	55.84	62.13	61.97	66.48	65.35	54.07	51.01	49.23	56.97	65.59	62.69
2009	56.08	60.19	60.35	61.72	62.69	65.35	60.11	56.89	56.33	57.29	49.23	47.54

Table D.2.4: Percentage of water source that originates within 85 km of land, for the BIOT MPA. For each monthly release, throughout the 10–year experiment, the percentage of particles which circulated within 85 km of the coast.

Year	**Jan**	**Feb**	**Mar**	**Apr**	**May**	**Jun**	**Jul**	**Aug**	**Sep**	**Oct**	**Nov**	**Dec**
2000	0	0	0	0	0	0	0	0	0	0	0	0
2001	0	10	0	0	0	0	0	0	0	0	0	0
2002	0	0	0	0	0	0	0	0	0	0	0	0
2003	10	11	0	0	0	0	0	0	0	0	0	0
2004	0	0	0	0	0	0	0	0	0	0	29	10
2005	0	0	0	0	0	0	0	0	0	0	0	0
2006	32	0	0	0	0	0	0	0	0	0	0	0
2007	0	0	0	0	0	0	0	0	0	0	0	14
2008	0	0	0	0	0	0	0	0	0	0	0	0
2009	0	0	0	0	0	0	0	0	0	34	10	0

Table D.2.5: Maximum population density, persons per km^2, encountered by trajectories from the Pitcairn MPA. For each monthly release of particles, throughout the 10–year experiment, of the particles than came within 85 km of the coast, the maximum population density encountered is given.

Year	**Jan**	**Feb**	**Mar**	**Apr**	**May**	**Jun**	**Jul**	**Aug**	**Sep**	**Oct**	**Nov**	**Dec**
2000	7	2683	1948	731	6	8	6	3	2	2	1	1
2001	2	3037	2094	3134	4	2	1	1	4	5	2	313
2002	6	2	2	132	2	1741	1212	2	2	68	2357	202
2003	12	2	2	1508	10	14	1	1360	1	159	1	1
2004	1	2	2	177	2	2	4	2	2	1	1	1
2005	2	2	2	2	326	5	2	114	1823	5	2	3
2006	7	1	1	1	1	1	1	2	1	2	5	2
2007	2	1	2	606	1	1	2	2	2	2368	2	2
2008	10	2	1	2	1	2	2	1	2	2	2	3
2009	3	1	2	1	2	2	2	2	2	2	2	2

Table D.2.6: Maximum population density, persons per km^2, encountered by trajectories from the South Georgia MPA. For each monthly release of particles, throughout the 10–year experiment, of the particles than came within 85 km of the coast, the maximum population density encountered is given.

Year	**Jan**	**Feb**	**Mar**	**Apr**	**May**	**Jun**	**Jul**	**Aug**	**Sep**	**Oct**	**Nov**	**Dec**
2000	2725	2454	1793	1924	2459	2915	3167	2237	3202	2960	3530	1911
2001	4399	2620	2280	2246	2063	2915	3202	1911	2449	2237	2008	5288
2002	2915	4771	5288	2063	2063	2866	3530	4399	3105	3530	2725	2725
2003	3665	3060	3530	3167	2928	4883	2555	2723	2866	2649	2383	2063
2004	2063	2246	3073	2008	2014	2702	2960	3783	3530	2357	2454	2725
2005	2393	3131	2246	2318	3984	3167	1911	5105	3530	3149	3073	2722
2006	2063	2393	2960	3742	3530	5225	3869	3869	3984	2620	2346	2407
2007	2725	3131	5288	2325	3344	2699	3116	3149	1911	2028	1996	2866
2008	1925	2620	2246	3060	3149	5288	3925	2491	2209	3530	2142	2228
2009	2178	3197	2280	3202	3907	5105	2960	2960	2866	3073	3105	2384

Table D.2.7: Maximum population density, persons per km^2, encountered by trajectories from the Ascension MPA. For each monthly release of particles, throughout the 10–year experiment, of the particles than came within 85 km of the coast, the maximum population density encountered is given.

Year	**Jan**	**Feb**	**Mar**	**Apr**	**May**	**Jun**	**Jul**	**Aug**	**Sep**	**Oct**	**Nov**	**Dec**
2000	1872	2162	4105	5133	4382	1826	2074	1587	1485	1528	1702	1635
2001	2131	4468	3933	3630	4098	4626	2089	1789	1824	1681	3034	1826
2002	7480	1830	4768	3166	2163	3880	1830	2163	2257	1793	2131	2077
2003	1966	3157	4961	4407	3816	1826	2163	2163	2017	2953	3777	1989
2004	2163	1830	2163	1722	2074	2163	2163	1455	1789	2442	3634	2442
2005	2729	4382	15203	4382	4783	4805	4625	2163	1717	2163	3471	2163
2006	2270	2116	2163	3753	1889	1889	2163	1472	2420	2784	3124	2420
2007	1830	1722	3648	4382	3369	1881	2074	1516	1811	1824	1890	2784
2008	2163	2078	3942	2074	3446	2163	2074	2163	1348	1717	3034	1824
2009	2074	1824	1830	4352	3984	1830	2163	1681	1592	2162	1989	2059

Table D.2.8: Maximum population density, persons per km^2, encountered by trajectories from the BIOT MPA. For each monthly release of particles, throughout the 10–year experiment, of the particles than came within 85 km of the coast, the maximum population density encountered is given.

Appendix E

Publications

E.1 How deep is deep enough? Ocean iron fertilization and carbon sequestration in the Southern Ocean

AGU PUBLICATIONS

Geophysical Research Letters

RESEARCH LETTER
10.1002/2013GL058799

Key Points:
- Carbon export to 1000 m does not guarantee sequestration in the Southern Ocean
- OIF requires consideration of the circulation as well as biogeochemistry
- Sequestered carbon is dispersed widely out of the Southern Ocean by circulation

Supporting Information:
- Readme
- Table S1
- Table S2
- Table S3
- Table S4
- Movie S1
- Movie S2
- Figure S1

Correspondence to:
J. Robinson,
josie.robinson@noc.soton.ac.uk

Citation:
Robinson, J., E. E. Popova, A. Yool, M. Srokosz, R. S. Lampitt, and J. R. Blundell (2014), How deep is deep enough? Ocean iron fertilization and carbon sequestration in the Southern Ocean, *Geophys. Res. Lett.*, *41*, doi:10.1002/2013GL058799.

Received 10 JAN 2014
Accepted 20 MAR 2014
Accepted article online 25 MAR 2014

How deep is deep enough? Ocean iron fertilization and carbon sequestration in the Southern Ocean

J. Robinson[1,2], E. E. Popova[2], A. Yool[2], M. Srokosz[2], R. S. Lampitt[2], and J. R. Blundell[1]

[1]Ocean and Earth Science, University of Southampton, Southampton, UK, [2]National Oceanography Centre, Southampton, UK

Abstract Artificial ocean iron fertilization (OIF) enhances phytoplankton productivity and is being explored as a means of sequestering anthropogenic carbon within the deep ocean. To be considered successful, carbon should be exported from the surface ocean and isolated from the atmosphere for an extended period (e.g., the Intergovernmental Panel on Climate Change's standard 100 year time horizon). This study assesses the impact of deep circulation on carbon sequestered by OIF in the Southern Ocean, a high-nutrient low-chlorophyll region known to be iron stressed. A Lagrangian particle-tracking approach is employed to analyze water mass trajectories over a 100 year simulation. By the end of the experiment, for a sequestration depth of 1000 m, 66% of the carbon had been reexposed to the atmosphere, taking an average of 37.8 years. Upwelling occurs predominately within the Antarctic Circumpolar Current due to Ekman suction and topography. These results emphasize that successful OIF is dependent on the physical circulation, as well as the biogeochemistry.

1. Introduction

The Intergovernmental Panel on Climate Change Fifth Assessment Report (IPCC AR5) states that the climate has and is warming, unequivocally, and we can now be 95–100% certain that since the midtwentieth century, it is primarily due to anthropogenic influence [*Intergovernmental Panel on Climate Change (IPCC), Working Group I (WGI)*, 2013]. Against this backdrop of increasing greenhouse gas emissions and global climate change, a number of schemes have been proposed to "geoengineer" the Earth's climate. Ocean iron fertilization (OIF) is one such scheme aimed at modifying the biogeochemical cycle of carbon in the ocean in order to increase the oceanic uptake of CO_2. OIF is intended to artificially stimulate the biological pump by exploiting the surplus macronutrients found in so-called high-nutrient low-chlorophyll (HNLC) regions where biological activity is restricted by the availability of the micronutrient iron [*Martin*, 1990]. The Southern Ocean (SO) is by far the largest expanse of HNLC waters and is iron stressed because overlying air masses circle the Earth in a latitude band that has sparse landmass and thus supplies little iron-rich aeolian dust. Consequently, the SO has been identified as a particularly favorable location for OIF [*Lampitt et al.*, 2008].

In the Intergovernmental Panel on Climate Change Fourth Assessment Report (IPCC AR4) successful iron fertilization is divided into phases, of which artificial stimulation of a surface phytoplankton bloom is only the first. For the second phase, a proportion of the particulate organic carbon (POC) produced must sink down the water column and reach the main thermocline or deeper before being remineralized. Finally, the third phase is long-term sequestration of the carbon at depth out of contact with the atmosphere. Characterizing the relevant time and space scales for sequestration is not a wholly objective procedure [*Leinen*, 2008]. Nonetheless, the 100 year time scale adopted in IPCC forecasting is frequently used [*Oschlies et al.*, 2010; *Rickels et al.*, 2010], and the typical depth of the main thermocline, 1000 m [*IPCC, WGI*, 2007, chapter 5], serves as a vertical horizon clearly removed from the surface ocean and atmosphere [*Passow and Carlson*, 2012].

Here we investigate these spatiotemporal scales, specifically the long-term fate of carbon that reaches the deep ocean. Model simulations of the trajectories of Lagrangian particles associated with geoengineered carbon are performed to establish the fate of such material. Statistical analysis of the resulting deep ocean pathways is then used to evaluate carbon sequestration in the SO, with a particular focus on the significance of the 1000 m depth horizon and centennial time scale.

2. Methodology

The Nucleus for European Modelling of the Ocean (NEMO) model is an ocean general circulation model (GCM). The NEMO 1/4° resolution model has been developed with particular emphasis on realistic representation of fine-scale circulation patterns [*Madec*, 2008] and provides an ideal platform to conduct Lagrangian particle-tracking experiments. Here we use 10 years of monthly averaged circulation output from 1997 to 2006 that we cycle 10 times to create a 100 year simulation. The Ariane package [*Blanke and Raynaud*, 1997] (available online at: http://stockage.univ-brest.fr/~grima/Ariane) is applied to the resulting 100 year NEMO velocity field to track water parcels using point particles that are released into the modeled ocean circulation [*Popova et al.*, 2013]. These particles are intended here to represent water masses within which sinking POC, produced through the activities of surface OIF, has been remineralized to dissolved inorganic carbon. They should not be confused with actual POC particles, since their modeled behavior (neutral buoyancy and indefinite lifespan) does not emulate that of sinking biogenic material.

To test the suitability of the 1000 m minimum depth recommendation by the IPCC AR4 [*IPCC WGI*, 2007, chapter 5; *IPCC WGIII*, 2007, chapter 11] for OIF, we deploy Lagrangian particles across the SO at a depth of 1000 m. Particles are placed south of the midpoint between the nitrate maxima to the south and nitrate-depleted waters to the north, which represents the northern limit of the HNLC region in the SO. The particles are spaced regularly across the model grid, and, accounting for bathymetric features shallower than 1000 m, this gives a total of 24982 particles, a sufficient number to resolve SO water mass pathways. During the 100 year simulation, particle trajectories (horizontal position and depth) are recorded at monthly intervals.

The upper mixed layer (UML) of the ocean is characterized by vigorous mixing and near-homogeneous physical and biogeochemical properties and represents the volume of water in close contact with the atmosphere [*Sprintall and Cronin*, 2009]. Here we use the base of the UML, referred to as the mixed layer depth (MLD), as the key boundary to separate failed and successful carbon sequestration, judging any Lagrangian trajectories that enter the UML as potential pathways for OIF carbon to escape back in to the atmosphere. In our analysis we specifically define our boundary, MLDX, as the modeled (local) mean annual maximum MLD rather than instantaneous MLD. The advantage of this approach is that it uses a single horizon to determine leakage of OIF carbon, however, a sensitivity analysis was performed using the maximum annual maximum depth of the MLD and also the actual monthly MLD which only minimally altered the results.

The accuracy of the model-derived MLD was examined by comparison with the MLD calculated from World Ocean Atlas (WOA) 2009 fields of temperature [*Locarnini et al.*, 2010] and salinity [*Antonov et al.*, 2010], using two criteria: a density change of 0.125 (sigma units) and a variable density change corresponding to a temperature change of 0.5°C [*Monterey and Levitus*, 1997], both calculated 10 m from the surface to avoid complications with ice cover. Repeating our central analysis using an observation-derived MLDX, we found that the difference between using the WOA- and NEMO-calculated MLDX to be relatively small. Therefore, and since it is consistent with NEMO's velocity field, we refer only to the NEMO-derived MLDX in the rest of this paper, which was determined using the density calculation method with a critical value of 0.01 (sigma units). Full details on the MLDX sensitivity analysis and comparison with observations, including the global and SO mean MLD, can be found in Tables S1 and S2 in the supporting information. Additionally, Figure S1 in the supporting information shows the NEMO-derived mean annual maximum MLD that is used in the analysis, MLDX, referred to as *NEMO Diagnostic (Sigma, 0.01)* in Table S2.

3. Results

Of the 24982 Lagrangian particles that were injected into the SO at 1000 m, 66% were advected above MLDX taking an average of 37.8 (σ = 22.2) years. In Figure 1 each marker represents the location where a particle crossed the MLDX boundary, with the color indicating the time in years. The most significant feature of Figure 1 is the large-scale sequestration failure within the SO, which accounts for the majority (97%) of all leakage into the UML (average: 37.4 (σ = 22.2) years to fail). The particle advection into the UML can be attributed to the Antarctic Circumpolar Current (ACC), which circulates Antarctica in an eastward direction [*Rintoul*, 2011]. Lagrangian particles caught in the ACC are transported across MLDX as the current is forced up and over sea floor topography, predominately the Scotia Ridge Arc System and the Kerguelen Plateau. The deep dense water (containing the particles at 1000 m) is mixed with the overlying lighter water mass, gaining buoyancy and gradually transporting the particles above MLDX. In addition to advection into the

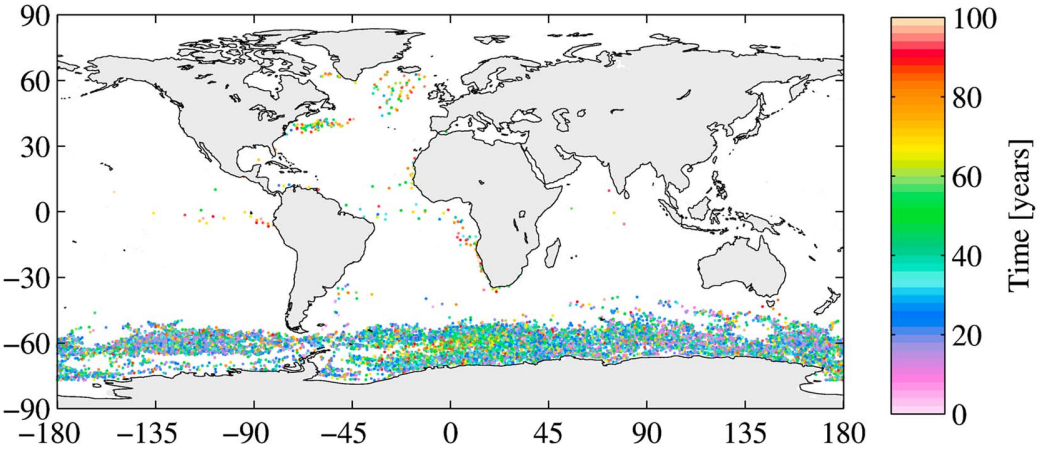

Figure 1. Colored markers represent locations where the Lagrangian particles enter the upper mixed layer. The color of a marker represents the time (years) it took to reach the upper mixed layer within the 100 year run.

UML, there is also Ekman suction occurring in the SO, which upwells the particles south of the Westerlies wind stress maximum over the axis of the ACC [*Sarmiento and Gruber*, 2006]. This is particularly visible in the Pacific and Atlantic sectors of Figure 1, between the latitude bands of 55°S–65°S.

The SO has a particularly energetic circulation connecting the three major ocean basins. Consequently, in our experiment the geographical extent of the particles trajectories covers the entire global ocean (see 1000 m and 2000 m Movies S1 and S2 in the supporting information). By studying the trajectories of successfully sequestered particles it becomes apparent that there is no well-defined deep advective pathway out of the SO. Instead, particle advection out of the SO is distributed relatively evenly across all longitudes, not including the western boundary currents. Figure 2 indicates the density of trajectories of particles that remained sequestered for the entire 100 year simulation. In Figure 2 the highest density of sequestered particle trajectories is within the Ross Gyre, which suggests that this location may facilitate carbon sequestration. In our model the Ross Gyre feeds Lagrangian particles into the narrow westward bound Antarctic Slope Current (ASC). Once within the ASC, particles can be entrained into Antarctic Bottom Water via deep-water formation along the slopes of the Antarctic continent [*Nicholls et al.*, 2009].

Figure 3a illustrates geographical patterns in the time taken for failed particles to be advected across MLDX, relative to their starting positions. The Weddell Gyre is a prominent feature within Figure 3a, where the time taken for particles to fail is longest in the center of the gyre, and then decreases toward its periphery. This pattern occurs because particles starting in the Weddell Gyre become trapped in its strong cyclonic motion

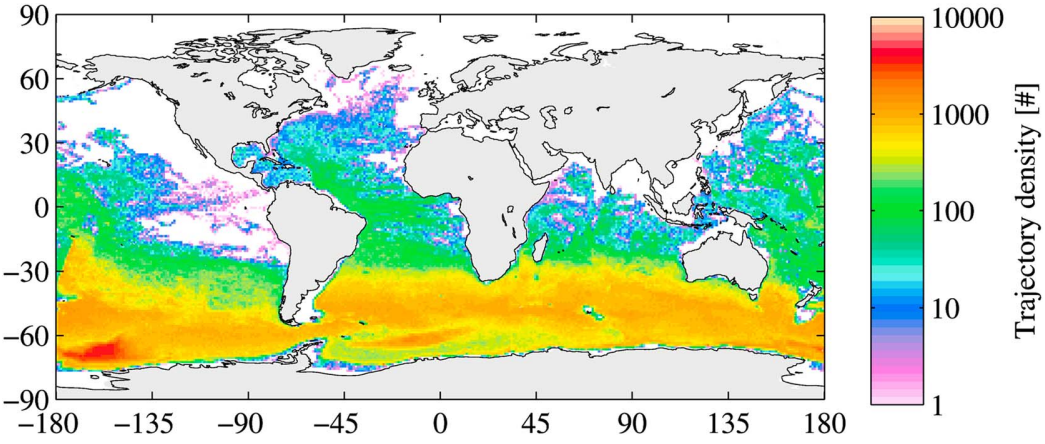

Figure 2. Time-integrated (0–100 years) census of successfully sequestered particles to illustrate their horizontal dispersal. Colors denote the cumulative "density" of particle trajectories based on monthly position throughout the simulation. Note that, for clarity, the color scale is shown in log units.

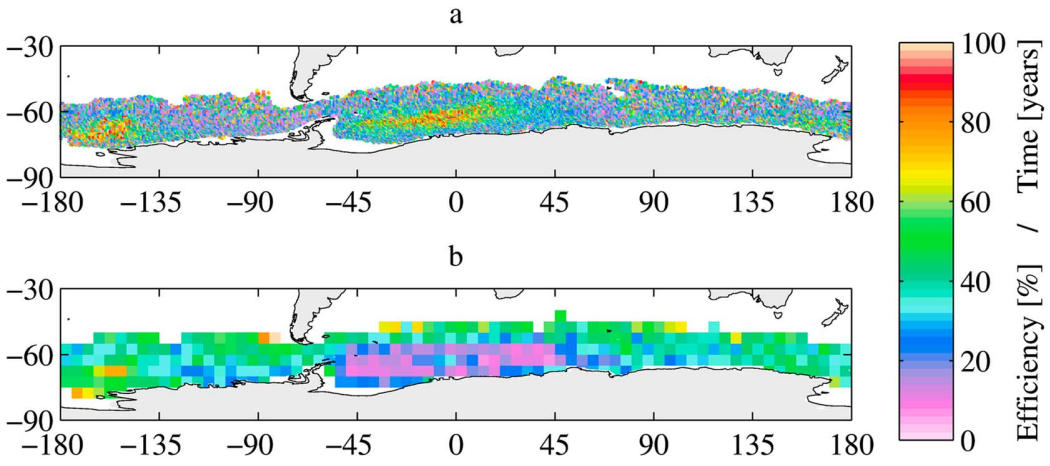

Figure 3. (a) Markers are located at the initial positions of unsuccessful Lagrangian particles at the beginning of the 100 year simulation. The color of a marker represents the time (years) at which the Lagrangian particle breached the mixed layer depth. Particles that did not upwell during the simulation are not included in the plot. (b) Efficiency of sequestration based on the criterion that a particle has to remain below the upper mixed layer to be classed as sequestered. The color of each 5° × 5° grid cell represents the percentage of particles initially in that cell which remain sequestered for the entire 100 year simulation. Grid cells with fewer than 10 particles have not been included in the plot.

[*Williams and Follows*, 2011] which prolongs upwelling to an average of 55.2 years (σ = 20.8) in the core of the gyre (experiment average: 37.8 years, σ = 22.2). Of the particles that start in the Weddell Sea, 85% are advected into the UML, which is the highest failure rate of any region within the SO. The Ross Gyre is also a prominent feature in Figure 3a, though unlike the Weddell Gyre, this location may instead be suitable for OIF due to the connection with the ASC and consequent deep-water formation along the edge of the continental shelf.

Aside from the Weddell and Ross Gyres, there is little clustering within Figure 3a which suggests that particles that start next to each other in the experiment can experience radically different fates. This high sensitivity to initial conditions may be attributed to the vigorous circulation of the SO which has a number of meandering fronts particularly between the latitude bands of 60°S and 40°S [*Rintoul*, 2011].

Based on our criterion for carbon sequestration, Figure 3b shows the geographical distribution of sequestration efficiency, indicating how much sequestration results from particles seeded in each area. As in Figure 3a, the Ross Sea shows up as an area that has high rates of success, while the Weddell Sea is a mixture of areas of relatively high (center of the gyre) and low (peripheral regions) sequestration. A notable low efficiency patch in Figure 3b occurs at roughly 45°E and 60°S. Particles starting in this location become trapped in the ACC eastbound flow and consequently are lifted up and over the Kerguelen Plateau. Note that sequestration efficiency here relates to the 100 year window of our simulation, and that numerous particles ostensibly sequestered here might escape in a longer simulation.

Having studied the depth criterion (1000 m) suggested by the IPCC AR4, we conducted a sensitivity experiment that injected Lagrangian particles at a depth of 2000 m. By the end of this experiment (100 years), only 29% of the particles had breached MLDX taking an average time of 58.4 years (σ = 22.1), with 71% of the particles remaining sequestered for the entire simulation. Further analysis revealed that, of the 29% of particles that did upwell, the vast majority (98%) were again upwelled within the SO, with an average time scale of 58.3 years (σ = 22.1).

4. Discussion

The SO has been repeatedly highlighted as the best area for OIF as it is the largest HNLC region on earth, with potential for large-scale OIF leading to a noticeable impact on atmospheric CO_2 concentrations [*Lampitt et al.*, 2008]. From the paleorecord it is evident that the SO plays a key role in regulating atmospheric CO_2 content, potentially sequestrating up to 100 Pg C in the past [*Kohfeld et al.*, 2005]. Consequently, the SO has been the site of a number of iron addition experiments [*Boyd et al.*, 2012] which generally suggest that OIF does result in enhanced export at the time of fertilization.

Based on these experiments, this study assumes that OIF can enhance export of POC to depth and assesses the impact of ocean circulation on the efficiency of intentional OIF in the SO, specifically focusing on how much deep-sequestered carbon is brought back into contact with the atmosphere downstream of the fertilization site. In our 1000 m experiment, designed to trace the fate of the sequestered carbon for 100 years, 66% was upwelled into the UML on a mean time scale of 37.8 (σ = 22.2) years (Figure 2). The majority (97%) of the carbon brought back into contact with the atmosphere is upwelled within the SO, taking an average time scale of 37.4 (σ = 22.2) years. Such a "leakage" within the vicinity of the fertilization patch questions whether the SO is as good a location for OIF as initially thought.

However, even if the carbon is leaked into the UML there is no guarantee that it would be immediately outgassed. To try and assess the robustness of the fail criteria used in the analysis, the percent failed was recalculated, but allowing the particles 12 consecutive months in the UML without being classed as failed so long as they are resubducted beneath MLDX within a year. This only reduced the failure rate by 4%, which suggests that advection into the UML generally results in a long stay in the mixed layer, which greatly increases the risk of outgassing. However, if the carbon is brought back to the surface, one must assume so too is the Fe associated with it; however, this is highly dependent on the time scales of upwelling, and whether this Fe would be bioavailable for further fertilization is nontrivial [*Jiang et al.*, 2013].

Focusing on successful sequestration for 100 years in our experiment, Figure 2 illustrates the wide geographical extent of the sequestered carbon dispersed by ocean circulation. At the end of the 100 years, only 46% of the sequestered carbon initialized at 1000 m remained within the SO, with the fraction being slightly higher (56%) for the 2000 m experiment. The dispersion evident in our results demands highly sophisticated methods of observation and modeling if validation of carbon sequestration is to be carried out to an acceptable level. In any future commercialization of OIF, the fraction of the sequestered carbon which remains in the deep ocean must be properly estimated [*Rickels et al.*, 2010]. However, as Figure 2 illustrates, the global-scale dispersal of over half of the sequestered carbon presents serious logistical difficulties for monitoring. Furthermore, this dispersal may additionally interfere with attempts to attribute ownership and to allocate carbon credits appropriately (see 1000 m and 2000 m Movies S1 and S2 in the supporting information).

To date, intentional OIF has been examined in a number of modeling studies employing different criteria to quantify the efficacy of OIF (Table S3 in the supporting information), such as the overall reduction in atmospheric CO_2 by the end of the simulation [*Aumont and Bopp*, 2006] or the cumulative CO_2 uptake divided by the cumulative iron addition [*Sarmiento et al.*, 2010]. These studies have effectively assessed OIF efficiency end to end: the impact on primary production, the impact on export of POC to the deep ocean, and the downstream return of carbon to the surface ocean. Our study is unique in that it separates out the impact of ocean circulation from other biogeochemical aspects of OIF to focus solely on phase 3 of OIF and the long-term fate of carbon that has ostensibly been sequestered to depth.

A number of studies [*Aumont and Bopp*, 2006; *Oschlies et al.*, 2010; *Sarmiento et al.*, 2010] report a high proportion of the sequestered carbon being reexposed to the atmosphere over a long time scale; however, the processes or time scales in these models were not discussed. A particular advantage of our study is the use of a much higher resolution 1/4° physical model. This provides an improved representation of important fine-scale circulation features that are not present in the coarse-resolution models (2°–3°) previously employed for OIF studies (see Table S3 in the supporting information). As our study highlights the importance of the circulation in determining global efficiency of OIF, this suggests that models of even higher resolution may be required for an accurate assessment of the geoengineering potential of OIF.

In a related study, which does discuss sequestration time scales, *DeVries et al.* [2012] find a biological pump sequestration efficiency over 100 years globally of about 0.3 (i.e., 30%) [*DeVries et al.*, 2012, Figure 3c], with higher efficiency in small regions, such as the Weddell Sea—results not dissimilar to those in this paper. However, their study does not address the question of OIF explicitly and is carried out with a steady state ocean circulation model at low resolution (2°).

Figure 4 compares the 1000 m and 2000 m experiments, showing a decadal time series of the fraction of carbon remaining below the UML. Unsurprisingly, carbon exported to depths of 2000 m has a significantly higher probability of remaining sequestered for a period of 100 years than carbon exported to only 1000 m depth. As only relatively modest sequestration of carbon reaching 1000 m occurs, this would suggest

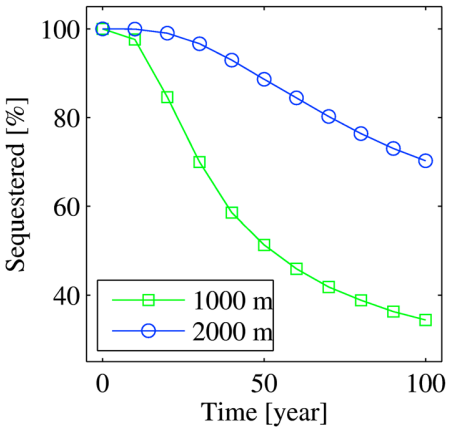

Figure 4. Decadal time series showing the number of particles that remain successfully sequestered below the upper mixed layer for both the 1000 m (green line) and 2000 m (blue line) experiments.

that 1000 m is insufficient as an ocean-wide standard for carbon sequestration and that deeper depth horizons are necessary to provide more reliable sequestration on a centennial time scale, for in the SO at least. This raises the question of how difficult is it to ensure such depth of export and sequestration. *de Baar et al.* [2008] state that below 100–250 m, particulate matter is vigorously respired and remineralized by bacteria so that on average only 1–10% of the sinking particulates reach depths below 1000 m. Using the *Martin et al.* [1987] export curve, we can estimate that of the sinking material from 100m, 14% makes it to 1000 m and 8% reaches 2000 m, which means that while more than 85% of the sinking flux is lost by 1000 m, the flux is decreased by less than a half between 1000 m and 2000 m. By choosing 2000 m as a reference depth, the 45% loss in exported material can be compensated by 40% gain in reducing advective leakage. This would increase the estimated efficiency of intentional OIF when the role of ocean circulation is taken into account. However, it is important to note that the *Martin et al.* [1987] curve is based on observations from the oligotrophic Pacific, whereas a recent experiment in a SO mesoscale eddy concluded that—in contrast—over 50% of the biomass was exported below 1000 m [*Smetacek et al.*, 2012].

There are several caveats for our work. One is that our experiments use present-day ocean circulation and do not take into account future climate change which is widely anticipated to have a significant impact on ocean circulation and mixing. The most pronounced impact on the conclusions of this study could be the effects of a warming ocean and freshening at middle to high latitudes, both of which will tend to increase vertical stratification [*Doney et al.*, 2012; *Sallée et al.*, 2013]. Within the framework of our experiments, increased stratification would potentially decrease the amount of carbon reexposed to the atmosphere and increase efficiency estimates. More generally, our work uses the ocean circulation from a single model at a single resolution. Future work involving a variety of models with varying resolutions, as well as using circulation fields from simulations that extend into perturbed projections of the 21st century ocean, may help resolve these uncertainties.

5. Conclusions

1. The export of carbon to a depth of 1000 m in the Southern Ocean does not guarantee its sequestration within the ocean for a period of 100 years.
2. More than 66% of sequestered carbon returns into contact with the atmosphere within 100 years, with a mean time scale of 37.8 years.
3. Within 100 years, carbon originally sequestered in the Southern Ocean is redistributed throughout the world ocean, with implications for monitoring.
4. The chaotic nature of Antarctic Circumpolar Current flow causes sequestered carbon initially in close proximity to be unpredictably and widely dispersed to different fates.
5. Carbon exported to 2000 m experiences lower leakage to the atmosphere (29%), suggesting that more stringent depth criteria may facilitate more accurate carbon credits systems.
6. Considering physical transport is just as critical as biogeochemical processes when evaluating the efficiency of OIF schemes.

Acknowledgments

We thank the National Environmental Research Council, part of the National capability in ocean modeling, for funding this research (NE/K500938/1). This study was carried out using the computational tool Ariane, developed by B. Blanke and N. Grima. The data presented in this study can be obtained by contacting the lead author. We are additionally grateful to a number of colleagues at NOC for suggestions and assistance, in particular A. L. New and M. Sonnewald.

The Editor thanks Michael Hiscock and an anonymous reviewer for their assistance in evaluating this paper.

References

Antonov, J. I., et al. (2010), NOAA Atlas NESDIS 69, in *World Ocean Atlas 2009, Volume 2: Salinity*, edited by S. Levitus, 184 pp., U. S. Gov. Printing Oficce, Washington, D. C.

Aumont, O., and L. Bopp (2006), Globalizing results from ocean in situ iron fertilization studies, *Global Biogeochem. Cycles*, *20*, GB2017, doi:10.1029/2005GB002591.

Blanke, B., and S. Raynaud (1997), Kinematics of the Pacific Equatorial Undercurrent: An Eulerian and Lagrangian approach from GCM results, *J. Phys. Oceanogr.*, *27*, 1038–1053.

Boyd, P. W., D. C. E. Bakker, and C. Chandler (2012), A new database to explore the findings from large-scale ocean iron enrichments experiments, *Oceanography*, *25*, 64–71, doi:10.5670/oceanog.2012.104.
de Baar, H. J. W., L. J. A. Gerringa, P. Laan, and K. R. Timmermans (2008), Efficiency of carbon removal per added iron in ocean iron fertilization, *Mar. Ecol. Prog. Ser.*, *364*, 269–282, doi:10.3354/meps07548.
DeVries, T., F. Primeau, and C. Deutsch (2012), The sequestration efficiency of the biological pump, *Geophys. Res. Lett.*, *39*, L13601, doi:10.1029/2012GL051963.
Doney, S. C., et al. (2012), Climate change impacts on marine ecosystems, *Annu. Rev. Mater. Sci.*, *4*, 11–37, doi:10.1146/annurev–marine-041911-111611.
Intergovernmental Panel on Climate Change (IPCC), Working Group I (WGI) (2007), Observations: Ocean climate change and sea level, in *Climate Change 2007: The Physical Science Basis*, edited by S. Solomon et al., pp. 385-432, Cambridge Univ. Press, Cambridge, U. K., and New York.
Intergovernmental Panel on Climate Change (IPCC), Working Group I (WGI) (2013), Summary for Policymakers, in *Climate Change 2013: The Physical Science Basis*, edited by T. F. Stocker et al., Cambridge Univ. Press, Cambridge, U. K., and New York.
Intergovernmental Panel on Climate Change (IPCC), Working Group III (WGIII) (2007), Mitigation from a cross-sectoral perspective, in *Climate Change 2007: Mitigation of Climate Change*, edited by B. Metz et al., pp. 619-690, Cambridge Univ. Press, Cambridge, U. K., and New York.
Jiang, M., et al. (2013), The role of organic ligands in iron cycling and primary productivity in the Antarctic Peninsula: A modeling study, *Deep Sea Res. Part II*, *90*, 112–133, doi:10.1016/j.dsr2.2013.01.029.
Kohfeld, K. E., C. Le Quéré, S. P. Harrison, and R. F. Anderson (2005), Role of marine biology in glacial-interglacial CO_2 cycles, *Science*, *308*, 74–77, doi:10.1126/science.1105375.
Lampitt, R. S., et al. (2008), Ocean fertilization: A potential means of geoengineering?, *Philos. Trans. R. Soc. A*, *366*, 3919–3945, doi:10.1098/rsta.2008.0139.
Leinen, M. (2008), Building relationships between sientists and business in ocean iron fertilization, *Mar. Ecol. Prog. Ser.*, *364*, 251–256, doi:10.3354/meps07546.
Locarnini, R. A., et al. (2010), NOAA Atlas NESDIS 68, in *World Ocean Atlas 2009, Volume 1: Temperature*, edited by S. Levitus, pp. 184, U. S. Gov. Printing Office, Washington, D. C.
Madec, G., (2008), NEMO reference manual, ocean dynamic component: NEMO-OPA, Notes du pole de modelisation, *Tech. Rep. 27*, Institut Pierre Simmon Laplace (IPSL), France.
Martin, J. H., G. A. Knauer, D. M. Karl, and W. W. Broenkow (1987), VERTEX: carbon cycling in the northeast Pacific, *Deep Sea Res. Part A*, *34*, 267–285.
Martin, J. M. (1990), Glacial-interglacial CO_2 change: The iron hypothesis, *Paleoceanography*, *5*, 1–13.
Monterey, G., and S. Levitus (1997), *Seasonal Variability of Mixed Layer Depth for the World Ocean. NOAA Atlas NESDIS 14*, 96, U. S. Gov. Printing Office, Washington, D. C.
Nicholls, K. W., et al. (2009), Ice-ocean processes over the continental shelf of the southern Weddell Sea, Antarctica: A review, *Rev. Geophys.*, *47*, RG3003, doi:10.1029/2007RG000250.
Oschlies, A., W. Koeve, W. Rickels, and K. Rehdanz (2010), Side effects and accounting aspects of hypothetical large-scale Southern Ocean iron fertilization, *Biogeosciences*, *7*, 4017–4035, doi:10.5194/bg-7-4017-2010.
Passow, U., and C. A. Carlson (2012), The biological pump in a high CO_2 world, *Mar. Ecol. Prog. Ser.*, *470*, 249–271, doi:10.3354/meps09985.
Popova, E. E., A. Yool, Y. Aksenov, and A. C. Coward (2013), Role of advection in Arctic Ocean lower trophic dynamics: A modeling perspective, *J. Geophys. Res. Oceans*, *118*, 1571–1586, doi:10.1002/jgrc.20126.
Rickels, W., K. Rehdanz, and A. Oschlies (2010), Methods for greenhouse gas offset accounting: A case study of ocean iron fertilization, *Ecol. Econ.*, *69*, 2495–2509, doi:10.1016/j.ecolecon.2010.07.026.
Rintoul, S. R. (2011), The Southern Ocean in the Earth System, in *Science Diplomacy: Antarctica, Science, and the Governance of International Spaces*, edited by P. A. Berkman et al., pp. 175–187, Smithsonian Institution Scholarly Press, Washington, D. C.
Sallée, J. B., E. Shuckburgh, N. Bruneau, A. J. S. Meijers, T. J. Bracegirdle, and Z. Wang (2013), Assessment of Southern Ocean mixed-layer depths in CMIP5 models: Historical bias and forcing response, *J. Geophys. Res. Oceans*, *118*, 1845–1862, doi:10.1002/jgrc.20157.
Sarmiento, J. L., and N. Gruber (2006), *Ocean Biogeochemical Dynamics*, Princeton Univ. Press, Princeton, N. J., and Oxford, U. K.
Sarmiento, J. L., et al. (2010), Efficiency of small scale carbon mitigation by patch iron fertilization, *Biogeosciences*, *7*, 3593–3624, doi:10.5194/bg-7-3593-2010.
Smetacek, V., et al. (2012), Deep carbon export from a Southern Ocean iron-fertilized diatom bloom, *Nature*, *487*, 313–319, doi:10.1038/nature11229.
Sprintall, J., and M. F. Cronin (2009), Upper Ocean Vertical Structure, in *Elements of Physical Oceanography*, edited by H. Steele, S. A. Thorpe, and K. K. Turekian, Elsevier Ltd., London, U. K.
Williams, R. G., and M. J. Follows (2011), *Ocean Dynamics and the Carbon Cycle Principles and Mechanisms*, Cambridge Univ. Press, Cambridge, U. K.

E.2 Location Location Location

This article was written following the publication of Robinson *et al.* 2014. It was published in the 2014 Winter Edition of NERC's Planet Earth Magazine.

location location location

If we could trap the CO_2 we produce in the deepest depths of the ocean, where should we do it? Maybe not where scientists first thought, says Josie Robinson. She explores the theory behind ocean iron fertilisation in the Southern Ocean, and describes her work on testing it.

The idea of scientists manipulating nature to avoid climate change evokes images of Dr Evil toying with volcanoes. Yet the concept – known as geoengineering – is a very real one. It's controversial, but it may be a necessary last resort if we don't lower our CO_2 emissions.

If we reach a fatal tipping point with climate change – a serious possibility – we would look to scientists for help, like in the film *The Day After Tomorrow*. So although geoengineering is far from ideal – it'd be better not to emit the CO_2 in the first place – scientists are a well-prepared bunch, and we research every option. Proposed geoengineering methods range from orbiting space mirrors to simply pumping CO_2 into the ground. The one I focus on is ocean iron fertilisation (OIF) which aims to make the oceans absorb more CO_2, removing it from the atmosphere before it can affect the climate.

You might remember from school biology that plants take up CO_2 during photosynthesis so they can grow. In the oceans this job is done by tiny plants, known as phytoplankton or algae – like the green sludge that grows in lakes. When the phytoplankton die, they slowly sink down into the depths. Most of the dead plant matter decomposes as it sinks, releasing the carbon that was absorbed during photosynthesis into the water; from there it ultimately escapes back into the atmosphere. But if the phytoplankton sink deep enough before being broken down, the sheer volume of the ocean could keep the carbon confined to the deep dense water – perhaps for centuries.

This happens naturally across the world's oceans, enabling the sea to sponge up a third of human CO_2 emissions and reducing our impact on the climate. It doesn't happen in the Southern Ocean, though. The water here contains lots of nutrients, but it lacks

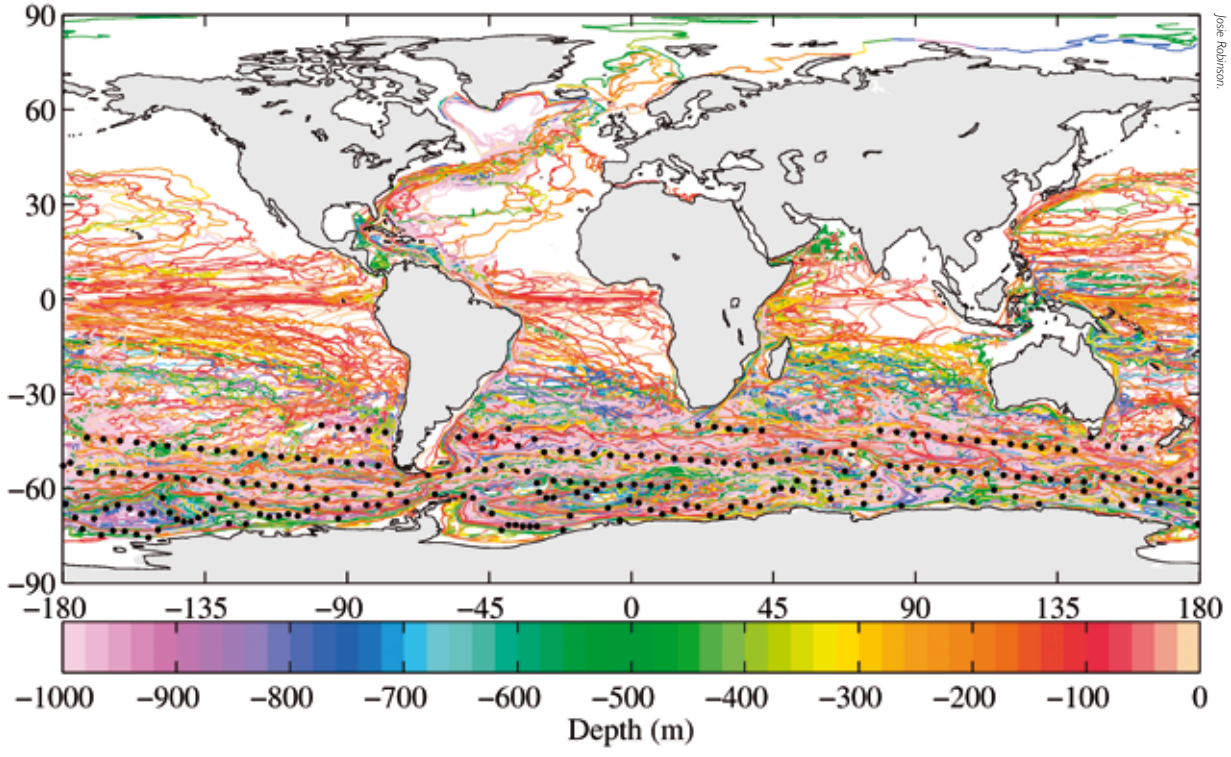

Output of the oceanographic model, showing where the ocean's circulation carried the carbon over the course of the experiment.

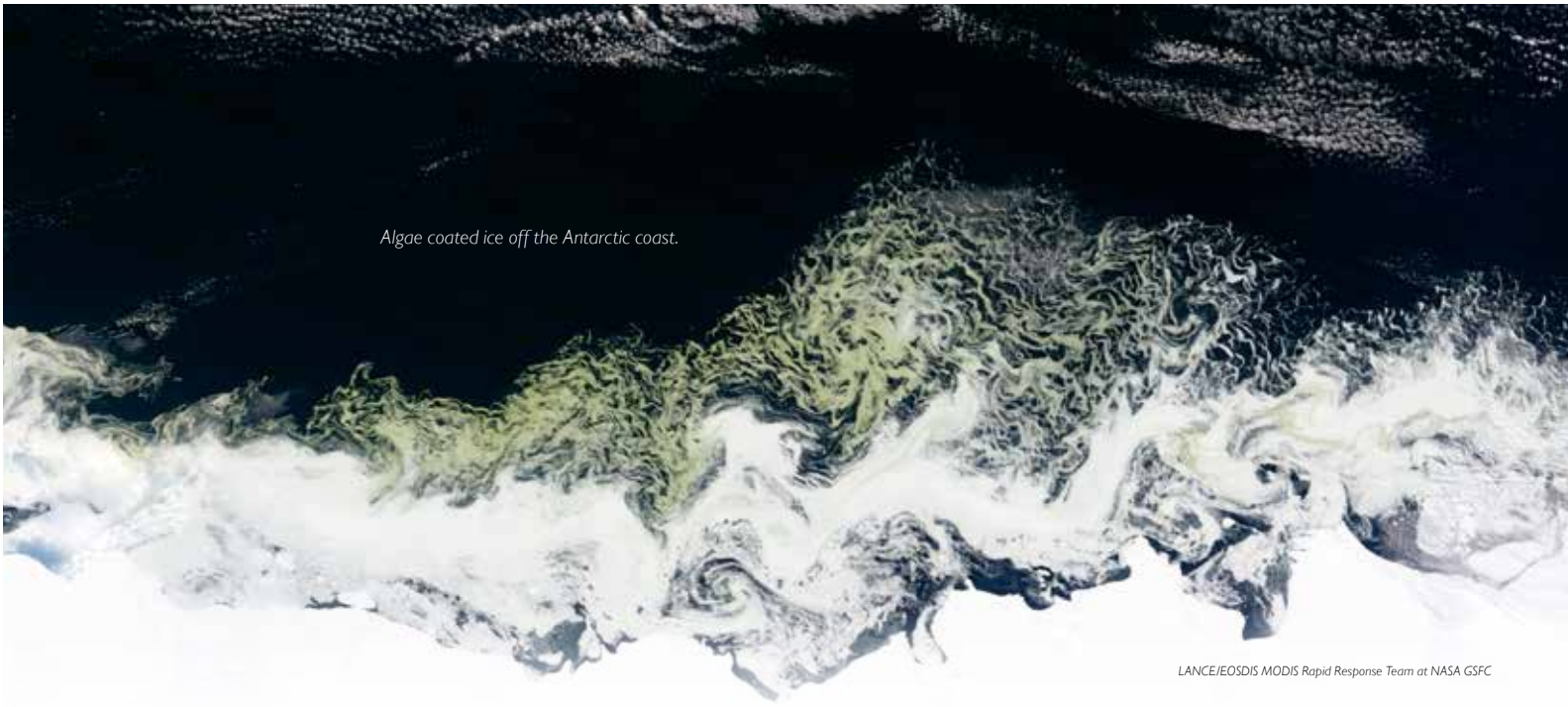

Algae coated ice off the Antarctic coast.

LANCE/EOSDIS MODIS Rapid Response Team at NASA GSFC

iron, which phytoplankton need to grow. So an oceanographer got the idea of fertilising the Southern Ocean with the missing nutrient iron to allow algae to grow there as well, soaking up more CO_2 into the ocean.

Just add iron?

That's the theory, but would it actually work? In field studies when scientists have gone to the Southern Ocean and thrown iron into the sea, they did indeed cause algal blooms. We've also looked at places around islands in the Southern Ocean where iron fertilisation happens naturally as iron is released from the mud; there, we do see more carbon sinking to the deep.

Now if the first stage of OIF is trapping CO_2 in plant form and the second is transporting the carbon to the deep ocean when the phytoplankton die, then what's the third and final stage? This is where I come in. The third stage is long-term carbon sequestration in the deep ocean. To sequester something means to keep it out of reach in a safe place; the goal is to keep CO_2 out of the atmosphere by trapping it deep under water for a long time, at least a century.

I assume that steps one and two have been successful, and we've managed to get a lot of carbon into the deep ocean – actually quite a big assumption and a hot research topic in itself. So what happens next? By using a computer model which replicates the ocean's circulation, we can predict what might happen to the carbon over 100 years. To do this I put markers, representing the carbon, across the Southern Ocean at a depth of 1,000m within the ocean circulation model. The markers have no weight so neither sink nor float; instead they ride the ocean currents, just like CO_2 molecules would. I tracked the markers within the simulated ocean for 100 years to see where they'd end up and, crucially, if the carbon would stay away from the atmosphere – the whole purpose of OIF.

Having analysed 25,000 markers, I can tell you that a lot of them (66 per cent) did find a way out of the deep ocean and back into contact with the atmosphere, taking on average 38 years. We expected some of the carbon would leak out over 100 years, but two thirds is quite a lot. Not only that, but it escaped very quickly!

With over half the carbon escaping back into the atmosphere, you may be beginning to wonder what the point is, but remember this is only one experiment and only a computer simulation of the ocean. The real ocean is such a complex system that recreating its behaviour in a computer model is immensely difficult, a bit of a black art of oceanography. We can never fully rely on simulations – although the level of accuracy in ours is impressive – but we can use them to provide us with potential scenarios, whose likelihood we can then check with further research.

So how did this Houdini carbon manage to escape in our experiment? The key factor is the ocean circulation. The Southern Ocean is like the M25; it connects all major oceans – not just horizontally, but also vertically. Here, deep water rises up to the surface on a massive scale. This is due to the trade winds, which push water near the surface away from Antarctica so that water from the deep rises to fill the gap. In our experiment this was the carbon's main escape route from the deep ocean.

The bottom line is that location is crucial. We were half right to think the Southern Ocean is a good place for OIF; it has an abundance of all essential nutrients except iron. Yet our research suggests that although there are some areas that are suitable for geoengineering, ultimately it's a bad location because of its highly dynamic circulation. Even carbon that did stay in deep water for the full century was spread all over the world by the circulation, making it almost impossible to monitor the sequestered carbon – this would be essential in a carbon credit market where someone would be paying to have carbon locked up on their behalf to offset the pollution they were causing.

All this suggests OIF alone is probably not the miracle cure for all our climate-change problems. But it may have a role to play alongside other geoengineering methods. There are places in the world's oceans that do seem to be suitable for OIF, so the research must continue. Of course, the best course of action is to cut our carbon emissions, and leave geoengineering to movie directors.

Josie Robinson is a PhD student at the University of Southampton and National Oceanography Centre.
Email: josie.robinson@noc.soton.ac.uk

E.3 Could the Madagascar bloom be fertilized by Madagascan iron?

This paper was co-authored with M A Srokosz along side the thesis work.

AGU PUBLICATIONS

JGR

Journal of Geophysical Research: Oceans

RESEARCH ARTICLE

10.1002/2015JC011075

Could the Madagascar bloom be fertilized by Madagascan iron?

M. A. Srokosz[1], J. Robinson[2], H. McGrain[2], E. E. Popova[1], and A. Yool[1]

[1]National Oceanography Centre, University of Southampton Waterfront Campus, Southampton, UK, [2]Ocean and Earth Science, National Oceanography Centre Southampton, University of Southampton, UK

Key Points:
- Madagascan iron can be advected east to fertilize the late austral summer bloom
- Lagrangian particle tracking shows that mesoscale eddies cause the advection
- interannual variability in the bloom is caused by eddy variability

Correspondence to:
M. A. Srokosz,
mas@noc.ac.uk

Citation:
Srokosz, M. A., J. Robinson, H. McGrain, E. E. Popova, and A. Yool (2015), Could the Madagascar bloom be fertilized by Madagascan iron?, *J. Geophys. Res. Oceans*, *120*, doi:10.1002/2015JC011075.

Received 24 JUN 2015
Accepted 29 JUL 2015
Accepted article online 4 AUG 2015

Abstract In the oligotrophic waters to the east of Madagascar, a large phytoplankton bloom is found to occur in late austral summer. This bloom is composed of nitrogen fixers and can cover up to ~1% of the world's ocean surface area. Satellite observations show that its spatial structure is closely tied to the underlying mesoscale eddy field in the region. The causes of the bloom and its temporal behavior (timing of its initiation and termination) and spatial variability are poorly understood, in part due to a lack of in situ observations. Here an eddy resolving 1/12° resolution ocean general circulation model and Lagrangian particle tracking are used to examine the hypothesis that iron from sediments around Madagascar could be advected east by the mesoscale eddy field to fertilize the bloom, and that variability in advection could explain the significant interannual variability in the spatial extent of the bloom. The model results suggest that this is indeed possible and furthermore imply that the bloom could be triggered by warming of the mixed layer, leading to optimal conditions for nitrogen fixers to grow, while its termination could be due to iron exhaustion. It is found that advection of Madagascan iron could resupply the bloom region with this micronutrient in the period between the termination of one bloom and the initiation of the next in the following year.

1. Introduction

The area to the east of Madagascar lies in the southwestern Indian Ocean subtropical gyre and biologically is one of the oligotrophic regions of the world's oceans. In the late austral summer, a major phytoplankton bloom develops in this region, which varies from year-to-year both in terms of timing and spatial extent. The bloom is easily observed in ocean color measurement of chlorophyll and is known to be composed of nitrogen fixing phytoplankton [*Poulton et al*., 2009]. In some years, when fully developed, this late austral summer Madagascar bloom can cover ~1% of the world's ocean surface area. It has been described as one of the strongest examples of interannual variability, with respect to ocean biology, after El Niño [*Uz*, 2007; *Srokosz and Quartly*, 2013]. Thus, the Madagascar bloom has a major impact on the biogeochemistry of the Indian Ocean basin [*Uz*, 2007]. Notably, unlike similar late summer blooms elsewhere in the ocean as documented by *Wilson and Qiu* [2008], the Madagascar bloom propagates to the east, away from Madagascar. Despite the significance of the bloom, the lack of supporting in situ data has led to uncertainty surrounding the mechanisms of its formation, propagation, and termination.

Longhurst [2001] was the first to describe the seasonal development of this major bloom, using ocean color observations from space (from POLDER and Sea-viewing Wide Field-of-view Sensor (SeaWiFS)). He noted that the bloom typically occurred during the period February to April but was not present every year. Subsequent studies have elucidated various aspects of the bloom [e.g., *Srokosz et al*., 2004; *Uz*, 2007; *Wilson and Qiu*, 2008; *Poulton et al*., 2009; *Huhn et al*., 2012; *Srokosz and Quartly*, 2013], but many questions still remain regarding its nature (see *Srokosz and Quartly* [2013] for a review of what is currently known about the bloom). Based on limited in situ observations [*Poulton et al*., 2009; *Srokosz and Quartly*, 2013], it is known that the bloom is composed of nitrogen fixing phytoplankton: *Trichodesmium* and the diatom *Rhizosolenia clevei* with its symbiont *Richelia intracellularis*. Other notable features of the bloom are that it propagates east away from Madagascar and exhibits significant interannual variability in terms of the timing of its initiation and termination, and also in terms of its spatial extent [*Wilson and Qiu*, 2008]. In his original study, *Longhurst* [2001] noted the importance of the mesoscale eddy field in the development of the bloom, describing

the bloom's spatial structure as dendritic. Subsequent studies have confirmed the impact of the eddy field on the bloom [e.g., *Huhn et al*., 2012; *Srokosz and Quartly*, 2013]. Although there have been recent studies of the effect of eddies on chlorophyll in the South Indian Ocean [*Dufois et al*., 2014; *Gaube et al*., 2013, 2014], these have been focused more on an area further east toward Australia and on austral winter conditions, so have not address the influence of eddies on the bloom directly.

The reasons for the occurrence of the bloom are unclear. *Uz* [2007] proposed that the bloom was fertilized by riverine iron washed off Madagascar by tropical cyclones and then advected to the east by the ocean circulation, and in particular by the mesoscale eddy field. *Srokosz and Quartly* [2013], while accepting the idea of iron fertilization, questioned the river runoff mechanism as the major Madagascan rivers flow into the Mozambique Channel to the west of Madagascar. Instead, they proposed that iron could be supplied from the sediments from the continental shelves to the east and south of Madagascar. As *Elrod et al*. [2004], *Jeandel et al*. [2011], and *Dale et al*. [2015] show, continental shelf sediments can be a major source of iron to the water column and then by advection to the open ocean. *Srokosz and Quartly* [2013] argued that a similar mechanism had been shown to explain both the Kerguelen and Crozet blooms in the Southern Ocean [*Blain et al*., 2007; *Pollard et al*., 2009] and, by analogy, could explain the Madagascar bloom. Unfortunately, unlike the Crozet and Kerguelen studies, there are no iron measurements from the Madagascan region. *Mongin et al*. [2009] used a modeling study to demonstrate that winter advection of iron could explain the Kerguelen bloom and a related approach will be used in this study. The hypothesis here is: iron from sediments around Madagascar is advected east by the mesoscale eddy field to fertilize the bloom, and the variability in the advection explains the significant interannual variability in the spatial extent of the bloom. This hypothesis will be examined using a high-resolution (1/12°) ocean model and Lagrangian particle tracking. Given the importance of the mesoscale eddy field for the development of the bloom [*Longhurst*, 2001], it is crucial to use a truly eddy resolving ocean model for this study [*Marzocchi et al*., 2015].

In the same region to the east of Madagascar, there is also an annual weak austral spring bloom [see, for example, *Uz*, 2007, Figure 2], which is followed by the development of a deep chlorophyll maximum [*Srokosz and Quartly*, 2013]. This austral spring bloom and the subsequent development of a deep chlorophyll maximum are reproduced in biogeochemical models without an iron component, whereas the late austral summer bloom studied here is not (see discussion by *Srokosz and Quartly* [2013] and references therein). In part, the inability of the models to reproduce the late austral summer bloom is due to the omission of the nitrogen fixing phytoplankton, composing the bloom [*Poulton et al*., 2009], from the ocean biogeochemical models. An exception is the global model of *Monteiro et al*. [2010] which shows pronounced variability over a year in diazotrophs to the east of Madagascar. However, they do not investigate the Madagascar bloom per se and their model resolution is only 1°, so it does not resolve the mesoscale features that are an important aspect of the bloom. The point to draw from these model results is that if iron is advected east from Madagascar probably not all of it will be used up during the weak austral spring bloom and so some will be available to fertilize the late austral summer bloom, which is the focus of this study.

The paper proceeds as follows: section 2 describes the data and model; section 3 explains the methodology used and gives the results obtained by applying Lagrangian particle tracking to the model output; section 4 discusses other factors that affect the bloom; section 5 gives the conclusions of this study.

2. Data and Model Description

2.1. Satellite Data

2.1.1. SeaWiFS Chlorophyll

For simplicity and because it provides a uniform data set, here a decade, 1998–2007, of SeaWiFS ocean color observations of chlorophyll for the bloom area are used. The specific products used are the SeaWiFS monthly, level 3 Standard Mapped Images with a 9 km resolution [*NASA*, 2009]. These were obtained from http://oceandata.sci.gsfc.nasa.gov/SeaWiFS/L3SMI/. In Figure 1, the SeaWiFS data for the bloom period January to April are plotted for each of the 10 years [cf. *Wilson and Qiu*, 2008, Figure 10]. The interannual variability of the bloom, both in terms of timing and of spatial extent, can be clearly seen over the decade of observations.

One point to note is that the criterion for the existence of a late austral summer bloom in the SeaWiFS ocean color data differs amongst studies. For example, *Uz* [2007] uses a ratio of the mean surface

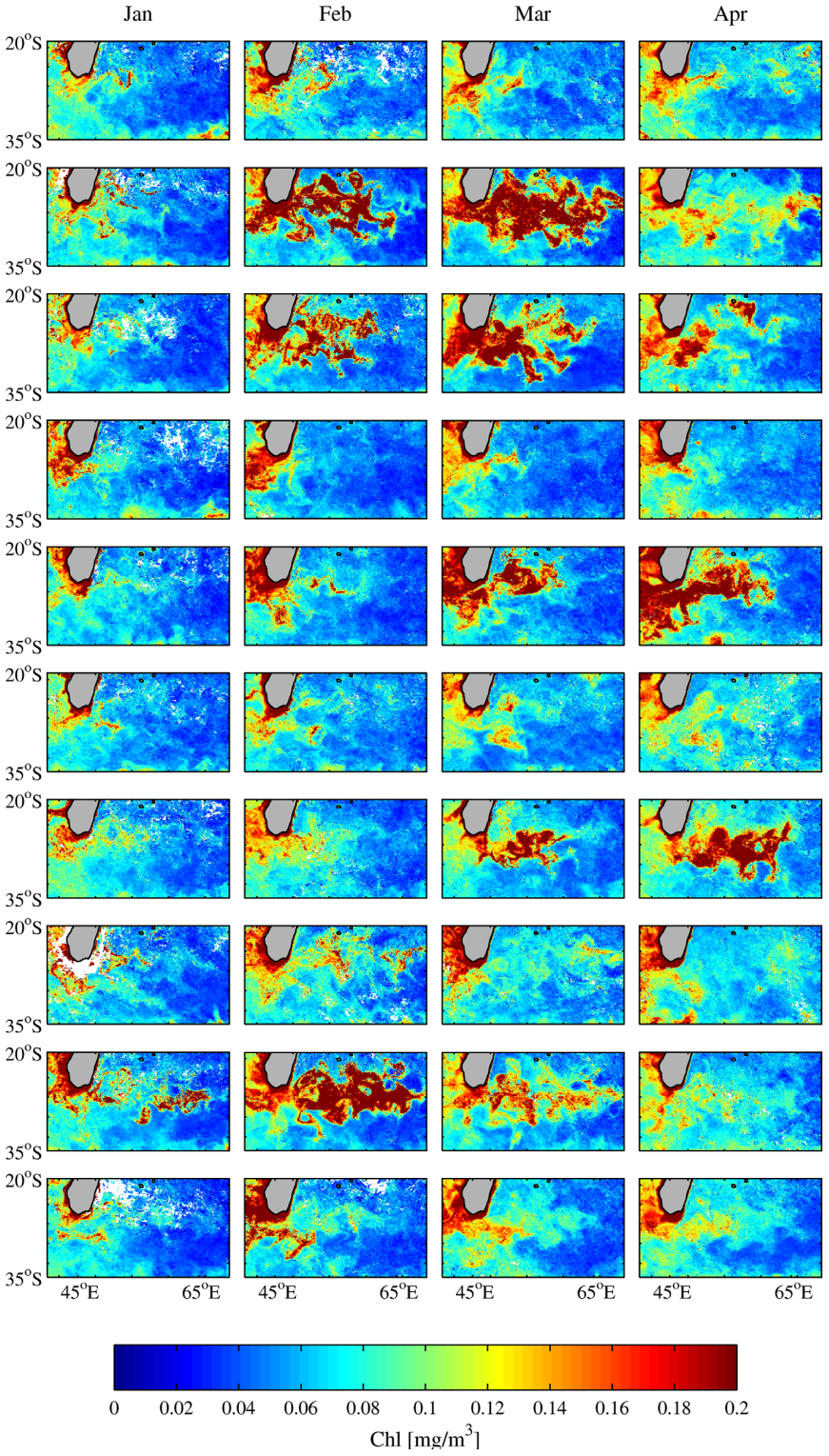

Figure 1. SeaWiFS monthly chlorophyll concentration in mg chl m^{-3}. Maps for (left to right) January to April for each year (top to bottom) from 1998 to 2007. The interannual variability of both the timing and the spatial extent of the bloom is apparent.

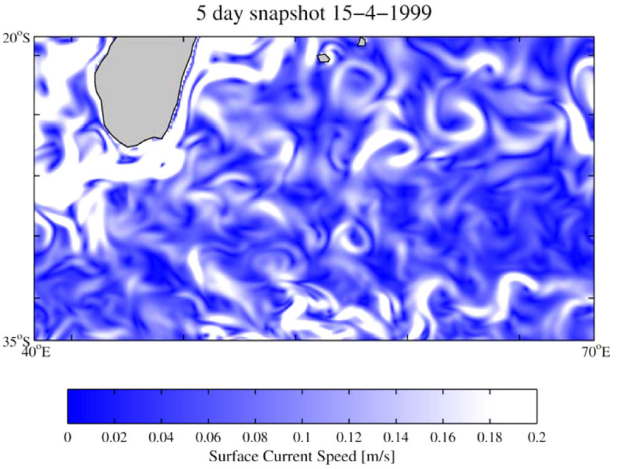

Figure 2. NEMO 1/12° model 5 day "snapshot" of the surface current speeds in the Madagascar bloom area, displaying a highly variable mesoscale eddy field that is accord with that seen in observations [cf. *Longhurst*, 2001, Figure 2]). This illustrates that the high resolution of the NEMO 1/12° model enables it to capture the behavior at the mesoscale that is important for the Madagascar bloom (see also Figure 10 below).

chlorophyll over the bloom area to the mean surface chlorophyll over an area further east, while *Wilson and Qiu*'s [2008] criterion for the existence of a bloom is that the chlorophyll concentration exceeds 0.15 mg m^3. Here the latter criterion will be used to define the presence and extent of the bloom, and to examine its interannual variability as it allows the spatial extent of the bloom to be delineated.

2.1.2. Altimetric Sea Surface Currents

The satellite altimeter data used here are produced by Ssalto/Duacs and distributed by AVISO (http://www.aviso.altimetry.fr/duacs/) [*AVISO*, 2014]. A merged data product, from only two satellites at any one time, is used as this provides consistent data set appropriate for interannual variability studies. The Absolute Dynamic Topography (ADT) is obtained by adding the Sea Level Anomaly to the Mean Dynamic Topography, which is the part of the Mean Sea Surface Height caused by permanent currents (Mean Sea Surface Height minus Geoid). A mapping procedure using optimal interpolation gives ADT maps (MADT or L4 products) at a given date (daily temporal resolution) on $1/4^\circ \times 1/4^\circ$ spatial grid. Here the sea surface geostrophic velocities computed from the ADT over the period of 1998–2007 are used, to match the SeaWiFS data record.

2.2. NEMO Model and Ariane Lagrangian Particle Tracking

The Nucleus for European Modelling of the Ocean (NEMO) model is an ocean general circulation model (GCM). The NEMO 1/12° resolution model has been developed with particular emphasis on realistic representation of fine-scale circulation patterns [*Madec*, 2008; *Marzocchi et al*., 2015] and provides an ideal platform to conduct Lagrangian particle-tracking experiments as it captures the mesoscale behavior, necessary to investigate the Madagascar bloom. The run of the 1/12° NEMO that is used here is that described by *Marzocchi et al*. [2015] (section 2.1). In brief, the run starts in 1978 and is 30 years long, ending in 2007. It is initialized with World Ocean Atlas (WOA) 2005 climatological fields and forced with 6 hourly winds, daily heat fluxes, and monthly precipitation fields [*Brodeau et al*., 2010]. There is moderate relaxation of the sea surface salinity fields, which are restored toward WOA 2005. Model outputs are stored as successive 5 day means throughout the model run and these are the outputs used for the particle tracking in this paper. For more details of the model setup and configuration, see *Marzocchi et al*. [2015].

Here we use 11 years of 5 day mean velocity fields (from 1997 to 2007 inclusive) to drive particle tracking in order to make a qualitative comparison with the SeaWIFS 1998–2007 observations. The reason for the extra year of model run is that particle tracking is applied in the period leading up to each year's bloom (see section 3.1 below). An example of a 5 day velocity field from NEMO for the bloom area is shown in Figure 2 and displays a highly variable mesoscale eddy field similar to that known to exist in the bloom area [cf. *Longhurst*, 2001, Figure 2]. It is recognized that the mesoscale eddy field plays a key role in the development and propagation of the bloom [*Longhurst*, 2001; *Srokosz et al*., 2004; *Srokosz and Quartly*, 2013]; therefore, it is important that the model is able to reproduce a realistic eddy field to the east of Madagascar. *Marzocchi et al*. [2015] have demonstrated that the NEMO 1/12° model produces a realistic mesoscale eddy field in the North Atlantic (their Figure 8), which gives added confidence in using the same model run here.

The Ariane package [*Blanke and Raynaud*, 1997] (available online at: http://stockage.univ-brest.fr/~grima/Ariane) is applied to the NEMO velocity field described above to track water parcels using point particles that are released into the modeled ocean circulation (cf. *Popova et al*. [2013] and *Robinson et al*. [2014], who

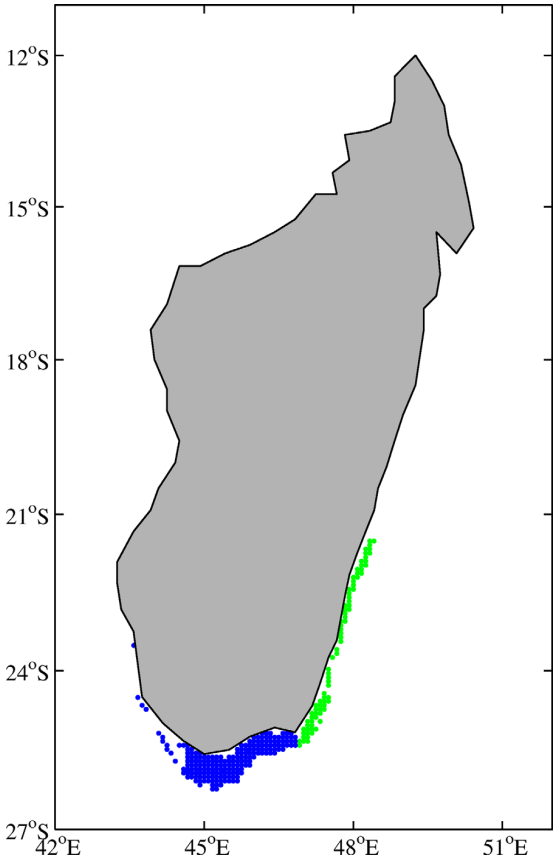

Figure 3. Lagrangian particle release area around Madagascar (as represented in the model grid)—differentiating particle to east (green—EMC) and south (blue—shallow shelf). A total of 275 particles are released every 5 days; of which 81 particles are released to the east and 194 particles to the south. The particles are released at the surface in the area that lies between the 50 and 300 m depth contours in the model. See text for discussion of release timings.

used output from a NEMO 1/4° run). The method is presented in detail and discussed by *Blanke and Raynaud* [1997] and *Blanke et al*. [1999].

3. Lagrangian Particle Tracking

3.1. Methodology

In order to study the possible advection of iron, either from sediments or from riverine input, 275 particles were deployed at the surface, on the 1/12° model grid, in the area to the south and east of Madagascar where the bathymetry lies between 50 and 300 m in depth (see Figure 3). This choice is a balance between remaining close to the coast yet avoiding particles bumping into it and covering the shelf region from which iron might enter the water column [*Elrod et al*., 2004; *Dale et al*., 2015]. This provides sufficient particles to track in order to get a reasonable representation of their dispersal away from Madagascar.

Initially, two Lagrangian particle-tracking experiments were performed. In both experiments, the particles were released at the ocean surface. No attempt was made to distinguish between possible upwelling from sediments or input from rivers per se. It was simply assumed that the particles tracked were representative of iron that had entered the surface waters around Madagascar from whichever source. The first experiment released particles every 5 days each year (73 releases per year, giving a total of 20,075 particles per year) and simply followed the particles from their release for 1 year to see whether advection could disperse them sufficiently to fertilize a bloom in the region to the east of Madagascar.

The second experiment was based on the assumption that the bloom would utilize all the available iron and addressed the question of whether advection could resupply iron for a bloom in the following year. In this experiment, particles were released from a nominal end of the bloom in May until January of the following year and tracked during the nine intervening months until the nominal start of the bloom in February of the following year.

A third particle-tracking experiment was also carried out to determine whether the particle released to the east of Madagascar, in the East Madagascar Current, or those released to the south of Madagascar on the shallow shelf were more likely to be advected to the east. Here the results of the second experiment were used, with the simple variation of subsetting the particles as shown in Figure 3; this results in 194 particles being released to the south and 81 to the east of Madagascar.

An important caveat to the results discussed below is that the NEMO 1/12° model, while run for specific years, will not be able to provide a direct comparison with the satellite observations for the same year. The reason for this is that the mesoscale eddy field in NEMO is not initialized to match the real-world eddy field (because of chaotic dynamics this is only possible using data assimilation). Therefore, while in a statistical sense, the model might be expected reproduce the mesoscale eddy field behavior [see *Marzocchi et al*., 2015], it is not expected to reproduce the exact eddy field behavior year-on-year. However, as will become

apparent below, this caveat does not affect the usefulness of the model results for testing the hypothesis stated in section 1.

3.2. Results

Consider, to begin with, the results from the first Lagrangian particle-tracking experiment. There are 275 particle starting positions spaced on the 1/12° grid to the east and south of Madagascar at the surface, with the region of release being bounded by the 50 and 300 m depth contours (Figure 3). Particles are released every 5 days and tracked for 1 year. During the 10 model years for which the experiment was run, it was found that in some years few particle trajectories entered the bloom area, while other years showed a significant spreading of particle trajectories into the bloom area. These initial results (not shown) indicate that Lagrangian particles released to the south and east, near to the coast of Madagascar, can be advected far enough to the east to potentially fertilize the bloom. In addition, they show that there is significant interannual variability in the Lagrangian particle trajectories and so the bloom area could be subject to an intermittent supply of iron from year-to-year. These results support the hypothesis stated at the beginning of the paper.

Having found that the advection of iron east away from Madagascar could fertilize the bloom in principle, a further question arises as to whether the bloom is terminated by the exhaustion of iron in the surface water by the phytoplankton. This question cannot be addressed directly using the NEMO 1/12° simulation, as it does not model iron per se. However, if the bloom is terminated by the exhaustion of iron then a question that can be addressed is: can advection resupply iron in the period between the end of one bloom and the start of the one in the following year? This corresponds to the question addressed by *Mongin et al.* [2009] for the Kerguelen bloom using a model tracer experiment. Here it is addressed using Lagrangian particle tracking. In this second experiment, the release of Lagrangian particles is restricted to the months between the end of one bloom and the start of the next, and they are tracked during the nine intervening months. For simplicity, the end of the bloom is taken to be the end of April and the start to be the beginning of February of the following year, while acknowledging that in practice there is interannual variability in the timing of both the initiation and the termination of the bloom. However, since the model does not reproduce perfectly the actual behavior in any specific year (due to chaotic dynamics as noted above) this simplification is not a problem as a qualitative, rather than quantitative, answer is all that is required from this experiment.

Figure 4 shows the results for all 10 years of the NEMO 1/12° model run, with the particles color coded by their release month. It can be seen that in some years, the Lagrangian particle trajectories extend sufficiently far to the east to allow iron fertilization of the bloom in the following year, even if the iron had been exhausted in the previous year. Unsurprisingly, the particles released first, at the end of the previous year's bloom in May, travel furthest generally. In contrast, the particles released last, in the January of the bloom year, are closest to Madagascar having had less time to be advected away. Note that particles are not just advected east, but also south and west, and even north into the Mozambique Channel. As expected from the first NEMO experiment, the spatial extent of the particle advection displays considerable interannual variability. This result is similar to that obtained by *Mongin et al* [2009] for the Kerguelen bloom using model tracers.

A further qualitative comparison is shown in Figure 5. Here model year results, for 2000 and 2007, have been overlaid with the SeaWiFS chl data for the month of March in the years 2002 and 1999, using the *Wilson and Qiu* [2008] criterion for the bloom of 0.15 mg chl m^{-3}. The SeaWiFS observation years were chosen to illustrate the case of an extensive (1999) and a less extensive bloom (2002). While the model years were chosen on being the best match to the observations, as noted above (section 3.1), there is no expectation that model results will match observations on a year-by-year basis. Nevertheless, this qualitative comparison shows that the behavior of the Lagrangian particles in the model can roughly match the observed spatial extent of the bloom, even though year-by-year the model cannot reproduce the details of the bloom as it has an internally generated chaotic mesoscale eddy field that may not match that in the real world (except in a statistical sense over many realizations). Of course, a better match between the extent of the particle trajectories and the extent of the bloom might have been obtained by varying the criterion for the bloom (to a different value than 0.15 mg chl m^{-3}) but it seemed a much more stringent test to use the independently chosen value of *Wilson and Qiu* [2008]. A further point to note from Figures 2, 4, and 5 is that the particle trajectories seem to spread further north and south than the bloom itself, a point confirmed by comparing 10 year composites of both fields (not shown). This could be an artifact of either the choice of bloom criterion or an indication that the model eddy field dispersing the particles differs somewhat from

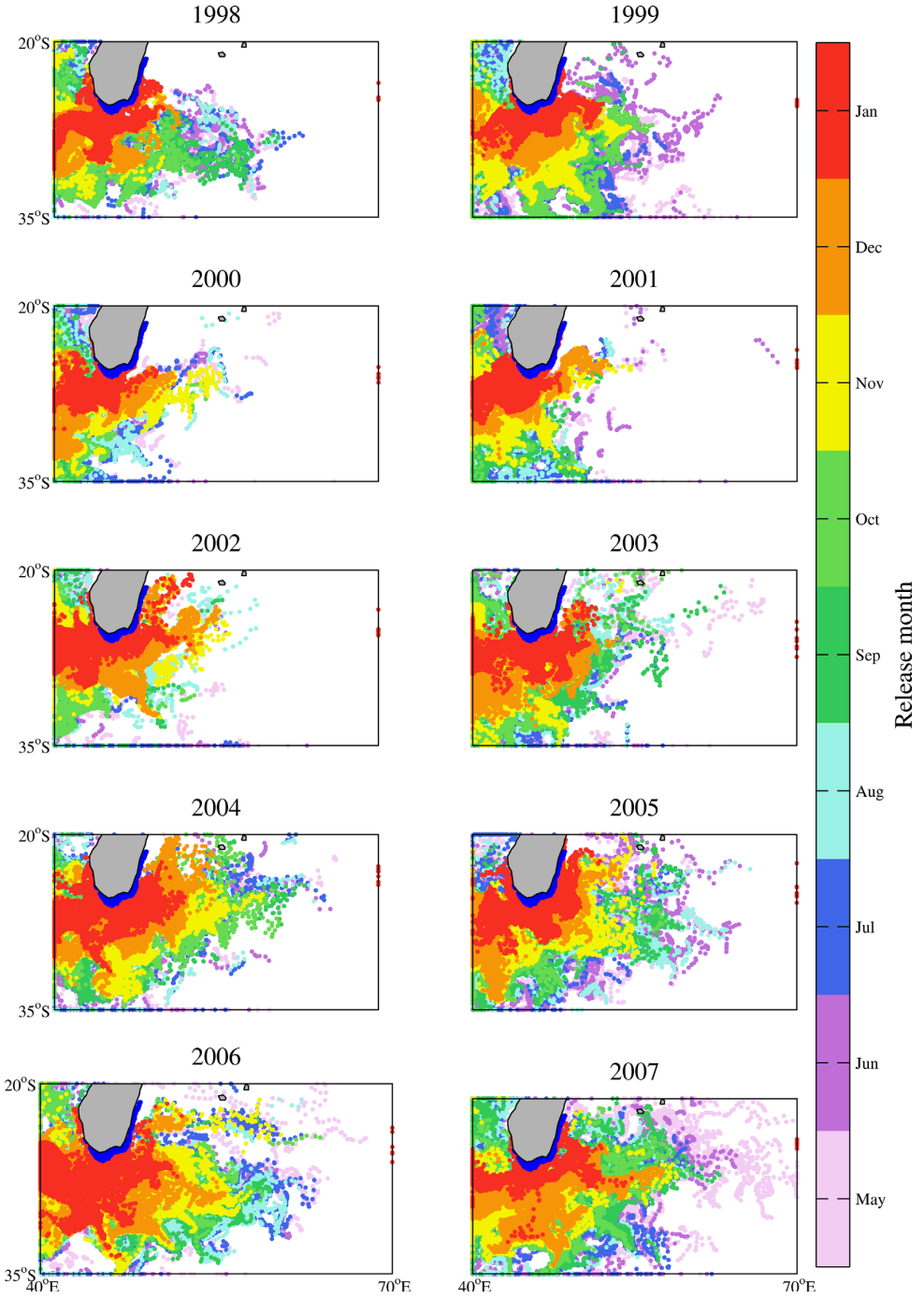

Figure 4. Lagrangian particle trajectories for NEMO model years 1998–2007. The blue area is where the particles are released. In this experiment, the 275 particles are released every 5 days outside the bloom period (taken as beginning of May of the previous year to the end of January of the bloom year) and tracked for the intervening 9 months. The particles are spaced 1/12° apart. The color scale gives the month of the particle release.

the real world, being less tightly constrained in the north-south direction (on this latter point see section 4.2 and Figure 10 below).

One question that the results so far do not answer is whether the iron would be primarily supplied from the shallow sediments to the south of Madagascar, where upwelling is known to occur [*DiMarco et al.*, 2000;

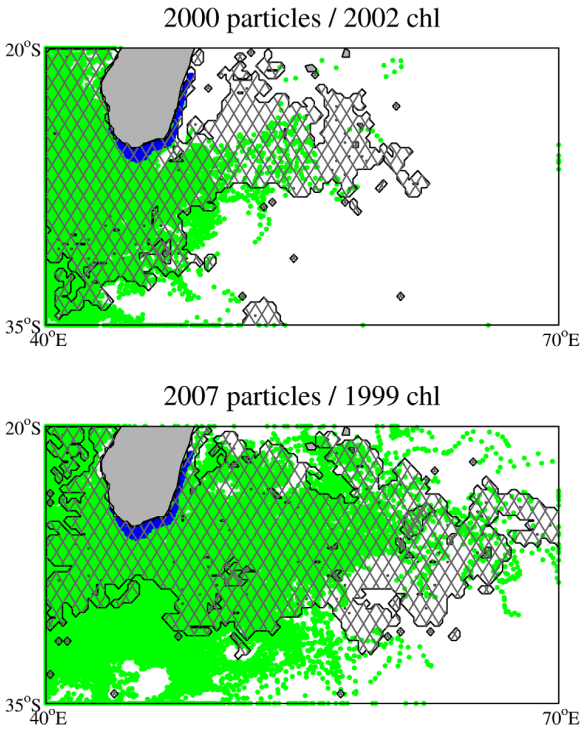

Figure 5. Lagrangian particle trajectories (green) for the NEMO model years (top) 2000 and (bottom) 2007. These are overlaid (hatched) with the SeaWiFS chl data for the month of March in the years 2002 and 1999, using the *Wilson and Qiu* [2008] criterion for the bloom of 0.15 mg chl m^{-3}. Note that this is only a qualitative comparison as the NEMO model is not expected to reproduce the actual mesoscale eddy field in a particular year.

Machu et al., 2002], or from the east where the strong East Madagascar Current could potentially scour sediment from the sea bed? To examine this question, the particles that are released are divided into those initially lying to the east and those lying to the south (see Figure 3). Tracking the two sets of particles reveals that both areas contribute to the particles that are advected to the east away from Madagascar. However, the particles released to the east tend to contribute more to the eastward advection. In contrast, the particles released to the south tend to contribute more to advection into the Mozambique Channel (see Figures 6 and 7; note that the results shown in Figure 4 are a combination of those in these two figures). Looking at all 10 years of particle releases from the east and south, there is considerable interannual variability as to where the trajectories end up without any simple discernible pattern emerging. Therefore, no strong conclusion can be drawn regarding whether the origin of any iron being advected is to the east or the south of Madagascar—both regions potentially contribute.

Having examined the potential for iron advection using Lagrangian particle tracking, the next step is to take advantage of the NEMO 1/12° model output to look at the possible effects of changes in mixed layer temperatures and depths, and of the South Indian Ocean Counter-Current (SICC), on the bloom.

4. Other Factors Affecting the Bloom

As noted by *Srokosz and Quartly* [2013, and references therein], other factors that affect the bloom are the mixed layer temperatures and depths needed to provide optimum conditions for the growth of the nitrogen fixing phytoplankton that form the bloom. *Ward et al.* [2013], in discussing diazotroph biogeography, note the preference of some species for warm temperatures and stratified, high-light environments, as found in this area in late austral summer [*Srokosz and Quartly*, 2013]. In addition, the South Indian Ocean Counter-Current (SICC) may play a role in the advection of iron, though its exact nature is disputed (see below) [*Palastanga et al.*, 2007; *Siedler et al.*, 2006; *Menezes et al.*, 2014]. Finally, the so-called Indian Ocean Dipole (IOD) may possibly influence the bloom through its effect on Indian Ocean circulation. These factors that could influence the bloom are examined next.

4.1. Temperature and Mixed Layer Depth

Wilson and Qiu [2008, and references therein] note that nitrogen fixing *Trichodesmium*, one of the key phytoplankton species that compose the Madagascar bloom, rarely bloom below 25°C. *Srokosz and Quartly* [2013] (Figure 3) found from in situ observations that the bloom was confined to near-surface waters with temperatures greater than 26.5°C, with mixed layer depths of ~20–30 m. Therefore, it is unlikely that the bloom will occur if the mixed layer temperature is less than 25°C. On examining the model output, the mixed layers are found to be relatively shallow (<30 m) in the periods leading up to, during, and following

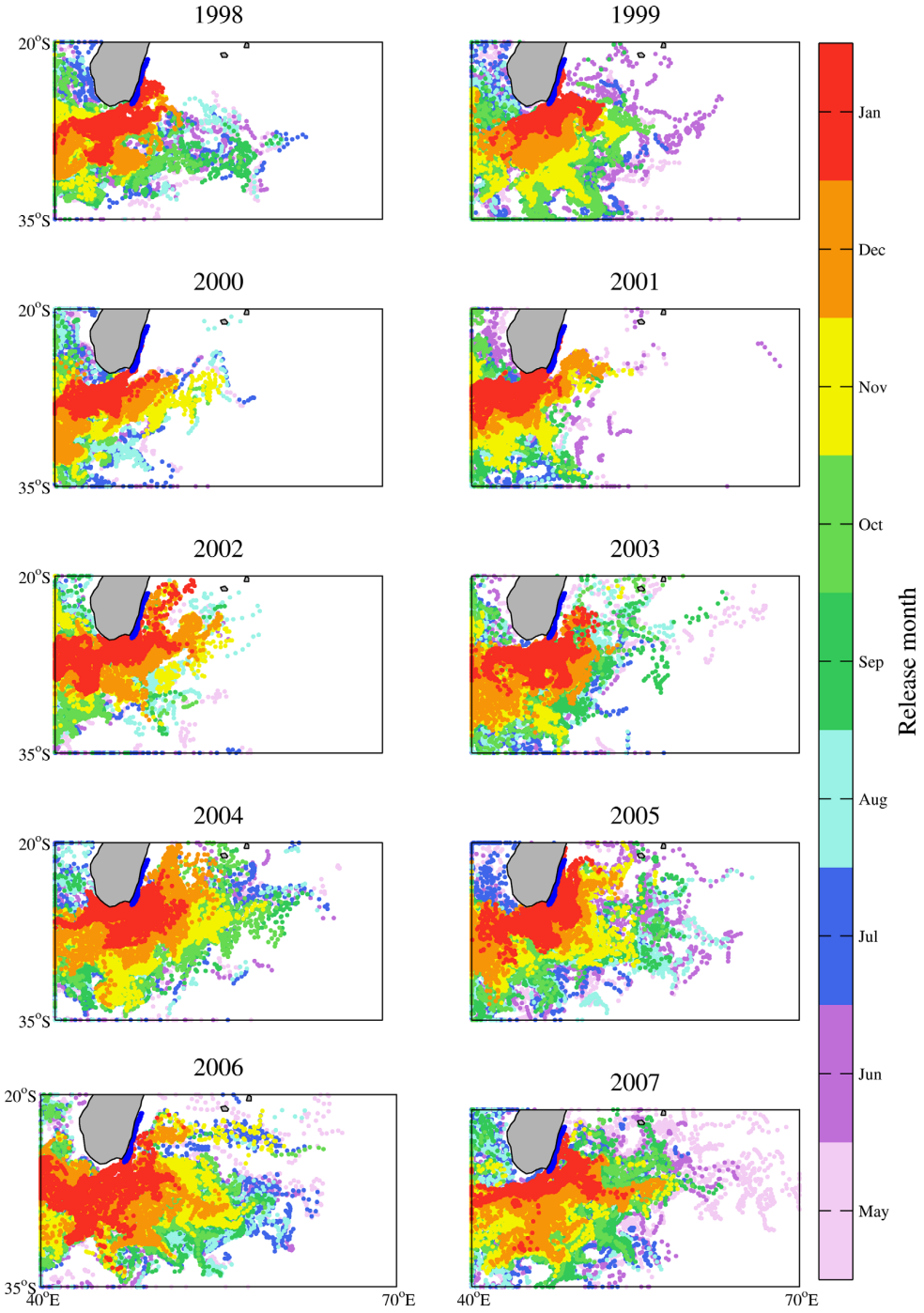

Figure 6. Lagrangian particle trajectories for NEMO model years 1998–2007. The blue area is where 81 particles are released every 5 days. This experiment is identical to that shown in Figure 4 but with the release of the particles restricted to the east of Madagascar in the area of the East Madagascar Current that runs south along the coast. The color scale gives the month of the particle release.

the bloom. Therefore, it seems doubtful that light limitation plays a role in its initiation and termination. However, the mixed layer temperatures may do so, so these are examined next.

Figure 8 shows results from the NEMO 1/12° ocean model for the months in which surface temperature (representative of the mixed layer temperature) exceeds 25°C, leading up to the bloom period. In contrast,

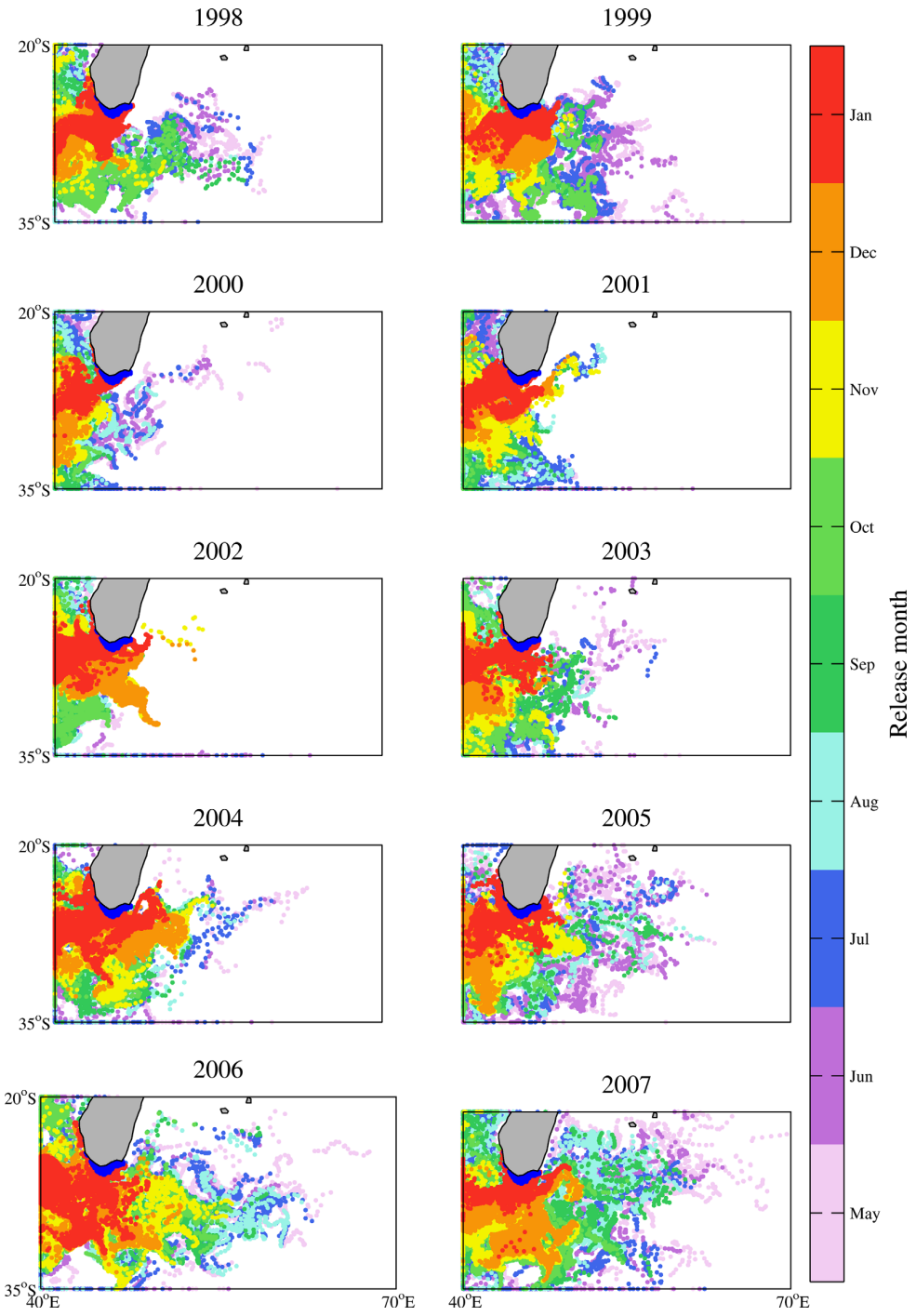

Figure 7. Lagrangian particle trajectories for NEMO model years 1998–2007. The blue area is where 194 particles are released every 5 days. This experiment is identical to that shown in Figure 4 but with the release of the particles restricted to the south of Madagascar in the upwelling area on the shelf. The color scale gives the month of the particle release.

Figure 9 shows when the surface temperature cools to 25°C, after the bloom period. In both figures, interannual variability can be seen in the spatial structure of the warming and cooling. For the bloom region, the surface waters warm to 25°C around January/February each year (Figure 8). In the postbloom period, the surface temperature drops below 25°C around June/July. These results suggest that the initiation of the

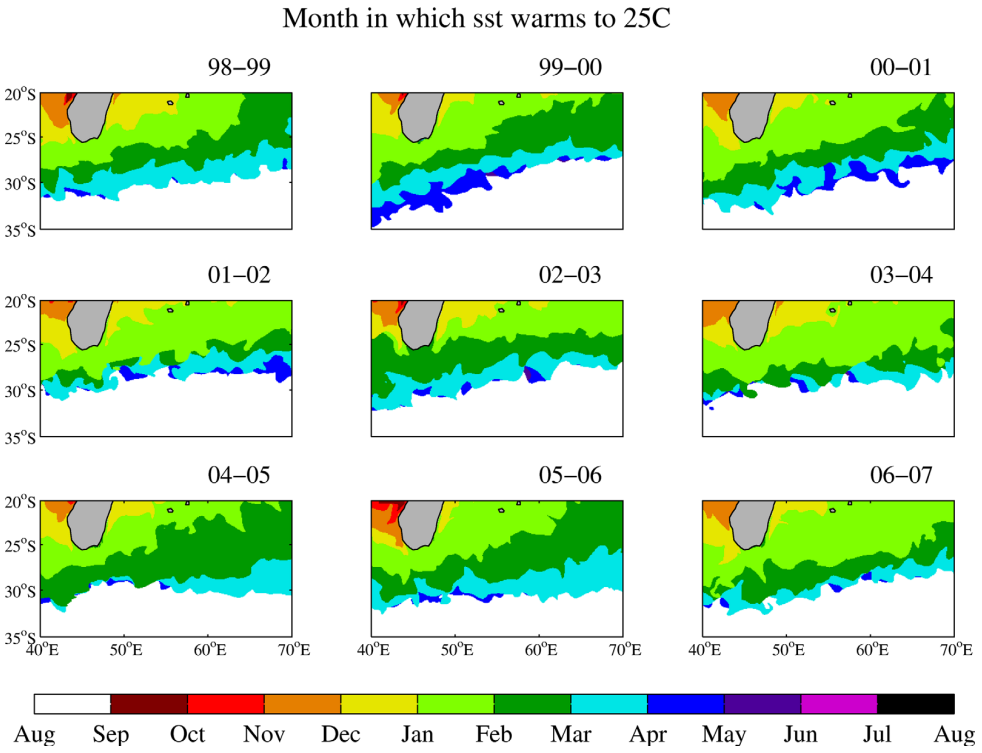

Figure 8. Results from NEMO showing the month in which surface temperatures exceed 25°C prior to the bloom period over the decade of model output examined. Note that in the white area, the temperatures never exceed 25°C.

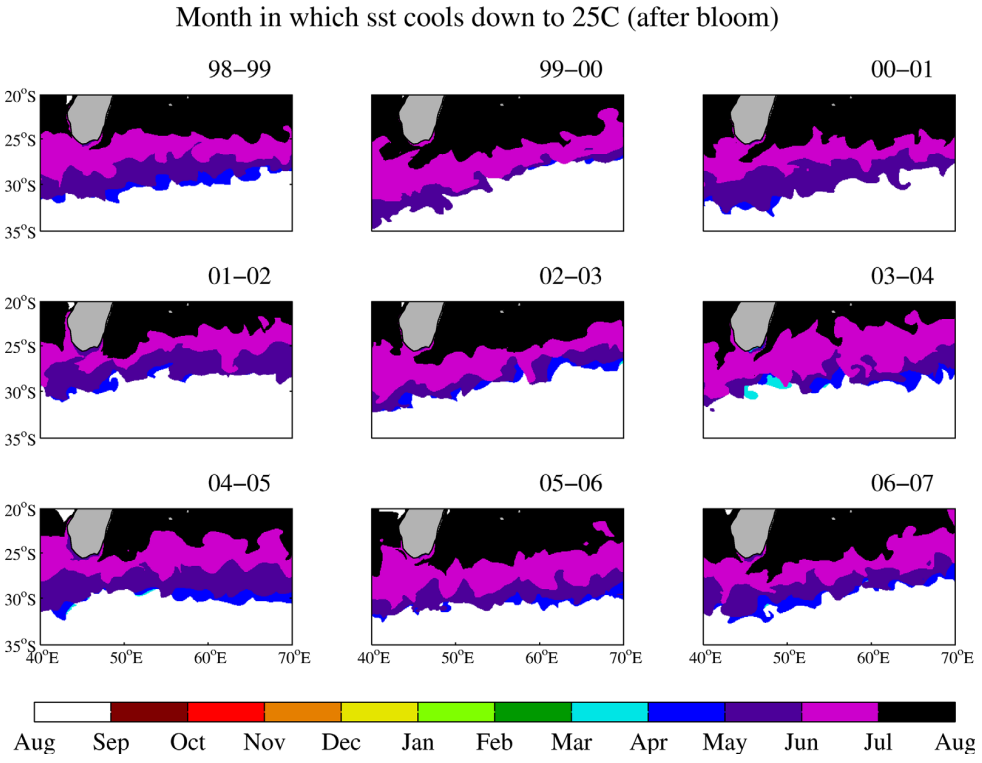

Figure 9. Results from NEMO showing the month in which surface temperatures drop below 25°C after the bloom period over the decade of model output examined. Note that in the white area, the temperatures never exceed 25°C, so cannot drop back below 25°C either.

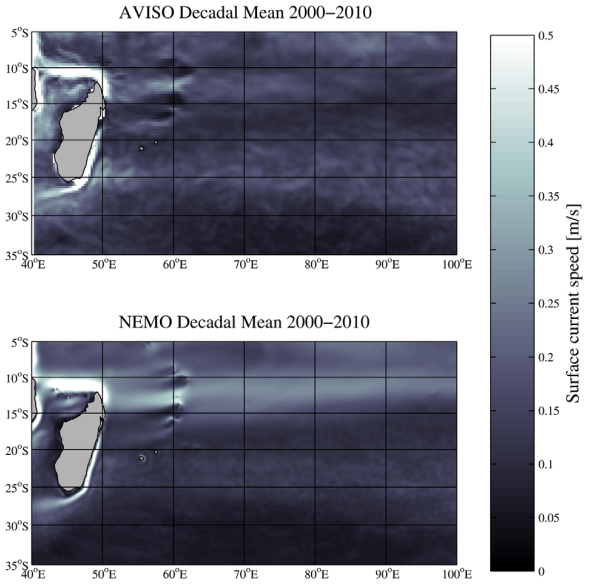

Figure 10. (top) Ten year (1998–2007) average of AVISO sea surface geostrophic current speeds, and a (bottom) 10 year (1998–2007) average of 1/12° NEMO sea surface current speed.

bloom could be triggered by the rise in the temperature of the surface water, as the mixed layer shallows. In contrast, from examining the model mixed layer depths (not shown), it would appear that the termination of the bloom is unlikely to be caused by either mixed layer deepening (for the bloom area it is never deep enough for light limitation to come into play) or by cooling as this occurs much later than the observed timing of the termination of the bloom (Figure 9).

These results are suggestive but not conclusive regarding the possible causes of the initiation and termination of the bloom and will be discussed further in section 5 (below).

4.2. South Indian Ocean Counter-Current (SICC) and Eddy Field

It has been suggested by *Wilson and Qiu* [2008] and *Huhn et al.* [2012] that the SICC, a shallow (∼200 m deep) current flowing eastward at approximately 25°S [*Palastanga et al.*, 2007], may play a role in the development and propagation of the Madagascar Bloom. One way that the existence of the SICC has been inferred is by averaging altimetric sea surface geostropic currents over a number of years [*Siedler et al.*, 2006]. Here the 10 year (1998–2007) average of AVISO produced altimetric sea surface geostropic current speeds is compared to the corresponding 10 year (1998–2007) average of 1/12° NEMO surface current speeds.

The results of comparing AVISO and NEMO surface currents are shown in Figure 10 and there is agreement generally, in line with similar comparisons by *Marzocchi et al.* [2015] for the North Atlantic (their Figure 8). The NEMO results are somewhat smoother overall and the residual variability in the 25°S band, on which the bloom is centered, slightly weaker. Both the AVISO and NEMO results show the existence of the East Madagascar Current flowing south along the east coast of Madagascar, then turning west to flow toward South Africa. Note that once the current leaves the Madagascan coast it interacts with the mesoscale eddy field and is less well defined. There is no clear evidence for the existence of the SICC in either the altimetry or the NEMO decadal means. Therefore, it can be concluded that the existence of the SICC is not necessary for iron advection to fertilize the bloom. The presence of the mesoscale eddy field (see Figure 2) is sufficient to transport particles, and therefore iron, east away from Madagascar. The averaging period used by *Siedler et al.* [2006], August 2001 to May 2006, was also examined for the AVISO data and their Figure1c reproduced (not shown), which appears to show the existence of the SICC. This seems at odds with our 10 year average which shows no SICC but this simply indicates that caution is required both in the choice of averaging period and in the interpretation of the results obtained from altimetry (see discussion in *Schlax and Chelton* [2008]). More recently, *Menezes et al.* [2014], based on Argo and hydrographic observations, have suggested that the SICC has a three-branched structure, three distinct eastward flowing jets that they denote as northern, central, and southern SICC. Therefore, the exact structure of the SICC seems to be a matter of some uncertainty at present but it is beyond the scope of this paper to pursue this question.

4.3. Indian Ocean Dipole (IOD)

Given the importance of the Indian Ocean Dipole [*Saji et al.*, 1999] for the Indian Ocean Circulation [*Schott et al.*, 2009], its possible role in the interannual variability of the Madagascar bloom is considered briefly here. Over the period studied here (1998–2007), the variability in the IOD dipole mode index seems to have no clear relationship to the behavior of the bloom from year-to-year. Indeed, over this period, the IOD mode index exhibits low variability except in 1998 (negative) and 2006 and 2007 (positive). The lack of a

relationship between the bloom and the IOD might be considered unsurprising as the impacts of the IOD on the circulation are seen primarily in the tropical Indian Ocean [*Schott et al*., 2009]. Previously, Srokosz *et al.* [2004] found no obvious link in this area to meteorological parameters (winds and fluxes) and *Uz* [2007] had concluded that the interannual variability did not correlate well with any obvious physical parameter. Likewise, the modeling and satellite observations study of *Currie et al*. [2013] shows no indication of IOD (or ENSO) influence on chlorophyll anomalies to the east of Madagascar, though their model does lack nitrogen fixers. Finally, *Longhurst* [2007] also noted the lack of any relationship between the bloom and climatic indices more generally. Consequently, the role of the IOD is not considered any further here.

5. Conclusions

The original hypothesis of this paper was that: iron from sediments around Madagascar is advected east by the mesoscale eddy field to fertilize the bloom, and the variability in the advection explains the significant interannual variability in the spatial extent of the bloom. The Lagrangian particle tracking results using NEMO 1/12° ocean model output (described in section 3) support this hypothesis by showing that iron could be advected east by the mesoscale eddy field in the nonbloom period to support a bloom in the following year. Furthermore, the model results show sufficient interannual variability in the spatial extent of the Lagrangian particle advection to explain the observed interannual variability in the spatial extent of the SeaWiFS ocean color observations of the bloom. The results also show (section 4.2) that the existence of the SICC is not necessary to explain either the extent or the interannual spatial variability of the bloom. The exact nature and form of the SICC seem unclear [*Palastanga et al*., 2007; *Siedler et al*., 2006; *Menezes et al*., 2014] but it is not necessary to solve these problems here, as the conclusions are not dependent on doing so.

From the numerical experiments presented in this paper, it is not possible to distinguish between iron advection from sediments and iron advection from riverine input [*Uz*, 2007; *Srokosz and Quartly*, 2013]. Both would enter the surface waters and be advected east. However, as noted by *Srokosz and Quartly* [2013], most of the major Madagascan rivers drain into the Mozambique Channel well away from the area of Lagrangian particle release (see Figure 3), so iron from sediments seems a more likely source (by analogy with Kerguelen and Crozet) [see *Blain et al*., 2007; *Pollard et al*., 2009]. *Jeandel et al*. [2011] note that 23 times more iron could reach the ocean from margin sources than that supplied by river fluxes. Only future in situ measurements are likely to be able to distinguish between these two possible sources of iron (possibly through the use of isotopic composition measurements) [*Jeandel et al*., 2011].

In addition to its use for Lagrangian particle tracking, the model output has also been examined to see whether it might give further insight into physical factors that could affect the initiation and termination of the bloom. The nitrogen fixing phytoplankton that compose the bloom are known to be sensitive to temperature and to require a relatively shallow mixed layer [*Srokosz and Quartly*, 2013; *Ward et al*., 2013; *Wilson and Qiu*, 2008, and references therein]. The model results (section 4.1) show that the interannual variability of mixed layer temperatures over the bloom area could explain the interannual variability in the timing of the initiation but not the termination of the bloom. The initiation of the bloom could be due to the warming of the surface waters leading to optimal conditions for the growth of the nitrogen fixing phytoplankton. Thereafter the termination of the bloom could be due to the exhaustion of iron by the phytoplankton as the bloom develops, since the model results suggest that the surface waters do not start to cool until after the bloom terminates. Again in situ observations of iron are required to confirm, or otherwise, that this is the case.

In summary, the picture that emerges from the above analysis is that the Madagascar bloom is fertilized by iron advected east from the island. The bloom is initiated in the late austral summer, when the upper ocean is depleted of nitrate due to the prior spring bloom, and the conditions (mixed layer temperatures) become suitable for nitrogen fixing phytoplankton to flourish. The bloom is terminated by the exhaustion of iron. This picture potentially explains both the interannual variability in the spatial extent of the bloom and of the timing of its initiation and termination. As noted above, this picture can only be confirmed (or disproved) by making further in situ measurements of the bloom, and particularly of iron availability for which no data are extant for this region.

Acknowledgments
M.A.S. is grateful to Alex Poulton for discussions regarding nitrogen fixers and the Madagascar Bloom. SeaWiFS data were obtained from NASA (http://oceandata.sci.gsfc.nasa.gov/SeaWiFS/L3SMI/). Altimeter products were produced by Ssalto/Duacs and distributed by Aviso, with support from CNES (http://www.aviso.oceanobs.com/duacs/). The study was carried out using the computational tool Ariane, developed by B. Blanke and N. Grima. The 1/12° NEMO simulation used in this work was produced using the ARCHER UK National Supercomputing Service (http://www.archer.ac.uk). This work was funded by the UK Natural Environment Research Council, in part through a PhD studentship for J.R. (NE/K500938/1) and national capability funding for M.A.S., E.E.P., and A.Y. It builds on the work of H.M. during her master's studies at the National Oceanography Centre (2013–2014).

References

AVISO (2014), *SSALTO/DUACS User Handbook: (M)SLA and (M)ADT Near-Real Time and Delayed Time Products, CLS-DOS-NT-06–034, SALP-MU-P-EA-21065-CLS*, 59 pp., Cent. Natl. D'études Spatiales, Ramonville St Agne, France. [Available at http://www.aviso.altimetry.fr/fileadmin/documents/data/tools/hdbk_duacs.pdf.]

Blain, S., et al. (2007), Effect of natural iron fertilisation on carbon sequestration in the Southern Ocean, *Nature*, *446*, 1070–1075.

Blanke, B., and S. Raynaud (1997), Kinematics of the Pacific Equatorial Undercurrent: An Eulerian and Lagrangian approach from GCM results, *J. Phys. Oceanogr.*, *27*, 1038–1053.

Blanke, B., M. Arhan, G. Madec, and S. Roche (1999), Warm water paths in the equatorial Atlantic as diagnosed with a general circulation model, *J. Phys. Oceanogr.*, *29*, 2753–2768.

Brodeau, L., B. Barnier, A.-M.Treguier, T. Penduff, and S. Gulev (2010), An ERA40-based atmospheric forcing for global ocean circulation models, *Ocean Model.*, *31*, 88–104.

Currie, J. C., M. Lengaigne, J. Vailard, D. M. Kaplan, O. Aumont, S. W. A. Naqvi, and O. Maury (2013), Indian Ocean Dipole and El Niño/Southern Oscillation impact son regional chlorophyll anomalies in the Indian Ocean, *Biogeosciences*, *10*, 6677–6698.

Dale, A. W., L. Nickelsen, F. Scholz, C. Hensen, A. Oschlies, and K. Wallman (2015), A revised global estimate of dissolved iron fluxes from marine sediments, *Global Biogeochem. Cycles*, *29*, 691–707, doi:10.1002/2014GB005017.

DiMarco, S. F., P. Chapman, and W. D. Nowlin (2000), Satellite observations of upwelling on the continental shelf south of Madagascar, *Geophys. Res. Lett.*, *27*, 3965–3968.

Dufois, F., N. J. Hardman-Mountford, J. Greenwood, A. J. Richardson, M. Feng, S. Herbette, and R. Matear (2014), Impact of eddies on surface chlorophyll in the South Indian Ocean, *J. Geophys. Res.*, *119*, 8061–8077, doi:10.1002/2014JC010164.

Elrod, V. A., W. M. Berelson, K. H. Coale, and K. S. Johnson (2004), The flux of iron from continental shelf sediments: A missing source for global budgets, *Geophys. Res. Lett.*, *31*, L12307, doi:10.1029/2004GL020216.

Gaube, P., D. B. Chelton, P. G. Strutton, and M. J. Behrenfeld (2013), Satellite observations of chlorophyll, phytoplankton biomass, and Ekman pumping in nonlinear mesoscale eddies, *J. Geophys. Res.*, *118*, 6349–6370, doi:10.1002/2013JC009027.

Gaube, P., D. J. McGillicuddy Jr., D. B. Chelton, M. J. Behrenfeld, and P. G. Strutton (2014), Regional variations in the influence of mesoscale eddies on near-surface chlorophyll, *J. Geophys. Res.*, *119*, 8195–8220, doi:10.1002/2014JC010111.

Huhn, F., A. von Kameke, V. Pérez-Muñuzuri, M. J. Olascoaga, and F. J. Beron-Vera (2012), The impact of advective transport by the South Indian Ocean countercurrent on the Madagascar bloom, *Geophys. Res. Lett.*, *39*, L06602, doi:10.1029/2012GL051246.

Jeandel, C., B. Peucker-Ehrenbrink, M. T. Jones, C. R. Pearce, E. H. Oelkers, Y. Godderis, F. Lacan, O. Aumont, and T. Arsouze (2011), Ocean margins: The missing term in the oceanic element budgets?, *Eos Trans. AGU*, *92*, 217–224.

Longhurst, A. (2001), A major seasonal phytoplankton bloom in the Madagascar Basin, *Deep Sea Res., Part I*, *48*, 2413–2422.

Longhurst, A. R. (2007), *The Ecological Geography of the Sea*, 2nd ed., Academic.

Machu, E., J. R. E. Lutjeharms, A. M. Webb, and H. van Aken (2002), First hydrographic evidence of the southeast Madagascar upwelling cell, *Geophys. Res. Lett.*, *29*(21), 2009, doi:10.1029/2002GL015381.

Madec, G. (2008), NEMO reference manual, ocean dynamic component: NEMO-OPA, Notes du pole de modelisation, *Tech. Rep. 27*, Inst. Pierre Simon Laplace, Paris, France.

Marzocchi, A., J. J.-M. Hirschi, N. P. Holliday, S. A. Cunningham, A. T. Blaker, and A. C. Coward (2015), The North Atlantic subpolar circulation in an eddy-resolving global ocean model, *J. Mar. Syst.*, *142*, 126–143.

Menezes, V. V., H. E. Phillips, A. Schiller, N. L. Bindoff, C. M. Domingues, and M. L. Vianna (2014), South Indian countercurrent and associated fronts, *J. Geophys. Res. Oceans*, *119*, 6763–6791, doi:10.1002/2014JC010076.

Mongin, M. M., E. R. Abraham, and T. W. Trull (2009), Winter advection of iron can explain the summer phytoplankton bloom that extends 1000km downstream of the Kerguelen Plateau in the Southern Ocean, *J. Mar. Res.*, *67*, 225–237.

Monteiro, F. M., M. J. Follows, and S. Dutkiewicz (2010), Distribution of diverse nitrogen fixers in the global ocean, *Global Biogeochem. Cycles*, *24*, GB3017, doi:10.1029/2009GB003731.

NASA (2009), *Ocean Colour Observations: Product Level Descriptions*. [Available at http://oceancolor.gsfc.nasa.gov/PRODUCTS/product_level_desc.html.]

Palastanga, V., P. J. van Leeuwen, M. W. Schouten, and W. P. M. de Ruijter (2007), Flow structure and variability in the subtropical Indian Ocean: Instability of the South Indian Counter Current, *J. Geophys. Res.*, *112*, C01001, doi:10.1029/2005JC003395.

Pollard, R. T., et al. (2009), Southern Ocean deep-water carbon export enhanced by natural iron fertilisation, *Nature*, *457*, 577–581.

Popova, E. E., A. Yool, Y. Aksenov, and A. C. Coward (2013), Role of advection in Arctic Ocean lower trophic dynamics: A modeling perspective, *J. Geophys. Res. Oceans*, *118*, 1571–1586, doi:10.1002/jgrc.20126.

Poulton, A. J., M. C. Stinchcombe, and G. D. Quartly (2009), High numbers of *Trichodesmium* and diazotrophic diatoms in the southwest Indian Ocean, *Geophys. Res. Lett.*, *36*, L15610, doi:10.1029/2009GL039719.

Robinson, J., E. E. Popova, A. Yool, M. Srokosz, R. S. Lampitt, and J. R. Blundell (2014), How deep is deep enough? Ocean iron fertilization and carbon sequestration in the Southern Ocean, *Geophys. Res. Lett.*, *41*, 2489–2495, doi:10.1002/2013GL058799.

Saji, N. H., B. N. Goswami, P. N. Vinayachandran, and T. Yamagata (1999), A dipole mode in the tropical Indian Ocean, *Nature*, *401*, 360–363.

Schlax, M. G., and D. B. Chelton (2008), The influence of mesoscale eddies on the detection of quasi-zonal jets in the ocean, *Geophys. Res. Lett.*, *35*, L24602, doi:10.1029/2008GL035998.

Schott, F. A., S-P. Xie, and J. P. McCreary (2009), Indian Ocean Circulation and climate variability, *Rev. Geophys.*, *47*, RG1002, doi:10.1029/2007RG000245.

Siedler, G., M. Rouault, and J. R. E. Lutjeharms (2006), Structure and origin of the subtropical South Indian Ocean Countercurrent, *Geophys. Res. Lett.*, *33*, L24609, doi:10.1029/2006GL027399.

Srokosz, M. A., and G. D. Quartly (2013), The Madagascar Bloom: A serendipitous study, *J. Geophys. Res. Oceans*, *118*, 14–25, doi:10.1029/2012JC008339.

Srokosz, M. A., G. D. Quartly, and J. J. H. Buck (2004), A possible plankton wave in the Indian Ocean, *Geophys. Res. Lett.*, *31*, L13301, doi:10.1029/2004GL019738.

Uz, B. M. (2007), What causes the sporadic phytoplankton bloom south-east of Madagascar?, *J. Geophys. Res.*, *112*, C09010, doi:10.1029/2006JC003685.

Ward, B. A., S. Dutkiewicz, C. M. Moore, and M. J. Follows (2013), Iron, phosphorus, and nitrogen supply ratios define the biogeography of nitrogen fixation, *Limnol. Oceanogr. Methods*, *58*, 2059–2075.

Wilson, C., and X. Qiu (2008), Global distribution of summer chlorophyll blooms in oligotrophic gyres, *Prog. Oceanogr.*, *78*, 107–134.

E.4 A tale of three islands: Downstream natural iron fertilization in the Southern Ocean

JOURNAL OF GEOPHYSICAL RESEARCH
Oceans
AN AGU JOURNAL
JGR
Volume 121 • Issue 5 • May 2016 • Pages 2857–3668

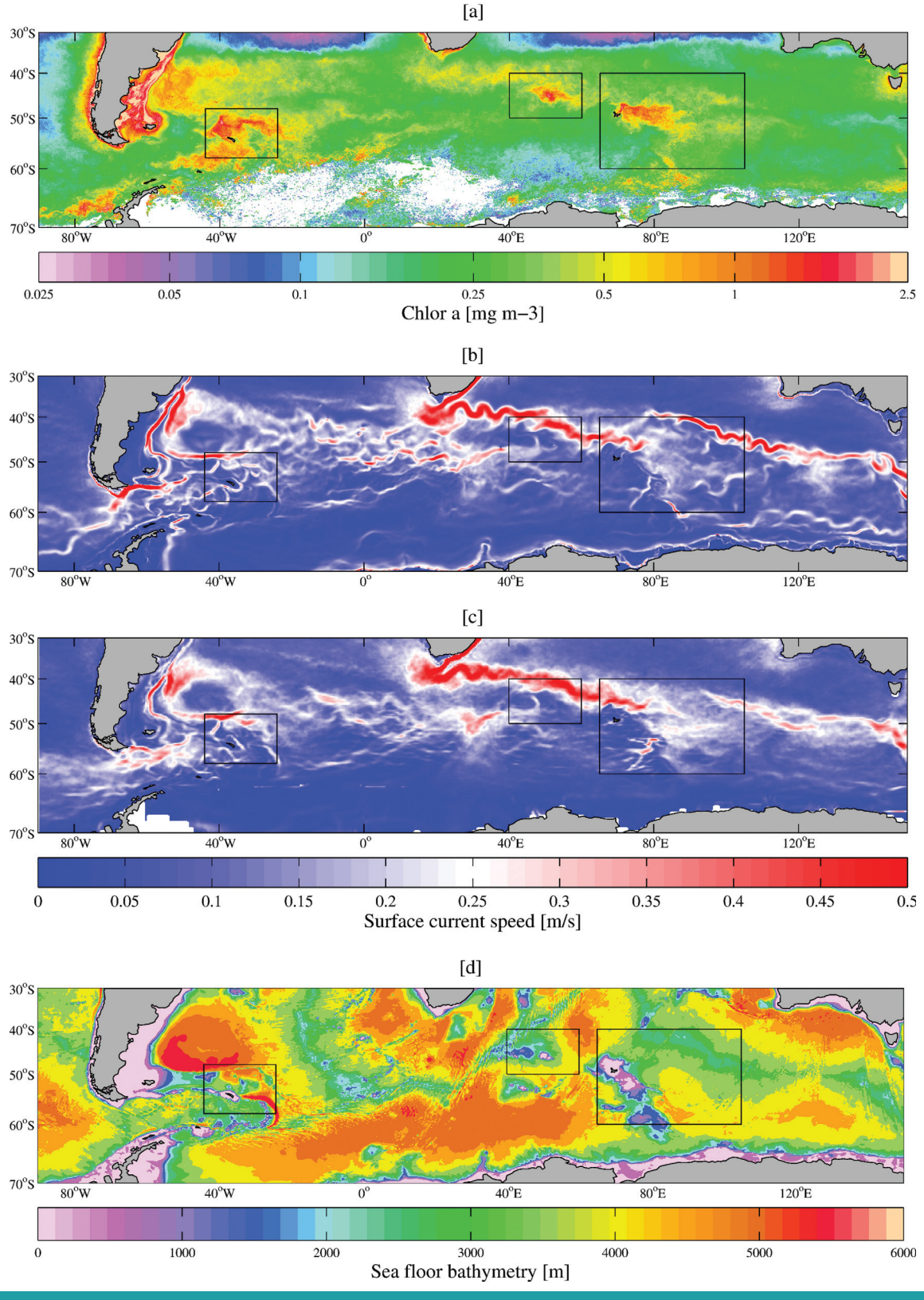

AGU PUBLICATIONS
WILEY

JOURNAL OF GEOPHYSICAL RESEARCH

Oceans

AN AGU JOURNAL

Aims and Scope. *JGR: Oceans* embraces the application of physics, chemistry, biology, and geology to the study of the oceans and their interaction with other components of the Earth system. Deepening the integrated knowledge of the sea utilizes new observational, analytical, computational and modeling capabilities to build upon established approaches in all areas of marine science.

AGU Editorial Team. For assistance with submitted manuscripts, file specifications, or AGU publication policy please contact jgr-oceans@agu.org.

For submission instructions or to submit a manuscript visit: http://jgr-oceans-submit.agu.org.

The journal to which you are submitting your manuscript employs a plagiarism detection system. By submitting your manuscript to this journal you accept that your manuscript may be screened for plagiarism against previously published works.

JGR: Oceans accepts articles for Open Access publication. Please visit http://olabout.wiley.com/WileyCDA/Section/id-406241.html for further information about OnlineOpen.

Publication Charges. The publication charge income received for *JGR: Oceans* helps support rapid publication, allows more articles per volume, makes possible the low subscription rates, and supports many of AGU's scientific and outreach activities. Publication charge information can be found here: http://publications.agu.org/author-resource-center/publication-fees.

To encourage papers to be written in a concise fashion, there is an excess length fee. For *JGR: Oceans* the fee is assessed only on the equivalent of more than 25 publication units. The excess length fee does not apply to review articles, and the editor may waive the fee on a limited number of concisely written papers that merit being longer. There is no charge for color in any format.

Individual Subscriptions. Member subscriptions are available through members.agu.org or by contacting the AGU Member Service Center. The Service Center is open from 8:00 a.m. to 6:00 p.m. Eastern time: +1 202 462 6900, +1 800 966 2481; Fax: +1 202 328 0566; e-mail: service@agu.org. Questions about meetings or membership will be referred to the appropriate staff.

Publisher. *JGR: Oceans* is published on behalf of the American Geophysical Union by Wiley Periodicals, Inc., 111 River St., Hoboken, NJ, 07030-5774, +1 201 748 6000.

Journal Customer Services. For institutional subscription information, claims and any enquiry concerning your journal subscription please go to www.wileycustomerhelp.com/ask or contact your nearest office.

Americas: Email: cs-journals@wiley.com; Tel: +1 781 388 8598 or +1 800 835 6770 (toll free in the USA & Canada).
Europe, Middle East and Africa: Email: cs-journals@wiley.com; Tel: +44 (0) 1865 778315.
Asia Pacific: Email: cs-journals@wiley.com; Tel: +65 6511 8000.
Japan: For Japanese speaking support, Email: cs-japan@wiley.com; Tel: +65 6511 8010 or Tel (toll-free): 005 316 50 480.

Visit our Online Customer Help available in 7 languages at www.wileycustomerhelp.com/ask.

Production Editor. For assistance with post-acceptance articles and other production issues please contact JGRCprod@wiley.com.

Access to this journal is available free online within institutions in the developing world through the AGORA initiative with the FAO, the HINARI initiative with the WHO, the OARE initiative with UNEP, and the ARDI initiative with WIPO. For information, visit www.aginternetwork.org, www.who.int/hinari/en/, www.oaresciences.org, or www.wipo.int/ardi/en.

ISSN 2169-9291 (Online)

View this journal online at jgr-oceans.agu.org.

Cover: In *Robinson et al.* [DOI: 10.1002/2015JC011319], a Southern Ocean overview of satellite ocean color, satellite and modeled surface current speed, and the bathymetry in the model. (a) Decadal average, 1998–2007, of the chlorophyll a concentration (mg m23) in the month of November. (b and c) The decadal averages (1998–2007) of surface current speed (m21), from the NEMO model, at 1/128, and the Aviso data, at 1/48 resolution, respectively. (d) The Southern Ocean bathymetry within the NEMO 1/128 model, contours are in meters below the sea surface. Black boxes denote the study areas: South Georgia, left; Crozet Islands, middle; Kerguelen, right. See pages 3349–3370.

Journal of Geophysical Research Oceans

Volume 121, Issue 5, May 2016
Pages 2857–3668
ISSN 2169-9291

Editorial

Research Articles

Commentary

AGU PUBLICATIONS

JGR

Journal of Geophysical Research: Oceans

RESEARCH ARTICLE

10.1002/2015JC011319

A tale of three islands: Downstream natural iron fertilization in the Southern Ocean

J. Robinson[1,2], E. E. Popova[1], M. A. Srokosz[1], and A. Yool[1]

[1]National Oceanography Centre, University of Southampton, Southampton, UK, [2]Ocean and Earth Science, University of Southampton, Southampton, UK

Key Points:
- Iron fertilization of blooms downstream of Southern Ocean islands studied with Lagrangian modeling
- Ocean areas fertilized by simulated iron transport overlap with observed spatial extent of blooms
- Inter-annual variability of iron input explains blooms at Crozet but not Kerguelen or South Georgia

Supporting Information:
- Supporting Information S1

Correspondence to:
J. Robinson,
josie.robinson@noc.soton.ac.uk

Citation:
Robinson, J., E. E. Popova, M. A. Srokosz, and A. Yool (2016), A tale of three islands: Downstream natural iron fertilization in the Southern Ocean, *J. Geophys. Res. Oceans*, *121*, doi:10.1002/2015JC011319.

Received 16 SEP 2015
Accepted 13 APR 2016
Accepted article online 19 APR 2016

Abstract Iron limitation of primary productivity prevails across much of the Southern Ocean but there are exceptions; in particular, the phytoplankton blooms associated with the Kerguelen Plateau, Crozet Islands, and South Georgia. These blooms occur annually, fertilized by iron and nutrient-rich shelf waters that are transported downstream from the islands. Here we use a high-resolution (1/12°) ocean general circulation model and Lagrangian particle tracking to investigate whether inter-annual variability in the potential lateral advection of iron could explain the inter-annual variability in the spatial extent of the blooms. Comparison with ocean color data, 1998–2007, suggests that iron fertilization via advection can explain the extent of each island's annual bloom, but only the inter-annual variability of the Crozet bloom. The area that could potentially be fertilized by iron from Kerguelen was much larger than the bloom, suggesting that there is another primary limiting factor, potentially silicate, that controls the inter-annual variability of bloom spatial extent. For South Georgia, there are differences in the year-to-year timing of advection and consequently fertilization, but no clear explanation of the inter-annual variability observed in the bloom's spatial extent has been identified. The model results suggest that the Kerguelen and Crozet blooms are terminated by nutrient exhaustion, probably iron and or silicate, whereas the deepening of the mixed layer in winter terminates the South Georgia bloom. Therefore, iron fertilization via lateral advection alone can explain the annual variability of the Crozet bloom, but not fully that of the Kerguelen and South Georgia blooms.

1. Introduction

It is now generally accepted that iron, in conjunction with light, is a major limiting factor of primary production in the Southern Ocean, indirectly controlling the biological pump and drawdown of carbon dioxide from the atmosphere [*Takahashi et al*., 2009; *Blain et al*., 2007; *Boyd et al*., 2007; *de Baar et al*., 1995; *Martin*, 1990; *Martin et al*., 1990]. However, there are exceptions to the high-nutrient, low-chlorophyll conditions that prevail across most of the Southern Ocean. Large phytoplankton blooms are observed downstream of continental shelf and land mass [*Blain et al*., 2007; *Pollard et al*., 2007; *Korb et al*., 2008], where iron is suggested to be supplied to surface waters predominately from ocean sediments [*Bakker et al*., 2007; *Tyrrell et al*., 2005; *Thomalla et al*., 2011]. In order to understand these important high-productivity regions, we need to characterize the time scales and mechanisms that transport iron to where primary production occurs [*Boyd et al*., 2012a, 2012b; *d'Ovidio et al*., 2015; *Wadley et al*., 2014]. Here we focus on three Southern Ocean islands groups, the Kerguelen Plateau, Crozet Islands, and South Georgia and Shag Rocks, outlined by black boxes in Figure 1a, specifically looking at the role of advection in determining the spatial extent of the downstream blooms.

Iron supply in the Southern Ocean comes from a variety of different sources including: aeolian input, brine rejection and drainage from sea ice, sediments, entrainment from the deep ocean via winter mixing, Ekman pumping, and upwelling at ocean fronts, and it is also constantly resupplied via rapid recycling of organic material [*Boyd and Ellwood*, 2010; *Gille et al*., 2014; *Graham et al*., 2015; *Korb et al*., 2008; *Schallenberg et al*., 2016; *Tagliabue et al*., 2014]. A recent study by *Graham et al*. [2015] suggests that coastlines, continental and island, are key sources of iron to the Southern Ocean, and also provides a comprehensive description of the behavior of iron in sediment pore waters and the mechanisms behind its flux into over-lying bottom water. Another source, recently found to be relevant to the Kerguelen Plateau, is riverine input associated with snowmelt. This source is important during spring, as there is increased rainfall and runoff, whereas freezing conditions during the winter inhibit this iron supply [*van der Merwe et al*., 2015]. In

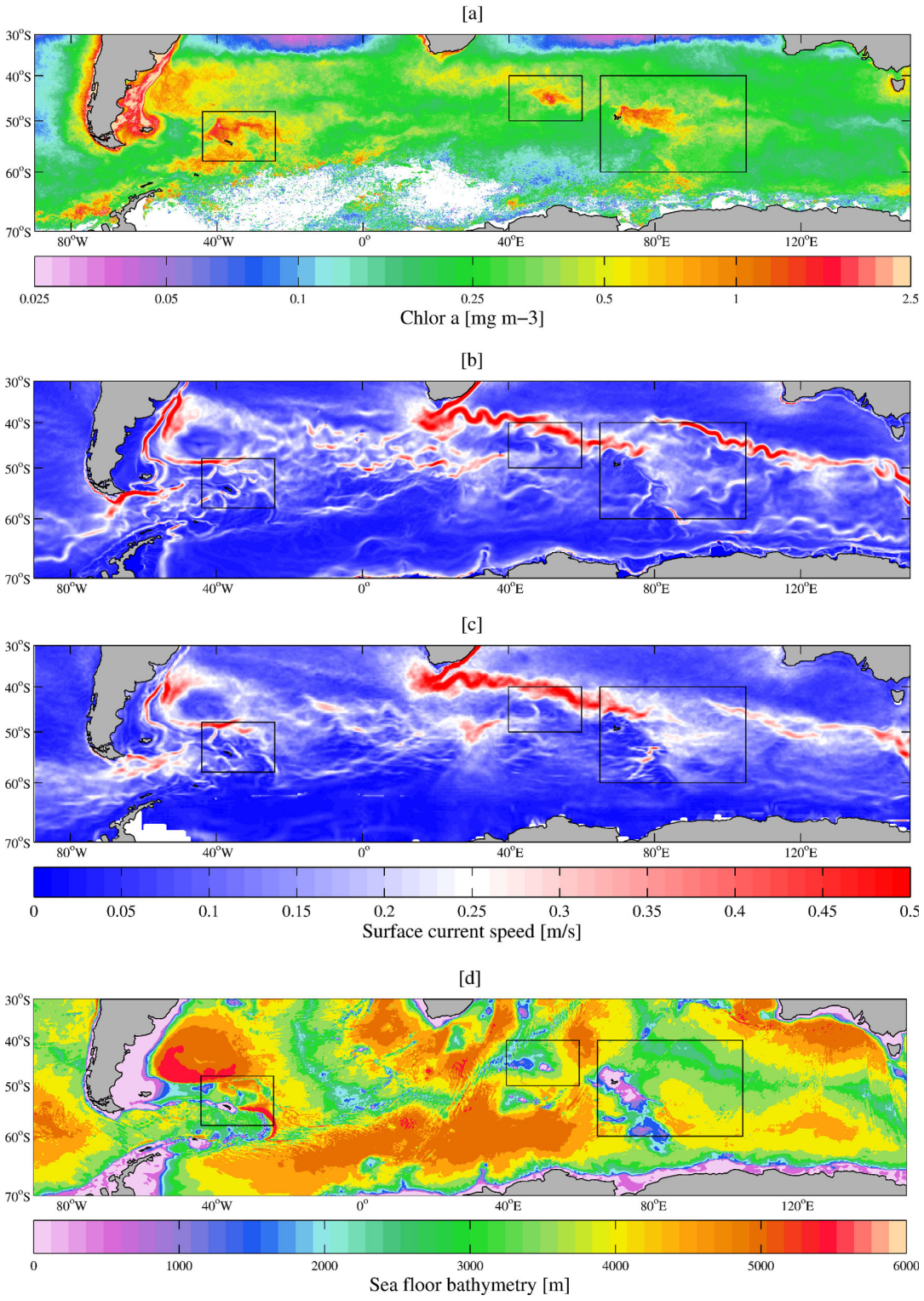

Figure 1. A Southern Ocean overview of satellite ocean color, satellite and modeled surface current speed, and the bathymetry in the model. (a) Decadal average, 1998–2007, of the chlorophyll *a* concentration (mg m^{-3}) in the month of November. (b and c) The decadal averages (1998–2007) of surface current speed (m^{-1}), from the NEMO model, at 1/12°, and the Aviso data, at 1/4° resolution, respectively. (d) The Southern Ocean bathymetry within the NEMO 1/12° model, contours are in meters below the sea surface. Black boxes denote the study areas: South Georgia, left; Crozet Islands, middle; Kerguelen, right.

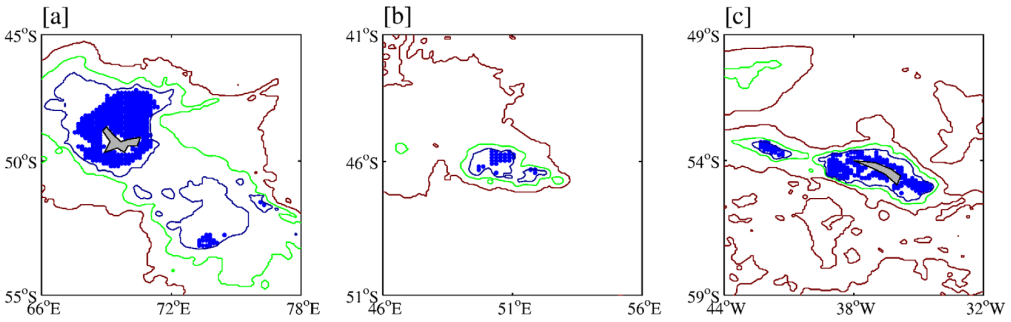

Figure 2. The starting positions of the Lagrangian particles around the islands. Particles are placed over shallow bathymetry (<180 m), around (a) Kerguelen and Heard Island, (b) Crozet Islands, and (c) South Georgia and Shag Rocks. In plots 2a and 2c, only every other particle is plotted for clarity. The plot also includes contours of 500 m (dark blue), 1500 m (green), and 3000 m (red) isobaths. Note that the axis for each plot is not consistent.

this paper, we focus on the potential for iron fertilization from island sources, primarily from sediments and runoff.

As iron is released from island sediments, internal waves and turbulence mix the iron up into surface waters which then fuels phytoplankton production [*Bowie et al*., 2015; *Boyd*, 2007; *Korb et al*., 2008; *Park et al*., 2008a, 2008b]. Iron that is not immediately utilized by biota or scavenged from the water column can be transported downstream of its source via lateral advection within the local circulation and also by stirring within mesoscale features [*Abraham et al*., 2000; *d'Ovidio et al*., 2015]. As it advects, iron can undergo many processes and transformations as part of the complex iron cycle, which can alter both the transport and bioavailability of iron. For instance, iron can be diluted by physical mixing, it can be kept in circulation by iron-binding ligands, or there can be luxury uptake of the iron by biota and hence "internal advection" [*Mongin et al*., 2008]. In various forms, iron can be lost from the surface by sinking or it can be retained in the surface water and then remineralized downstream of the original source and supply a new area with iron [*Boyd et al*., 2000; *Boyd*, 2007].

In order to test the hypothesis that inter-annual variability observed in the spatial extent of downstream island blooms could be explained by horizontal advection, the details of the iron cycle are not considered here. In this paper, the term "iron advection" refers to any iron from island sources in a form that can be laterally transported, via either advection or stirring, and is also bioavailable at the bloom site, hence what is demonstrated in this paper is the potential for iron fertilization. To diagnose the advection around each island, Lagrangian particles were released within velocity fields from the NEMO (Nucleus for European Modelling of the Ocean) 1/12° ocean general circulation model, a resolution high enough to resolve eddies and small-scale circulation patterns around the islands. In the analysis, the Lagrangian trajectories, representing water mass potentially fertilized with iron, are compared against the observed bloom areas in the satellite data. Additionally, the possible causes for bloom termination will be considered for each island, utilizing the model diagnostics and also World Ocean Atlas nutrient data.

2. Methodology

In order to assess the impact of iron that could potentially be advected downstream of Southern Ocean islands, satellite-derived data (chlorophyll *a* concentrations and sea surface currents) were compared with Lagrangian particle trajectories within velocity output from the NEMO 1/12° model. Here we give a brief description of each of the three study sites, the tools used, and explain the experimental design.

2.1. Study Sites

The Kerguelen Plateau and Heard Island (southeast of the Kerguelen Island), depicted by the box on the right of Figure 1d (bathymetry plot), is a major bathymetry feature within the Indian Ocean sector of the Southern Ocean, extending from 46°S to 64°S at the 3000 m isobath. It forms a major barrier to the eastward flowing Antarctic Circumpolar Current (ACC), with most of the flow being deflected to the north of the plateau (~100 Sv), and the substantial remainder to the south (30–40 Sv), steered primarily by the

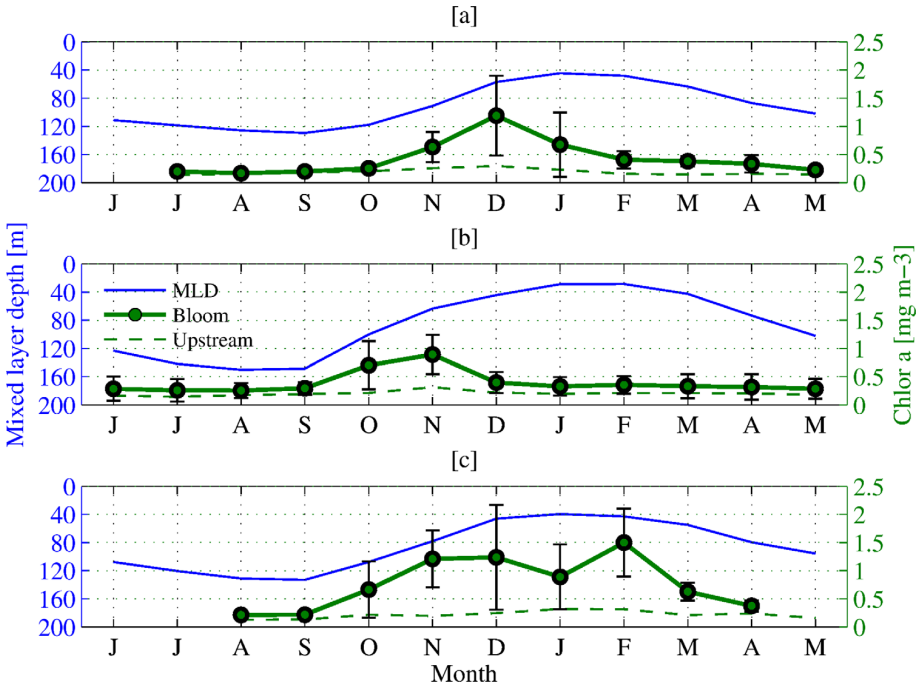

Figure 3. The average chlorophyll *a* concentration (mg m^{-3}) (satellite ocean color) of each month over the 10 year period. Concentrations are from two locations, one inside (thick green line with markers) and one outside of the bloom region (dashed green line), for each island. The data points from inside the bloom region include error bars which are plus and minus one standard deviation in chlorophyll *a* for each month, over the 10 year period. The blue line represents the decadal average of the mixed layer depth of each location inside the bloom. (a) Kerguelen, (b) Crozet, and (c) South Georgia. Note the *x* axis, "Month," begins from June to May.

topography. The circulation over the plateau between the two islands is rather stagnant, <5 cm^{-s} on average. A major circulation feature within the region is the Polar Front (PF), which cuts between the two islands, flowing close to the southeast Kerguelen Island [*Park et al*., 2008a, 2008b, 2014]. The Kerguelen bloom occurs on decadal average during November to January, as demonstrated in Figure 3a, and is predominately made up of diatom species above the plateau [*Blain et al*., 2001]. However, note that the Kerguelen bloom can persist for much longer periods, due to a concurrent resupply of essential nutrients via remineralization and entrainment from the deep ocean during vertical mixing [*Boyd*, 2007].

Crozet Islands (46°S, 52°E), depicted by the central black box in Figure 1d, are separated from the Del Cano Rise plateau to the west by the Subantarctic Front (SAF), which is the dominant circulation feature in the area. The SAF predominately lies west to east within the ACC, but turns sharply north between the two plateaus (Crozet and Del Cano Rise), before turning eastward to the north of Crozet as it comes into contact with the Agulhas Return Current [*Bakker et al*., 2007; *Pollard et al*., 2007]. Over the plateau and to the north of the island (bounded by the SAF) is an area of Polar Frontal Zone characterized by weak circulation (15–20 Sv), within which iron can accumulate during the winter months that can subsequently fuel a bloom [*Planquette et al*., 2007]. The phytoplankton community structure of the Crozet bloom, described by *Poulton et al*. [2007], is made up of varying sizes of diatoms, and very small prymnesiophyte *Phaeocystis antarctica*. Biomass varies considerably near to the plateau between species, but further away from the plateau, to the northwest and east, prymnesiophyte *P. antarctica* can dominate.

South Georgia and Shag Rocks (northwest of South Georgia), hereafter referred to collectively as South Georgia, are located to the east of Drake Passage, highlighted by the left black box in Figure 1d. The islands form part of the North Scotia Ridge at roughly 54°S, 37°W, directly in the path of the ACC. The PF lies north of the islands, and the Southern ACC Front flows to the south, looping anticyclonically around South Georgia before flowing east again [*Orsi et al*., 1995; *Meredith et al*., 2003]. North of the island, enclosed by the PF and Southern ACC Front, is the South Georgia Basin, within which prolonged blooms exist throughout the

growing season [*Borrione and Schlitzer*, 2013]. This paper will focus on the South Georgia Basin bloom, but there are blooms occurring to the south and west of the islands [*Ward et al*., 2007], although these blooms are partly subsurface and may not be represented by satellite observations. Furthermore, the region is one of the most productive regions across the entire Southern Ocean, with various sources of iron and phytoplankton [*Ardelan et al*., 2010; *Murphy et al*., 2013; *Thomalla et al*., 2011]. Consequently, from satellite ocean color data alone, it is not possible to delineate blooms fertilized by iron from South Georgia sediments or from elsewhere within the basin (Antarctic peninsula or ice melt). The South Georgia Basin bloom (hereafter referred to as the South Georgia bloom) is dominated by large diatom species, but is described as "patchy" over scales of 10–20 km, with fragmented diatom colonies occurring alongside a more invariant community of small autotrophs and heterotrophs [*Atkinson et al*., 2001; *Korb et al*., 2008].

Each of the three islands has different characteristics which determine the ecosystem that they support and its functioning, but for a generalized overview of the Southern Ocean ecosystem, see *Boyd* [2002]. These islands have been selected for this study as their blooms have been extensively explored in the field [*Blain et al*., 2008; *Pollard et al*., 2007; *Korb et al*., 2008; *Murphy et al*., 2013], the results from which can be used to support our own analysis.

2.2. Satellite Data

2.2.1. Chlorophyll Observations

The ocean color data used in this study come from the ESA Ocean Colour Climate Change Initiative. Here we use a (level 3 geographically mapped) merged and bias corrected product from the MERIS, MODIS, and SeaWiFS data sets, with a horizontal resolution of up to 4 km [*Storm et al*., 2013]. Because of the low solar elevation and sea-ice coverage in winter, data are unavailable in some areas, most visibly the Weddell Sea in Figure 1a, but by averaging over a month, year, and decade, we can fill in many of the gaps. This study has utilized monthly chlorophyll *a* (chl *a*) concentrations over the period 1998–2007, the first decade in which we have good satellite coverage across the world. In this study, the chlorophyll data are used to represent phytoplankton biomass, defining the island blooms.

2.2.2. Altimetric Sea Surface Currents

The satellite altimeter data are produced by Ssalto/Duacs and distributed by the Archiving Validation and Interpretation of Satellite Data in Oceanography (Aviso) group, with support from CNES (http://www.aviso.altimetry.fr/duacs/). Here we utilize a merged data set, from only two satellites at any one time, each having the same ground track and stable sampling which provides a homogenous time series. This along-track, delayed time data product has great stability and therefore is the ideal product for use in inter-annual comparison studies [*Le Bars et al*., 2014].

The along-track Absolute Dynamic Topography (ADT) is obtained by adding the Sea Level Anomaly to the Mean Dynamic Topography (Mean Sea Surface Height minus Geoid). A mapping procedure using optimal interpolation with realistic correlation functions is applied to produce ADT maps (MADT or L4 products) onto a Cartesian 1/4° × 1/4° grid [*Aviso*, 2014]. Here we use the sea surface geostrophic velocities computed from the ADT over the period of 1998–2007.

2.3. NEMO Model and Ariane Lagrangian Particle Tracking

The NEMO 1/12° resolution ocean general circulation model has been developed with particular emphasis on realistic representation of fine-scale circulation patterns [*Madec*, 2008], which provides an ideal platform to conduct Lagrangian particle-tracking experiments around the small islands of the Southern Ocean. Full details of the model run, including model setup and configuration, can be found in *Marzocchi et al*. [2015] as only a brief description will be given here. The model is initialized with World Ocean Atlas (WOA) 2005 climatological fields and forced with 6 hourly winds, daily heat fluxes, and monthly precipitation fields [*Brodeau et al*., 2010]. The run begins in 1978, with output through to 2010, of which we are interested in 1998–2007. Model output is stored offline as successive 5 day means throughout the model run, of which the velocity fields are used for the particle tracking in this paper.

The Ariane package [*Blanke and Raynaud*, 1997] (available online at: http://stockage.univ-brest.fr/~grima/Ariane) is applied to the NEMO velocity field to track water parcels using point particles that are released into the modeled ocean circulation (cf. *Popova et al*. [2013] and *Robinson et al*. [2014], who used output from the NEMO 1/4° model). These particles are intended here to represent water masses fertilized by iron

scoured from the island sediments. Further details about the Ariane package can be found in *Blanke and Raynaud* [1997] and *Blanke et al*. [1999].

An important caveat to the results is that we do not expect the NEMO 1/12° model to reproduce the detailed mesoscale flows year-by-year due to chaotic dynamics, as the mesoscale eddy field is not initialized to match that of the real world (only possible using data assimilation). Nevertheless, the model does reproduce the larger-scale flow field in the vicinity of the islands, which is important for downstream advection (see Figures 1b and 1c).

2.4. Experiment Design

In order to study the advection of iron from island sources and make a qualitative comparison with the ocean color 1998–2007 observations, Lagrangian particles were released monthly into the modeled circulation from around the shelf regions of each island, from January 1998 to December 2007. Particles are deployed in every other grid cell of the 1/12° model grid along the horizontal (latitudinally and longitudinally), and at each level of the NEMO grid depth domain down to a maximum depth of 180 m (30 depth levels, not equally spaced see *Madec* [2008]), around each of the three islands (cf. *Srokosz et al*. [2015], who used a similar analysis for the Madagascar bloom). Figure 2 shows the starting positions of the particles around each of the islands. The particles had to be spaced at a high enough resolution to resolve the fine-scale circulation patterns around each island, but the experiments were limited computationally, as the islands are not of a comparable area, so there could not be a particle within every model grid cell. The particles are released in both the horizontal and vertical extent, to represent iron that is scoured from the shelf sediment (down to 180 m in this experiment) and mixed upward [*Ardelan et al*., 2010; *Blain et al*., 2001; *Hewes et al*., 2008; *Planquette et al*., 2007] as well as other island sources, such as river runoff [*van der Merwe et al*., 2015]. Particles that are subducted deeper than 200 m, i.e., out of the euphotic zone, along their trajectory are removed from the analysis. At the horizontal and vertical grid spacing described, that results in 8240 Lagrangian particles being released each month from the Kerguelen and Heard Island, 465 particles from Crozet, and 2820 particles from South Georgia and Shag Rocks.

2.4.1. Assumptions and Limitations of Method

The main assumption in this study is that surface waters in the Southern Ocean are iron limited, and that the addition of iron to an area, via horizontal advection, would initiate a bloom. However in reality, productivity can be colimited in the Southern Ocean, with light or silicate, for example, and there are also seasonal factors which control phytoplankton growth, which can vary in both time and space [*Boyd*, 2002].

In the analysis to follow, the advection time over a period of 12 months is discussed. Note that the residence time of bioavailable iron in surface waters is not yet fully understood, but thought to be relatively short, on the order of only weeks to months [*Boyd and Ellwood*, 2010; *Shaked and Lis*, 2012; *Schallenberg et al*., 2016]. However, studies have also shown that iron can be transported during winter months and remain in the upper ocean to be available to stimulate blooms in the summer months [*Mongin et al*., 2009; *d'Ovidio et al*., 2015]. *Graham et al*. [2015] postulates that this might be possible due to intense biological recycling of iron, or the long-range transport of particulate iron, or even by currently unknown processes. For the time being, these questions remain unanswered, and so for the purpose of this study all of the iron from the islands is assumed to remain available throughout the year. A further assumption is that all advective pathways have the potential to be fertilized with iron.

A caveat to this analysis is that, in using satellite ocean color data, it is not possible to detect subsurface chlorophyll maxima, which are known to exist in certain regions of the Southern Ocean [*Holm-Hansen et al*., 2005; *Tripathy et al*., 2015]. Therefore, we cannot use our analysis to draw any conclusions on the location or variability of known subsurface chlorophyll maxima [*Ward et al*., 2007], and make the distinction now that only surface blooms are considered, hereafter just referred to as blooms.

As touched upon in section 1, the representation of iron and its transport in this method is a simplification. Ideally, this study would be performed using tracers in a high-resolution, fully coupled biogeochemical model, but the computational resources required for this would be extreme. Such a study would need a coupled model at a resolution high enough to formally resolve the small-scale circulation features that occur around the islands at the center of this study. As such, the analysis presented in our results and discussion is restricted to consider only potential iron advection and consequent fertilization.

3. Results

3.1. Ocean Color

Figure 1a is a 10 year average of satellite-derived sea surface chl *a* concentrations in November, over 1998–2007. The islands of interest are highlighted by black boxes, from which it is clear that these island blooms can be more than double the magnitude of productivity anywhere else in the Southern Ocean. Figure 3 is the decadal monthly averages, of surface chl *a* concentration, for a single location inside, and a single location outside of the bloom sites for each island. Each location was selected arbitrarily based on persistence either inside or outside (upstream of the ACC) of the annual bloom. The latitude and longitude coordinates of each location inside the bloom are 72°E and 49°S, 52.5°E and 45.5°S, and 38.5°W and 52.5°S for Kerguelen, Crozet, and South Georgia, respectively. The coordinates of each location upstream of the bloom are 66°E and 48°S, 45.5°E and 46.5°S, and 49.5°W and 52.5°S (cf. *Park et al*. [2008a, 2008b, Figure 11], *Pollard et al*. [2009, Figure 1], and *Korb et al*. [2004, Figure 1], for schematic positioning of the ACC around Kerguelen, Crozet and South Georgia respectively). In this paper, a bloom is defined by chl *a* concentrations higher than 0.5 mg m^{-3}, as it is consistently higher than chl *a* outside of each islands typical bloom regions [*Comiso et al*., 1993; *Moore and Abbott*, 2000]. Also, when 0.5 mg m^{-3} of chl *a* is exceeded in Figure 3, it occurs on a steep gradient from 1 month to the next, indicating the start of a bloom. Additionally, this concentration is low enough to avoid complications with double peaks in chl *a* associated with South Georgia, as can be seen in Figure 3c. South Georgia is a region that frequently has two bloom peaks per year [*Borrione and Schlitzer*, 2013]; however, it is outside of the scope of this work to analyze peak bloom events. Therefore, in order to focus on inter-annual rather than inter-seasonal variability, we consider the average chl *a* concentration over the bloom period. The error bars in Figure 3 are 1 standard deviation in chl *a* for each month, over the 10 year period. The size of the error bars is an indication of the seasonality across the regions and annual cycles. South Georgia, in particular, has large error bars which are due to the range in magnitude of annual blooms. For instance, the average chl *a* for January over 1998–2007 is <1 mg m^{-3}, however, in January of 2002, the concentration was as high as 15 mg m^{-3} [*Korb and Whitehouse*, 2004].

Figure 3 also includes the averaged (decadal) monthly mixed layer depth (MLD) in the "bloom" site for each island, calculated online in the NEMO model. Comparing the bloom and MLD curves, we see that the bloom is likely triggered by the onset of a shallowing mixed layer [*Venables and Moore*, 2010]. The MLD, specifically its role in terminating the blooms, is considered in further detail in the discussion.

Figure 4 shows example years of a small and a large averaged bloom period (hereafter referred to as the bloom) for each island, during 1998–2007. Maximum and minimum blooms for Kerguelen occur in 2003 and 2000, Crozet is 2004 and 2001, and South Georgia is 2002 and 2006. Strikingly, Figure 4 demonstrates the strong inter-annual variability in both bloom magnitude and area, which may be explainable by studying the potential iron advection from the islands.

3.2. NEMO Versus Aviso Surface Current Speed

The ability of the chosen model to accurately represent the circulation in the study area is critical to the quality of the results. In order to assess the performance of the NEMO 1/12° model, we can compare with satellite-derived sea surface currents (Aviso). The Aviso data are the geostrophic component of the velocity, whereas the NEMO model is the absolute velocity, but this should not impact a comparison between the two as they are near equal at the surface. By comparing the decadal averages of NEMO and Aviso, side by side (Figure 1), we can assess the models performance.

Figures 1b and 1c are a comparison of the decadal (1998–2007) average ocean surface current speed, from NEMO and Aviso, respectively, across the Southern Ocean. Qualitatively, the model correctly captures the major features, and also their magnitude. Fast flowing currents are stronger in the model than Aviso, and also boundaries of fast flowing currents within the modeled circulation are more defined than in the observations. This may be due to data smoothing caused by the correlation function applied to the Aviso data or due to the model under representing submesoscale features. Figures S1–S3 in the supporting information show the decadal, annual, and monthly averaged circulation, of both model and satellite-derived velocities, for each island for illustrative purposes.

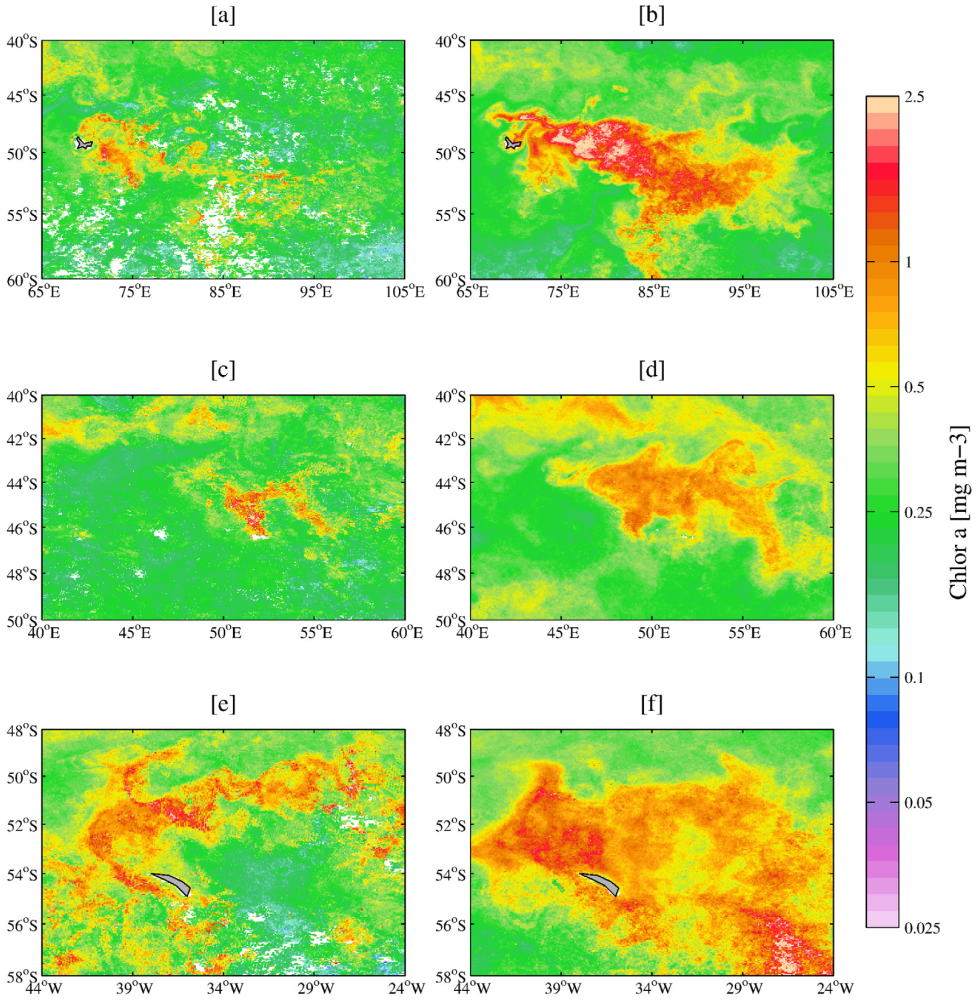

Figure 4. Example years of satellite ocean color plots of each island. Chlorophyll *a* concentrations have been averaged over the bloom period for each year. The top row is Kerguelen (bloom period: November–January), years (a) 2000 and (b) 2003; the middle row is Crozet (bloom period: October–December), years (c) 2001 and (d) 2004; and the bottom row is South Georgia (bloom period: October–April), years (e) 2006 and (f) 2002. Figures 4a, 4c, and 4e are examples of a small bloom extent during the 1998–2007 year period, and Figures 4b, 4d, and 4f are years with a large bloom extent.

3.3. Advection of Iron Toward the Bloom Site

In this paper, we hypothesize that the advection of iron downstream of islands allows blooms to occur in the otherwise high-nutrient, low-chlorophyll regime of the Southern Ocean. Here we investigate the time scales of fertilization, and the degree to which the circulation can impact inter-annual variability, during the period 1998–2007.

The Kerguelen bloom occurs on decadal average during November to January, as demonstrated in Figure 3a. For this analysis, we focus on the average surface chl *a* concentration over the bloom period (November to January in Kerguelen's case) for each year, referred to as the bloom. Figure 5 shows the patch around Kerguelen that could potentially be fertilized with iron by the local circulation in the NEMO model. The fertilized patch is depicted by colored markers, which represent the location of trajectories in October for each year, with the different colors indicating the month in which the particles were released from the island. Strikingly, the fertilized patch is much larger than the bloom extent, represented by black contours in each annual subplot. The trajectories propagate east from the island between the latitude band of roughly 45°S–54°S, but then spread both northward and southward in extent from roughly 77°E. However, despite the fertilized patch reaching as far north as 40°S in Figure 5, we can see from the black contours that the bloom area is never north of 45°S in any of the years.

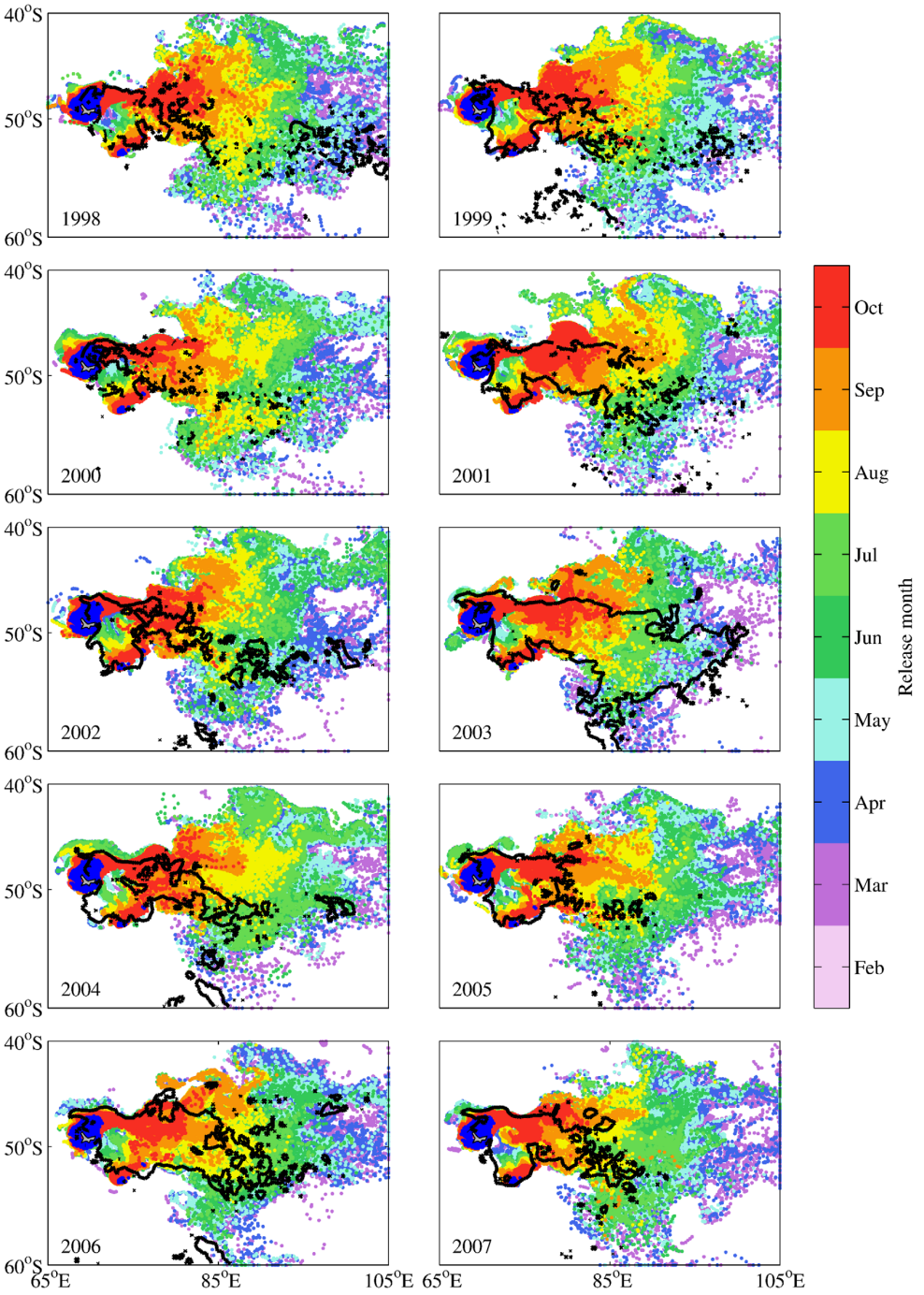

Figure 5. Extent of Lagrangian trajectories around Kerguelen. Eight thousand two hundred forty particles were released monthly from their starting positions, denoted in blue; however, only every second particle is shown here for clarity. Particle trajectories in October (preceding the start of the bloom) are depicted by colored markers. The color of the trajectory relates to the month in which it was released as indicated by the color bar. The black contour represents the averaged bloom area, over November–January, of chlorophyll *a* concentrations above 0.5 mg m^{-3}. Only trajectories that are shallower than 200 m are included in this plot.

Having found that the horizontal advection of iron would be sufficient to fertilize the bloom in principle, a further question arises as to whether the bloom is terminated by the exhaustion of iron in the surface water. This question cannot be addressed directly using the NEMO 1/12° simulation, as it is not a coupled

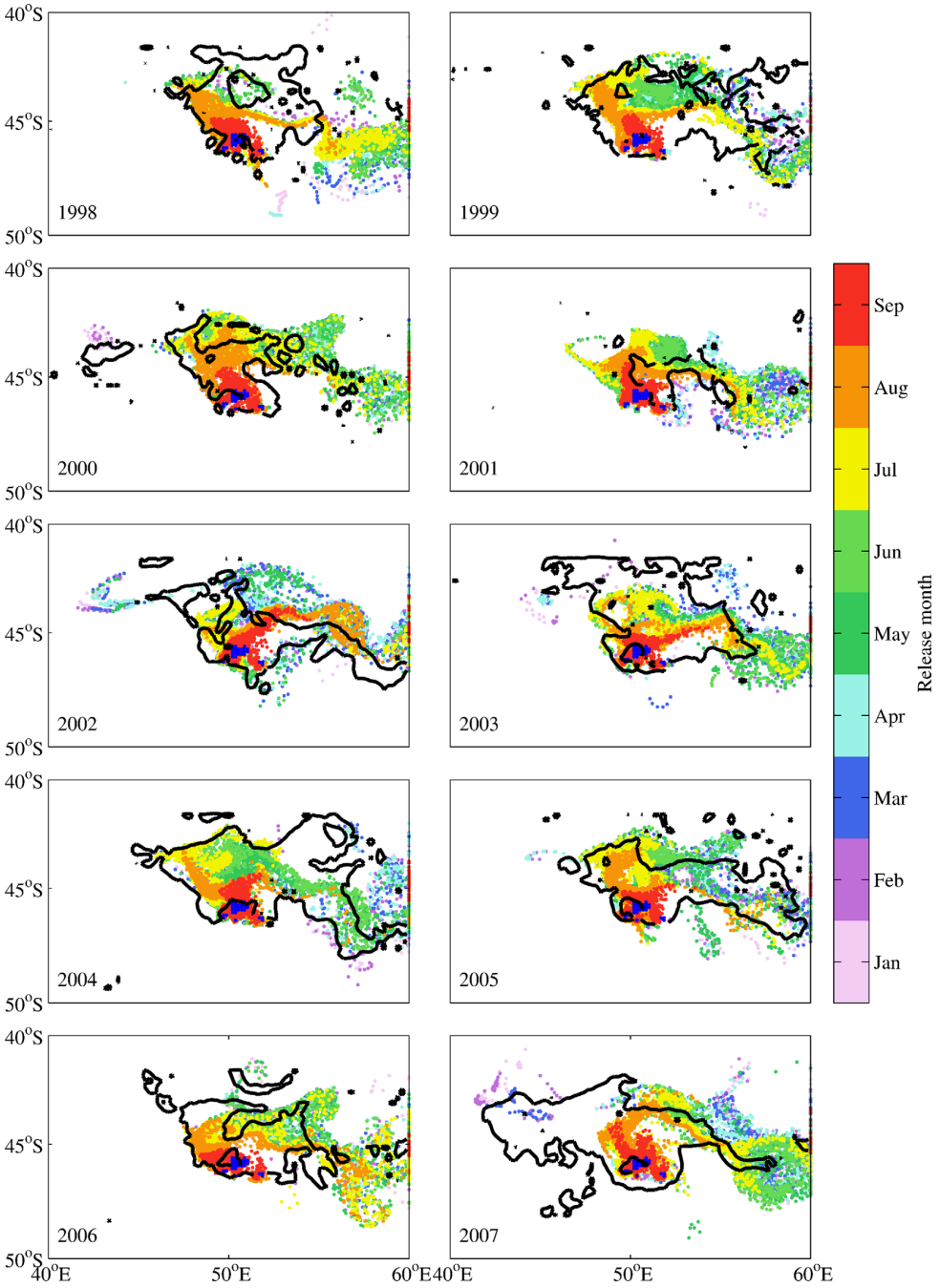

Figure 6. Extent of Lagrangian trajectories around Crozet. Four hundred sixty-five particles were released monthly from their sing positions, denoted in blue; however, only every second particle is shown here for clarity. Trajectories in September (preceding the start of the bloom) are depicted by colored markers. The color of the trajectory relates to the month in which it was released as indicated by the color bar. The black contour represents the averaged bloom area, over October–December, of chlorophyll *a* concentrations above 0.5 mg m^{-3}. Only trajectories that are shallower than 200 m are included in this plot.

biogeochemistry model. However, if the bloom is terminated by the exhaustion of iron then a question that can be addressed is: can advection resupply iron in the period between the end of one bloom and the start of the next? as addressed by *Mongin et al.* [2009], and more recently by *d'Ovidio et al.* [2015]. For Kerguelen, the location of the fertilized patch was very consistent, however, there are temporal differences in the

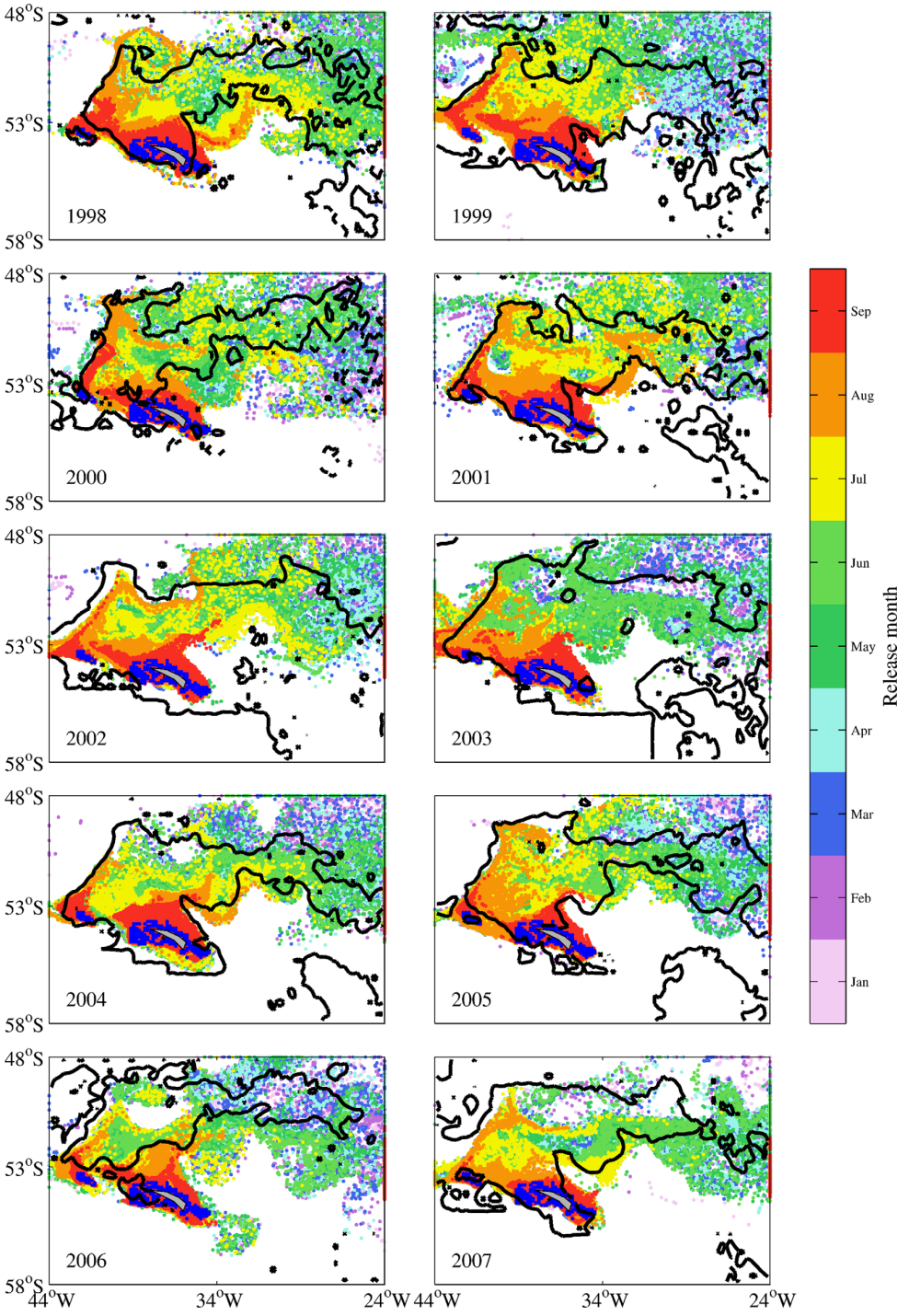

Figure 7. Extent of Lagrangian trajectories around South Georgia. Two thousand eight hundred twenty particles were released monthly from their starting positions, denoted in blue; however, only every second particle is shown here for clarity. Trajectories, in October (preceding the start of the bloom), are depicted by colored markers. The color of the trajectory relates to the month in which it was released as indicated by the colorbar. The black contour represents the averaged bloom area, over October–April, of chlorophyll *a* concentrations above 0.5 mg m^{-3}. Only trajectories that are shallower than 200 m are included in this plot.

Table 1. Size of the Annual Bloom and Fertilized Patch Around Kerguelen, and the Percent of Each Area That is Overlapped by the Other[a]

Year	Bloom Area (km^2)	Fertilized Patch (km^2)	Bloom Overlap (%)	Fertilized Overlap (%)
1998	674,572	2,731,476	74	18
1999	803,847	2,676,533	64	19
2000	339,783	2,693,883	78	10
2001	832,765	2,593,000	84	27
2002	613,450	2,621,786	75	18
2003	1,602,173	2,435,464	73	48
2004	729,515	2,637,034	72	20
2005	532,218	2,568,354	84	17
2006	1,056,154	2,539,699	82	34
2007	640,068	2,358,635	86	23

[a]Bloom Area is the total area of the average (November–January) chl *a* concentration above 0.5 mg m^{-3}; Fertilized Patch is the extent of particle trajectories in October (prior to the start of the bloom); Bloom Overlap is the percent of the bloom area overlapped by the fertilized patch; Fertilized Overlap is the percent of the fertilized patch overlapped by the bloom.

timing of advection. Nevertheless, the results show the maximum advection time for the particles to reach the furthest extents of the bloom is on the order of 5–6 months, suggesting that horizontal advection is sufficient to resupply the bloom area with iron, in agreement with *Mongin et al*. [2009] and *d'Ovidio et al*. [2015].

Figure 6 is the same as 5, but focusing on Crozet. The Crozet bloom occurs 1 month earlier than the Kerguelen bloom, on decadal average during October to December [*Pollard et al*., 2007], and so the trajectories shown in Figure 6 represent the fertilized patch in September. Figure 6 suggests that there is more inter-annual variability in the circulation around Crozet than Kerguelen, both spatially and temporally. In Figure 6, the fertilized patch tends to be north of the island and to the east, made up of particles released in June–August (light green to orange on the color bar). This indicates that the time scale for fertilization, of water mass being within the immediate vicinity of Crozet (where the particles are released) to outside of the bloom area (the black contours), is on the order of 3–4 months; however, Figure 6 clearly shows the inter-annual variability in this time scale. There are some years in Figure 6 where we see the fertilized patch extending to the west of the island, most visibly in the years 2000, 2002, 2003, and 2007. The color of the markers seen to the west of the island in some of the years show the particles were released earlier in the year, ranging from January (2000) to April (2002). Focusing on the black contours in Figure 6, representing chl *a* concentrations above 0.5 mg m^{-3} during the bloom period, there are years in which the bloom is propagated to the west also, most clearly apparent in 2000 and 2007.

The bloom associated with South Georgia occurs on decadal average, during October to April; however, South Georgia experiences the highest seasonality of all the three islands in this study. Here we discuss the South Georgia bloom, although the surrounding area is one of the most productive regions within the Southern Ocean [*Ardelan et al*., 2010; *Young et al*., 2014], so separating a bloom associated with iron-only advected from South Georgia is not nontrivial. In order to address this issue, we have applied a mask to the ocean color data, to remove chl *a* that was most likely fertilized from other iron sources in the region, guided by the surface chl *a* climatology around South Georgia produced by *Borrione and Schlitzer* [2013]. Figure 7 is again the same as Figures 5 and 6, with the colored markers representing the particle locations in September (preceding the start of the bloom). The extent of the fertilized patch around South Georgia changes annually, although to a lesser degree than around Crozet. What does remain almost annually consistent is the north and eastward advection of the particles (with the exception of 2006) and an associated bloom occurring within the Georgia Basin, which is just north of the island. In some of the years, most distinctly in 2004 and 2005, there is a well-defined boundary edge to the trajectories on the western side of the fertilized patch. This sloping western boundary edge is also apparent in the average bloom area in almost all years (2006 being the most apparent exception). The trajectories and bloom are restricted to the east of this boundary due to the eastward flowing PF which acts as a physical barrier [*Moore et al*., 1999; *Korb and Whitehouse*, 2004]. The colored markers represent the particles locations in the month of September, and therefore particles that are released at the beginning of September have only had 1 month to be advected, and consequently are the closest to South Georgia. Focusing just on the recently released particles, from August and September (orange and red), it is apparent that, for the majority of the years, this western boundary of both the fertilized patch and bloom area is an important route for iron to be advected away from South Georgia, flowing toward Shag Rocks and then along the PF. This circulation feature was also found by *Young et al*. [2011] in their higher-resolution regional model, described as a unidirectional link between the two land masses (see their Figure 7).

Table 2. Size of the Annual Bloom and Fertilized Patch Around Crozet, and the Percent of Each Area That is Overlapped by the Other[a]

Year	Bloom Area (km^2)	Fertilized Patch (km^2)	Bloom Overlap (%)	Fertilized Overlap (%)
1998	223,784	216,357	35	36
1999	300,810	251,913	52	62
2000	168,707	259,734	59	38
2001	70,586	231,342	60	18
2002	195,589	238,834	42	34
2003	299,167	232,525	41	52
2004	355,097	252,176	48	67
2005	258,354	246,721	54	56
2006	209,982	244,683	47	40
2007	342,084	282,999	32	39

[a]Bloom Area is the total area of the average (October–December) chl *a* concentration above 0.5 mg m^{-3}; Fertilized Patch is the extent of particle trajectories in September (prior to the start of the bloom); Bloom Overlap is the percent of the bloom area overlapped by the fertilized patch; Fertilized Overlap is the percent of the fertilized patch overlapped by the bloom.

Table 1 provides the size of both the annual blooms and fertilized patches around Kerguelen. As can also be seen in Figure 5, the fertilized patch is much larger than the bloom, and there is more variability in the bloom size than in the fertilized patch. Consequently, the annual percentage of the bloom area that is within the fertilized patch is consistently very high, with an average of 77% (st dev ±6.5). As the fertilized patch is much larger than the bloom area, it would suggest that iron availability is not the only, or at least most important, factor controlling the Kerguelen bloom extent and inter-annual variability. The year 2003 had the largest bloom in our study period, in which the bloom did extend out across and to the southern edges of the fertilized patch. It is possible, that in 2003 the primary limiting factor to the Kerguelen bloom was alleviated so the bloom could extend further out into the regions of available iron. This hypothesis will be considered later in the study.

Looking at Table 2, the Crozet bloom is a third of the size of the Kerguelen bloom, with an average bloom size of 242,416 km^2 compared to the Kerguelen average of 782,455 km^2. Focusing on the percentage of the bloom site overlapped by the trajectories (*Fertilized patch*) for each year, there is a range of 60%–32% overlap. This is reflected in the percentage of the fertilized patch overlapped by the bloom, ranging from 67% to 34%. Both the bloom area and fertilized patch around Crozet vary annually, and Crozet has the lowest overlap out of the three islands studied.

The average size of the South Georgia bloom over 1998–2007 was 618,645 km^2, smaller than the average size of the fertilized patch at 742,038 km^2. In Table 3, we can see a large range in the bloom area around South Georgia across the years, the maximum being 946,833 km^2 in 2002 and the minimum being 414,108 km^2 in 2006 (see Figure 4). There is also a range in the size of the fertilized patch, although not as large as the range in bloom size. Focusing on the amount of overlap between the bloom and trajectories, we see that the annual bloom overlaps are generally larger than the fertilized patch overlaps (2002 and 2003 being the exceptions). This is due to the fertilized patch being larger than the bloom area for the majority of the years. However, as with the other two islands, there is a range in the annual overlaps, which can be explained by a combination of inter-annual variability in the sizes and locations of the annual blooms, and also, to differing degrees for each island, the inter-annual variability in the size and locations of the fertilized patches (Kerguelen being the most consistent, and Crozet exhibiting the most variation).

Table 3. Size of the Annual Bloom and Fertilized Patch Around South Georgia, and the Percent of Each Area That is Overlapped by the Other[a]

Year	Bloom Area (km^2)	Fertilized Patch (km^2)	Bloom Overlap (%)	Fertilized Overlap (%)
1998	527,788	801,679	79	52
1999	671,337	864,382	70	54
2000	453,359	810,443	79	44
2001	560,929	798,532	74	52
2002	946,833	704,231	50	67
2003	854,692	750,085	56	64
2004	587,281	713,427	69	57
2005	626,285	700,466	66	59
2006	414,108	703,676	56	33
2007	543,833	573,456	61	58

[a]Bloom Area is the total area of the average (October–April) chl *a* concentration above 0.5 mg m^{-3}; Fertilized Patch is the extent of particle trajectories in September (prior to the start of the bloom); Bloom Overlap is the percent of the bloom area overlapped by the fertilized patch; Fertilized Overlap is the percent of the fertilized patch overlapped by the bloom.

Figure 8 shows the overlap of the bloom (bloom period average, chl *a* concentration greater than 0.5 mg m^{-3}) by the fertilized patch from each individual monthly release of particles. In the Kerguelen plot, we see a maximum range of around 10–25% between years, in the overlap between monthly releases of particles and the average bloom. The cause of this range is a combination of inter-annual variability in both the advection and bloom extent. In comparison with Figure 5 and Table 1, it is apparent that the highest degree of variability

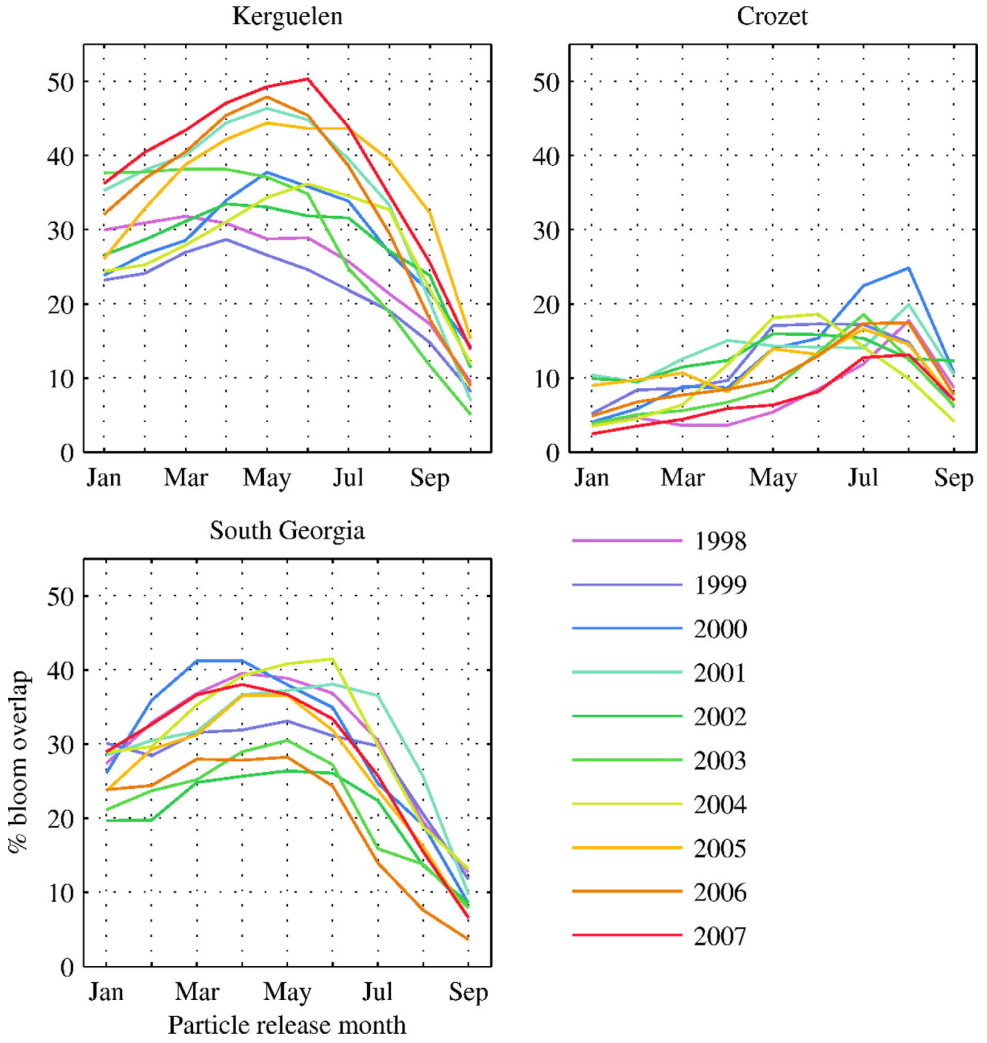

Figure 8. The percent of the bloom area overlapped by Lagrangian trajectories from each monthly release for each year. For each monthly release of particles, trajectories that were within the bloom area, in the month that is prior to the start of the bloom, were recorded and used to calculate the percentage area coverage of the bloom by Lagrangian trajectories. Any particles deeper than 200 m were not included. The *y* axis, *% bloom overlap*, indicates the percentage of the bloom area overlapped by particles from each monthly release shown on the *x* axis, *Particle release month*. Each colored line represents an individual year.

comes from the bloom, although the inter-seasonal variation in advection timing and consequently fertilization could also impact bloom development. Particles released in October, just prior to the start of the bloom, cover around 10–15% of the bloom area, with the maximum bloom coverage from releases in April–June for the majority of the years. This gives an advective fertilization time scale of between 5 and 7 months for maximum bloom coverage. The circulation on the Kerguelen Plateau itself is known to be sluggish, certain parts even described as stagnant [*Park et al.*, 2014]. This localized slow moving water on the plateau (where particles start) may account for the low bloom overlap percentage by particles released just prior to the start of the bloom (November).

In Figure 8, Crozet shows less inter-annual variability than Kerguelen, of less than 10% difference between years. The most apparent difference between Crozet, and the other two islands, is that the advective fertilization time scale is much shorter, with maximum bloom overlap from particles released in June–August, which is 2–4 months prior to the start of the bloom (typically October). However, Crozet has the lowest bloom overlap, with a maximum of 25% from an August release in 2000. For the majority of the years, the maximum percent coverage of the bloom is below 20%.

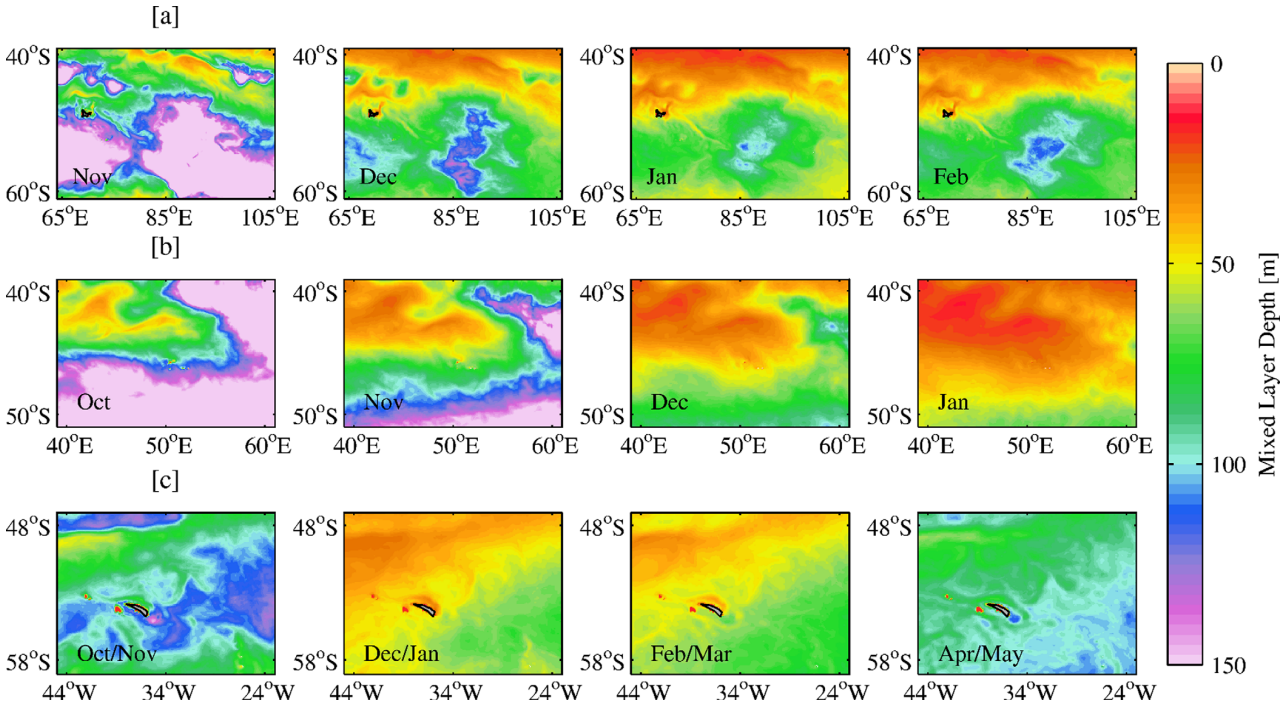

Figure 9. Monthly climatologies (decadal, 1998–2007) of the modeled mixed layer depth, calculated online by the NEMO model, around Kerguelen, Crozet, and South Georgia. The color scale is meter below the surface, with warm colors indicating shallow depths and cold colors representing deeper depths.

The South Georgia plot of Figure 8 shows a degree of consistency in the timing of fertilization, but high variability in the bloom overlap from each monthly release, across the years. The variability in bloom overlap is on the order of 10–15%, and the advective fertilization time scale is roughly April–June, 4–6 months prior to the typical start of the bloom. The maximum percentage bloom overlap is 40%.

4. Discussion

Here we consider other factors that could impact the bloom, light limitation, and nutrient control, before addressing our three main research questions: Can advection explain the extent of the bloom area? Can advection explain the bloom inter-annual variability? And what factors could cause bloom termination?

4.1. Light Limitation

In addition to iron limitation in the Southern Ocean, light limitation also plays an important role in controlling productivity [*Wadley et al*., 2014]. The light levels encountered by phytoplankton cells is partly determined by the mixed layer depth (MLD), as they are vertically mixed between high surface irradiance and low subsurface irradiance (*Venables and Moore* [2010]—explanations and references therein). To assess the light availability around the islands during the typical bloom periods, Figure 9 shows the decadal average monthly depths of the mixed layer, calculated online in the NEMO model, over 1998–2007.

The top row of Figure 9 shows the MLD around Kerguelen which remains in a similar spatial pattern during the bloom period, with a distinct divide between the shallower north and deeper south. During the period 1998–2007, the Kerguelen bloom is constrained to the south of this divide where the MLD is deepest. The middle row shows the MLD around Crozet which exhibits the typical shallowing north to south of the MLD from winter into summer. In Figure 9, the bottom row is a 2 month decadal average of the mixed layer for the South Georgia region. Two months have been averaged together in order to capture the entire bloom period within the plot, from which we can see the typical north to south shallowing of the mixed layer from winter into summer. Both the Kerguelen and Crozet Islands blooms have typically terminated when the mixed layer is shallow enough for there still to be light available, which suggests that neither bloom is terminated by light limitation [*Venables et al*., 2007; *Venables and Moore*, 2010]. The South Georgia bloom,

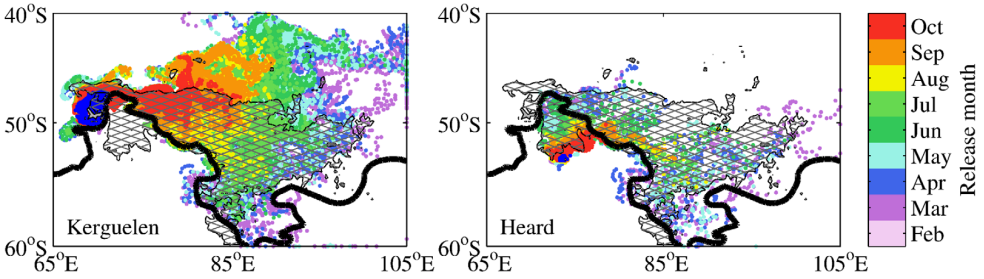

Figure 10. Lagrangian trajectories originating from the Kerguelen and Heard Islands in 2003. Collectively, 8240 particles were released monthly from their starting positions, denoted in blue; however, only every second particle is shown here for clarity. Particle trajectories are depicted by colored markers, with the color of the marker relating to the month in which it was released as indicated by the color bar. Gray hatching represents the bloom area, averaged over November–January, where chlorophyll *a* concentrations are above 0.5 mg m^{-3}. The thick black contour represents the approximate location of the Polar Front in the model for 2003. Only trajectories that are shallower than 200 m are included in this plot.

however, persists for the entire season and typically ends when the mixed layer begins to deepen in winter, strongly indicating that the bloom is terminated by diminishing light, and not by the exhaustion of iron.

4.2. Nutrient Control

The depth of the mixed layer is also significant for the amount of nutrients being brought to the surface from the deep, such as nitrate and silicate as well as iron. WOA climatologies show the concentration of nitrate to be high across much of the Southern Ocean, south of the Subantarctic Front, whereas silicate concentrations decrease rapidly north of the Polar Front [*Boyer et al*., 2013]. At Kerguelen, during the recent KEOPS 2 cruise (October–November 2011), *Lasbleiz et al*. [2014] found higher concentrations of silicate south of the PF at roughly 72°E, close to the plateau.

One possible hypothesis is that silicate is the primary limiting factor controlling the large and highly variable Kerguelen offshore bloom (i.e., longitudinally far away from the plateau), both in spatial extent and interannual variability. This could explain why the bloom is contained to the south (bloom northern limit of 44°S), where a deeper MLD can mix silicate to the surface, despite the iron potentially being advected and available as far north as 40°S (see Figure 5). Many previous Southern Ocean iron fertilization studies, both artificial and natural, have reported the development of a large diatom bloom in the fertilized patch [*Blain et al*., 2001; *de Baar et al*., 2008; *Mongin et al*., 2008] and consequently, in the region of Kerguelen, depletion of silicate over the plateau [*Mosseri et al*., 2008]. The absence of a nondiatom bloom is explained by the efficient grazing of microbial communities by copepods and salps as suggested by *Banse* [1996] and *Smetacek et al*. [2004]. However, the majority of studies have been focused on the bloom above the plateau rather than further downstream, whereas the 2011 KEOPS II cruise focused mainly on the bloom located just northeast of the Kerguelen Islands above the abyssal plain. Their results suggest that the majority of diatom silica production during the bloom event is sustained by "new" silica, supplied primarily from prebloom winter water and also vertical supply. As the bloom progresses, the silicon pump is strengthened by the sinking of biogenic silica, and consequently the standing stock of available silica diminishes over time. Estimates for the duration of the high-productivity bloom period are on the order of 85–86 days, after which the bloom declines [*Mongin et al*., 2008; *Closset et al*., 2014]. These conditions could also be true of the far offshore bloom, which in some years extends further east than 95°S (2003, in Figure 5), but further in situ observations, of both silicate concentrations and bloom composition, would be necessary to either prove or disprove this.

4.3. Can Advection Explain the Extent of the Bloom Area?

Focusing now on the circulation around each island, we discuss if the modeled advection can explain the spatial extent of the island blooms. Our results suggest that iron advected from the Kerguelen and Heard Islands could fertilize an area which overlaps the annual bloom extent, but is actually much larger than the area of the bloom. Figure 10 shows that the bloom which occurs over the plateau (southeast of the Kerguelen Island) is predominately fertilized by iron advected from Heard Island [*Zhang et al*., 2008]. This is in agreement with a water mass pathway study on the plateau using radium isotopes during the 2005 KEOPS

cruise, which also found the water mass on the plateau to have originated from Heard Island [*van Beek et al*., 2008].

We find that the larger bloom event, which extends as far as 100°E in some years, is mostly fertilized by iron advected from Kerguelen Island (see Figure 10), in agreement with *Mongin et al*. [2009] who also performed a modeled advection study on the Kerguelen bloom.

During the recent KEOPS II cruise, iron budgets were calculated focusing on blooms occurring on the plateau, and also offshore in the "plume," which show the importance of a horizontal supply of iron particularly, for the offshore bloom [*Bowie et al*., 2015]. This separation, in the fertilization of the plateau bloom and offshore bloom, is due to the PF which occurs between the two islands, and flows close to the southern and eastern edge of Kerguelen. Using the definition described in *Park et al*. [2014], the thick black contour in Figure 10 represents the modeled location of the PF for the year 2003. The general position and shape of the PF is fairly consistent each year, however the modeled PF does exhibit small annual variations. In Figure 10, it is apparent that the extent of the Kerguelen Island trajectories, and also in 2003 the bloom, is strongly bounded (in the south) by the location of the PF.

The location of the Crozet bloom was different annually, in some years propagating northwest, but most frequently to the north east of the island. The fertilized patch is also predominately to the north east of Crozet, but there are exceptions in some years when small narrow currents flow northwest from the island. Meridionally, both the fertilized patch and consequently bloom area occur northward of the islands, due to the formation of a Taylor Column around the island vicinity [*Popova et al*., 2007]. Zonally, the majority of particles are advected by water which has detrained from a branch of the Subantarctic Front (SAF), and are advected eastward which corresponds with the orange Argo float trajectories in *Pollard et al*. [2007, Figure 5]. Lagrangian particles which are advected westward are entrained into a secondary branch from the main SAF, which flows anticyclonic around Del Cano Rise (blue drifter trajectories in *Pollard et al*., 2007, Figure 5]), before eventually turning eastward at roughly 44°. In Figure 6, we see that the years in which the fertilized patch is propagated to the west (2000, 2002, 2003, and 2007), the particle trajectories are from releases earlier in the year, roughly from January to April. This is due to the water mass north of the island (but south of the SAF) being very sluggish, resulting in particle entrainment into the anticyclonic component of the SAF around Del Cano Rise, taking several months.

The model does show potential iron advection extending into all regions of the Crozet annual bloom areas; however, the fertilized patch in the northwest was never as large as the blooms which occurred in the northwest. *Read et al*. [2007] found that submesoscale features were important in the development and duration of the Crozet bloom, and accounted for the bloom's "patchiness." Though the physical model used in this study is at a very high resolution (1/12°), it cannot reproduce the exact eddy field behavior year-on-year, and therefore we do not expect the annual bloom to match the annual fertilized patch. Considering the stochastic nature of eddies, we believe the model to have demonstrated that the local Crozet advection is sufficient to disperse iron into all annual extents of the bloom. Furthermore, the NEMO modeled Lagrangian pathways are in general agreement with drifter data and also altimetry-based Lagrangian model results [*Pollard et al*., 2007; *Sanial et al*., 2014].

A bloom associated specifically with iron advected from South Georgia is impossible to delineate in this study, as the surrounding region is one of the most productive areas of the Southern Ocean (Figure. 1a), due to various other sources of iron, e.g., the Antarctic Peninsula [*Ardelan et al*., 2010; *Murphy et al*., 2013]. Advection from South Georgia is predominately northward and then eastward, joining with the ACC, overlapping with the annual blooms that occur in the north easterly region of South Georgia [*Korb et al*., 2004]. There is a striking sloped western edge to both the bloom area and fertilized patch in most years, caused by the position of the PF, which is bounded by the local topography [*Moore et al*., 1999]. Between South Georgia and the PF and ACC, the modeled advection was annually consistent and likely to fertilize the annually occurring bloom in this area.

4.4. Can Advection Explain the Bloom Inter-Annual Variability?

The area that could potentially be fertilized with iron via advection around Kerguelen annually extends into a fairly consistent spatial coverage, although there are significant inter-seasonal variations. Despite this, the fertilized patch was much larger than the bloom area in all years of the study period, suggesting that

advection alone cannot explain the blooms inter-annual variability. Focusing on 2003, in Figure 10, we see the open ocean bloom extending as far south as 60°S between a southward and then northward deviation of the PF (creating a v shape). However, in most years, the bloom area does not closely match the fertilized patch, and in no years does the bloom propagate as far north (bloom northern limit of 44°S) as the Lagrangian particles. Assuming that the modeled spread of Lagrangian particles is correct, this would suggest that another factor is limiting the spread of the bloom into all areas of available iron, a factor which could be the predominate driver of the inter-annual variability. This would support the theory of silicate limiting the Kerguelen bloom, but without more silicate concentration observations in the far offshore area we can only speculate.

The Crozet blooms during 1998–2007 show a high degree of inter-annual variability, most frequently extending far to the east, but in some years to the west and on occasion extending further north than typical. Our results find a similar degree of inter-annual variability in the modeled local circulation around Crozet, both in the timing of fertilization (i.e., the speed of advection) and the extent of the fertilized patch (i.e., size and direction of patch). Although the fertilized patch in our model does not closely match the observed blooms, our results do suggest that iron advection could predominately control the inter-annual variability seen in the Crozet bloom.

The advection of iron from South Georgia annually covers a similar region (a predominately north, then eastward flow), although there are exceptions. The time scale for fertilization is highly variable (distance traveled from the iron source out into the bloom area per month), which could have an impact on the bloom.

4.5. Factors Controlling Bloom Termination

As the NEMO model offers a range of diagnostics, we can also propose possible bloom termination mechanisms for each island. In the modeled MLD data, the region surrounding Kerguelen does not clearly follow the north to south shallowing of the MLD in summer typical of the Southern Ocean (Figure 9a). There is a very clear divide in the depths of the mixed layer between the shallower north and deeper south at roughly 45°S–50°S. The Kerguelen bloom is always to the south of 45°S, however, in the WOA data set, there is nitrate available north of this, as well as iron according to our advection results (Figure. 5). Additionally, the WOA nitrate concentration is still high in February, so it is unlikely to be nitrate exhaustion that terminates the bloom. We conjecture that as the bloom is constrained to regions with a deep mixed layer, it is dependent on a deep supply of silicate as suggested by *Mongin et al*. [2008], and found to be the case by *Closset et al*. [2014] in the bloom just offshore of the plateau. There is partial evidence from the WOA that the surface silicate concentration downstream of Kerguelen is lower in February, than in the previous 3 months, however, this is based upon very few data. Looking at data from the first KEOPS cruise, Figure 1 in the supplementary material of *Blain et al*. [2007] shows the concentrations of both nitrate and silicate from locations inside and outside of the bloom. It shows that inside the bloom there is no silicate but there is nitrate, whereas outside the bloom there is plenty of both, suggesting silicate to be the limiting nutrient. This suggests that the sampling conducted during the KEOPS II expedition close to the plateau [*Closset et al*., 2014] needs to be repeated further downstream in future field work in order to determine whether the offshore bloom has similar dynamics longitudinally.

The modeled monthly MLD around the Crozet region does exhibit some inter-annual variability, but typically, shallows north to south from winter into summer, and is shallower than 50 m by the end of the Crozet bloom. However, the WOA climatology suggests that there is still nitrate available in January, which suggests that iron exhaustion most likely terminates the bloom. This is supported by an experiment performed on the CROZEX cruise, where the addition of iron to an area of bloom decline resulted in the stimulation of further phytoplankton growth [*Moore et al*., 2007].

The South Georgia bloom is the most variable in this study, varying in both timing and extent. The decadal average bloom period is from October to April, although it can last longer and also start earlier in some years. The nitrate concentration remains high throughout the bloom period, which suggests that a deepening mixed layer being the limiting factor for the otherwise persistent South Georgia bloom. This is supported by *Korb et al*. [2008], who found evidence of a persistent supply of both macronutrients and iron, by physical processes, to the area throughout the growing season.

5. Conclusions

In the high-nutrient, low-chlorophyll Southern Ocean [*Martin et al*., 1990; *de Baar et al*., 1995; *Boyd et al*., 2007], blooms are observed in satellite ocean color data occurring annually downstream of Kerguelen, Crozet, and the South Georgia Islands. It is generally accepted that the iron limitation prevailing across the Southern Ocean is locally overcome by the horizontal advection of iron from island sources [*Blain et al*., 2001; *Murphy et al*., 2013; *Sanial et al*., 2014]. In this study, Lagrangian particle tracking, with the NEMO 1/12° ocean general circulation model, was used to assess whether potential iron advection can explain the extent of the blooms, and also their inter-annual variability over the period 1998–2007. We also use the modeled circulation and diagnostic variables to consider possible causes of bloom termination for each of the islands.

We find that lateral advection downstream of the Southern Ocean islands is sufficient to fertilize all areas where annual blooms can occur. The patch fertilized by iron-rich water from Kerguelen is much larger in extent than the area of the bloom, whereas the patch fertilized around Crozet is comparable in size, taking into account inter-annual variability, to the size of the bloom. The patch of water fertilized by iron-rich South Georgia sediments also closely matches with the annual bloom, however, delineating a bloom associated only with South Georgia proved problematic.

The advection around Kerguelen was consistent in spatial extent annually, however, the timing of potential fertilization varied inter-seasonally across the years. This could contribute to the blooms inter-annual variability, however, the results suggest that the far offshore Kerguelen bloom (in some years occurring as far east as 100°E) has another primary factor controlling its inter-annual variability, and we offer the hypothesis of silicate being the ultimate limiting factor on a diatom-dominated Kerguelen bloom. This hypothesis could be tested with in situ nutrient sampling of the area, similar to the recent KEOPS II expedition [*Closset et al*., 2014], or alternatively by a high-resolution coupled biogeochemical model to properly resolve the key biogeochemical and physical processes. The results suggest that the inter-annual variability seen in the Crozet bloom can be explained by variations in the advected iron supply. The fertilized patch around South Georgia was fairly consistent spatially, however, it did have variations in the timing of advection from the island out to the bloom site. This potentially could account for the inter-annual variability seen in the South Georgia bloom.

In assessing the possible causes of bloom termination, we find that nutrient exhaustion is most likely to cause the Kerguelen and Crozet blooms to collapse (silica and iron, respectively). Whereas winter convection causing the mixed layer to deepen is most likely the terminating factor of the South Georgia bloom, as physical processes maintain a continual supply of macronutrients and iron to the area, these are unlikely to be limiting [*Korb et al*., 2008]. Typically, both the Kerguelen and Crozet blooms end well before the mixed layer begins to deepen in winter, whereas the South Georgia bloom persists for the entire season until the mixed layer deepens.

Acknowledgments
The velocity altimeter products were produced by Ssalto/Duacs and distributed by Aviso, with support from CNES (http://www.aviso.oceanobs.com/duacs/). Ocean Colour Climate Change Initiative data set, Version 2.0, European Space Agency, available online at http://www.esa-oceancolour-cci.org/. This study was carried out using the computational tool Ariane, developed by B. Blanke and N. Grima. The 1/12°S NEMO simulation used in this work was produced using the ARCHER UK National Supercomputing Service (http://www.archer.ac.uk). This work was funded by the UK Natural Environment Research Council through a PhD studentship for J.R. (NE/K500938/1), and National Capability Funding for E.E.P., M.A.S., and A.Y. The data presented in this study can be obtained by contacting the lead author. The authors would like to thank Phillip Boyd and Eugene Murphy, for their feedback which greatly improved the work.

References

Abraham, E. R., C. S. Law, P. W. Boyd, S. J. Lavender, M. T. Maldonado, and A. R. Bowie (2000), Importance of stirring in the development of an iron-fertilized phytoplankton bloom, *Nature*, *407*(6805), 727–730, doi:10.1038/35037555.

Ardelan, M. V., O. Holm-Hansen, C. D. Hewes, C. S. Reiss, N. S. Silva, H. Dulaiova, E. Steinnes, and E. Sakshaug (2010), Natural iron enrichment around the Antarctic Peninsula in the Southern Ocean, *Biogeosciences*, *7*(1), 11–25.

Atkinson, A., M. J. Whitehouse, J. Priddle, G. C. Cripps, P. Ward, and M. A. Brandon (2001), The pelagic ecosystem of South Georgia, Antarctica, *Mar. Ecol. Prog. Ser.*, *216*, 279–308.

Aviso (2014), *SSALTO/DUACS User Handbook: (M)SLA and (M)ADT Near–Real Time and Delayed Time Products*, CLS–DOS–NT–06–034, SALP–MU–P–EA–21065–CLS, 59 pp., Cent. Natl. D'études Spatiales, Ramonville St. Agne, France. [Available at http://www.aviso.altimetry.fr/fileadmin/documents/data/tools/hdbk_duacs.pdf.]

Bakker, D. C., M. C. Nielsdottir, P. J. Morris, H. J. Venables, and A. J. Watson (2007), The island mass effect and biological carbon uptake for the subantarctic Crozet Archipelago, *Deep Sea Res., Part II*, *54*, 2174–2190, doi:10.1016/j.dsr2.2007.06.009.

Banse, K. (1996), Low seasonality of low concentrations of surface chlorophyll in the Subantarctic water ring: Underwater irradiance, iron, or grazing?, *Prog. Oceanogr.*, *37*(3-4), 241–291.

Blain, S., et al. (2001), A biogeochemical study of the island mass effect in the context of the iron hypothesis: Kerguelen Islands, Southern Ocean, *Deep Sea Res., Part I*, *48*(1), 163–187, doi:10.1016/S0967-0637(00)00047-9.

Blain, S., et al. (2007), Effect of natural iron fertilization on carbon sequestration in the Southern Ocean, *Nature*, *446*(7139), 1070–1074, doi:10.1038/nature05700.

Blain, S., B. Quguiner, and T. Trull (2008), The natural iron fertilization experiment KEOPS (KErguelen Ocean and Plateau compared Study): An overview, *Deep Sea Res., Part II*, *55*(5–7), 559–565, doi:10.1016/j.dsr2.2008.01.002.

Blanke, B., and S. Raynaud (1997), Kinematics of the Pacific Equatorial Undercurrent: An Eulerian and Lagrangian approach from GCM results, *J. Phys. Oceanogr.*, *27*(6), 1038–1053, doi:10.1175/1520-0485.
Blanke, B., M. Arhan, G. Madec, and S. Roche (1999), Warm water paths in the equatorial Atlantic as diagnosed with a general circulation model, *J. Phys. Oceanogr.*, *29*, 2753–2768.
Borrione, I., and R. Schlitzer (2013), Distribution and recurrence of phytoplankton blooms around South Georgia, Southern Ocean, *Biogeosciences*, *10*(1), 217–231, doi:10.5194/bg-10-217-2013.
Bowie, A. R., et al. (2015), Iron budgets for three distinct biogeochemical sites around the Kerguelen Archipelago (Southern Ocean) during the natural fertilization study, KEOPS-2, *Biogeosciences*, *12*(14), 4421–4445, doi:10.5194/bg-12-4421-2015.
Boyd, P. W. (2002), Environmental factors controlling phytoplankton processes in the Southern Ocean, *J. Phycol.*, *38*(5), 844–861, doi:10.1046/j.1529-8817.2002.t01-1-01203.x.
Boyd, P. W. (2007), Biogeochemistry: Iron findings, *Nature*, *446*(7139), 989–991, doi:10.1038/446989a.
Boyd, P. W., and M. J. Ellwood (2010), The biogeochemical cycle of iron in the ocean, *Nat. Geosci.*, *3*(10), 675–682, doi:10.1038/ngeo964.
Boyd, P. W., et al. (2000), A mesoscale phytoplankton bloom in the polar Southern Ocean stimulated by iron fertilization, *Nature*, *407*(6805), 695–702, doi:10.1038/35037500.
Boyd, P. W., et al. (2007), Mesoscale iron enrichment experiments 1993–2005: Synthesis and future directions, *Science*, *315*(5812), 612–617, doi:10.1126/science.1131669.
Boyd, P. W., K. R. Arrigo, R. Strzepek, and G. L. van Dijken (2012a), Mapping phytoplankton iron utilization: Insights into Southern Ocean supply mechanisms, *J. Geophys. Res.*, *117*, C06009, doi:10.1029/2011JC007726.
Boyd, P. W., D. C. E. Bakker, and C. Chandler (2012b), A new database to explore the findings from large–scale ocean iron enrichments experiments, *Oceanography*, *25*(4), 64–71, doi:10.5670/oceanog.2012.104.
Boyer, T. P., et al. (2013), World Ocean Database 2013, in *Sydney Levitus*, edited by A. Mishonov, and NOAA Atlas NESDIS 72, 209 pp, doi:10.7289/V5NZ85MT.
Brodeau, L., B. Barnier, A.-M. Treguier, T. Penduff, and S. Gulev (2010) An ERA40-based 461 atmospheric forcing for global ocean circulation models, *Ocean Model.*, *31*, 88–104.
Closset, I., M. Lasbleiz, K. Leblanc, B. Quguiner, A. J. Cavagna, M. Elskens, J. Navez, and D. Cardinal (2014), Seasonal evolution of net and regenerated silica production around a natural Fe-fertilized area in the Southern Ocean estimated with Si isotopic approaches, *Biogeosciences*, *11*(20), 5827–5846, doi:10.5194/bg-11-5827-2014.
Comiso, J. C., C. R. McClain, C. W. Sullivan, J. P. Ryan, and C. L. Leonard (1993), Coastal zone color scanner pigment concentrations in the Southern Ocean and relationships to geophysical surface features, *J. Geophys. Res.*, *98*(C2), 2419–2451, doi:10.1029/92JC02505.
de Baar, H. J., J. T. M. de Jong, D. C. Bakker, B. M. Loscher, C. Veth, U. Bathmann, and V. Smetacek (1995), Importance of iron for plankton blooms and carbon dioxide drawdown in the Southern Ocean, *Nature*, *373*, 412–415, doi:10.1038/373412a0.
de Baar, H. J. W., L. J. A. Gerringa, P. Laan, and K. R. Timmermans (2008), Efficiency of carbon removal per added iron in ocean iron fertilization, *Mar. Ecol. Prog. Ser.*, *364*, 269–282, doi:10.3354/meps07548.
d'Ovidio, F., A. Della Penna, T. W. Trull, F. Nencioli, M. I. Pujol, M. H. Rio, Y. H. Park, C. Cott, M. Zhou, and S. Blain (2015), The biogeochemical structuring role of horizontal stirring: Lagrangian perspectives on iron delivery downstream of the Kerguelen Plateau, *Biogeosciences*, *12*(19), 5567–5581, doi:10.5194/bg-12-5567-2015.
Gille, S. T., M. M. Carranza, and R. Cambra (2014), Wind-induced upwelling in the Kerguelen Plateau region, *Biogeosciences*, *11*(22), 6389–6400, doi:10.5194/bg-11-6389-2014.
Graham, R. M., A. M. De Boer, E. van Sebille, K. E. Kohfeld, and C. Schlosser (2015), Inferring source regions and supply mechanisms of iron in the Southern Ocean from satellite chlorophyll data, *Deep Sea Res., Part I*, *104*, 9–25, doi:10.1016/j.dsr.2015.05.007.
Hewes, C. D., C. S. Reiss, M. Kahru, B. G. Mitchell, and O. Holm–Hansen (2008), Control of phytoplankton biomass by dilution and mixed layer depth in the western Weddell–Scotia Confluence, *Mar. Ecol. Prog. Ser.*, *366*, 15–29, doi:10.3354/meps07515.
Holm-Hansen, O., M. Kahru, and C. D. Hewes (2005), Deep chlorophyll a maxima (DCMs) in pelagic Antarctic waters. II. Relation to bathymetric features and dissolved iron concentrations, *Mar. Ecol. Prog. Ser.*, *297*, 71–81.
Korb, R. E., and M. Whitehouse (2004), Contrasting primary production regimes around South Georgia, Southern Ocean: Large blooms versus high nutrient, low chlorophyll waters, *Deep Sea Res., Part I*, *51*(5), 721–738, doi:10.1016/j.dsr.2004.02.006.
Korb, R. E., M. J. Whitehouse, and P. Ward (2004), SeaWiFS in the southern ocean: Spatial and temporal variability in phytoplankton biomass around South Georgia, *Deep Sea Res., Part II*, *51*, 99–116, doi:10.1016/j.dsr2.2003.04.002.
Korb, R. E., M. J. Whitehouse, A. Atkinson, and S. E. Thorpe (2008), Magnitude and maintenance of the phytoplankton bloom at South Georgia: A naturally iron-replete environment, *Mar. Ecol. Prog. Ser.*, *368*, 75–91, doi:10.3354/meps07525.
Lasbleiz, M., K. Leblanc, S. Blain, J. Ras, V. Cornet-Barthaux, S. Hlias Nunige, and B. Quguiner (2014), Pigments, elemental composition (C, N, P, and Si), and stoichiometry of particulate matter in the naturally iron fertilized region of Kerguelen in the Southern Ocean, *Biogeosciences*, *11*(20), 5931–5955, doi:10.5194/bg-11-5931-2014.
Le Bars, D., J. V. Durgadoo, H. A. Dijkstra, A. Biastoch, and W. P. M. De Ruijter (2014), An observed 20–year time series of Agulhas leakage, *Ocean Sci.*, *10*(4), 601–609, doi:10.5194/os-10-601-2014.
Madec, G. (2008), NEMO reference manual, ocean dynamic component: NEMO–OPA, Notes du pole de modelisation, *Tech. Rep. 27*, Inst. Pierre Simmon Laplace, Paris.
Martin, J. H., R. M. Gordon, and S. E. Fitzwater (1990), Iron in Antarctic waters, *Nature*, *345*(6271), 156–158, doi:10.1038/345156a0.
Martin, J. M. (1990), Glacial-interglacial CO_2 change: The iron hypothesis, *Paleoceanography*, *5*(1), 1–13.
Marzocchi, A., J. J.-M. Hirschi, N. P. Holliday, S. A. Cunningham, A. T. Blaker, and A. C. Coward (2015), The North Atlantic subpolar circulation in an eddy–resolving global ocean model, *J. Mar. Syst.*, *142*, 126–143, doi:10.1016/j.jmarsys.2014.10.007.
Meredith, M. P., J. L. Watkins, E. J. Murphy, N. J. Cunningham, A. G. Wood, R. Korb, M. J. Whitehouse, S. E. Thorpe, and F. Vivier (2003), An anticyclonic circulation above the Northwest Georgia Rise, Southern Ocean, *Geophys. Res. Lett.*, *30*(20), 2061, doi:10.1029/2003GL018039.
Mongin, M., E. Molina, and T. W. Trull (2008), Seasonality and scale of the Kerguelen plateau phytoplankton bloom: A remote sensing and modeling analysis of the influence of natural iron fertilization in the Southern Ocean, *Deep Sea Res., Part II*, *55*(5–7), 880–892, doi:10.1016/j.dsr2.2007.12.039.
Mongin, M. M., E. R. Abraham, and T. W. Trull (2009), Winter advection of iron can explain the summer phytoplankton bloom that extends 1000 km downstream of the Kerguelen Plateau in the Southern Ocean, *J. Mar. Res.*, *67*, 225–237.
Moore, C. M., S. Seeyave, A. E. Hickman, J. T. Allen, M. I. Lucas, H. Planquette, R. T. Pollard, and A. J. Poulton (2007), Iron–light interactions during the CROZet natural iron bloom and EXport experiment (CROZEX) I: Phytoplankton growth and photophysiology, *Deep Sea Res., Part II*, *54*(18–20), 2045–2065, doi:10.1016/j.dsr2.2007.06.011.

Moore, J. K., and M. R. Abbott (2000), Phytoplankton chlorophyll distributions and primary production in the Southern Ocean, *J. Geophys. Res.*, *105*(C12), 28,709–28,722, doi:10.1029/1999JC000043.
Moore, J. K., M. R. Abbott, and J. G. Richman (1999), Location and dynamics of the Antarctic Polar Front from satellite sea surface temperature data, *J. Geophys. Res.*, *104*(C2), 3059, doi:10.1029/1998JC900032.
Mosseri, J., B. Quguiner, L. Armand, and V. Cornet-Barthaux (2008), Impact of iron on silicon utilization by diatoms in the Southern Ocean: A case study of Si/N cycle decoupling in a naturally iron–enriched area, *Deep Sea Res., Part II*, *55*(5–7), 801–819, doi:10.1016/j.dsr2.2007.12.003.
Murphy, E. J., et al. (2013), Comparison of the structure and function of Southern Ocean regional ecosystems: The Antarctic Peninsula and South Georgia, *J. Mar. Syst.*, *109–110*, 22–42, doi:10.1016/j.jmarsys.2012.03.011.
Orsi, A. H., T. Whitworth III, and W. D. Nowlin Jr. (1995), On the meridional extent and fronts of the Antarctic Circumpolar Current, *Deep Sea Res., Part I*, *42*(5), 641–673.
Park, Y.-H., J.-L. Fuda, I. Durand, and A. C. Naveira Garabato (2008a), Internal tides and vertical mixing over the Kerguelen Plateau, *Deep Sea Res., Part II*, *55* (5-7), 582–593, doi:10.1016/j.dsr2.2007.12.027.
Park, Y.-H., F. Roquet, I. Durand, and J.-L. Fuda (2008b), Large–scale circulation over and around the Northern Kerguelen Plateau, *Deep Sea Res., Part II*, *55*(5–7), 566–581, doi:10.1016/j.dsr2.2007.12.030.
Park, Y.-H., I. Durand, E. Kestenare, G. Rougier, M. Zhou, F. d'Ovidio, C. Cott, and J.-H. Lee (2014), Polar Front around the Kerguelen Islands: An up-to-date determination and associated circulation of surface/subsurface waters, *J. Geophys. Res. Oceans*, *119*, 6575–6592, doi:10.1002/2014JC010061.
Planquette, H., et al. (2007), Dissolved iron in the vicinity of the Crozet Islands, Southern Ocean, *Deep Sea Res., Part II*, *54*, 1999–2019, doi:10.1016/j.dsr2.2007.06.019.
Pollard, R., R. Sanders, M. Lucas, and P. Statham (2007), The Crozet Natural Iron Bloom and Export Experiment (CROZEX), *Deep Sea Res., Part II*, *54*(18–20), 1905–1914, doi:10.1016/j.dsr2.2007.07.023.
Pollard, R. T., H. J. Venables, J. F. Read, and J. T. Allen (2007), Large–scale circulation around the Crozet Plateau controls an annual phytoplankton bloom in the Crozet Basin, *Deep Sea Res., Part II*, *54*, 1915–1929, doi:10.1016/j.dsr2.2007.06.012.
Pollard, R. T., et al. (2009), Southern Ocean deep-water carbon export enhanced by natural iron fertilization, *Nature*, *457*(7229), 577–580, doi:10.1038/nature07716.
Popova, E. E., R. T. Pollard, M. I. Lucas, H. J. Venables, and T. R. Anderson (2007), Real-time forecasting of ecosystem dynamics during the CROZEX experiment and the roles of light, iron, silicate, and circulation, *Deep Sea Res., Part II*, *54*(18-20), 1966–1988, doi:10.1016/j.dsr2.2007.06.018.
Popova, E. E., A. Yool, Y. Aksenov, and A. C. Coward (2013), Role of advection in Arctic Ocean lower trophic dynamics: A modeling perspective, *J. Geophys. Res. Oceans*, *118*, 1571–1586, doi:10.1002/jgrc.20126.
Poulton, A. J., C. Mark Moore, S. Seeyave, M. I. Lucas, S. Fielding, and P. Ward (2007), Phytoplankton community composition around the Crozet Plateau, with emphasis on diatoms and Phaeocystis, *Deep Sea Res., Part II*, *54*(18-20), 2085–2105, doi:10.1016/j.dsr2.2007.06.005.
Read, J. F., R. T. Pollard, and J. T. Allen (2007), Sub–mesoscale structure and the development of an eddy in the Subantarctic Front north of the Crozet Islands, *Deep Sea Res., Part II*, *54*(18–20), 1930–1948, doi:10.1016/j.dsr2.2007.06.013.
Robinson, J., E. E. Popova, A. Yool, M. Srokosz, R. S. Lampitt, and J. R. Blundell (2014), How deep is deep enough? Ocean iron fertilization and carbon sequestration in the Southern Ocean, *Geophys. Res. Lett.*, *41*, 2489–2495, doi:10.1002/2013GL058799.
Sanial, V., P. van Beek, B. Lansard, F. d'Ovidio, E. Kestenare, M. Souhaut, M. Zhou, and S. Blain (2014), Study of the phytoplankton plume dynamics off the Crozet Islands (Southern Ocean): A geochemical-physical coupled approach, *J. Geophys. Res. Oceans*, *119*, 2227–2237, doi:10.1002/2013JC009305.
Schallenberg, C., P. van der Merwe, F. Chever, J. T. Cullen, D. Lannuzel, and A. R. Bowie (2016), Dissolved iron and iron(II) distributions beneath the pack ice in the East Antarctic (120°E) during the winter/spring transition, *Deep Sea Res., Part II*, doi:10.1016/j.dsr2.2015.02.019, in press.
Shaked, Y., and H. Lis (2012), Disassembling iron availability to phytoplankton, *Frontiers Microbiol.*, *3*(123), 1–26, doi:10.3389/fmicb.2012.00123.
Smetacek, V., P. Assmy, and J. Henjes (2004), The role of grazing in structuring Southern Ocean pelagic ecosystems and biogeochemical cycles, *Antarct. Sci.*, *16*(4), 541–558, doi:10.1017/S0954102004002317.
Srokosz, M. A., J. Robinson, H. McGrain, E. E. Popova, and A. Yool (2015), Could the Madagascar bloom be fertilized by Madagascan iron?, *J. Geophys. Res. Oceans*, *120*, 5790–5803, doi:10.1002/2015JC011075.
Storm, T., M. Boettcher, M. Grant, M. Zuhlke, N. Fomferra, T. Jackson, and S. Sathyendranath (2013), Product user guide, in *Ocean Colour Climate Change Initiative (OC_CCI)—Phase One*, edited by S. Groom, Plymouth Mar. Lab., 14 pp., Plymouth, U. K.
Tagliabue, A., J.-B. Salle, A. R. Bowie, M. Lvy, S. Swart, and P. W. Boyd (2014), Surface-water iron supplies in the Southern Ocean sustained by deep winter mixing, *Nat. Geosci.*, *7*(4), 314–320, doi:10.1038/ngeo2101.
Takahashi, T., et al. (2009), Climatological mean and decadal change in surface ocean pCO_2, and net sea–air CO_2 flux over the global oceans, *Deep Sea Res., Part II*, *56*(8-10), 554–577, doi:10.1016/j.dsr2.2008.12.009.
Thomalla, S. J., N. Fauchereau, S. Swart, and P. M. S. Monteiro (2011), Regional scale characteristics of the seasonal cycle of chlorophyll in the Southern Ocean, *Biogeosciences*, *8*(10), 2849–2866, doi:10.5194/bg-8-2849-2011.
Tripathy, S. C., S. Pavithran, P. Sabu, H. U. K. Pillai, D. R. G. Dessai, and N. Anilkumar (2015), Deep chlorophyll maximum and primary productivity in Indian Ocean sector of the Southern Ocean: Case study in the Subtropical and Polar Front during austral summer 2011, *Deep Sea Res., Part II*, *118*, 240–249, doi:10.1016/j.dsr2.2015.01.004.
Tyrrell, T., A. Merico, J. J. Waniek, C. S. Wong, N. Metzl, and F. Whitney (2005), Effect of seafloor depth on phytoplankton blooms in high-nitrate, low-chlorophyll (HNLC) regions, *J. Geophys. Res.*, *110*, G02007, doi:10.1029/2005JG000041.
van Beek, P., M. Bourquin, J. L. Reyss, M. Souhaut, M. A. Charette, and C. Jeandel (2008), Radium isotopes to investigate the water mass pathways on the Kerguelen Plateau (Southern Ocean), *Deep Sea Res., Part II*, *55*(5–7), 622–637, doi:10.1016/j.dsr2.2007.12.025.
van der Merwe, P., et al. (2015), Sourcing the iron in the naturally fertilised bloom around the Kerguelen Plateau: Particulate trace metal dynamics, *Biogeosciences*, *12*(3), 739–755, doi:10.5194/bg-12-739-2015.
Venables, H., and C. M. Moore (2010), Phytoplankton and light limitation in the Southern Ocean: Learning from high-nutrient, high-chlorophyll areas, *J. Geophys. Res.*, *115*, C02015, doi:10.1029/2009JC005361.
Venables, H. J., R. T. Pollard, and E. E. Popova (2007), Physical conditions controlling the development of a regular phytoplankton bloom north of the Crozet Plateau, Southern Ocean, *Deep Sea Res., Part II*, *54*, 1949–1965, doi:10.1016/j.dsr2.2007.06.014.
Wadley, M. R., T. D. Jickells, and K. J. Heywood (2014), The role of iron sources and transport for Southern Ocean productivity, *Deep Sea Res., Part I*, *87*, 82–94, doi:10.1016/j.dsr.2014.02.003.

Ward, P., M. Whitehouse, R. Shreeve, S. Thorpe, A. Atkinson, R. Korb, D. Pond, and E. Young (2007), Plankton community structure south and west of South Georgia (Southern Ocean): Links with production and physical forcing, *Deep Sea Res., Part I*, *54*, 1871–1889, doi: 10.1016/j.dsr.2007.08.008.

Young, E. F., M. P. Meredith, E. J. Murphy, and G. R. Carvalho (2011), High-resolution modelling of the shelf and open ocean adjacent to South Georgia, Southern Ocean, *Deep Sea Res., Part II*, *58*, 1540–1552, doi:10.1016/j.dsr2.2009.11.003.

Young, E. F., S. E. Thorpe, N. Banglawala, and E. J. Murphy (2014), Variability in transport pathways on and around the South Georgia shelf, Southern Ocean: Implications for recruitment and retention, *J. Geophys. Res. Oceans*, *119*, 241–252, doi:10.1002/2013JC009348.

Zhang, Y., F. Lacan, and C. Jeandel (2008), Dissolved rare earth elements tracing lithogenic inputs over the Kerguelen Plateau (Southern Ocean), *Deep Sea Res., Part II*, *55*, 638–652, doi:10.1016/j.dsr2.2007.12.029.

E.5 Far–field connectivity of the UK's four largest marine protected areas: Four of a kind?

AGU PUBLICATIONS

Earth's Future

RESEARCH ARTICLE
10.1002/2016EF000516

Special Section:
Assessing Risk Governance Performance in the Face of Global Change

Far-field connectivity of the UK's four largest marine protected areas: Four of a kind?

J. Robinson[1,2], A. L. New[1], E. E. Popova[1], M. A. Srokosz[1], and A. Yool[1]

[1]National Oceanography Centre, University of Southampton Waterfront Campus, Southampton, UK, [2]Ocean and Earth Science, National Oceanography Centre Southampton, University of Southampton Waterfront Campus, Southampton, UK

Abstract Marine Protected Areas (MPAs) are established to conserve important ecosystems and protect marine species threatened in the wider ocean. However, even MPAs in remote areas are not wholly isolated from anthropogenic impacts. "Upstream" activities, possibly thousands of kilometers away, can influence MPAs through ocean currents that determine their connectivity. Persistent pollutants, such as plastics, can be transported from neighboring shelf regions to MPAs, or an ecosystem may be affected if larval dispersal is reduced from a seemingly remote upstream area. Thus, improved understanding of exactly where upstream is, and on what timescale it is connected, is important for protecting and monitoring MPAs. Here, we use a high-resolution (1/12°) ocean general circulation model and Lagrangian particle tracking to diagnose the connectivity of four of the UK's largest MPAs: Pitcairn; South Georgia and Sandwich Islands; Ascension; and the British Indian Ocean Territory (BIOT). We introduce the idea of a circulation "connectivity footprint", by which MPAs are connected to upstream areas. Annual connectivity footprints were calculated for the four MPAs, taking into account seasonal and inter-annual variability. These footprints showed that, on annual timescales, Pitcairn was not connected with land, whereas there was increasing connectivity for waters reaching South Georgia, Ascension, and, especially, BIOT. BIOT also had a high degree of both seasonal and inter-annual variability, which drastically changed its footprint, year-to-year. We advocate that such connectivity footprints are an inherent property of all MPAs, and need to be considered when MPAs are first proposed or their viability as refuges evaluated.

Plain Language Summary Marine Protected Areas (MPAs) are typically established to conserve important ecosystems and protect marine species. However, even remote MPAs are not wholly isolated from impacts elsewhere, and can be connected via energetic ocean currents to impacts in "upstream areas" hundreds or even thousands of kilometres away. For instance, separate populations of marine species can be connected through larval dispersal by ocean currents, such that negative ecosystem impacts—overfishing or pollution—in a seemingly remote location may drastically affect a MPA. Here, we present "connectivity footprints" of four UK MPAs using a Lagrangian particle-tracking technique within a high-resolution ocean model, and evaluate their connectivity with land. At the 1-year timescale, Pitcairn is essentially unconnected with land, whereas the South Georgia, Ascension and BIOT MPAs are increasingly connected with remote land, with variability (seasonal and interannual) notably high for BIOT. In terms of exposure to pollution, we also consider the population density of connected coastlines, and identify this as an important risk factor in the management of MPAs. We advocate connectivity footprints of MPAs as a tool to improve future MPA designation, and in spatial planning of current MPA networks, and we suggest future work to better diagnose connectivity of MPAs.

Key Points:
- Marine protected areas (MPAs), set up to protect endangered species, are vulnerable to upstream impacts from land due to ocean circulation
- Particle-tracking simulations show the land connectivity of four major British MPAs and give a "connectivity footprint" at annual timescales
- Connectivity to land differs substantially between MPAs with strong seasonal/inter-annual variability showing the utility of the footprints

Supporting Information:
- Supporting Information S1

Corresponding author:
A. Yool, axy@noc.ac.uk

Citation:
Robinson, J., A. L. New, E. E. Popova, M. A. Srokosz, and A. Yool (2017), Far-field connectivity of the UK's four largest marine protected areas: Four of a kind?, *Earth's Future*, *5*, doi:10.1002/2016EF000516.

Received 6 DEC 2016
Accepted 5 APR 2017
Accepted article online 13 APR 2017

1. Introduction

The world's oceans were once widely considered to be an inexhaustible resource, and consequently undervalued. However, it is now clear that the health of various ecosystems, and the fishery assets that they support, are deteriorating [*Mills et al.,* 2013; *Doney et al.*, 2014]. Global trends in world fisheries show a marked decline since the late 1980s, with over 500 species added to the Red List of Threatened Species of International Union for Conservation of Nature (IUCN)—the World Conservation Union [*The World Bank*, 2006; and references therein]. Consequently, food security issues are mounting with vulnerable communities in developing countries worst affected [*Watson and Pauly*, 2001; *Pauly et al.*, 2005; *Golden et al*., 2016].

In response to this danger, and the mounting threat of climate change, new marine management and novel biodiversity conservation efforts are being developed and deployed worldwide in order to curb the negative trends [*Halpern et al.*, 2008; *Day et al.*, 2012; *Barner et al.*, 2015]. One such management tool is marine protected areas (MPAs), the definition of which varies considerably internationally, but a basic premise given by the IUCN describes "a clearly defined geographical space, recognized, dedicated and managed, through legal or other effective means, to achieve the long-term conservation of nature with associated ecosystem services and cultural values" [*Dudley*, 2008, p. 60]. The biodiversity, conservation, and fishery goals associated with MPAs are numerous and wide ranging, including habitat and biodiversity protection, ecosystem restoration, improved or restored fishery, the maintenance of spawning stock and spillover benefits into fishing grounds [*Christie and White*, 2007]. To validate the IUCN definition and realize these goals, it is necessary to minimize the impact of human activities on the MPAs, primarily achieved through designating "no-take zones" to either completely stop or sustainably manage fishing in the area [*Edgar et al.*, 2014].

An important component of the MPA framework is the areas' connectivity with its surroundings. In the marine environment, connectivity plays a much more important role than on land, as in the ocean everything is connected over long timescales [*Jonsson and Watson*, 2016]. Much work has gone into diagnosing biological outcomes of the downstream connectivity of MPAs, as it informs whether MPAs are successful in achieving conservation goals, such as seeding species in other areas, and also directs spatial management for further conservation efforts [*Fogarty and Botsford*, 2007; *Christie et al.*, 2010]. In order for sessile species to seed downstream, the timescale of connectivity is crucial, as the pelagic larval duration of the species obviously needs to be equal or greater than the connectivity timescale [*Cowen et al.*, 2007; *Gawarkiewicz et al.*, 2007]. However, both directions of connectivity are important, and one aspect of MPA connectivity, which has received relatively little research attention or policy consideration, is the possible negative impact of upstream connectivity. Upstream connectivity can determine an MPAs exposure to pollution, for instance it is a known issue that coastal MPAs, within close proximity to populated land, are at risk of pollution and other human impacts [*Partelow et al.*, 2015], but it is unclear whether these same risks apply to open sea MPAs as a consequence of oceanic circulation. Additionally, there could be an impact on the conservation efforts of the MPA if a key species in the ecosystem is being overfished upstream of the MPA [*Stoner et al.*, 2012], or risks from alien species which may become invasive as climate change forces species poleward [*Wernberg et al.*, 2011; *Constable et al.*, 2014].

In order to understand the upstream risks that an MPA is exposed to, and help MPAs achieve their conservation goals [*Jameson et al.*, 2002], it is necessary to diagnose the pathways of the water that flows into the region, and the timescales on which this occurs. In doing so, one needs to take into account seasonal and inter-annual variability of the ocean circulation. This study introduces the idea of a "connectivity footprint", by which an MPA is connected to the upstream area via ocean currents, which can be estimated using high-resolution ocean circulation models. This paper examines the upstream connectivity of the UK's largest currently designated open seas MPAs, detailing the key circulation features and timescales in Section 3, then discusses an application of the concept of advective footprints to marine plastic which is considered to be the most significant and most widely spread form of marine pollution [*Shahidul Islam and Tanaka*, 2004; *Gall and Thompson*, 2015]. It should be noted, however, that with some minor modification of the experimental design, advective footprints can be applied to numerous other forms of marine pollution (e.g., oil spills or radioactive leaks), or to ecological impacts such as introduction of alien or invasive species by ocean currents.

In the first instance, we introduce the MPAs at the center of this study, followed by the methodology and experiment design.

1.1. Study Sites: Marine Protected Areas

In 2010, the United Nations set a target of protecting over 10% of the World Ocean by 2020 [*Secretariat of the Convention on Biological Diversity*, 2014]. Currently, however, only 2.8% is protected [*International Union for Conservation of Nature (IUCN) and United Nations Environment Programme-World Conservation Monitoring Centre (UNEP-WCMC)*, 2013]. In view of this conservation target, in its 2015 manifesto the UK Conservative party promised to work toward preserving UK marine habitats, and outlined plans to create a "blue belt" of

Table 1. A Table of Basic Information on Each of the MPAs in This Study

	Pitcairn	S. Georgia	Ascension	BIOT[a]
Year designated	2015[b]	2012	2016[c]	2010
Location	24°S, 127°W	54°S, 36°W	7°S, 14°W	6°S, 71°E
SST[d](°C)	24.75	1.78	25.89	28.19
MPA size (km^2)	834,334[e]	1,070,000	234,291	545,000
No-take (%)	100	2	52.6[f]	100
Island size (km^2)	62	3,755	88	60
Inhabitants[g](#)	56	20	1,122	4,000
Threatened species[h]	37	9	53[i]	81

BIOT, British Indian Ocean Territory; IUCN, International Union for Conservation of Nature; MPA, marine protected areas.
Information from [*Petit and Prudent*, 2010] and [*Pelembe and Cooper*, 2011], unless otherwise stated in the footnotes.
[a]Status currently under dispute, see *Lunn* [2016] for latest update.
[b]Officially designated, but not yet implemented [*Alexander and Osborne,* 2015].
[c]Officially designated, but not yet implemented [*BLUE Marine Foundation,* 2016].
[d]Sea surface temperature at the *Lat/Lon* given for each MPA, which is an average of six decadal climatologies (1955–2012) *Locarnini et al.* [2013].
[e]*The Pew Charitable Trusts* [2015].
[f]Could be declared, subject to local agreement, as soon as 2017 [*BLUE Marine Foundation,* 2016].
[g]Includes temporary visitors at the time of census.
[h]IUCN threatened species version 2015-4 *Animals* [*The Red List,* 2015].
[i]Note that reported total threatened species for Ascension Island also include those of Saint Helena and Tristan da Cunha.

protected oceans around the UK's Overseas Territories [*Alexander and Osborne*, 2015]. Since then, it has designated an additional two new large MPAs in quick succession. However, monitoring these requires constant data-gathering and evaluation, in order to provide the best protection and conservation.

In this paper, we compare four of the largest, managed, marine British Overseas Territories: Pitcairn Island Marine Reserve (henceforth Pitcairn), South Georgia and South Sandwich Islands Marine Protected Area (South Georgia), Ascension Island Ocean Sanctuary (Ascension) and Chagos British Indian Ocean Territory Marine Protected Area (BIOT). For the purpose of this paper, we avoid the international ambiguity surrounding MPA terminology (*The World Bank*, 2006; see chapter 2) and will only consider the IUCN definition (*Dudley*, 2008, p. 60). We compare all four sites as equals, referring to them in text as MPAs, however, first we briefly introduce them here individually describing their current management as well as their general biomes and ecosystems.

Table 1 details some basic information about each of the MPAs included in this study, the locations of which can be seen in Figure 1, with the initial indicating each MPA. What is immediately apparent is the vast difference in size between the areas, with South Georgia being the largest and Ascension the smallest. In terms of threatened species, BIOT is the most precious habitat being home to over 80 IUCN Red List species [*The Red List,* 2015], however, all of the MPAs are important sanctuaries for threatened species.

Situated centrally in the South Pacific subtropics is the Pitcairn MPA, consisting of four remote islands which form part of the Polynesia/Micronesia biodiversity hotspot [*Myers et al.*, 2000]. The Pitcairn Island is of volcanic origin, and is the only inhabited island of the four, whereas Henderson Island is a raised coral island, and the islands of Oeno and Ducie are small atolls. Currently, these coral reef communities are healthy environments, largely due to their uniquely isolated location and resulting near-pristine conditions [*Friedlander et al.*, 2014]. In a bid to maintain the unspoilt nature of the Pitcairn Islands, the Exclusive Economic Zone (EEZ) surrounding Pitcairn has been designated as a marine reserve which will ban all commercial fishing in the area, but allow for the continuation of local fishing activities, once implemented. Due to the remote location of the islands', enforcing the ban will require satellite monitoring rather than the usual costly patrol

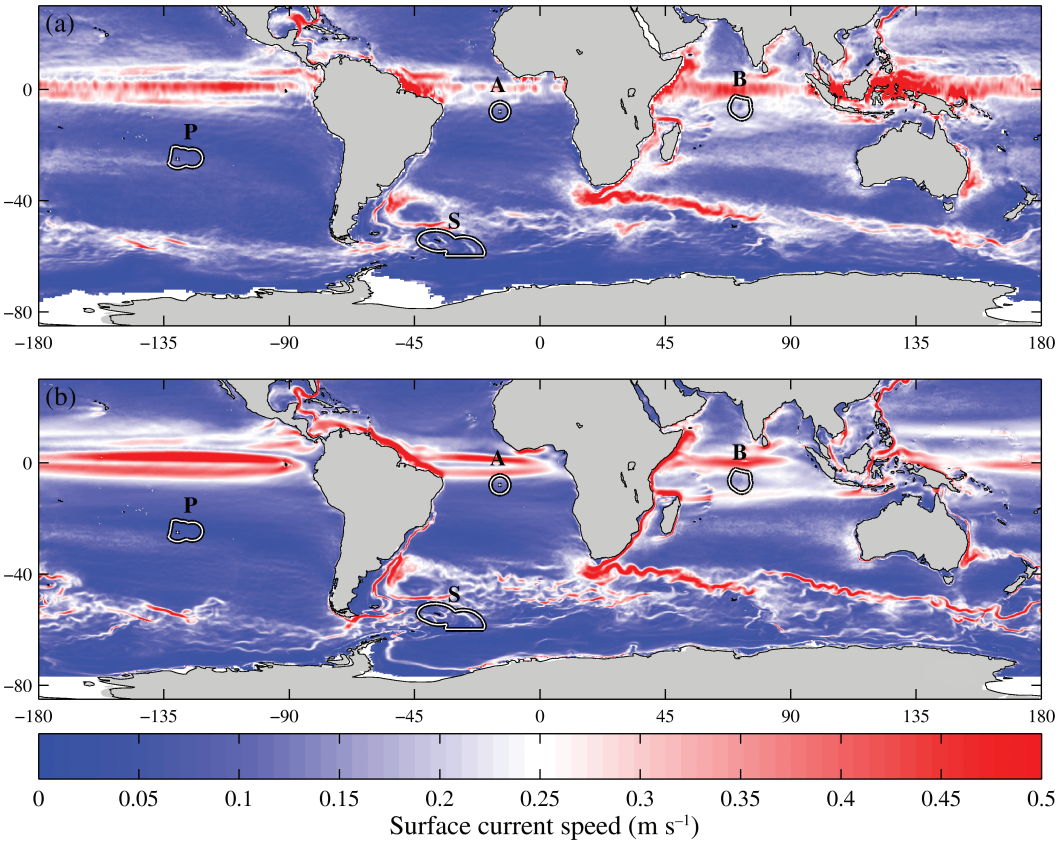

Figure 1. Observed and modeled decadal average, 2000–2009, surface current speed (m s^{-1}). The observed velocity, panel (a), is the Ocean Surface Current Analysis-Real-time data set at 1/3° resolution and the modeled velocity, panel (b), is the Nucleus for European Modelling of the Ocean ocean general circulation model at 1/12° resolution. The black and white contours denote the boundaries of the marine protected areas. The initials above each contour, represents: P for Pitcairn, S for South Georgia, A for Ascension, and B for British Indian Ocean Territory.

boats. Once an effective monitoring and enforcement regime is established and agreed upon by the Pitcairn community, interested non-governmental organisations (NGOs) and the UK government, the Pitcairn marine reserve will become one of the largest no-take areas in the world [*Avagliano et al.*, 2015].

Parts of the most productive waters of the Southern Ocean are found within the South Georgia MPA, located in the Atlantic sector, just east of Drake Passage. The MPA includes the South Sandwich Islands, which are approximately 700 km south-east of South Georgia. This diverse marine ecosystem is sustained by the nutrient-rich cold water, which upwells from the deep ocean, and supports an abundance of wildlife within its harsh polar environment [*Murphy et al.*, 2013]. Due to the nature of this inhospitable island, there are no permanent inhabitants, just temporary populations of government officials, scientists, and tourists. The islands are home to diverse communities of seabird species, a number of which are on the threatened species Red List [*The Red List*, 2015], and they are considered to be one of the most important seabird habitats in the world. Consequently, the MPA was designated in 2012, which prohibits all bottom trawling, a ban on bottom fishing at depths less than 700 m, and no-take zones (IUCN Category 1) around areas of high benthic biodiversity, totaling 20,431 km^2. Additionally, there are seasonal restrictions on certain fisheries to protect local predators [*Petit and Prudent*, 2010; *Collins*, 2013].

The most recently designated MPA in this study is the Ascension Island, which is situated just south of the equator in the Atlantic Ocean. Ascension Island is of volcanic origin and includes a few small uninhabited islands just offshore. The islands are young, formed only 1 million years ago, and consequently have relatively poor terrestrial biodiversity. However, due to its isolated location there are many endemic species, and the marine biodiversity is high. The island is also home to one of the most important populations of breeding Green turtles in the world, and is consequently considered to be an important habitat that needs

to be preserved [*Pelembe and Cooper*, 2011]. Ascension was designated as a marine reserve in 2016, closing just over half the reserve area to allow research to scope the eventual boundaries of the MPA, with the intention to assign the region a no-take area.

The BIOT MPA, also known as the Chagos Archipelago, is situated centrally within the Indian Ocean, half way between Africa and Indonesia and to the south of India. The area includes 55 coral islands spread over five atolls, of which Diego Garcia is the largest, with approximately 4,000 temporary residents. The 25,000 km^2 coral reefs of BIOT are unspoilt by human activity and in great health, owing to the protected status and the pristine waters, which could act as a global benchmark for unpolluted water [*Guitart et al.*, 2007]. This unique reef system supports a rich ecosystem that includes over 80 species on the threatened species list, and is consequently judged as possessing outstanding ecological value [*Sheppard et al.*, 2012]. In order to preserve this environment, in 2010 the UK government declared the area around BIOT as the then largest no-take marine reserve in the world at 544,000 km^2. Since that time, there have been legal issues surrounding BIOT's designation as an MPA. However, efforts are being made to confirm its status and ensure the future protection of this exceptionally well-preserved marine ecosystem [*Lunn*, 2016].

2. Methodology

In order to understand the potential exposure of MPAs to pollution and other risks, here we diagnose the connectivity to neighboring land masses through ocean circulation for each MPA. Once the connectivity is defined, it is then possible to assess the level of contact with human activity, and therefore risk. The tools and data used in this analysis are described here, along with the experimental design aimed at addressing these issues.

2.1. Ocean GCM and Lagrangian Particle Tracking

The Nucleus for European Modelling of the Ocean (NEMO) 1/12° resolution global ocean general circulation model (GCM) has been developed with particular emphasis on realistic representation of fine-scale circulation patterns [*Marzocchi et al.*, 2014], which provides an ideal platform to conduct Lagrangian particle-tracking experiments. Full details of the model run, including model setup and configuration, can be found in [*Marzocchi et al.*, 2014] so only a brief description will be given here. The model is initialized with World Ocean Atlas 2005 climatological fields and forced with realistic 6-hourly winds, daily heat fluxes, and monthly precipitation fields [*Brodeau et al.*, 2010]. The run begins in 1978, with output through to 2010, of which we are interested in 2000–2009. Model output is stored offline as successive 5 days means throughout the model run, of which the velocity fields are used for the particle tracking in this paper.

The Ariane package (http://www.univ-brest.fr/lpo/ariane) [*Blanke and Raynaud*, 1997] is applied to the NEMO velocity field to track 3D trajectories of water parcels using virtual particles that are released into the modeled ocean circulation [cf. *Robinson et al.*, 2014; *Srokosz et al.*, 2015; *Popova et al.*, 2016; who use a similar approach]. In our approach, the Lagrangian particles follow 3D velocity fields, and are not constrained to fixed release depths. Such an approach is most suitable to the dissolved marine pollutants, suspended type of plastic or larvae of marine organisms which have no or limited ability to control its vertical position. No diffusive processes were added to the transport of particles. These Lagrangian particles are intended here to represent water that enters within the boundaries of the MPAs. Further details about the Ariane package can be found in [*Blanke and Raynaud*, 1997; *Blanke et al.*, 1999].

The reader should note, however, that the Lagrangian approach used here is an approximation of online tracer release experiments. However, the latter are extremely computationally expensive both because they need to be performed in the full ocean model, and because each separate release experiments require its own separate tracer. The Lagrangian approach of offline approximation provides an alternative that allows large ensembles of computationally efficient experiments.

2.1.1. Modeled Versus Observed Surface Currents

The ability of the chosen model to accurately represent the circulation in the study areas is critical to the quality of the results. In order to qualitatively assess the performance of the NEMO 1/12° model, we compare the modeled surface velocity with the Ocean Surface Current Analysis-Real-time (OSCAR) dataset. The dataset provides global sea surface currents at 1/3° spatial resolution and a time resolution of 5-day

averages (available at http://www.oscar.noaa.gov/). The OSCAR velocity field is calculated by a linear combination of geostrophic, Ekman–Stommel, and thermal-wind currents [*Johnson et al.*, 2007]. OSCAR velocities provide accurate estimates of zonal and meridional time-mean circulation in comparison with the ship-board acoustic Doppler current profiler (ADCP) and drifter velocity estimates, although the product has weaker agreement with meridional currents in the near-equatorial region [*Johnson et al.*, 2007].

Figures 1a and 1b provide a comparison of the decadal (2000–2009) average ocean surface current speed, from OSCAR and NEMO, respectively, encompassing the four MPAs. The comparison shows good agreement between observed and modeled surface current speed, in terms of both the correct spatial pattern and magnitudes. The model does have known peculiarities at the equator, namely unexpected overturning cells at depth, however, this is unlikely to impact the surface or near-surface circulation. Additionally, the Antarctic Circumpolar Current, is known to be weaker in the model than the real world ocean, but the main circulation features of the Southern Ocean are in the correct location. There is also less small-scale variability in the model, owing to lower levels of eddy kinetic energy than the real ocean, despite the model being eddy-resolving at 1/12° resolution. Nevertheless, studies have shown the model to realistically reproduce key circulation features, such as the North Atlantic Current and the Gulf Stream separation [*Marzocchi et al.*, 2014], and several western boundary currents [*Popova et al.*, 2016].

Figures S1–S4, Supporting Information, show the decadal, annual, and monthly averaged circulation, of both NEMO and OSCAR surface current speeds, around the region of each MPA for illustrative purposes.

2.2. Experiment Design

In order to diagnose the circulation pathways by which water reaches the four MPAs, Lagrangian particles were released at the start of each month into the modeled circulation, and followed backwards in time (backtracked) during January 2000 to December 2009. Consequently, each monthly release of particles is essentially the month in which the particles arrive at the MPA. Particle positions are recorded at 5-daily time intervals, for a total of 72 time-steps with 5-day intervals, an advection period of 1 year. For the purpose of this study, we found 1 year's worth of trajectories to be sufficient in assessing connectivity, as all but one MPA was connected to land within a 12-month period (details in Section 3). Nevertheless, we additionally performed 10-year duration sensitivity experiments to address the longer-term connectivity especially pertinent to the issues of plastic pollution (see Figures 3 and S5–S7). Particles are deployed at every fifth grid cell of the 1/12° model grid horizontally (latitudinally and longitudinally) within the MPA boundaries, and at depths of 1, 20, 40, and 60 m to keep our approach generic and applicable to a wide range of problems. Figures S12 and S13 present a subsampling analysis that illustrates the low sensitivity of our analysis to the selected horizontal pattern of particle release. In case of plastics, such an approach would recognize both floating and suspended types, the latter being mostly spread over the well-mixed upper layer of the ocean. Particles were placed down to a depth of 60 m to approximate the euphotic zone (within which most planktonic organisms reside). The final boundaries of the Ascension MPA are not yet designated, so for the purpose of this study we have used the Ascension EEZ as the boundary. The particle placement was designed to be consistent in resolution across all MPAs for comparable analysis. However, the MPAs vary drastically in size (see Table 1), resulting in a different number of particles within each MPA experiment. At the horizontal and vertical grid spacing described, 1,888 Lagrangian particles are released at the beginning of each month for 10 years from the Pitcairn MPA, 6,155 particles from South Georgia MPA, 844 particles from the Ascension MPA, and 1,241 from the BIOT MPA.

2.3. Population Density Data

In discussing the MPAs connectivity with land in Section 3, exposure to risk is discussed in terms of connectivity with highly populated areas in Section 4. The population density data used for this is the Gridded Population of the World, Version 3 (GPWv3) Future Estimates for 2015 produced by [*Center for International Earth Science Information Network, Columbia University United Nations, Food Agriculture Programme, and Centro Internacional de Agricultura Tropical*, 2005], and can be seen in Figure 2. The GPWv3 dataset provides estimated population density in persons per square km at 1/4° resolution across the globe. More information, as well as the dataset itself, is available at: http://sedac.ciesin.columbia.edu/data/set/gpw-v3-population-density-future-estimates.

As a first-order approximation of population density effects, the 1/4° gridded population density field was extrapolated out from the land into the ocean, using the Matlab v2013a scatteredInterpolant function and

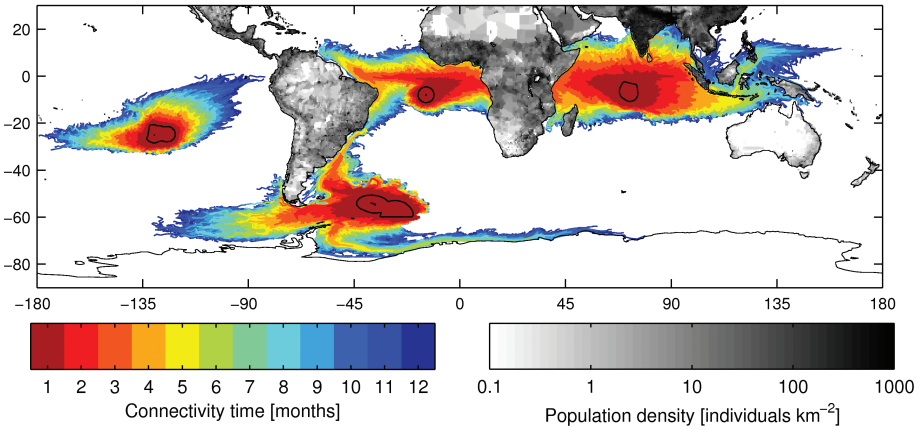

Figure 2. The time, in months, that it takes for ocean surface waters to reach the marine protected areas. The colored area represents the trajectories of particles, which arrive at the marine protected areas, each month during 2000–2009. The color of the trajectories indicate the time in months for the particles to be advected to the marine protected area, termed on the color bar as the connectivity time. The black contours represent the boundaries of the marine protected areas. The grayscale land indicates the population density, in persons per km^2 at 1/4° resolution. Note that trajectories representing shorter connectivity times are plotted after those representing longer times so that it is clear what the shortest connection time of a particular location to an marine protected areas.

natural neighbor interpolation. This approach does not factor in the effect of inland population density, i.e., where a stretch of coastline may be impacted by a significant inland population. However, restrictions in the availability of data mean that the GPWv3 dataset frequently averages population over an extended area, decreasing the significance of such errors (albeit locally). Note that this analysis also uses human population density as a proxy for impact, when the latter may actually be a stronger function of local technology, environmental regulations, and resource management.

The extrapolated population density was recorded for Lagrangian particle trajectories, which were within 85 km of the coastline. This distance is the global average width of the continental shelf [*Elrod et al.*, 2004], and we use such a fixed boundary to avoid biases introduced by the highly varying width of the continental shelf around the globe. Within this near-coastal zone, the water is considered as well-mixed [*Nash et al.*, 2012], and references therein), and, consequently, we assume water properties or human pollution, are evenly distributed throughout the shelf water mass.

3. Results

In order to assess the degree of exposure to pollution risk from upstream sources, we diagnose the pathways of the water that enters the MPAs and the associated timescales. Across parts of the World's Oceans, the circulation can shift both seasonally and inter-annually, and at varying magnitudes, which can significantly alter an MPA's connectivity. In this section, we describe the general circulation around the four MPAs, and the connectivity timescales with land. We then address the seasonal and inter-annual variability of the circulation, across a 10-year period.

3.1. General Circulation and Connectivity of MPAs

Figure 2 includes all of the particle data, across all months and years, in the experiments. Dark red trajectories represent an advection time of 1 month, before reaching the MPAs and consequently are the closest to the boundaries (black contours). Dark blue trajectories represent an advection time of 12 months, and are therefore at a greater distance from the MPAs. This figure illustrates the dominant pathways to the MPAs throughout a 10-year period, including inter-annual and seasonal variability.

What is apparent from Figure 2, is that all the MPA's, except Pitcairn, are connected with land within a 1 year timescale. As can be seen from Figure 1, the Pitcairn marine reserve is in an area of relatively slow surface currents. This is due to it being positioned toward the center of the basin-wide, anti-cyclonic South Pacific Gyre [*Maes et al.*, 2016]. There are two lobes of source water into the Pitcairn reserve, the main pathway originates in the northeast, and the second originates in the west. To further understand the circulation pattern around Pitcairn, a 10-year back tracking simulation was performed in order to identify the key circulation

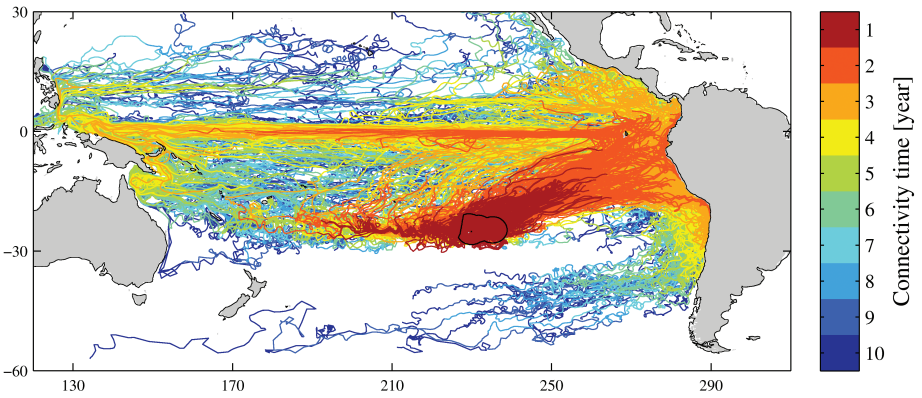

Figure 3. The time, in years, that it takes for ocean surface waters to reach the Pitcairn marine protected area. The colored area represents the trajectories of particles, which arrive at Pitcairn, each year during 2000–2009. The color of the trajectories indicate the time in years for the particles to be advected to the marine protected area, termed on the color bar as the connectivity time. The black contour represents the boundary of the Pitcairn marine protected areas. Note that trajectories representing shorter connectivity times are plotted after those representing longer times so that it is clear what the shortest connection time of a particular location to an marine protected areas.

features that influence the Pitcairn MPA (Figure 3). This revealed that two major currents feed the Pitcairn MPA, namely the Pacific Equatorial Undercurrent and the Humboldt Current. Particles traveling in the undercurrent across the entire basin, are at roughly 200 m on the western side, and gradually shoal as they travel toward the east [*Grenier et al.*, 2011]. Once reaching the west coast of South America, wind-driven coastal upwelling brings all particles to the surface [*Talley et al.*, 2011] eventually feeding into the Pitcairn surface waters by the circulation of the gyre. The Humboldt Current is an eastern boundary current flowing northwards along the west coast of the South American continent [*Fiedler and Talley*, 2006]. The northeastern lobe of the dominant pathway flows from the northwest coast of South America, whereas the western pathway is formed of water that has spent more time circulating in the anti-clockwise current of the sub-tropical gyre. Ekman transport causes the surface water to move toward the central region of a subtropical gyre [*Eriksen et al.*, 2013]. In terms of Pitcairn's connectivity, the MPA is connected to the South American continent within a 2-year timescale (via the northern arm of the South Pacific Gyre), and also the Malay Archipelago within 3–4 years (via the Pacific Equatorial Undercurrent). The longer-term (multiannual) connectivity described above for the Pitcairn MPA is important when the concept of circulation pathways is applied to issues such as plastic pollution, as marine plastic may degrade slowly [but see *van Sebille et al.*, 2015]. The corresponding long-term (10-year) connectivities of the other three MPAs are shown in Figures S5–S7.

The South Georgia MPA is fed by three dominant pathways: the Antarctic Circumpolar Current flowing from west to east around Antarctica; a southern pathway from the Antarctic Slope Current, with flows east to west along the Antarctic shelf [*Rintoul et al.*, 2001]; and a northern pathway via the return flow of the Malvinas Current, and also small but frequent eddies which are shed from the Brazil Current and are associated with the Subantarctic Front [*Peterson and Stramma*, 1991]. From these pathways, we can see in Figure 2 that the South Georgia MPA has a connectivity timescale in the order of 3–4 months. However, in considering the exposure to human activity, the only pathway for the South Georgia MPA that could be significant, taking into account population density, is from the Brazil Western Boundary Current, which flows southward along the east coast of the South American continent.

The Ascension MPA is positioned just south of the equator in the mid-Atlantic. Consequently, it is fed by two main pathways of water, the westward flowing South Equatorial Current and the eastward flowing North Equatorial Countercurrent. There is also an eastward flowing pathway, just sub-surface, via the Atlantic Equatorial Undercurrent [*Brandt et al.*, 2014]. The dominant pathway of water to the Ascension MPA is from the eastern side of the Atlantic, as seen in Figure 2. Parallel to the west coast of Africa, are two main currents each flowing in a meridional direction, which meet in a confluence region at about 15°S before turning west to become part of the South Equatorial Current. Flowing north to south is the Guinea Current and its extension the Angola Current, and flowing south to north is the Benguela Coastal Current [*Lass et al.*, 2000]. The highly seasonal eastward flowing North Equatorial Countercurrent originates from the western side of the

Atlantic at roughly 5–10°N [*Richardson et al.*, 1992]. A small proportion of the North Equatorial Countercurrent is fed by the northward flowing North Brazil Current, but the majority of the countercurrent is fed by northern hemisphere waters originating in the North Equatorial Current at roughly 10°N [*Goes et al.*, 2005]. The eastward flowing North Equatorial Countercurrent is strongest in the late boreal summer into fall, with a reversal of the near-surface current in spring due to a change in the Northeast Trade winds [*Richardson et al.*, 1992]. The Atlantic Equatorial current system connects the Ascension MPA with the west coast of Africa within a time period of 2–3 months, and with the east coast of Brazil within 3–4 months.

The BIOT MPA is positioned toward the center of the Indian Ocean, just south of the equator. In Figure 2, it is apparent that the BIOT MPA is fed by various water pathways from across the entire Indian Ocean, and also from the Pacific through the Indonesia Throughflow. The circulation of the Indian Ocean is extremely complex [*Wyrtki*, 1973], owing in part to the geographical configuration, but primarily to the unique monsoonal wind forcing. Here, we provide a brief description of the typical surface ocean circulation from the literature, focusing on key features relevant to the analysis.

The Indian Ocean is the smallest of the three major ocean basins, extending only as far north as 25°N on either side of the Indian subcontinent. The southern sector of the Indian Ocean is bounded by the Antarctic Circumpolar Current through which it is connected with the Atlantic and Pacific Oceans. There is also an important connection with the low latitude Pacific via the Indonesian Throughflow, which flows unidirectionally from the Pacific into the Indian through the Indonesian Archipelago. Once exiting the Archipelago, it flows westward within the South Equatorial Current. However, annual variability is high, and an El Niño/Southern Oscillation (ENSO) signal has been observed [*Sprintall et al.*, 2014]. In the southern half of the Indian Ocean is a basin-wide subtropical gyre, which flows anti-cyclonically driven by westerly winds at high (Southern) latitudes and south-easterly trade winds at low latitudes, similar to the mean wind patterns of the Atlantic and Pacific. The South Equatorial Current flows westward across the basin throughout the year at roughly 10–16°S, with a transport of some 50–55 Sv, and separates the subtropical south from the tropical and northern Indian Ocean [*New et al.*, 2007]. For parts of the year, a confluence of two currents at roughly 2–3°S along the east coast of Africa, results in the eastward flowing South Equatorial Countercurrent, which together with the South Equatorial Current, becomes the northern and southern branches of a transitory tropical cyclonic gyre [*Schott and McCreary*, 2001; *Talley et al.*, 2011].

North of the South Equatorial Current, is a unique circulation regime, which seasonally reverses driven by monsoonal wind forcing. The Southwest Monsoon winds peaks in July–August, and the Northeast Monsoon winds in January–Februrary, driving seasonal reversals in the ocean currents in this region [*Schott and McCreary,* 2001]. Greatly influenced by the reversing Southwest and Northeast Monsoons, are the two large embayments to the east and west of the Indian subcontinent, the Arabian Sea and the Bay of Bengal, respectively. During the Southwest Monsoon (winds blowing to the north-east over India) the open-ocean currents that circulate between the Arabian Sea and the Bay of Bengal flow eastward (Southwest Monsoon Current), whereas flow is westward during the Northeast Monsoon (Northeast Monsoon Current), influencing the formation of the South Equatorial Countercurrent. These monsoon currents are made up of many different branches, each forced individually by a combination of both local and remote processes. However, the Northeast Monsoon Current is notably weaker and more disorganized than the Southwest Monsoon Current, as the Southwest Monsoon winds are stronger than the Northeast Monsoon winds. Consequently, the ocean response is stronger and more consistent to the Southwest Monsoon. The transition between Southwest to Northeast Monsoons, and vice versa, occurs relatively quickly during March–April and October, during which the equatorial winds are westerlies, rather than the typical trade winds [*Schott and McCreary*, 2001; *Shankar et al.*, 2002; *Talley et al.*, 2011]. This brief dominance of westerlies forms the eastward flowing Wyrtki Jets, which are significantly stronger than the westward flowing South Equatorial Current during this time [*Wyrtki*, 1973].

For a schematic diagram of the Indian Ocean circulation and a thorough description of the entire regime, see [*Schott and McCreary*, 2001; Figures 8 and 9]. For a more in-depth discussion specifically of the northern Indian Ocean monsoonal circulation, see [*Shankar et al.*, 2002].

In terms of connectivity timescales, the BIOT MPA is connected to: the east coast of Africa within 3 months advection time; to Indonesia within 3–4 months, and via the Indonesian Throughflow, to the Malay Archipelago within 4–7 months; and to India within a range of 3–6 months. Northwards of 20°S, particle

trajectories from the BIOT MPA fill the entire Indian Ocean basin, with the exception of the northern Arabian Sea.

Similarly to Figure 3's Pitcairn pathways, Figures S5–S7 show the decadal-scale connectivity for the South Georgia, Ascension and BIOT MPAs. In the case of the South Georgia MPA, its proximity to the Antarctic Circumpolar Current means that the entire Southern Ocean is connected to the MPA within a time period of around 5 years. However, in spite of this fast connectivity, pathways remain constrained within the Southern Ocean even out to 10 years—with a few exceptions in continental boundary currents. For the Ascension MPA, most connectivity is confined to the equatorial region of the Atlantic (30°S to 10°N) on the 5-year timescale. Beyond this, some pathways extend further, notably via Agulhas Leakage from the Indian Ocean (with limited connectivity to the Indonesian Throughflow), though also with pathways from the subtropical gyres of the north and, especially, south Atlantic. Finally, for the BIOT MPA, most pathways remain within, and completely fill, the Indian Ocean, with connectivity of 4 years or less throughout this basin. There is also connectivity with the equatorial Pacific (20°S to 20°N) through the Indonesian Throughflow, with a few pathways almost connecting to the west coast of the Americas at the 10-year timescale.

3.2. Seasonal and Inter-Annual Variability

Figure 4 shows all the particles from the monthly releases for each year of the experiment, indicating the density of the trajectories and the inter-annual variability for each MPA. For comparison, Figures S9–S11 show corresponding trajectory densities for shorter time periods.

Focusing on Pitcairn in Figure 4, the trajectory density "footprint" in each subplot is generally the same in each year with the two distinct lobes to the northeast and west. In some years, the particles backtrack further away from Pitcairn, such as in years 2006 and 2007, and in others the particles remain closer to the MPA boundary, such as in years 2002 and 2003. However, these variations are not large enough for any significant connectivity to any coastline.

For the South Georgia MPA, the highest trajectory density is within the Antarctic Circumpolar Current, indicating this to be the dominant pathway. Conversely, Figure 4 also shows that the lowest density of trajectories advecting toward the South Georgia MPA comes from the northern pathway. As with Pitcairn, the South Georgia MPA has little inter-annual variability.

Focussing next on the Ascension MPA, Figure 4 shows the dominant pathway of water to originate from the west coast of Africa, specifically the Benguela Current and South Equatorial Current, showing low inter-annual variability.

Finally, focusing on the BIOT MPA in Figure 4, there are two dominant pathways of surface water for the MPA, one each from the east and the west. However, there is a high degree of variability both across and within the years. In 2009, the dominant pathway is from the west, indicated by the logarithmic color bar. Whereas in 2003, the highest trajectory density is from the east, and in some years there are equally pronounced pathways from both the east and west. This variability has a significant impact on the connectivity of the BIOT MPA to various continents. The BIOT MPA experiences by far the highest degree of inter-annual circulation variability out of the four MPAs in this study.

In order to examine the seasonal variability of circulation around the BIOT MPA, Figure 5 shows the pathways for each climatological month that arrives at BIOT, from which the impact of the seasonally reversing circulation is apparent. Figure 5 shows that the key features that determine the dominant pathways to the BIOT MPA are the South Equatorial Current (including the Indonesian Throughflow), the periodic Countercurrent and Wyrtki Jets, and the reversing Monsoonal Currents.

Focusing on one of the clearer features within Figure 5, it is apparent that the Indonesian Throughflow is an important pathway to the BIOT MPA of water arriving during September–December. *Meyers et al.* [1995], found that flow through the Indonesian Archipelago is largest during the Boreal summer, and taking into account an appropriate time lag between water passing through the Archipelago and arriving at BIOT, agrees with Figure 5 where there is a high density of particles within the Indonesian Throughflow during September–December arrival months. Other than the Indonesian Throughflow, the remaining picture is unclear, due to the reversal of the northern circulation and periodic appearance of the South Equatorial Countercurrent and Wyrtki Jets.

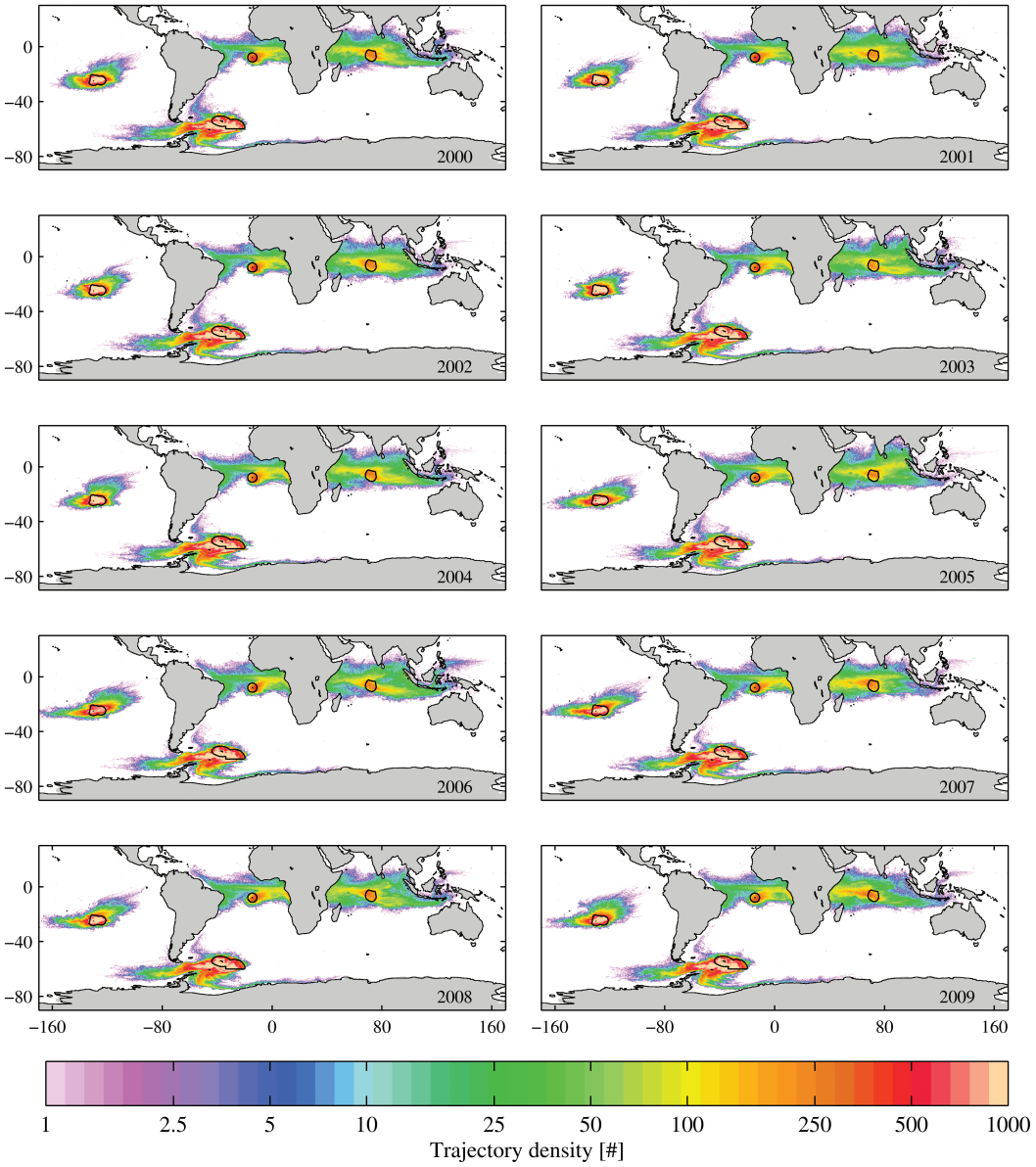

Figure 4. Census of particle advection toward the marine protected areas for each year's trajectories. The annual plots include all the particles released monthly from the marine protected area, each with an advection time of 1 year. Colors denote the cumulative "density" of particle trajectories based on their 5-daily position throughout the 10-year experiment, representing the total number of trajectories that have passed through each grid cell.

The complex, seasonally transforming, circulation pattern of the Indian Ocean is neither spatially nor temporally consistent year-on-year [*Shankar et al.*, 2002; *Schott et al.*, 2009]. This explains why Figure 5 does not clearly represent the monsoon driven circulation presented in Indian Ocean schematic circulation plots [such as *Schott and McCreary*, 2001; Figures 8 and 9]. As Figure 5 represents climatological months, the inter-annual variability smooths out the presence of any distinct features visible in the trajectories. To provide a clearer example, and also to demonstrate the degree of inter-annual variability in addition to the seasonal variability, Figure 6 shows four individual experiments of particle releases, arriving at the BIOT MPA within January and July, from a selection of years within the 10-year study period. Focusing on the top two panels, the predominant pathway arriving in January 2005 was from the northeast, the Bay of Bengal and Indonesia region, whereas in January 2009 the majority came from the western side of the basin. This inter-annual variability also occurs at other times of the year, as shown by the bottom two panels of water

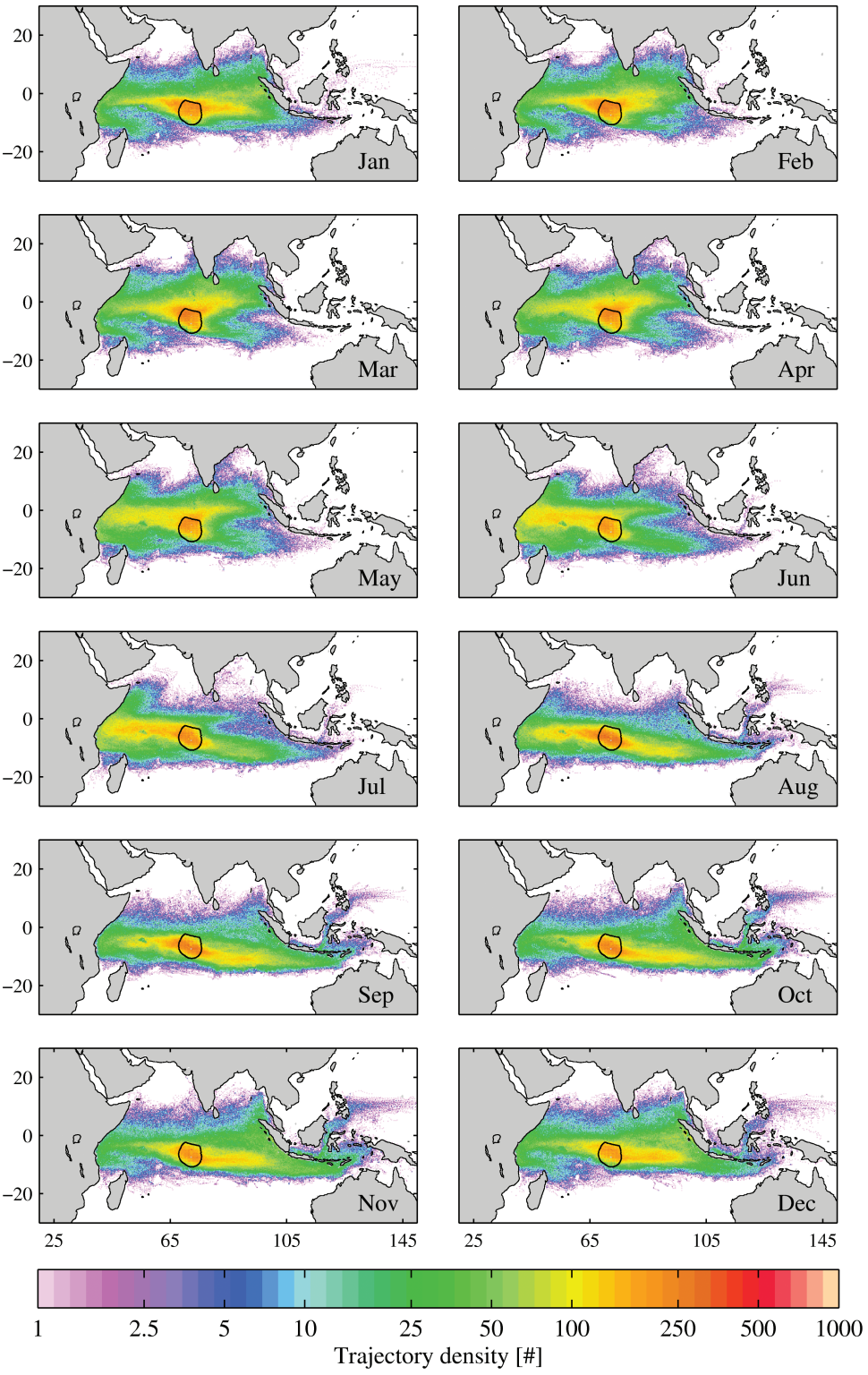

Figure 5. Census of particle advection toward the British Indian Ocean Territory marine protected area for each climatological month. Each plot includes the particles released in a given month for every year of the 10-year experiment, with an advection time of 1 year. Colors denote the cumulative "density" of particle trajectories based on their 5-daily position throughout the 10-year experiment, representing the total number of trajectories that have passed through each grid cell.

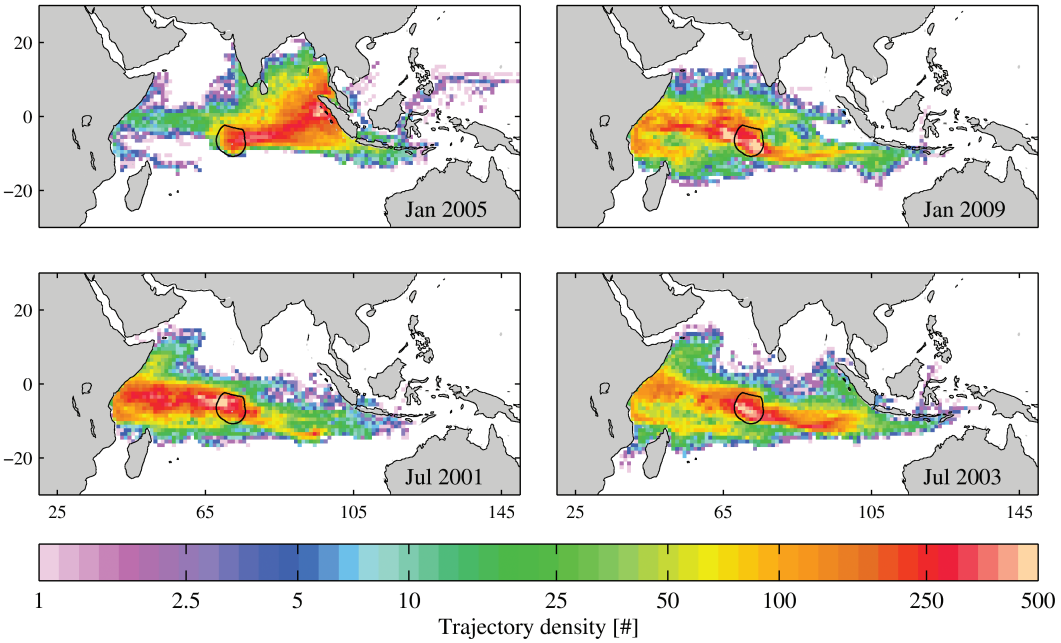

Figure 6. Census of particle advection toward the British Indian Ocean Territory marine protected area for 4 months of the experiment. The plots include the particles released in a given month for every year of the 10-year experiment, with an advection time of 1 year. Bottom left annotation details which month and year each plot represents. Colors denote the cumulative "density" of particle trajectories based on their 5-daily position throughout the 10-year experiment, representing the total number of trajectories that have passed through each grid cell.

arriving at BIOT in July for two different years. In 2001, the water is predominantly from the west, whereas in 2003 there are clear pathways from both the western and eastern sides of the Indian Ocean.

These variations in the circulation can arise as direct impacts of remote external factors, as well as from the inter-annual and seasonal variability that exists in the monsoonal wind forcing. The two principal large-scale climatological features which can impact the Indian Ocean circulation, although there are several other seasonal oscillations, are the local Indian Ocean Dipole (IOD) [*Saji et al.*, 1999], and the globally impacting ENSO [*Bjerknes*, 1969; *Diaz et al.*, 2001]. It is outside the scope of this work to describe these features in detail, but briefly the IOD is a shift in sea surface temperatures between the western and eastern Indian Ocean sectors, with each alternately becoming warmer and then colder in an irregular oscillation, typically lasting the boreal summer and autumn [*Saji et al.*, 1999]. The ENSO is an irregularly periodical occurrence of a warm phase (El Niño), and cool phase (La Niña) in sea surface temperatures, caused by a variation in winds over the tropical eastern Pacific Ocean, affecting much of the tropics and subtropics [*Schott et al.*, 2009]. El Niño typically lasts for 9–12 months, whereas La Niña can last for 1–3 years. There is much research and evidence of the influence of these phenomena directly on the currents of the Indian Ocean [*Gnanaseelan et al.*, 2012], indirectly via impacts on the monsoon cycle [*Pillai and Chowdary*, 2016], and importantly on how they interact [*Luo et al.*, 2010]. For a thorough discussion on Indian Ocean circulation variability and associated climate variability, see *Schott et al.* [2009] and references therein.

4. Discussion

4.1. Coastal Connectivity and Exposure to Human Activity

In Figure 2, it is apparent that three of the four MPAs in this study are strongly connected with land, over a 1-year timescale. Connectivity with land could be detrimental to the MPAs pristine condition, as land is the main source of pollution to the ocean, of which plastic makes up the most significant part [*Shahidul Islam and Tanaka*, 2004; *Gall and Thompson*, 2015]. *Jambeck et al.* [2015] estimated that in 2010, 275 million metric tons of plastic waste was generated in 192 coastal countries, of which 4.8–12.7 million metric tons entered the ocean (approximately 1.8–4.6%). Plastics are produced as many different varieties of polymers, and from macro to micro in size, but the key characteristic which makes plastic so commercially popular

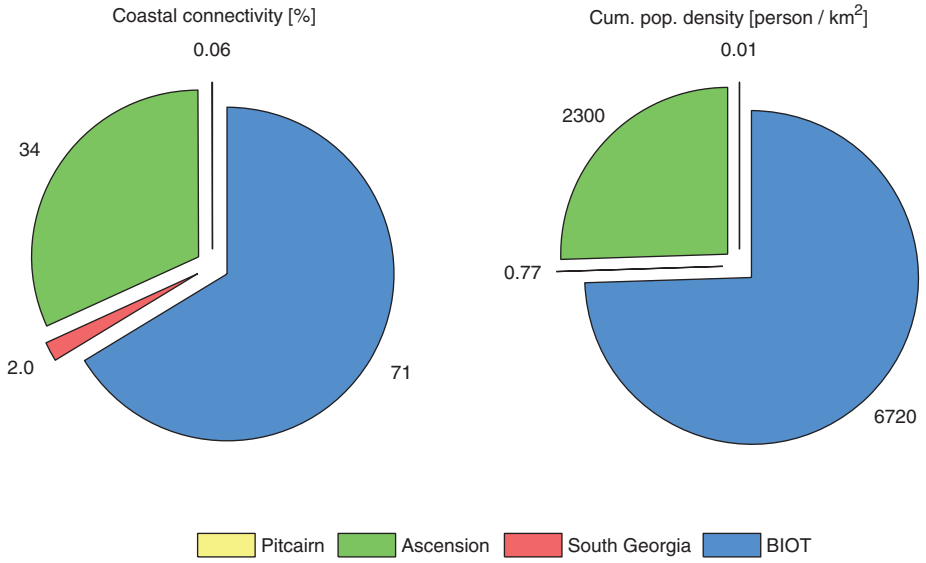

Figure 7. A comparison of the coastal connectivity and average cumulative population density encountered of water reaching each marine protected areas (MPA) over a 1 year advection period. In both cases, the charts are the averages across all 10 years of releases. The left pie chart shows the percentage of trajectories reaching each MPA that originate in coastal waters (i.e., have been within 85 km of the coast within 1 year of reaching the MPA). The right pie chart shows the corresponding average population density encountered over the same period. Both the connectivity and population density encountered of the Pitcairn MPA are too small to be clearly seen but are those at the 12 o'clock position on both charts.

is also the reason why they are so harmful and wide spread in the ocean: their durability [*Cole et al.*, 2011; *United Nations Environment Programme*, 2016]. Depending on the type of plastic, once in the ocean it can either sink to the ocean floor or be transported worldwide by surface currents [*van Sebille et al.*, 2015]. Most famously, there is a relatively high concentration of floating plastic, which has accumulated in so called "garbage patches" in the five sub-tropical gyres in the Indian Ocean, North and South Atlantic, and North and South Pacific [*Maximenko et al.*, 2012; *Eriksen et al.*, 2013]. Marine plastics can have significant detrimental ecological impacts, and consequently there has been much research on the impacts of both macro- and micro-plastics on biota. Direct impacts on marine species includes entanglement in macro-plastics, and ingestion of micro-plastic and subsequent absorption of toxic chemicals, namely polychlorinated biphenyls. Indirect negative impacts can come from the trophic transfer of plastics or toxins, and also floating plastic debris transporting "invader" species [*Wright et al.*, 2013; *Gall and Thompson*, 2015]. For a thorough synthesis on the issue of marine plastics, see [*UNEP*, 2016].

Having outlined the issues surrounding marine plastics, and noting the findings of [*Jambeck et al.*, 2015], who states that population size is a significant factor in the amount of plastic litter from coastal regions, we now discuss the MPAs in this context. Using the trajectory data presented in Figure 2, the percentage of trajectories that are within 85 km of the coast (the global average width of the shelf) within 1 year of release was calculated for each monthly experiment from each MPA, and presented in Tables S1–S4. The tables demonstrate the degree of seasonal and inter-annual variability discussed in Section 3, but also quantifies what is apparent in Figure 2. Over a 1 year timescale, the Pitcairn MPA is weakly connected with land, whereas of the water than flows into the South Georgia MPA, a fraction of 2% originates from the coast, a fraction of 34% for Ascension, and 71% for BIOT (see Figure 7).

However, connectivity with land is only significant for the MPAs if the land is highly populated and, thus, vulnerable in terms of pollution [*Jambeck et al.*, 2015]. In Figure 2, the land is filled with population density data [*CIESIN, FAO, CIAT*, 2005], and we now use this to further assess the impact-potential of trajectories originating from the coast. As is apparent in Figure 2, India, and parts of Indonesia and Africa, have the highest population densities of the regions that are connected with the MPAs, most notably to BIOT in the Indian Ocean. To quantify this, Tables S5–S8 in the supplementary material detail the average cumulative population density (persons/km^2) encountered by the circulation pathways, from each monthly experiment for each year for each MPA (Figure S8 shows time series of population density encountered as average across

all trajectories and the corresponding cumulative average). This information is important, since, even if only a small fraction of the pathways that reach a MPA have been in close proximity to land, they can be significant if the coast is relatively densely populated. While Tables S5–S8 report cumulative numbers averaged across all trajectories, the highest population density encountered by South Georgia pathways, was 3,134 person/km^2, originating from the coastal cities of the State of São Paulo; for Ascension, 5,288 person/km^2, originating from the coastal region of Lagos; and for the BIOT MPA, 15,203 person/km^2, originating from the coastal region of Mumbai. By contrast, trajectories reaching Pitcairn had encountered only a maximum of 34 person/km^2 in the preceding year.

We note that this approach is a simplification, assuming that a high population density equates to high levels of pollution. In reality, the situation is more complex and depends on the economic status of the coastal region which can determine factors such as the quality of waste management systems [*Jambeck et al.*, 2015]. Nevertheless, we use this approach as a first-order approximation of the possible pollution risk as a consequence of coastal connectivity. We also note that a large proportion of plastics which enter the marine environment do not float, and therefore would not impact the MPAs via circulation connectivity.

4.1.1. Four of a Kind?

Having outlined the average coastal connectivity, and the population density encountered by the MPA pathways, Figure 7 presents this information for cross-comparison of each MPA over a 1 year advection period.

Focusing first on the Pitcairn MPA in Figure 7, it is immediately apparent that the model suggests there is no risk of coastal pollution via ocean circulation. The South Georgia MPA has a very low coastal connectivity fraction (2%), however, the coasts that it is connected with include the relatively highly populated southeast coast of Brazil. Nevertheless, with such a low coastal connectivity the exposure to coastal pollution is low. The Ascension MPA, has an coastal connectivity of 34%, of which the average cumulative population density encountered over 1 year is 2,300 person/km^2. As such, the Ascension MPA is exposed to a significant pollution risk via ocean circulation. This is a particular threat to the islands important rookery for the endangered green turtle [*Petit and Prudent*, 2010], as the juveniles can perish by ingesting less than 1 g of marine debris [*Santos et al.*, 2015]. Finally, the BIOT MPA is the most vulnerable to coastal pollution via ocean circulation of all the MPAs in this study, as it has both the highest coastal connectivity, at 71%, and population density encountered, at 6,720 person/km^2. The BIOT MPA is comprised of 55 coral islands spread between five atolls, with more than 220 species of coral, and is currently considered to be one of the best preserved reefs in the world [*Sheppard et al.*, 2012]. However, the high degree of exposure to densely populated coastlines shown here, together with the discovery that corals are ingesting micro-plastics [*Hall et al.*, 2015], suggest that the pristine condition of the BIOT corals may be under threat.

4.2. Further Negative Impacts of Connectivity

This paper has focused on the pollution threat from land, specifically discussing plastic, however, connectivity with the coast and marine plastics are not the only issue. Many other human activities take place in the ocean, from which a variety of hazards to the marine environment can arise. Here, we will briefly discuss other threats to MPAs through their connectivity, namely issues associated with shipping, oil spills, and fishing.

The industrial-scale shipping of cargo, which makes up 90% of world trade movement [*Kaluza et al.*, 2010], takes the risks associated with human activity out into the open ocean, across all major ocean basins. Although the MARPOL 73/78 Convention [*Lethbridge*, 1991] was developed to prevent or minimize operational or accidental discharges of pollutants from vessels at sea (though restrictions largely stop 12 nautical miles offshore), these remain significant. For instance, an early estimate from 1982 reported that as many as 600,000 plastic containers worldwide were being dumped at sea per day from shipping [*Wace*, 1995], and there remains significant daily disposal of onboard garbage and sewage from both commercial and tourism ships [*Shahidul Islam and Tanaka*, 2004]. In addition to marine litter, there is the threat of oil spills, which are rare but devastating. One of the most public and notorious spills, was the Exxon Valdez oil tanker spill in 1989, which emitted 41.6 million liters of oil, and had a dramatic impact on Alaskan wildlife [*Atlas and Hazen*, 2011]. The incident killed more than 30,000 birds of 90 different species in just over 4 months [*Piatt et al.*, 1990]. Over 25 years on since the disaster, and the effect on the marine environment is still being felt, through the persistence of toxic sub-surface oil and chronic exposure resulting in delayed

population reductions and cascades of indirect effects [*Peterson et al.*, 2003]. A final known threat strongly associated with shipping, is marine bioinvasion. The two major routes by which invasive species spread, is via discharged water from ships' ballast tanks [*Ruiz et al.*, 2000] and hull fouling [*Drake and Lodge*, 2007]. In several parts of the world, invasive species have caused species extinction and habitat alteration [*Mack et al.*, 2000]. *Kaluza et al.* [2010] produced a network map of global ship movements (their Figure 1), the style of which can be overlaid with an MPAs connectivity footprint, to show which major shipping routes could potentially affect the MPAs, either through an oil spill disaster or increasing exposure to marine litter or invasive species.

The threat of oil spills is not solely limited to shipping incidents, there can also be rare but catastrophic spills from oil wells, the most famous recently being the Deepwater Horizon Oil Spill in 2010. The oil from the spill, 779 million liters [*Atlas and Hazen*, 2011], was spread across the Gulf of Mexico region by ocean circulation [*Liu et al.*, 2011], with 847 km of shoreline still contaminated 1 year after the spill despite clean up efforts [*Michel et al.*, 2013]. In the aftermath of this disaster, similar methods to that used here have been used to calculate the "circulation footprint" from possible oil spills, in order to reduce risk through better response and improved situational awareness [*Main et al.*, 2017]. This approach, in combination with the results presented here, can enable MPA managers to likewise be more aware of potential oil spill risks within their connectivity footprint, and consequently be prepared in the event of a spill.

Fishing activities provide both direct pressure on marine ecosystems as well as indirect pressures from marine littering, such as fishing tackle [*Shahidul Islam and Tanaka*, 2004]. Marine species can have various stages to their life cycles, which can involve larval dispersal during a pelagic stage. Dispersal via ocean currents determines the connectivity of local populations and therefore the knowledge and understanding of it is vital for conservation strategies [*Mora and Sale*, 2002]. Unless a system is efficiently self-sustaining (retainment exceeds or equals overspill), overfishing in one region, can impact populations downstream, and consequently even remote MPA ecosystems could be vulnerable. [*Figueira*, 2009] looked at identifying "patches" as either sources or sinks within a metapopulation, in order to more effectively designate marine reserves. Knowing a location's contribution to the ecosystem, and using the MPA connectivity footprints, can help fill in the knowledge gaps of population connectivity, and aid in the spatial management of protection efforts at time scales relevant to the pelagic larval duration of the species of interest [*Sale et al.*, 2005].

4.3. Future Work

In this study, we have produced a 1 year connectivity "footprint" for each MPA, and used it to assess connectivity with land. However, as discussed in the Section 4.2, pollution is not restricted to the coast, there are various other sources of potential hazards. The connectivity footprints produced in this study could be compared with other risk factors, such as shipping lanes, oil rigs, or fishing grounds, similar to the global human impact study by *Halpern et al.* [2008]. Additionally, the work here focuses on a timescale of 1 year, but a more detailed study of the timescales of particular risks could be considered. This would fully assess the pollution threat, and or, ecological implications posed to each MPA through connectivity.

In the introduction, the implications of downstream (forward) connectivity were introduced, namely seeding species to other areas. In order to seed species downstream, the timescale of connectivity is crucial, as the pelagic larval duration of the species needs to be equal to or greater than the connectivity timescale [*Cowen et al.*, 2007; *Gawarkiewicz et al.*, 2007]. The methodology and analysis used in this study can be performed in exactly the same way, but with forward Lagrangian particle tracking, enabling the timescales of downstream connectivity to be determined. Forward connectivity footprints, in addition to the backward connectivity footprints, would be extremely useful in the formation of networks, or ecological zones of MPAs, to protect ecological processes and areas that are necessary for the full life cycle of marine species [*Halpern*, 2003); *The World Bank*, 2006]. Additionally, this could also be a tool to aid marine spatial planning, as there are increasing calls for the integration of MPAs with fisheries management to aid global biodiversity [*Gell and Roberts*, 2003; *Hilborn*, 2016].

One final consideration, whether considering the forward or backward circulation connectivity of MPAs, is the potential for the circulation itself to change, under the stress of climate change. Observations show that the intensity and position of western boundary currents are already changing [*Wu et al.*, 2012; *Yang et al.*, 2016]. Also, a model projection has forecast further deviations in the circulation between the 2000–2010

and 2050–2059 decadal averages [*Popova et al.*, 2016]. In order to assess the impact such circulation changes may impose on ocean ecosystems, such as on the connectivity, nutrient pathways, and migration of species, further in-depth Lagrangian study using model future projections would be required.

5. Summary

- MPAs are typically established to conserve important ecosystems and protect marine species, but their success in achieving these goals requires evaluation, particularly with regard to their vulnerability to upstream impacts.
- Here, we present the "connectivity footprints" of four MPAs, for a timescale of 1 year, using a Lagrangian particle-tracking technique within a high-resolution ocean GCM, and specifically consider their connectivity with land.
- Over a 1 year timescale, Pitcairn MPA is essentially unconnected with land, whereas of the water than flows into the South Georgia MPA, around 2% originates from the coast, with 34% for Ascension, and 71% for BIOT, with variability (both seasonal and inter-annual) found to be notably high for BIOT.
- Population density of the connected coastlines is considered in terms of exposure to pollution, specifically plastics, and identified as a coastal connectivity risk that needs to be considered in the management of MPAs.
- Further risks to MPAs, associated with open-ocean connectivity, namely shipping, oil spills, and fishing, are discussed and highlight the potential use of the connectivity footprint in relation to these threats.
- We advocate connectivity footprints of MPAs should be used as a tool to improve future MPA designation, and in spatial planning of current MPA networks, and suggest future work to improve the diagnosis of connectivity footprints of MPAs.

Acknowledgments
This study was carried out using the computational tool Ariane, developed by B. Blanke and N. Grima, available at http://stockage.univ-brest.fr/grima/Ariane/ariane.html. The 1/12° NEMO simulation used in this work was produced using the ARCHER UK National Supercomputing Service (http://www.archer.ac.uk), and is available at http://gws-access.ceda.ac.uk/public/nemo/. This work was funded by the UK Natural Environment Research Council through a PhD studentship for J.R. (NE/K500938/1), and national capability funding for A.L.N, E.E.P., M.A.S., and A.Y. The model output generated during this study is available upon request to the communicating author A.Y. (axy@noc.ac.uk).

References

Alexander, D., and G. Osborne (2015), *Budget 2015* , pp. 124 , HM Treasury, London, U. K.
Atlas, R. M., and T. C. Hazen (2011), Oil biodegradation and bioremediation: A tale of the two worst spills in U.S. history, *Environ. Sci. Technol.*, *45*(16), 6709–6715. https://doi.org/10.1021/es2013227.
Avagliano, E., A. Bocquet, and J. Kape (2015), *Pitcairn Islands Ecosystem Profile* , pp. 53 , Comité français de l'UICN, Paris, France.
Barner, A., J. Lubchenco, C. Costello, S. Gaines, A. Leland, B. Jenks, S. Murawski, E. Schwaab, and M. Spring (2015), Solutions for recovering and sustaining the bounty of the ocean: Combining fishery reforms, rights-based fisheries management, and marine reserves, *Oceanography*, *25*(2), 252–263. https://doi.org/10.5670/oceanog.2015.51.
Bjerknes, J. (1969), Atmospheric teleconnections from the equatorial Pacific, *Mon. Weather Rev.*, *97*, 163–172. https://doi.org/10.1175/1520-0493(1969)097<0163:atftep>2.3.co;2.
Blanke, B., and S. Raynaud (1997), Kinematics of the Pacific equatorial undercurrent: An Eulerian and Lagrangian approach from GCM results, *J. Phys. Oceanogr.*, *27*(6), 1038–1053. https://doi.org/10.1175/1520-0485(1997)027<1038:KOTPEU>2.0.CO;2.
Blanke, B., M. Arhan, G. Madec, and S. Roche (1999), Warm water paths in the equatorial Atlantic as diagnosed with a general circulation model, *J. Phys. Oceanogr.*, *29*(11), 2753–2768. https://doi.org/10.1175/1520-0485(1999)029<2753:wwpite>2.0.co;2.
BLUE Marine Foundation (2016), *2016 Begins With the Creation of the Largest Marine Reserve in Atlantic Ocean*, edited by C. Clover, BLUE Mar. Found., London, U. K.
Brandt, P., A. Funk, A. Tantet, W. E. Johns, and J. Fischer (2014), The equatorial undercurrent in the central Atlantic and its relation to tropical Atlantic variability, *Clim. Dyn.*, *43*(11), 2985–2997. https://doi.org/10.1007/s00382-014-2061-4.
Brodeau, L., B. Barnier, A.-M. Treguier, T. Penduff, and S. Gulev (2010), An ERA40-based atmospheric forcing for global ocean circulation models, *Ocean Model.*, *31*(3–4), 88–104. https://doi.org/10.1016/j.ocemod.2009.10.005.
Center for International Earth Science Information Network, Columbia University United Nations, Food Agriculture ProgrammeCentro Internacional de Agricultura Tropical (2005), *Gridded Population of the World, Version 3 (GPWv3): Population Count Grid, Future Estimates*, NASA Socioecon. Data and Appl. Center (SEDAC), Palisades, N. Y. https://doi.org/10.7927/h42B8vzz.
Christie, P. and A.T. White (2007), Best practices in governance and enforcement of marine protected areas: An overview, *Rep. for the Workshop on Marine Protected Areas and Fisheries Management: Review of Issues and Considerations*, pp. 183–220, Rome, Italy.
Christie, M. R., B. N. Tissot, M. A. Albins, J. P. Beets, Y. Jia, D. M. Ortiz, S. E. Thompson, and M. A. Hixon (2010), Larval connectivity in an effective network of marine protected areas, *PLoS One*, *5*(12), e15715. https://doi.org/10.1371/journal.pone.0015715.
Cole, M., P. Lindeque, C. Halsband, and T. S. Galloway (2011), Microplastics as contaminants in the marine environment: A review, *Mar. Pollut. Bull.*, *62*(12), 2588–2597. https://doi.org/10.1016/j.marpolbul.2011.09.025.
Collins, M. (2013), *Press Release: New Spatial and Temporal Closed Areas Added to the South Georgia and the South Sandwich Islands Marine Protected Area, Government of South Georgia and the South Sandwich Islands*, Govern. House, Stanley, Falkland Islands.
Constable, A. J., et al. (2014), Climate change and Southern Ocean ecosystems I: How changes in physical habitats directly affect marine biota, *Glob. Change Biol.*, *20*(10), 3004–3025. https://doi.org/10.1111/gcb.12623.
Cowen, R. K., G. Gawarkiewic, J. Pineda, S. R. Thorrold, and F. E. Werner (2007), Population connectivity in marine systems: An overview, *Oceanography*, *20*(3), 14–21. https://doi.org/10.5670/oceanog.2007.26.
Day, J., N. Dudley, M. Hockings, G. Holmes, D. Laffoley, S. Stolton, and S. Wells (2012), *Guidelines for Applying the IUCN Protected Area Management Categories to Marine Protected Areas*, IUCN, Gland, Switzerland.
Diaz, H. F., M. P. Hoerling, and J. K. Eischeid (2001), ENSO variability, teleconnections and climate change, *Int. J. Climatol.*, *21*(15), 1845–1862. https://doi.org/10.1002/joc.631.
Doney, S., L. Bopp, and M. Long (2014), Historical and future trends in ocean climate and biogeochemistry, *Oceanography*, *27*(1), 108–119. https://doi.org/10.5670/oceanog.2014.14.

Drake, J. M., and D. M. Lodge (2007), Hull fouling is a risk factor for intercontinental species exchange in aquatic ecosystems, *Aquat. Invasions*, *2*(2), 121–131. https://doi.org/10.3391/ai.2007.2.2.7.
Dudley, N. (Ed) (2008), *Guidelines for Applying Protected Area Management Categories*, IUCN, Gland, Switzerland.
Edgar, G. J., et al. (2014), Global conservation outcomes depend on marine protected areas with five key features, *Nature*, *506*(7487), 216–220. https://doi.org/10.1038/nature13022.
Elrod, V. A., W. M. Berelson, K. H. Coale, and K. S. Johnson (2004), The flux of iron from continental shelf sediments: A missing source for global budgets, *Geophys. Res. Lett.*, *31*(12), L12307. https://doi.org/10.1029/2004gl020216.
Eriksen, M., N. Maximenko, M. Thiel, A. Cummins, G. Lattin, S. Wilson, J. Hafner, A. Zellers, and S. Rifman (2013), Plastic pollution in the South Pacific subtropical gyre, *Mar. Pollut. Bull.*, *68*(1–2), 71–76. https://doi.org/10.1016/j.marpolbul.2012.12.021.
Fiedler, P. C., and L. D. Talley (2006), Hydrography of the eastern tropical Pacific: A review, *Prog. Oceanogr.*, *69*(2–4), 143–180. https://doi.org/10.1016/j.pocean.2006.03.008.
Figueira, W. F. (2009), Connectivity or demography: Defining sources and sinks in coral reef fish metapopulations, *Ecol. Model.*, *220*(8), 1126–1137. https://doi.org/10.1016/j.ecolmodel.2009.01.021.
Fogarty, M. J., and L. W. Botsford (2007), Population connectivity and spatial management of marine fisheries, *Oceanography*, *20*(3), 112–123. https://doi.org/10.5670/oceanog.2007.34.
Friedlander, A. M., J. E. Caselle, E. Ballesteros, E. K. Brown, A. Turchik, and E. Sala (2014), The real bounty: Marine biodiversity in the Pitcairn Islands, *PLoS One*, *9*(6), e100142. https://doi.org/10.1371/journal.pone.0100142.
Gall, S. C., and R. C. Thompson (2015), The impact of debris on marine life, *Mar. Pollut. Bull.*, *92*(1–2), 170–179. https://doi.org/10.1016/j.marpolbul.2014.12.041.
Gawarkiewicz, G., S. Monismith, and J. Largier (2007), Observing larval transport processes affecting population connectivity progress and challenges, *Oceanography*, *20*(3), 40–53. https://doi.org/10.5670/oceanog.2007.28.
Gell, F. R., and C. M. Roberts (2003), Benefits beyond boundaries: The fishery effects of marine reserves, *Trends Ecol. Evol.*, *18*(9), 448–455. https://doi.org/10.1016/s0169-5347(03)00189-7.
Gnanaseelan, C., A. Deshpande, and M. J. McPhaden (2012), Impact of Indian Ocean Dipole and El Niño/southern oscillation wind-forcing on the Wyrtki jets, *J. Geophys. Res. Oceans*, *117*(C8), C08005. https://doi.org/10.1029/2012jc007918.
Goes, M., R. Molinari, I. da Silveira, and I. Wainer (2005), Retroflections of the North Brazil Current during February 2002, *Deep-Sea Res. I Oceanogr. Res. Pap.*, *52*(4), 647–667. https://doi.org/10.1016/j.dsr.2004.10.010.
Golden, C. D., E. H. Allison, W. W. L. Cheung, M. M. Dey, B. S. Halpern, D. J. McCauley, M. Smith, B. Vaitla, D. Zeller, and S. S. Myers (2016), Fall in fish catch threatens human health, *Nature*, *534*, 317–320. https://doi.org/10.1038/534317a.
Grenier, M., S. Cravatte, B. Blanke, C. Menkes, A. Koch-Larrouy, F. Durand, A. Melet, and C. Jeandel (2011), From the western boundary currents to the Pacific equatorial undercurrent: Modeled pathways and water mass evolutions, *J. Geophys. Res.*, *116*(C12), 1–16. https://doi.org/10.1029/2011jc007477.
Guitart, C., A. Sheppard, T. Frickers, A. R. Price, and J. W. Readman (2007), Negligible risks to corals from antifouling booster biocides and triazine herbicides in coastal waters of the Chagos Archipelago, *Mar. Pollut. Bull.*, *54*(2), 226–232. https://doi.org/10.1016/j.marpolbul.2006.10.012.
Hall, N. M., K. L. E. Berry, L. Rintoul, and M. O. Hoogenboom (2015), Microplastic ingestion by scleractinian corals, *Mar. Biol.*, *162*(3), 725–732. https://doi.org/10.1007/s00227-015-2619-7.
Halpern, B. S. (2003), The impact of marine reserves: Do reserves work and does reserve size matter? *Ecol. Appl.*, *13*(1), S117–S137. https://doi.org/10.1890/1051-0761(2003)013[0117:tiomrd]2.0.co;2.
Halpern, B. S., et al. (2008), A global map of human impact on marine ecosystems, *Science*, *319*(5865), 948–952. https://doi.org/10.1126/science.1149345.
Hilborn, R. (2016), Marine biodiversity needs more than protection, *Nature*, *535*, 224–226. https://doi.org/10.1038/535224a.
International Union for Conservation of Nature (IUCN), and United Nations Environment Programme-World Conservation Monitoring Centre (UNEP-WCMC) (2013), *The World Database on Protected Areas (WDPA)*, UNEP-WCMC, Cambridge, U. K. [Available at: https://www.protectedplanet.net/].
Jambeck, J. R., R. Geyer, C. Wilcox, T. R. Siegler, M. Perryman, A. Andrady, R. Narayan, and K. L. Law (2015), Marine pollution. Plastic waste inputs from land into the ocean, *Science*, *347*(6223), 768–771. https://doi.org/10.1126/science.1260352.
Jameson, S. C., M. H. Tupper, and J. M. Ridley (2002), The three screen doors: Can marine "protected" areas be effective? *Mar. Pollut. Bull.*, *44*(11), 1177–1183. https://doi.org/10.1016/s0025-326x(02)00258-8.
Johnson, E. S., F. Bonjean, G. S. E. Lagerloef, J. T. Gunn, and G. T. Mitchum (2007), Validation and error analysis of OSCAR sea surface currents, *J. Atmos. Oceanic Tech.*, *24*(4), 688–701. https://doi.org/10.1175/jtech1971.1.
Jonsson, B. F., and J. R. Watson (2016), The timescales of global surface-ocean connectivity, *Nat. Commun.*, *7*, 11239. https://doi.org/10.1038/ncomms11239.
Kaluza, P., A. Kolzsch, M. T. Gastner, and B. Blasius (2010), The complex network of global cargo ship movements, *J. R. Soc. Interface*, *7*(48), 1093–1103. https://doi.org/10.1098/rsif.2009.0495.
Lass, H. U., M. Schmidt, V. Mohrholz, and G. Nausch (2000), Hydrographic and current measurements in the area of the Angola–Benguela Front, *J. Phys. Oceanogr.*, *30*, 2589–2609. https://doi.org/10.1175/1520-0485(2000)030<2589:hacmit>2.0.co;2.
Lethbridge, J. R. (1991), MARPOL 73/78 (International Convention for the Prevention of Pollution from Ships), *Infrastructure Notes, No. PS-4*, World Bank, Washington, D. C.
Liu, Y., R. H. Weisberg, C. Hu, and L. Zheng (2011), Tracking the deepwater horizon oil spill: A modeling perspective, *Eos. Trans. AGU*, *92*(6), 45–52. https://doi.org/10.1029/2011EO060001.
Locarnini, R. A., et al. (2013), in *World Ocean Atlas 2013, Volume 1: Temperature*, edited by S. Levitus and A. Mishonov (technical editor), NOAA Atlas NESDIS 73.
Lunn, J. (2016), Disputes over the British Indian Ocean Territory: April 2016 update, *Commons Briefing Papers SN06908*, edited by House of Commons.
Luo, J.-J., R. Zhang, S. K. Behera, Y. Masumoto, F.-F. Jin, R. Lukas, and T. Yamagata (2010), Interaction between El Niño and extreme Indian ocean dipole, *J. Clim.*, *23*(3), 726–742. https://doi.org/10.1175/2009jcli3104.1.
Mack, R. N., D. Simberloff, W. M. Lonsdale, H. Evans, M. Clout, and F. A. Bazzaz (2000), Biotic invasions: Causes, epidemiology, global consequences, and control, *Ecol. Appl.*, *10*, 689–710. https://doi.org/10.1890/1051-0761(2000)010.
Maes, C., B. Blanke, and E. Martinez (2016), Origin and fate of surface drift in the oceanic convergence zones of the eastern Pacific, *Geophys. Res. Lett.*, *43*, 3398–3405. https://doi.org/10.1002/2016GL068217.

Main, C. E., A. Yool, N. P. Holliday, E. E. Popova, D. O. B. Jones, and H. A. Ruhl (2017), Simulating pathways of subsurface oil in the Faroe–Shetland Channel using an ocean general circulation model, *Mar. Pollut. Bull.*, *114*, 315–326. https://doi.org/10.1016/j.marpolbul.2016.09.041.

Marzocchi, A., J. J.-M. Hirschi, N. P. Holliday, S. A. Cunningham, A. T. Blaker, and A. C. Coward (2014), The North Atlantic subpolar circulation in an eddy-resolving global ocean model, *J. Mar. Syst.*, *142*, 126–143. https://doi.org/10.1016/j.jmarsys.2014.10.007.

Maximenko, N., J. Hafner, and P. Niiler (2012), Pathways of marine debris derived from trajectories of Lagrangian drifters, *Mar. Pollut. Bull.*, *65*(1–3), 51–62. https://doi.org/10.1016/j.marpolbul.2011.04.016.

Meyers, G., R. J. Bailey, and A. P. Worby (1995), Geostrophic transport of Indonesian throughflow, *Deep-Sea Res. I*, *42*(7), 1163–1174. https://doi.org/10.1016/0967-0637(95)00037-7.

Michel, J., et al. (2013), Extent and degree of shoreline oiling: Deepwater horizon oil spill, Gulf of Mexico, USA, *PLoS One*, *8*(6), e65087. https://doi.org/10.1371/journal.pone.0065087.

Mills, K., et al. (2013), Fisheries management in a changing climate: Lessons from the 2012 ocean heat wave in the Northwest Atlantic, *Oceanography*, *26*(2), 191–195. https://doi.org/10.5670/oceanog.2013.27.

Mora, C., and P. F. Sale (2002), Are populations of coral reef fish open or closed? *Trends Ecol. Evol.*, *17*(9), 422–428. https://doi.org/10.1016/s0169-5347(02)02584-3.

Murphy, E. J., et al. (2013), Comparison of the structure and function of Southern Ocean regional ecosystems: The Antarctic Peninsula and South Georgia, *J. Mar. Syst.*, *109–110*, 22–42. https://doi.org/10.1016/j.jmarsys.2012.03.011.

Myers, N., R. A. Mittermeier, C. G. Mittermeier, G. A. da Fonseca, and J. Kent (2000), Biodiversity hotspots for conservation priorities, *Nature*, *403*(6772), 853–858. https://doi.org/10.1038/35002501.

Nash, J., E. Shroyer, S. Kelly, M. Inall, T. Duda, M. Levine, N. Jones, and R. Musgrave (2012), Are any coastal internal tides predictable? *Oceanography*, *25*(2), 80–95. https://doi.org/10.5670/oceanog.2012.44.

New, A. L., S. G. Alderson, D. A. Smeed, and K. L. Stansfield (2007), On the circulation of water masses across the Mascarene Plateau in the South Indian Ocean, *Deep-Sea Res. I*, *54*, 42–74. https://doi.org/10.1016/j.dsr.2006.08.016.

Partelow, S., H. von Wehrden, and O. Horn (2015), Pollution exposure on marine protected areas: A global assessment, *Mar. Pollut. Bull.*, *100*(1), 352–358. https://doi.org/10.1016/j.marpolbul.2015.08.026.

Pauly, D., R. Watson, and J. Alder (2005), Global trends in world fisheries: Impacts on marine ecosystems and food security, *Philos. Trans. R. Soc. Lond. B Biol. Sci.*, *360*(1453), 5–12. https://doi.org/10.1098/rstb.2004.1574.

Pelembe, T., and G. Cooper (Eds) (2011), *UK Overseas Territories and Crown Dependencies: 2011 Biodiversity Snapshot*, Joint Nat. Conserv. Comm., Peterborough, U. K.

Peterson, R. G., and L. Stramma (1991), Upper-level circulation in the South Atlantic Ocean, *Progr. Oceanogr.*, *26*, 1–73. https://doi.org/10.1016/0079-6611(91)90006-8.

Peterson, C. H., S. D. Rice, J. W. Short, D. Esler, J. L. Bodkin, B. E. Ballachey, and D. B. Irons (2003), Long-term ecosystem response to the Exxon Valdez oil spill, *Science*, *302*(5653), 2082–2086. https://doi.org/10.1126/science.1084282.

Petit, J., and G. Prudent (2010), *Climate Change and Biodiversity in the European Union Overseas Entities*, 192 pp., IUCN, Gland, Switzerland and Brussels, Belgium.

Piatt, J. F., C. J. Lensink, W. Butler, K. Marshal, and D. R. Nysewander (1990), Immediate impact of the 'Exxon Valdez' oil spill on marine birds, *Auk*, *107*(2), 387–397. https://doi.org/10.2307/4087623.

Pillai, P. A., and J. S. Chowdary (2016), Indian summer monsoon intra-seasonal oscillation associated with the developing and decaying phase of El Niño, *Int. J. Climatol.*, *36*(4), 1846–1862. https://doi.org/10.1002/joc.4464.

Popova, E., et al. (2016), From global to regional and back again: Common climate stressors of marine ecosystems relevant for adaptation across five ocean warming hotspots, *Glob. Change Biol.*, *22*(6), 2038–2053. https://doi.org/10.1111/gcb.13247.

Richardson, P. L., S. Arnault, S. Garzoli, and J. G. Bruce (1992), Annual cycle of the Atlantic North Equatorial Countercurrent, *Deep-Sea Res.*, *39*(6), 997–1014. https://doi.org/10.1016/0198-0149(92)90036-s.

Rintoul, S. R., C. Hughes, and D. Olbers (2001), The Antarctic circumpolar current system, in *Ocean Circulation and Climate: Observing and Modelling the Global Ocean*, edited by G. Siedler, J. Church, and J. Gould , pp. 271–302 , Acad. Press, London, U. K.

Robinson, J., E. E. Popova, A. Yool, M. Srokosz, R. S. Lampitt, and J. R. Blundell (2014), How deep is deep enough? Ocean iron fertilization and carbon sequestration in the Southern Ocean, *Geophys. Res. Lett.*, *41*(7), 2489–2495. https://doi.org/10.1002/2013GL058799.

Ruiz, G. M., T. K. Rawlings, F. C. Dobbs, L. A. Drake, T. Mullady, A. Huq, and R. R. Colwell (2000), Global spread of microorganisms by ships, *Nature*, *408*, 49–50. https://doi.org/10.1038/35040695.

Saji, N. H., B. N. Goswami, P. N. Vinayachandran, and T. Yamagata (1999), A dipole mode in the tropical Indian Ocean, *Nature*, *401*(6751), 360–363. https://doi.org/10.1038/43854.

Sale, P. F., et al. (2005), Critical science gaps impede use of no-take fishery reserves, *Trends Ecol. Evol.*, *20*(2), 74–80. https://doi.org/10.1016/j.tree.2004.11.007.

Santos, R. G., R. Andrades, M. A. Boldrini, and A. S. Martins (2015), Debris ingestion by juvenile marine turtles: An underestimated problem, *Mar. Pollut. Bull.*, *93*(1–2), 37–43. https://doi.org/10.1016/j.marpolbul.2015.02.022.

Schott, F. A., and J. P. McCreary (2001), The monsoon circulation of the Indian Ocean, *Prog. Oceanogr.*, *51*(1), 1–123. https://doi.org/10.1016/s0079-6611(01)00083-0.

Schott, F. A., S.-P. Xie, and J. P. McCreary (2009), Indian Ocean circulation and climate variability, *Rev. Geophys.*, *47*(1), RG1002. https://doi.org/10.1029/2007rg000245.

van Sebille, E., C. Wilcox, L. Lebreton, N. Maximenko, B. D. Hardesty, J. A. van Franeker, M. Eriksen, D. Siegel, F. Galgani, and K. L. Law (2015), A global inventory of small floating plastic debris, *Environ. Res. Lett.*, *10*(12), 124006. https://doi.org/10.1088/1748-9326/10/12/124006.

Secretariat of the Convention on Biological Diversity (2014), *Global Biodiversity Outlook 4*, Secr. of the Conv. on Biol. Divers., Montreal, Canada.

Shahidul Islam, M., and M. Tanaka (2004), Impacts of pollution on coastal and marine ecosystems including coastal and marine fisheries and approach for management: A review and synthesis, *Mar. Pollut. Bull.*, *48*(7–8), 624–649. https://doi.org/10.1016/j.marpolbul.2003.12.004.

Shankar, D., P. N. Vinayachandran, and A. S. Unnikrishnan (2002), The monsoon currents in the north Indian Ocean, *Prog. Oceanogr.*, *52*(1), 63–120. https://doi.org/10.1016/s0079-6611(02)00024-1.

Sheppard, C. R., et al. (2012), Reefs and islands of the Chagos Archipelago, Indian Ocean: Why it is the world's largest no-take marine protected area, *Aquat. Conserv.: Mar. Freshw. Ecosyst.*, *22*(2), 232–261. https://doi.org/10.1002/aqc.1248.

Sprintall, J., A. L. Gordon, A. Koch-Larrouy, T. Lee, J. T. Potemra, K. Pujiana, and S. E. Wijffels (2014), The Indonesian seas and their role in the coupled ocean–climate system, *Nat. Geosci.*, *7*(7), 487–492. https://doi.org/10.1038/ngeo2188.

Srokosz, M. A., J. Robinson, H. McGrain, E. E. Popova, and A. Yool (2015), Could the Madagascar bloom be fertilized by Madagascan iron? *J. Geophys. Res. Oceans*, *120*, 5790–5803. https://doi.org/10.1002/2015JC011075.

Stoner, A. W., M. H. Davis, and C. J. Booker (2012), Abundance and population structure of queen conch inside and outside a marine protected area: Repeat surveys show significant declines, *Mar. Ecol. Prog. Ser.*, *460*, 101–114. https://doi.org/10.3354/meps09799.

Talley, L. D., G. L. Pickard, W. J. Emery, and J. H. Swift (2011), *Descriptive Physical Oceanography: An Introduction*, 6th ed. , pp. , Elsevier, Oxford, U. K.; Burlington, Vermont and San Diego, Calif.

The Pew Charitable Trusts (2015), *Pew, National Geographic Applaud Creation of Pitcairn Islands Marine Reserve*, edited by A. Risotto, The Pew Charitable Trusts, London, U. K.

The Red List (2015), The IUCN Red List of threatened species. Version 2015–4, *Table 6a: Red List Category Summary Country Totals (Animals)*.

The World Bank (2006), Scaling up marine management: The role of marine protected areas, *Rep. No. 36635*, The Int. Bank for Reconstr. and Dev./The World Bank, Washington, D. C.

United Nations Environment Programme (2016), *Marine Plastic Debris and Microplastics? Global Lessons and Research to Inspire Action and Guide Policy Change*, United Nations Environ. Program., Nairobi, Kenya.

Wace, N. (1995), Ocean litter stranded on Australian coast, in *State of the Marine Environment Report for Australia: Technical Annex 2 – Pollution*, edited by L. P. Zann and D. Sutton, Great Barrier Reef Mar. Park Auth., Townsville, Australia.

Watson, R., and D. Pauly (2001), Systematic distortions in world fisheries catch trends, *Nature*, *414*(6863), 534–536. https://doi.org/10.1038/35107050.

Wernberg, T., B. D. Russell, P. J. Moore, S. D. Ling, D. A. Smale, A. Campbell, M. A. Coleman, P. D. Steinberg, G. A. Kendrick, and S. D. Connell (2011), Impacts of climate change in a global hotspot for temperate marine biodiversity and ocean warming, *J. Exp. Mar. Biol. Ecol.*, *400*(1–2), 7–16. https://doi.org/10.1016/j.jembe.2011.02.021.

Wright, S. L., R. C. Thompson, and T. S. Galloway (2013), The physical impacts of microplastics on marine organisms: A review, *Environ. Pollut.*, *178*, 483–492. https://doi.org/10.1016/j.envpol.2013.02.031.

Wu, L., et al. (2012), Enhanced warming over the global subtropical western boundary currents, *Nat. Clim. Change*, *2*(3), 161–166. https://doi.org/10.1038/nclimate1353.

Wyrtki, K. (1973), An equatorial jet in the Indian Ocean, *Science*, *181*, 262–264. https://doi.org/10.1126/science.181.4096.262.

Yang, H., G. Lohmann, W. Wei, M. Dima, M. Ionita, and J. Liu (2016), Intensification and poleward shift of subtropical western boundary currents in a warming climate, *J. Geophys. Res. Oceans*, *121*, 4928–4945. https://doi.org/10.1002/2015jc011513.

References

Abbriano, R., Carranza, M., Hogle, S., Levin, R., Netburn, A., Seto, K., Snyder, S., and Franks, P. (2011). Deepwater horizon oil spill: A review of the planktonic response. *Oceanography*, 24(3):294–301.

Abraham, E. R., Law, C. S., Boyd, P. W., Lavender, S. J., Maldonado, M. T., and Bowie, A. R. (2000). Importance of stirring in the development of an iron-fertilized phytoplankton bloom. *Nature*, 407(6805):727–730.

Alexander, D. and Osborne, G. (2015). Budget 2015.

Amante, C. and Eakins, B. (2009). Etopo1 1 arc-minute global relief model: Procedures, data sources and analysis. Report.

Antonov, J. I., Seidov, D., Boyer, T. P., Locarnini, R. A., Mishonov, A. V., Garcia, H. E., Baranova, O. K., Zweng, M. M., and Johnson, D. R. (2010). World ocean atlas 2009, volume 2: Salinity.

Arakawa, A. (1972). Design of the ucla general circulation model. numerical simulation of weather and climate. tech. rep. 7.

Ardelan, M. V., Holm-Hansen, O., Hewes, C. D., Reiss, C. S., Silva, N. S., Dulaiova, H., Steinnes, E., and Sakshaug, E. (2010). Natural iron enrichment around the antarctic peninsula in the southern ocean. *Biogeosciences*, 7(1):11–25.

Arrigo, K. R. (2005). Marine microorganisms and global nutrient cycles. *Nature*, 437(7057):349–355.

Ashok, K., Guan, Z., and Yamagata, T. (2001). Impact of the indian ocean dipole on the relationship between the indian monsoon rainfall and enso. *Geophysical Research Letters*, 28(23):4499–4502.

Atkinson, A., Whitehouse, M. J., Priddle, J., Cripps, G. C., Ward, P., and Brandon, M. A. (2001). South georgia, antarctica: a productive, cold water, pelagic ecosystem. *Marine Ecology Progress Series*, 216:279 – 308.

Atlas, R. M. and Hazen, T. C. (2011). Oil biodegradation and bioremediation: a tale of the two worst spills in u.s. history. *Environ Sci Technol*, 45(16):6709–15.

Aumont, O. and Bopp, L. (2006). Globalizing results from ocean in situ iron fertilization studies. *Global Biogeochemical Cycles*, 20(2):GB2017.

AVISO (2014). Ssalto/duacs user handbook: (m)sla and (m)adt near-real time and delayed time products.

Baas Becking, L. (1934). *Geobiologie of inleiding tot de milieukunde*. W.P. Van Stockum & Zoon (in Dutch)., The Hague, the Netherlands.

Bakker, D. C., Nielsdottir, M. C., Morris, P. J., Venables, H. J., and Watson, A. J. (2007). The island mass effect and biological carbon uptake for the subantarctic crozet archipelago. *Deep Sea Research II*, 54:2174 – 2190.

Bank, T. W. (2006). Scaling up marine management : The role of marine protected areas. Report, The International Bank for Reconstruction and Development / The World Bank.

Banse, K. (1996). Low seasonality of low concentrations of surface chlorophyll in the subantarctic water ring: underwater irradiance, iron, or grazing? *Progress in Oceanography*, 37(3-4):241–291.

Barker, T. and Bashmakov, I. (2007). *Mitigation from a cross-sectoral perspective*, pages 619–690. Cambridge University Press, Cambridge and New York.

Barner, A., Lubchenco, J., Costello, C., Gaines, S., Leland, A., Jenks, B., Murawski, S., Schwaab, E., and Spring, M. (2015). Solutions for recovering and sustaining the bounty of the ocean: Combining fishery reforms, rights-based fisheries management, and marine reserves. *Oceanography*, 25(2):252–263.

Barnes, D. K., Galgani, F., Thompson, R. C., and Barlaz, M. (2009). Accumulation and fragmentation of plastic debris in global environments. *Phil. Trans. R. Soc. B*, 364(1526):1985–98.

Batchelor, G. K. (1973). *An introduction to fluid dynamics*. Cambridge University Press, Cambridge.

Bernard, B., Madec, G., Penduff, T., Molines, J.-M., Treguier, A.-M., Sommer, J., Beckmann, A., Biastoch, A., Bning, C., Dengg, J., Derval, C., Durand, E., Gulev, S., Remy, E., Talandier, C., Theetten, S., Maltrud, M., McClean, J., and Cuevas, B. (2006). Impact of partial steps and momentum advection schemes in a global ocean circulation model at eddy-permitting resolution. *Ocean Dynamics*, 56(5-6):543–567.

Bindoff, N. and Willebrand, J. (2007). *Observation: Oceanic Climate Change and Sea Level*, pages 385–432. Cambridge University Press, Cambridge and New York.

Bjerknes, J. (1969). Atmospheric teleconnections from the equatorial pacific. *Monthly Weather Review*, 97:163172.

Blain, S., Queguiner, B., Armand, L., Belviso, S., Bombled, B., Bopp, L., Bowie, A., Brunet, C., Brussaard, C., Carlotti, F., Christaki, U., Corbiere, A., Durand, I., Ebersbach, F., Fuda, J. L., Garcia, N., Gerringa, L., Griffiths, B., Guigue, C., Guillerm, C., Jacquet, S., Jeandel, C., Laan, P., Lefevre, D., Lo Monaco, C., Malits, A., Mosseri, J., Obernosterer, I., Park, Y. H., Picheral, M., Pondaven, P., Remenyi, T., Sandroni, V., Sarthou, G., Savoye, N., Scouarnec, L., Souhaut, M., Thuiller, D., Timmermans, K., Trull, T., Uitz, J., van Beek, P., Veldhuis, M., Vincent, D., Viollier, E., Vong, L., and Wagener, T. (2007). Effect of natural iron fertilization on carbon sequestration in the southern ocean. *Nature*, 446(7139):1070–4.

Blain, S., Quguiner, B., and Trull, T. (2008). The natural iron fertilization experiment keops (kerguelen ocean and plateau compared study): An overview. *Deep Sea Research Part II: Topical Studies in Oceanography*, 55(5-7):559–565.

Blain, S., Treguer, P., Belviso, S., Bucciarelli, E., Denis, M., Desabre, S., Fiala, M., Jezequel, V. M., Le Fevre, J., Mayzaud, P., Marty, J. C., and Razouls, S. (2001). A biogeochemical study of the island mass effect in the context of the iron hypothesis: Kerguelen islands, southern ocean. *Deep-Sea Research Part I-Oceanographic Research Papers*, 48(1):163–187.

Blanke, B., Arhan, M., Madec, G., and Roche, S. (1999). Warm water paths in the equatorial atlantic as diagnosed with a general circulation model. *Journal of Physical Oceanography*, 29(11):2753–2768.

Blanke, B. and Raynaud, S. (1997). Kinematics of the pacific equatorial undercurrent: An eulerian and lagrangian approach from gcm results. *Journal of Physical Oceanography*, 27(6):1038–1053.

Boebel, O., Lutjeharms, J., Schmid, C., Zenk, W., Rossby, T., and Barron, C. (2003). The cape cauldron, a regime of turbulent inter-ocean exchange. *Deep Sea Research II*, 50:57–86.

Boehlert, G. W. (1996). Biodiversity and the sustainability of marine fisheries. *Oceanography*, 9(1):2835.

Borrione, I. and Schlitzer, R. (2013). Distribution and recurrence of phytoplankton blooms around south georgia, southern ocean. *Biogeosciences*, 10(1):217–231.

Botsford, L. W., Hastings, A., and Gaines, S. D. (2001). Dependence of sustainability on the configuration of marine reserves and larval dispersal distance. *Ecology Letters*, 4(2):144–150.

Bourdalle Badie, R., Treguier, A., Molines, J., Coward, A., Scheinert, M., Lu, Y., Lecointre, A., and Tranchant, B. (2012). The orca12 bathymetry v3.2. technical report. Report.

Bowie, A. R., van der Merwe, P., Qurou, F., Trull, T., Fourquez, M., Planchon, F., Sarthou, G., Chever, F., Townsend, A. T., Obernosterer, I., Salle, J. B., and Blain, S. (2015). Iron budgets for three distinct biogeochemical sites around the kerguelen archipelago (southern ocean) during the natural fertilisation study, keops-2. *Biogeosciences*, 12(14):4421–4445.

Boyd, P. W. (2002). Environmental factors controlling phytoplankton processes in the southern ocean1. *Journal of Phycology*, 38(5):844–861.

Boyd, P. W. (2007). Biogeochemistry: iron findings. *Nature*, 446(7139):989–91.

Boyd, P. W., Arrigo, K. R., Strzepek, R., and van Dijken, G. L. (2012a). Mapping phytoplankton iron utilization: Insights into southern ocean supply mechanisms. *Journal of Geophysical Research: Oceans*, 117(C6):C06009.

Boyd, P. W., Bakker, D. C. E., and Chandler, C. (2012b). A new database to explore the findings from large-scale ocean iron enrichments experiments. *Oceanography*, 25(4):64–71.

Boyd, P. W. and Ellwood, M. J. (2010). The biogeochemical cycle of iron in the ocean. *Nature Geoscience*, 3(10):675–682.

Boyd, P. W., Jickells, T., Law, C. S., Blain, S., Boyle, E. A., Buesseler, K. O., Coale, K. H., Cullen, J. J., de Baar, H. J., Follows, M., Harvey, M., Lancelot, C., Levasseur, M., Owens, N. P., Pollard, R., Rivkin, R. B., Sarmiento, J., Schoemann, V., Smetacek, V., Takeda, S., Tsuda, A., Turner, S., and Watson, A. J. (2007). Mesoscale iron enrichment experiments 1993-2005: synthesis and future directions. *Science*, 315(5812):612–7.

Boyd, P. W., Watson, A. J., Law, C. S., Abraham, E. R., Trull, T., Murdoch, R., Bakker, D. C., Bowie, A. R., Buesseler, K. O., Chang, H., Charette, M., Croot, P., Downing, K., Frew, R., Gall, M., Hadfield, M., Hall, J., Harvey, M., Jameson, G., LaRoche, J., Liddicoat, M., Ling, R., Maldonado, M. T., McKay, R. M., Nodder, S., Pickmere, S., Pridmore, R., Rintoul, S., Safi, K., Sutton, P., Strzepek, R., Tanneberger, K., Turner, S., Waite, A., and Zeldis, J. (2000). A mesoscale phytoplankton bloom in the polar southern ocean stimulated by iron fertilization. *Nature*, 407(6805):695–702.

Boyer, T. P., e. a. (2013). World ocean database 2013. Report.

Brandt, P., Funk, A., Tantet, A., Johns, W. E., and Fischer, J. (2014). The equatorial undercurrent in the central atlantic and its relation to tropical atlantic variability. *Climate Dynamics*, 43(11):2985–2997.

Brodeau, L., Barnier, B., Treguier, A.-M., Penduff, T., and Gulev, S. (2010). An era40-based atmospheric forcing for global ocean circulation models. *Ocean Modelling*, 31(3-4):88–104.

Brody, S. R., Lozier, M. S., and Mahadevan, A. (2016). Quantifying the impact of submesoscale processes on the spring phytoplankton bloom in a turbulent upper ocean using a lagrangian approach. *Geophysical Research Letters*, 43(10):5160–5169.

Camilli, R., Reddy, C. M., Yoerger, D. R., Van Mooy, B. A., Jakuba, M. V., Kinsey, J. C., McIntyre, C. P., Sylva, S. P., and Maloney, J. V. (2010). Tracking hydrocarbon plume transport and biodegradation at deepwater horizon. *Science*, 330(6001):201–4.

Chenillat, F., Blanke, B., Grima, N., Franks, P. J. S., Capet, X., and Rivire, P. (2015). Quantifying tracer dynamics in moving fluids: a combined eulerian-lagrangian approach. *Frontiers in Environmental Science*, 3.

Christie, M. R., Tissot, B. N., Albins, M. A., Beets, J. P., Jia, Y., Ortiz, D. M., Thompson, S. E., and Hixon, M. A. (2010). Larval connectivity in an effective network of marine protected areas. *PLoS One*, 5(12):e15715.

Christie, P. and White, A. T. (2007). *Best Practices in Governance and Enforcement of Marine Protected Areas: An Overview*, pages 183–220. Rome, Italy.

Closset, I., Lasbleiz, M., Leblanc, K., Quguiner, B., Cavagna, A. J., Elskens, M., Navez, J., and Cardinal, D. (2014). Seasonal evolution of net and regenerated silica

production around a natural fe-fertilized area in the southern ocean estimated with si isotopic approaches. *Biogeosciences*, 11(20):5827–5846.

Cole, M., Lindeque, P., Halsband, C., and Galloway, T. S. (2011). Microplastics as contaminants in the marine environment: a review. *Marine Pollution Bulletin*, 62(12):2588–97.

Collins, M. (2013). New spatial and temporal closed areas added to the south georgia and the south sandwich islands marine protected area.

Comiso, J. C., McClain, C. R., Sullivan, C. W., Ryan, J. P., and Leonard, C. L. (1993). Coastal zone color scanner pigment concentrations in the southern ocean and relationships to geophysical surface features. *Journal of Geophysical Research*, 98(C2):2419.

Constable, A. J., Melbourne-Thomas, J., Corney, S. P., Arrigo, K. R., Barbraud, C., Barnes, D. K., Bindoff, N. L., Boyd, P. W., Brandt, A., Costa, D. P., Davidson, A. T., Ducklow, H. W., Emmerson, L., Fukuchi, M., Gutt, J., Hindell, M. A., Hofmann, E. E., Hosie, G. W., Iida, T., Jacob, S., Johnston, N. M., Kawaguchi, S., Kokubun, N., Koubbi, P., Lea, M. A., Makhado, A., Massom, R. A., Meiners, K., Meredith, M. P., Murphy, E. J., Nicol, S., Reid, K., Richerson, K., Riddle, M. J., Rintoul, S. R., Smith, W. O., J., Southwell, C., Stark, J. S., Sumner, M., Swadling, K. M., Takahashi, K. T., Trathan, P. N., Welsford, D. C., Weimerskirch, H., Westwood, K. J., Wienecke, B. C., Wolf-Gladrow, D., Wright, S. W., Xavier, J. C., and Ziegler, P. (2014). Climate change and southern ocean ecosystems i: how changes in physical habitats directly affect marine biota. *Global Change Biology*, 20(10):3004–25.

Cousteau, J.-Y. (1971). Statement on global marine degradation. *Biological Conservation*, 4(1):61–65.

Cowen, R. K., Gawarkiewic, G., Pineda, J., Thorrold, S. R., and Werner, F. E. (2007). Population connectivity in marine systems an overview. *Oceanography*, 20(3):14–21.

Cowen, R. K., Lwiza, K. M., Sponaugle, S., Paris, C. B., and Olson, D. B. (2000). Connectivity of marine populations: open or closed? *Science*, 287(5454):857–9.

Cowen, R. K. and Sponaugle, S. (2009). Larval dispersal and marine population connectivity. *Ann Rev Mar Sci*, 1:443–66.

Davis, R. E. (1983). Oceanic property transport, lagrangian particle statistics, and their prediction. *Journal of Marine Research*, 41(1):163–194.

Day, J., Dudley, N., Hockings, M., Holmes, G., Laffoley, D., Stolton, S., and Wells, S. (2012). Guidelines for applying the iucn protected area management categories to marine protected areas. Report, IUCN.

de Baar, H. J. W. (2005). Synthesis of iron fertilization experiments: From the iron age in the age of enlightenment. *Journal of Geophysical Research*, 110(C9).

de Baar, H. J. W., de Jong, J. T. M., Bakker, D. C. E., Lscher, B. M., Veth, C., Bathmann, U., and Smetacek, V. (1995). Importance of iron for plankton blooms and carbon dioxide drawdown in the southern ocean. *Nature*, 373(6513):412–415.

de Baar, H. J. W., Gerringa, L. J. A., Laan, P., and Timmermans, K. R. (2008). Efficiency of carbon removal per added iron in ocean iron fertilization. *Marine Ecology Progress Series*, 364:269–282.

Defne, Z., Ganju, N. K., and Aretxabaleta, A. (2016). Estimating time-dependent connectivity in marine systems. *Geophysical Research Letters*, pages n/a–n/a.

Derraik, J. G. (2002). The pollution of the marine environment by plastic debris: a review. *Mar Pollut Bull*, 44(9):842–52.

DeVries, T., Primeau, F., and Deutsch, C. (2012). The sequestration efficiency of the biological pump. *Geophysical Research Letters*, 39(13).

Diaz, H. F., Hoerling, M. P., and Eischeid, J. K. (2001). Enso variability, teleconnections and climate change. *International Journal of Climatology*, 21(15):1845–1862.

Diversity, S. o. t. C. o. B. (2014). *Global Biodiversity Outlook 4*. Montral.

Doney, S., Bopp, L., and Long, M. (2014). Historical and future trends in ocean climate and biogeochemistry. *Oceanography*, 27(1):108–119.

Doney, S. C., Ruckelshaus, M., Emmett Duffy, J., Barry, J. P., Chan, F., English, C. A., Galindo, H. M., Grebmeier, J. M., Hollowed, A. B., Knowlton, N., Polovina, J., Rabalais, N. N., Sydeman, W. J., and Talley, L. D. (2012). Climate change impacts on marine ecosystems. *Annual Review of Marine Science*, 4(1):11–37.

d'Ovidio, F., Della Penna, A., Trull, T. W., Nencioli, F., Pujol, M. I., Rio, M. H., Park, Y. H., Cott, C., Zhou, M., and Blain, S. (2015). The biogeochemical structuring role of horizontal stirring: Lagrangian perspectives on iron delivery downstream of the kerguelen plateau. *Biogeosciences*, 12(19):5567–5581.

Drake, J. M. and Lodge, D. M. (2007). Hull fouling is a risk factor for intercontinental species exchange in aquatic ecosystems. *Aquatic Invasions*, 2(2):121–131.

Duchez, A., Frajka-Williams, E., Castro, N., Hirschi, J., and Coward, A. (2014). Seasonal to interannual variability in density around the canary islands and their influence on the atlantic meridional overturning circulation at 26 degrees n. *Journal of Geophysical Research-Oceans*, 119(3):1843–1860.

Ducklow, H., Steinberg, D., and Buesseler, K. (2001). Upper ocean carbon export and the biological pump. *OCEANOGRAPHY*, 14(4):50 – 58.

Edgar, G. J., Stuart-Smith, R. D., Willis, T. J., Kininmonth, S., Baker, S. C., Banks, S., Barrett, N. S., Becerro, M. A., Bernard, A. T., Berkhout, J., Buxton, C. D., Campbell, S. J., Cooper, A. T., Davey, M., Edgar, S. C., Forsterra, G., Galvan, D. E., Irigoyen, A. J., Kushner, D. J., Moura, R., Parnell, P. E., Shears, N. T., Soler, G., Strain, E. M., and Thomson, R. J. (2014). Global conservation outcomes depend on marine protected areas with five key features. *Nature*, 506(7487):216–20.

Elrod, V. A., Berelson, W. M., Coale, K. H., and Johnson, K. S. (2004). The flux of iron from continental shelf sediments: A missing source for global budgets. *Geophysical Research Letters*, 31(12):L12307.

Eriksen, M., Maximenko, N., Thiel, M., Cummins, A., Lattin, G., Wilson, S., Hafner, J., Zellers, A., and Rifman, S. (2013). Plastic pollution in the south pacific subtropical gyre. *Mar Pollut Bull*, 68(1-2):71–6.

Fiedler, P. C. and Talley, L. D. (2006). Hydrography of the eastern tropical pacific: A review. *Progress in Oceanography*, 69(2-4):143–180.

Figueira, W. F. (2009). Connectivity or demography: Defining sources and sinks in coral reef fish metapopulations. *Ecological Modelling*, 220(8):1126–1137.

Fogarty, M. J. and Botsford, L. W. (2007). Population connectivity and spatial management of marine fisheries. *Oceanography*, 20(3):112–123.

for International Earth Science Information Network, C., Nations, C. U. U., Programme, F. A., and Tropical, C. I. d. A. (2005). Gridded population of the world, version 3 (gpwv3): Population count grid, future estimates.

Fossette, S., Putman, N. F., Lohmann, K. J., Marsh, R., and Hays, G. C. (2012). A biologists guide to assessing ocean currents: a review. *Marine Ecology Progress Series*, 457:285–301.

Foundation, B. M. (2016). 2016 begins with the creation of the largest marine reserve in atlantic ocean.

France, U., Avagliano, E., Bocquet, A., and Kape, J. (2015). Pitcairn islands ecosystem profile.

Friedlander, A. M., Caselle, J. E., Ballesteros, E., Brown, E. K., Turchik, A., and Sala, E. (2014). The real bounty: marine biodiversity in the pitcairn islands. *PLoS One*, 9(6):e100142.

Froyland, G., Stuart, R. M., and van Sebille, E. (2014). How well-connected is the surface of the global ocean? *Chaos*, 24(3):033126.

Fuchs, H. L., Neubert, M. G., and Mullineaux, L. S. (2007). Effects of turbulence-mediated larval behavior on larval supply and settlement in tidal currents. *Limnology and Oceanography*, 52(3):1156–1165.

Gall, S. C. and Thompson, R. C. (2015). The impact of debris on marine life. *Mar Pollut Bull*, 92(1-2):170–9.

Ganachaud, A. and Wunsch, C. (2000). Improved estimates of global ocean circulation, heat transport, and mixing from hydrographic data. *Nature*, 408:453–456.

Gao, Y., Xu, G., Zhan, J., Zhang, J., Li, W., Lin, Q., Chen, L., and Lin, H. (2013). Spatial and particle size distributions of atmospheric dissolvable iron in aerosols and its input to the southern ocean and coastal east antarctica. *Journal of Geophysical Research: Atmospheres*, 118(22):2013JD020367.

Gawarkiewicz, G., Monismith, S., and Largier, J. (2007). Observing larval transport processes affecting population connectivity progress and challenges. *Oceanography*, 20(3):40–53.

Gell, F. R. and Roberts, C. M. (2003). Benefits beyond boundaries: the fishery effects of marine reserves. *Trends in Ecology and Evolution*, 18(9):448–455.

Gerber, L. R., Botsford, L. W., Hastings, A., Possingham, H. P., Gaines, S. D., Palumbi, S. R., and Andelman, S. (2003). Population models for marine reserve design: A retrospective and prospective synthesis. *Ecological Applications*, 13(1):S47–S64.

Gille, S. T., Carranza, M. M., and Cambra, R. (2014). Wind-induced upwelling in the kerguelen plateau region. *Biogeosciences*, 11(22):6389–6400.

Gilmartin, M. and Revelante, N. (1974). The island mass effect on the phytoplankton and primary production of the hawaiian islands. *Journal of Experimental Marine Biology and Ecology*, 16(2):181–204.

Gnanaseelan, C., Deshpande, A., and McPhaden, M. J. (2012). Impact of indian ocean dipole and el nio/southern oscillation wind-forcing on the wyrtki jets. *Journal of Geophysical Research: Oceans*, 117(C8):C08005.

Goes, M., Molinari, R., da Silveira, I., and Wainer, I. (2005). Retroflections of the north brazil current during february 2002. *Deep Sea Research Part I: Oceanographic Research Papers*, 52(4):647–667.

Golden, C. D., Allison, E. H., Cheung, W. W. L., Dey, M. M., Halpern, B. S., McCauley, D. J., Smith, M., Vaitla, B., Zeller, D., and Myers, S. S. (2016). Nutrition: Fall in fish catch threatens human health. *Nature*, 534(7607):317–320.

Gordon, A., Susanto, R., and Ffield, A. (1999). Throughflow within makassar strait. *Geophysical Research Letters*, 26:3325–3328.

Graham, R. M., De Boer, A. M., van Sebille, E., Kohfeld, K. E., and Schlosser, C. (2015). Inferring source regions and supply mechanisms of iron in the southern ocean from satellite chlorophyll data. *Deep Sea Research Part I: Oceanographic Research Papers*, 104:9–25.

Gregory, M. R. (2009). Environmental implications of plastic debris in marine settings–entanglement, ingestion, smothering, hangers-on, hitch-hiking and alien invasions. *Philos Trans R Soc Lond B Biol Sci*, 364(1526):2013–25.

Grenier, M., Cravatte, S., Blanke, B., Menkes, C., Koch-Larrouy, A., Durand, F., Melet, A., and Jeandel, C. (2011). From the western boundary currents to the pacific equatorial undercurrent: Modeled pathways and water mass evolutions. *Journal of Geophysical Research*, 116(C12).

Guitart, C., Sheppard, A., Frickers, T., Price, A. R., and Readman, J. W. (2007). Negligible risks to corals from antifouling booster biocides and triazine herbicides in coastal waters of the chagos archipelago. *Marine Pollution Bulletin*, 54(2):226–32.

Hall, N. M., Berry, K. L. E., Rintoul, L., and Hoogenboom, M. O. (2015). Microplastic ingestion by scleractinian corals. *Marine Biology*, 162(3):725–732.

Halpern, B. S. (2003). The impact of marine reserves: Do reserves work and does reserve size matter? *Ecological Applications*, 13(1):S117S137.

Halpern, B. S., Walbridge, S., Selkoe, K. A., Kappel, C. V., Micheli, F., D'Agrosa, C., Bruno, J. F., Casey, K. S., Ebert, C., Fox, H. E., Fujita, R., Heinemann, D., Lenihan, H. S., Madin, E. M., Perry, M. T., Selig, E. R., Spalding, M., Steneck,

R., and Watson, R. (2008). A global map of human impact on marine ecosystems. *Science*, 319(5865):948–52.

Hastings, A. and Harrison, S. (1994). Metapopulation dynamics and genetics. *Annu. Rev. Ecol. Syst.*, 25:167–188.

Hautala, S. L., Sprintall, J., Potemra, J. T., Chong, J. C., Pandoe, W., Bray, N., and Ilahude, A. G. (2001). Velocity structure and transport of the indonesian throughflow in the major straits restricting flow into the indian ocean. *Journal of Geophysical Research: Oceans*, 106(C9):19527–19546.

Heath, M. R. (2008). Comment on "a global map of human impact on marine ecosystems". *Science*, 321(5895):1446.

Hewes, C. D., Reiss, C. S., Kahru, M., Mitchell, B. G., and Holm-Hansen, O. (2008). Control of phytoplankton biomass by dilution and mixed layer depth in the western weddell-scotia confluence. *Marine Ecology Progress Series*, 366:15–29.

Hilborn, R. (2016). Marine biodiversity needs more than protection. *Nature*, 535:224–226.

Holm-Hansen, O., Kahru, M., and Hewes, C. D. (2005). Deep chlorophyll a maxima (dcms) in pelagic antarctic waters. ii. relation to bathymetric features and dissolved iron concentrations. *Marine Ecology Progress Series*, 297:71 –81.

Hutchings, J. A. (2000). Collapse and recovery of marine fishes. *Nature*, 406(6798):882–5.

IUCN and UNEP-WCMC (2013). The world database on protected areas (wdpa).

Jackett, D. and McDougall, T. (1995). Minimal adjustment of hydrographic data to achieve static stability. *J. Atmos. Ocean Tech*, 12:381–389.

Jacobs, Z. L., Popova, E. E., Hirschi, J. J.-M., Coward, A. C., Yool, A., van Gennip, S. J., Anifowose, B., and Harrington-Missin, L. (submitted). Oil spills in marine environments: The role of ocean circulation on far-field impacts.

Jambeck, J. R., Geyer, R., Wilcox, C., Siegler, T. R., Perryman, M., Andrady, A., Narayan, R., and Law, K. L. (2015). Marine pollution. plastic waste inputs from land into the ocean. *Science*, 347(6223):768–71.

Jameson, S. C., Tupper, M. H., and Ridley, J. M. (2002). The three screen doors: can marine protected areas be effective? *Marine Pollution Bulletin*, 44(11):1177–1183.

Jiang, M., Barbeau, K. A., Selph, K. E., Measures, C. I., Buck, K. N., Azam, F., Greg Mitchell, B., and Zhou, M. (2013). The role of organic ligands in iron cycling and primary productivity in the antarctic peninsula: A modeling study. *Deep Sea Research Part II: Topical Studies in Oceanography*, 90:112–133.

Jickells, T. D., An, Z. S., Andersen, K. K., Baker, A. R., Bergametti, G., Brooks, N., Cao, J. J., Boyd, P. W., Duce, R. A., Hunter, K. A., Kawahata, H., Kubilay, N., laRoche, J., Liss, P. S., Mahowald, N., Prospero, J. M., Ridgwell, A. J., Tegen, I., and Torres, R. (2005). Global iron connections between desert dust, ocean biogeochemistry, and climate. *Science*, 308:67–71.

Johnson, E. S., Bonjean, F., Lagerloef, G. S. E., Gunn, J. T., and Mitchum, G. T. (2007). Validation and error analysis of oscar sea surface currents. *Journal of Atmospheric and Oceanic Technology*, 24(4):688–701.

Johnson, K. S., Chavez, F. P., and Friederich, G. E. (1999). Continental-shelf sediment as a primary source of iron for coastal phytoplankton. *Nature*, 398(6729):697–700.

Jones, G. P., Srinivasan, M., and Almany, G. R. (2007). Population connectivity and conservation of marine biodiversity. *Oceanography*, 20(3):100–111.

Jonsson, B. F. and Watson, J. R. (2016). The timescales of global surface-ocean connectivity. *Nat Commun*, 7:11239.

Kaluza, P., Kolzsch, A., Gastner, M. T., and Blasius, B. (2010). The complex network of global cargo ship movements. *Journal of the Royal Society Interface*, 7(48):1093–103.

Katsanevakis, S. (2008). *Marine debris, a growing problem: Sources, distribution, composition, and impacts*, book section 2, pages 53–100. Nova Science Publishers, New York.

Kohfeld, K., Le Quere, C., Harrison, S., and Anderson, R. (2005). Role of marine biology in glacialinterglacial co2 cycles. *Science*, 308:74–77.

Korb, R. E. and Whitehouse, M. (2004). Contrasting primary production regimes around south georgia, southern ocean: large blooms versus high nutrient, low chlorophyll waters. *Deep Sea Research Part I: Oceanographic Research Papers*, 51(5):721–738.

Korb, R. E., Whitehouse, M. J., Atkinson, A., and Thorpe, S. E. (2008). Magnitude and maintenance of the phytoplankton bloom at south georgia: a naturally iron-replete environment. *Marine Ecology Progress Series*, 368:75–91.

Korb, R. E., Whitehouse, M. J., and Ward, P. (2004). Seawifs in the southern ocean: spatial and temporal variability in phytoplankton biomass around south georgia. *Deep Sea Research Part II: Topical Studies in Oceanography*, 51:99–116.

Kubota, M. (1994). A mechanism for the accumulation of floating marine debris north of hawaii. *Journal of Physical Oceanography*, 24(5):1059–1064.

Lagerloef, G. S. E., Mitchum, G. T., Lukas, R. B., and Niiler, P. P. (1999). Tropical pacific near-surface currents estimated from altimeter, wind, and drifter data. *Journal of Geophysical Research*, 104(C10):23313–23326.

Lampitt, R. S., Achterberg, E. P., Anderson, T. R., Hughes, J. A., Iglesias-Rodriguez, M. D., Kelly-Gerreyn, B. A., Lucas, M., Popova, E. E., Sanders, R., Shepherd, J. G., Smythe-Wright, D., and Yool, A. (2008). Ocean fertilization: a potential means of geoengineering? *Philos Transact A Math Phys Eng Sci*, 366(1882):3919–45.

Lasbleiz, M., Leblanc, K., Blain, S., Ras, J., Cornet-Barthaux, V., Hlias Nunige, S., and Quguiner, B. (2014). Pigments, elemental composition (c, n, p, and si), and stoichiometry of particulate matter in the naturally iron fertilized region of kerguelen in the southern ocean. *Biogeosciences*, 11(20):5931–5955.

Lass, H., Schmidt, M., Mohrholz, V., and Nausch, G. (2000). Hydrographic and current measurements in the area of the angolabenguela front. *Journal of Physical Oceanography*, 30:2589–2609.

Le Bars, D., Durgadoo, J. V., Dijkstra, H. A., Biastoch, A., and De Ruijter, W. P. M. (2014). An observed 20-year time series of agulhas leakage. *Ocean Science*, 10(4):601–609.

Lebreton, L. C., Greer, S. D., and Borrero, J. C. (2012). Numerical modelling of floating debris in the world's oceans. *Marine Pollution Bulletin*, 64(3):653–61.

Leinen, M. (2008). Building relationships between scientists and business in ocean iron fertilization. *Mar. Ecol. Prog. Ser.*, 364:251–256.

Levins, R. (1970). *Extinction*, pages 77 – 107. American Mathematical Society, Providence, Rhode Island, USA.

List, T. R. (2015). The iucn red list of threatened species. version 2015-4. table 6a: Red list category summary country totals (animals).

Liu, Y., Weisberg, R. H., Hu, C., and Zheng, L. (2011). Tracking the deepwater horizon oil spill: A modeling perspective. *Eos Trans. AGU*, 92(6):45–52.

Liu, Y., Weisberg, R. H., Vignudelli, S., and Mitchum, G. T. (2014). Evaluation of altimetry-derived surface current products using lagrangian drifter trajectories in the eastern gulf of mexico. *Journal of Geophysical Research: Oceans*, pages n/a–n/a.

Locarnini, R. A., Mishonov, A. V., Antonov, J. I., Boyer, T. P., Garcia, H. E., Baranova, O. K., Zweng, M. M., and Johnson, D. R. (2010). World ocean atlas 2009, volume 1: Temperature.

Longhurst, A. R. and Harrison, W. G. (1989). The biological pump: Profiles of plankton production and consumption in the upper ocean. *Progress In Oceanography*, 22(1):47–123.

Lunn, J. (2016). Disputes over the british indian ocean territory: April 2016 update.

Luo, J.-J., Zhang, R., Behera, S. K., Masumoto, Y., Jin, F.-F., Lukas, R., and Yamagata, T. (2010). Interaction between el nio and extreme indian ocean dipole. *Journal of Climate*, 23(3):726–742.

Mack, R. N., Simberloff, D., Lonsdale, W. M., Evans, H., Clout, M., and Bazzaz, F. A. (2000). Biotic invasions: causes, epidemiology, global consequences, and control. *Ecol. Appl.*, 10:689–710.

Madec, G. and Imbard, M. (1996). A global ocean mesh to overcome the north pole singularity. *Climate Dynamics*, 12(6):381 – 388.

Madec, G. and the NEMO team (2008). *NEMO ocean engine*. poop du Pole de modelisation de lInstitut Pierre-Simon Laplace, France.

Martin, J. (1990). Glacial-interglacial co2 change: the iron hypothesis. *Paleoceanography*, 5(1):1–13.

Martin, J. and Fitzwater, S. E. (1988). Iron deficiency limits phytoplankton growth in the north-east pacific subarctic. *Nature*, 331:341 – 343.

Martin, J., Knauer, G., Karl, D., and Broenkow, W. (1987). Vertex: carbon cycling in the northeast pacific. *Deep-Sea Research*, 34(2):267–285.

Martin, J. H., Gordon, R. M., and Fitzwater, S. E. (1990). Iron in antarctic waters. *Nature*, 345(6271):156–158.

Martinez, E., Maamaatuaiahutapu, K., and Taillandier, V. (2009). Floating marine debris surface drift: convergence and accumulation toward the south pacific subtropical gyre. *Mar Pollut Bull*, 58(9):1347–55.

Marzocchi, A., Hirschi, J. J. M., Holliday, N. P., Cunningham, S. A., Blaker, A. T., and Coward, A. C. (2015). The north atlantic subpolar circulation in an eddy-resolving global ocean model. *Journal of Marine Systems*.

Maximenko, N., Hafner, J., and Niiler, P. (2012). Pathways of marine debris derived from trajectories of lagrangian drifters. *Marine Pollution Bulletin*, 65(1-3):51–62.

Meredith, M. P., Watkins, J. L., Murphy, E. J., Cunningham, N. J., Wood, A. G., Korb, R., Whitehouse, M. J., Thorpe, S. E., and Vivier, F. (2003). An anticyclonic

circulation above the northwest georgia rise, southern ocean. *Geophysical Research Letters*, 30(20).

Meyers, G., Bailey, R. J., and Worby, A. P. (1995). Geostrophic transport of indonesian throughflow. *Deep-Sea Research Part I-Oceanographic Research Papers*, 42(7):1163–1174.

Michael Beman, J., Arrigo, K. R., and Matson, P. A. (2005). Agricultural runoff fuels large phytoplankton blooms in vulnerable areas of the ocean. *Nature*, 434(7030):211–4.

Michel, J., Owens, E. H., Zengel, S., Graham, A., Nixon, Z., Allard, T., Holton, W., Reimer, P. D., Lamarche, A., White, M., Rutherford, N., Childs, C., Mauseth, G., Challenger, G., and Taylor, E. (2013). Extent and degree of shoreline oiling: Deepwater horizon oil spill, gulf of mexico, usa. *PLoS One*, 8(6):e65087.

Mills, K., Pershing, A., Brown, C., Chen, Y., Chiang, F.-S., Holland, D., Lehuta, S., Nye, J., Sun, J., Thomas, A., and Wahle, R. (2013). Fisheries management in a changing climate: Lessons from the 2012 ocean heat wave in the northwest atlantic. *Oceanography*, 26(2).

Mongin, M., Molina, E., and Trull, T. W. (2008). Seasonality and scale of the kerguelen plateau phytoplankton bloom: A remote sensing and modeling analysis of the influence of natural iron fertilization in the southern ocean. *Deep Sea Research Part II: Topical Studies in Oceanography*, 55(5-7):880–892.

Mongin, M. M., Abraham, E. R., and Trull, T. W. (2009). Winter advection of iron can explain the summer phytoplankton bloom that extends 1000 km downstream of the kerguelen plateau in the southern ocean. *Journal of Marine Research*, 67:225–237.

Monterey, G. and Levitus, S. (1997). Seasonal variability of mixed layer depth for the world ocean. Report.

Monzon-Arguello, C., Dell'Amico, F., Moriniere, P., Marco, A., Lopez-Jurado, L. F., Hays, G. C., Scott, R., Marsh, R., and Lee, P. L. (2012). Lost at sea: genetic, oceanographic and meteorological evidence for storm-forced dispersal. *J R Soc Interface*, 9(73):1725–32.

Moore, C. J. (2008). Synthetic polymers in the marine environment: A rapidly increasing, long-term threat. *Environmental Research*, 108(2):131–139.

Moore, C. M., Seeyave, S., Hickman, A. E., Allen, J. T., Lucas, M. I., Planquette, H., Pollard, R. T., and Poulton, A. J. (2007). Ironlight interactions during the crozet natural iron bloom and export experiment (crozex) i: Phytoplankton growth and photophysiology. *Deep Sea Research Part II: Topical Studies in Oceanography*, 54(18-20):2045–2065.

Moore, J. K. and Abbott, M. R. (2000). Phytoplankton chlorophyll distributions and primary production in the southern ocean. *Journal of Geophysical Research*, 105(C12):28709.

Moore, J. K., Abbott, M. R., and Richman, J. G. (1999). Location and dynamics of the antarctic polar front from satellite sea surface temperature data. *Journal of Geophysical Research*, 104(C2):3059.

Mora, C. and Sale, P. F. (2002). Are populations of coral reef fish open or closed? *Trends in Ecology and Evolution*, 17(9):422–428.

Mosseri, J., Quguiner, B., Armand, L., and Cornet-Barthaux, V. (2008). Impact of iron on silicon utilization by diatoms in the southern ocean: A case study of si/n cycle

decoupling in a naturally iron-enriched area. *Deep Sea Research Part II: Topical Studies in Oceanography*, 55(5-7):801–819.

Murphy, E. J., Hofmann, E. E., Watkins, J. L., Johnston, N. M., Pinones, A., Ballerini, T., Hill, S. L., Trathan, P. N., Tarling, G. A., Cavanagh, R. A., Young, E. F., Thorpe, S. A., and Fretwell, P. (2013). Comparison of the structure and function of southern ocean regional ecosystems: The antarctic peninsula and south georgia. *Journal of Marine Systems*, 109-110:22–42.

Myers, N., Mittermeier, R. A., Mittermeier, C. G., da Fonseca, G. A., and Kent, J. (2000). Biodiversity hotspots for conservation priorities. *Nature*, 403(6772):853–8.

Nash, J., Shroyer, E., Kelly, S., Inall, M., Duda, T., Levine, M., Jones, N., and Musgrave, R. (2012). Are any coastal internal tides predictable? *Oceanography*, 25(2):80–95.

Nations, U. (1972). Report of the united nations conference on the human environment. Report A/CONF.48/14/Rev.1.

Naveira Garabato, A. C. (2009). *Energetics of Ocean Mixing*, pages 262–270. Elsevier Ltd, London.

Naveira Garabato, A. C., Stevens, D. P., Watson, A. J., and Roether, W. (2007). Short-circuiting of the overturning circulation in the antarctic circumpolar current. *Nature*, 447(7141):194–7.

New, A. L., Alderson, S. G., Smeed, D. A., and Stansfield, K. L. (2007). On the circulation of water masses across the mascarene plateau in the south indian ocean. *Deep Sea Research Part I: Oceanographic Research Papers*, 54(1):42–74.

Nicholls, K. W., sterhus, S., Makinson, K., Gammelsrd, T., and Fahrbach, E. (2009). Ice-ocean processes over the continental shelf of the southern weddell sea, antarctica: A review. *Reviews of Geophysics*, 47(3).

Nixon, Z., Zengel, S., Baker, M., Steinhoff, M., Fricano, G., Rouhani, S., and Michel, J. (2016). Shoreline oiling from the deepwater horizon oil spill. *Mar Pollut Bull*, 107(1):170–8.

Orsi, A. H., Whitworth III, T., and Nowlin Jr, W. D. (1995). On the meridional extent and fronts of the antarctic circumpolar current. *Deep Sea Research I*, 42(5):641–673.

Oschlies, A., Koeve, W., Rickels, W., and Rehdanz, K. (2010). Side effects and accounting aspects of hypothetical large-scale southern ocean iron fertilization. *Biogeosciences*, 7(12):4017–4035.

Paris, C. B., Helgers, J., van Sebille, E., and Srinivasan, A. (2013). Connectivity modeling system: A probabilistic modeling tool for the multi-scale tracking of biotic and abiotic variability in the ocean. *Environmental Modelling and Software*, 42:47–54.

Paris, C. B., Henaff, M. L., Aman, Z. M., Subramaniam, A., Helgers, J., Wang, D. P., Kourafalou, V. H., and Srinivasan, A. (2012). Evolution of the macondo well blowout: simulating the effects of the circulation and synthetic dispersants on the subsea oil transport. *Environ Sci Technol*, 46(24):13293–302.

Park, Y.-H., Durand, I., Kestenare, E., Rougier, G., Zhou, M., dOvidio, F., Cott, C., and Lee, J.-H. (2014). Polar front around the kerguelen islands: An up-to-date determination and associated circulation of surface/subsurface waters. *Journal of Geophysical Research: Oceans*, 119:n/a–n/a.

Park, Y.-H., Fuda, J.-L., Durand, I., and Naveira Garabato, A. C. (2008a). Internal tides and vertical mixing over the kerguelen plateau. *Deep Sea Research Part II: Topical Studies in Oceanography*, 55(5-7):582–593.

Park, Y.-H., Roquet, F., Durand, I., and Fuda, J.-L. (2008b). Large-scale circulation over and around the northern kerguelen plateau. *Deep Sea Research Part II: Topical Studies in Oceanography*, 55(5-7):566–581.

Partelow, S., von Wehrden, H., and Horn, O. (2015). Pollution exposure on marine protected areas: A global assessment. *Mar Pollut Bull*, 100(1):352–8.

Passow, U. and Carlson, C. A. (2012). The biological pump in a high co2 world. *Marine Ecology Progress Series*, 470:249 – 271.

Pauly, D., Watson, R., and Alder, J. (2005). Global trends in world fisheries: impacts on marine ecosystems and food security. *Philos Trans R Soc Lond B Biol Sci*, 360(1453):5–12.

Pelembe, T. and Cooper, G. e. (2011). *UK Overseas Territories and Crown Dependencies: 2011 Biodiversity snapshot*. Joint Nature Conservation Committee, Peterborough, UK.

Peterson, C. H., Rice, S. D., Short, J. W., Esler, D., Bodkin, J. L., Ballachey, B. E., and Irons, D. B. (2003). Long-term ecosystem response to the exxon valdez oil spill. *Science*, 302(5653):2082–6.

Peterson, R. G. and Stramma, L. (1991). Upper-level circulation in the south atlantic ocean. *Progress In Oceanography*, 26:1–73.

Petit, J. and Prudent, G. (2010). *Climate Change and Biodiversity in the European Union Overseas Entities*. IUCN, Gland, Switzerland and Brussels, Belgium.

Piatt, J. F., Lensink, C. J., Butler, W., Marshal, K., and Nysewander, D. R. (1990). Immediate impact of the 'exxon valdez' oil spill on marine birds. *The Auk*, 107(2):387–397.

Piecuch, C. G. and Rynearson, T. A. (2012). Quantifying dispersal and connectivity of surface waters using observational lagrangian measurements. *Journal of Atmospheric and Oceanic Technology*, 29(8):1127–1138.

Pillai, P. A. and Chowdary, J. S. (2016). Indian summer monsoon intra-seasonal oscillation associated with the developing and decaying phase of el nio. *International Journal of Climatology*, 36(4):1846–1862.

Planquette, H., Statham, P. J., Fones, G. R., Charette, M. A., Moore, C. M., Salter, I., Nedelec, F. H., Taylor, S. L., French, M., Baker, A. R., Mahowald, N., and Jickells, T. D. (2007). Dissolved iron in the vicinity of the crozet islands, southern ocean. *Deep Sea Research II*, 54:1999 – 2019.

Pollard, R., Sanders, R., Lucas, M., and Statham, P. (2007a). The crozet natural iron bloom and export experiment (crozex). *Deep Sea Research Part II: Topical Studies in Oceanography*, 54(18-20):1905–1914.

Pollard, R. T., Salter, I., Sanders, R. J., Lucas, M. I., Moore, C. M., Mills, R. A., Statham, P. J., Allen, J. T., Baker, A. R., Bakker, D. C., Charette, M. A., Fielding, S., Fones, G. R., French, M., Hickman, A. E., Holland, R. J., Hughes, J. A., Jickells, T. D., Lampitt, R. S., Morris, P. J., Nedelec, F. H., Nielsdottir, M., Planquette, H., Popova, E. E., Poulton, A. J., Read, J. F., Seeyave, S., Smith, T., Stinchcombe, M., Taylor, S., Thomalla, S., Venables, H. J., Williamson, R., and Zubkov, M. V. (2009). Southern ocean deep-water carbon export enhanced by natural iron fertilization. *Nature*, 457(7229):577–80.

Pollard, R. T., Venables, H. J., Read, J. F., and Allen, J. T. (2007b). Large-scale circulation around the crozet plateau controls an annual phytoplankton bloom in the crozet basin. *Deep Sea Research II*, 54:1915 – 1929.

Popova, E., Yool, A., Byfield, V., Cochrane, K., Coward, A. C., Salim, S. S., Gasalla, M. A., Henson, S. A., Hobday, A. J., Pecl, G. T., Sauer, W. H., and Roberts, M. J. (2016). From global to regional and back again: common climate stressors of marine ecosystems relevant for adaptation across five ocean warming hotspots. *Glob Chang Biol*, 22(6):2038–53.

Popova, E. E., Pollard, R. T., Lucas, M. I., Venables, H. J., and Anderson, T. R. (2007). Real-time forecasting of ecosystem dynamics during the crozex experiment and the roles of light, iron, silicate, and circulation. *Deep Sea Research Part II: Topical Studies in Oceanography*, 54(18-20):1966–1988.

Popova, E. E., Yool, A., Aksenov, Y., and Coward, A. C. (2013). Role of advection in arctic ocean lower trophic dynamics: A modeling perspective. *Journal of Geophysical Research*, 118:1571–1586.

Poulton, A. J., Mark Moore, C., Seeyave, S., Lucas, M. I., Fielding, S., and Ward, P. (2007). Phytoplankton community composition around the crozet plateau, with emphasis on diatoms and phaeocystis. *Deep Sea Research Part II: Topical Studies in Oceanography*, 54(18-20):2085–2105.

Quartly, G. D., de Cuevas, B. A., and Coward, A. C. (2013). Mozambique channel eddies in gcms: A question of resolution and slippage. *Ocean Modelling*, 63:56–67.

Read, J. F., Pollard, R. T., and Allen, J. T. (2007). Sub-mesoscale structure and the development of an eddy in the subantarctic front north of the crozet islands. *Deep-Sea Research Part Ii-Topical Studies in Oceanography*, 54(18-20):1930–1948.

Redfield, A. C. (1958). The biological control of chemical factors in the environment. *American Scientist*, 46(3):230A, 205–221.

Richardson, P. L., Arnault, S., Garzoli, S., and Bruce, J. G. (1992). Annual cycle of the atlantic north equatorial countercurrent. *Deep-Sea Research*, 39(6):997–1014.

Rickels, W., Rehdanz, K., and Oschlies, A. (2010). Methods for greenhouse gas offset accounting: A case study of ocean iron fertilization. *Ecological Economics*, 69(12):2495–2509.

Ridderinkhof, H., Van der Werf, P., Ullgren, J., Van Aken, H., Van Leeuwen, P., and De Ruijter, W. (2010). Seasonal and interannual variability in the mozambique channel from moored current observations. *Journal of Geophysical Research*.

Rimaud, J., Speich, S., Blanke, B., and Grima, N. (2012). The exchange of intermediate water in the southeast atlantic: Water mass transformations diagnosed from the lagrangian analysis of a regional ocean model. *Journal of Geophysical Research: Oceans*, 117(C8):n/a–n/a.

Rintoul, S. R. (2011). *The Southern Ocean in the Earth System*, pages 175–187. Smithsonian Institution Scholarly Press, Washington, D.C.

Rintoul, S. R., Hughes, C., and Olbers, D. (2001). *The Antarctic Circumpolar Current System*, book section 4.6, pages 271 – 302. Academic Press, London.

Roberts, C. M. (1997). Connectivity and management of caribbean coral reefs. *Science*, 278(5342):1454–7.

Robinson, J., New, A. L., Popova, E. E., Srokosz, M. A., and Yool, A. (2017). Far-field connectivity of the uk's four largest marine protected areas: Four of a kind? *Earth's Future*.

Robinson, J., Popova, E. E., Srokosz, M. A., and Yool, A. (2016). A tale of three islands: Downstream natural iron fertilization in the southern ocean. *Journal of Geophysical Research: Oceans*, 121.

Robinson, J., Popova, E. E., Yool, A., Srokosz, M., Lampitt, R. S., and Blundell, J. R. (2014). How deep is deep enough? ocean iron fertilization and carbon sequestration in the southern ocean. *Geophysical Research Letters*, 41(7):2489–2495.

Rogers, A. D. and Laffoley, D. (2013). Introduction to the special issue: The global state of the ocean; interactions between stresses, impacts and some potential solutions. synthesis papers from the international programme on the state of the ocean 2011 and 2012 workshops. *Mar Pollut Bull*, 74(2):491–4.

Rossi, V., Van Sebille, E., Sen Gupta, A., Garon, V., and England, M. H. (2013). Multi-decadal projections of surface and interior pathways of the fukushima cesium-137 radioactive plume. *Deep Sea Research Part I: Oceanographic Research Papers*, 80:37–46.

Rosso, I., Hogg, A. M., Strutton, P. G., Kiss, A. E., Matear, R., Klocker, A., and van Sebille, E. (2014). Vertical transport in the ocean due to sub-mesoscale structures: Impacts in the kerguelen region. *Ocean Modelling*, 80:10–23.

Ruiz, G. M., Rawlings, T. K., Dobbs, F. C., Drake, L. A., Mullady, T., Huq, A., and Colwell, R. R. (2000). Global spread of microorganisms by ships. *Nature*, 408:49–50.

Rhs, S., Durgadoo, J. V., Behrens, E., and Biastoch, A. (2013). Advective timescales and pathways of agulhas leakage. *Geophysical Research Letters*, 40(15):3997–4000.

Saji, N. H., Goswami, B. N., Vinayachandran, P. N., and Yamagata, T. (1999). A dipole mode in the tropical indian ocean. *Nature*, 401(6751):360–3.

Sale, P. F., Cowen, R. K., Danilowicz, B. S., Jones, G. P., Kritzer, J. P., Lindeman, K. C., Planes, S., Polunin, N. V., Russ, G. R., Sadovy, Y. J., and Steneck, R. S. (2005). Critical science gaps impede use of no-take fishery reserves. *Trends Ecol Evol*, 20(2):74–80.

Salle, J.-B., Shuckburgh, E., Bruneau, N., Meijers, A. J. S., Bracegirdle, T. J., and Wang, Z. (2013). Assessment of southern ocean mixed-layer depths in cmip5 models: Historical bias and forcing response. *Journal of Geophysical Research*, 118:1845–1862.

Sanial, V., van Beek, P., Lansard, B., d'Ovidio, F., Kestenare, E., Souhaut, M., Zhou, M., and Blain, S. (2014). Study of the phytoplankton plume dynamics off the crozet islands (southern ocean): A geochemical-physical coupled approach. *Journal of Geophysical Research-Oceans*, 119(4):2227–2237.

Santos, R. G., Andrades, R., Boldrini, M. A., and Martins, A. S. (2015). Debris ingestion by juvenile marine turtles: an underestimated problem. *Mar Pollut Bull*, 93(1-2):37–43.

Sarmiento, J. L. and Gruber, N. (2006). *Ocean Biogeochemical Dynamics*. Princeton University Press, Princeton USA and Oxford UK.

Sarmiento, J. L., Slater, R. D., Dunne, J., Gnanadesikan, A., and Hiscock, M. R. (2010). Efficiency of small scale carbon mitigation by patch iron fertilization. *Biogeosciences*, 7(11):3593–3624.

Schallenberg, C., van der Merwe, P., Chever, F., Cullen, J. T., Lannuzel, D., and Bowie, A. R. (2015). Dissolved iron and iron(ii) distributions beneath the pack ice in the east antarctic (120e) during the winter/spring transition. *Deep Sea Research Part II: Topical Studies in Oceanography*.

Scheld, A. M., Bilkovic, D. M., and Havens, K. J. (2016). The dilemma of derelict gear. *Scientific Reports*, 6:19671.

Schmitz, W. J. (1995). On the interbasin-scale thermohaline circulation. *Reviews of Geophysics*, 33(2):151–173.

Schott, F. A. and McCreary, J. P. (2001). The monsoon circulation of the indian ocean. *Progress in Oceanography*, 51(1):1–123.

Schott, F. A., Xie, S.-P., and McCreary, J. P. (2009). Indian ocean circulation and climate variability. *Reviews of Geophysics*, 47(1).

Scott, R., Marsh, R., and Hays, G. C. (2014). Ontogeny of long distance migration. *Ecology*, 95(10):2840–2850.

Shahidul Islam, M. and Tanaka, M. (2004). Impacts of pollution on coastal and marine ecosystems including coastal and marine fisheries and approach for management: a review and synthesis. *Mar Pollut Bull*, 48(7-8):624–49.

Shaked, Y. and Lis, H. (2012). Disassembling iron availability to phytoplankton. *Frontiers in Microbiology*, 3(123):1–26.

Shankar, D., Vinayachandran, P. N., and Unnikrishnan, A. S. (2002). The monsoon currents in the north indian ocean. *Progress in Oceanography*, 52(1):63–120.

Shepherd, J. G., Caldeira, K., Cox, P., Haigh, J., Keith, D., Launder, B., Mace, G., MacKerron, G., Pyle, J., Rayner, S., Redgewell, C., and Watson, A. J. (2009). *Geoengineering the climate: Science, governance and uncertainty*. The Royal Society, London, UK.

Sheppard, C. R., Ateweberhan, M., Bowen, B. W., Carr, P., Chen, C. A., Clubbe, C., Craig, M. T., Ebinghaus, R., Eble, J., Fitzsimmons, N., Gaither, M. R., Gan, C. H.,

Gollock, M., Guzman, N., Graham, N. A., Harris, A., Jones, R., Keshavmurthy, S., Koldewey, H., Lundin, C. G., Mortimer, J. A., Obura, D., Pfeiffer, M., Price, A. R., Purkis, S., Raines, P., Readman, J. W., Riegl, B., Rogers, A., Schleyer, M., Seaward, M. R., Sheppard, A. L., Tamelander, J., Turner, J. R., Visram, S., Vogler, C., Vogt, S., Wolschke, H., Yang, J. M., Yang, S. Y., and Yesson, C. (2012). Reefs and islands of the chagos archipelago, indian ocean: why it is the world's largest no-take marine protected area. *Aquatic Conservation: Marine and Freshwater Ecosystems*, 22(2):232–261.

Sheppard, C. R. C., Harris, A., and Sheppard, A. L. S. (2008). Archipelago-wide coral recovery patterns since 1998 in the chagos archipelago, central indian ocean. *Marine Ecology Progress Series*, 362:109–117.

Sherman, P. and van Sebille, E. (2016). Modeling marine surface microplastic transport to assess optimal removal locations. *Environmental Research Letters*, 11(1):014006.

Shoji, K. and Jones, I. S. F. (2001). The costing of carbon credits from ocean nourishment plants. *Sci. Total Environ.*, 277(1-3):27 31.

Sloyan, B. M. and Rintoul, S. R. (2001). The southern ocean limb of the global deep overturning circulation. *Journal of Physical Oceanography*, 31:143–173.

Smetacek, V., Assmy, P., and Henjes, J. (2004). The role of grazing in structuring southern ocean pelagic ecosystems and biogeochemical cycles. *Antarctic Science*, 16(4):541–558.

Smetacek, V., Klaas, C., Strass, V. H., Assmy, P., Montresor, M., Cisewski, B., Savoye, N., Webb, A., d'Ovidio, F., Arrieta, J. M., Bathmann, U., Bellerby, R., Berg, G. M., Croot, P., Gonzalez, S., Henjes, J., Herndl, G. J., Hoffmann, L. J., Leach, H., Losch, M., Mills, M. M., Neill, C., Peeken, I., Rottgers, R., Sachs, O., Sauter, E., Schmidt,

M. M., Schwarz, J., Terbruggen, A., and Wolf-Gladrow, D. (2012). Deep carbon export from a southern ocean iron-fertilized diatom bloom. *Nature*, 487(7407):313–319.

Sonnewald, M. (2016). *Ocean model utility dependence on horizontal resolution*. Thesis.

Sprintall, J. and Cronin, M. F. (2009). *Upper Ocean Vertical Structure*, pages 217–224. Elsevier Ltd., London.

Sprintall, J., Gordon, A. L., Koch-Larrouy, A., Lee, T., Potemra, J. T., Pujiana, K., and Wijffels, S. E. (2014). The indonesian seas and their role in the coupled oceanclimate system. *Nature Geoscience*, 7(7):487–492.

Srokosz, M. A., Robinson, J., McGrain, H., Popova, E. E., and Yool, A. (2015). Could the madagascar bloom be fertilized by madagascan iron? *Journal of Geophysical Research: Oceans*, 120(8):5790–5803.

Stommel, H. (1958). The abyssal circulation. *Deep Sea Research (1953)*, 5(1):80–82.

Stoner, A. W., Davis, M. H., and Booker, C. J. (2012). Abundance and population structure of queen conch inside and outside a marine protected area: repeat surveys show significant declines. *Marine Ecology Progress Series*, 460:101–114.

Storm, T., Boettcher, M., Grant, M., Zuhlke, M., N., F., Jackson, T., and Sathyendranath, S. (2013). Product user guide. In Groom, S., editor, *Ocean Colour Climate Change Initiative (OCCCI) - Phase One*, volume 1.0.1. Plymouth Marine Laboratory, Plymouth, UK.

Stramma, L., Fischer, J., and Schott, F. A. (1996). The flow field off southwest india at 8n during the southwest monsoon of august 1996. *Journal of Marine Research*, 54:55–72.

Tagliabue, A., Bowie, A. R., Boyd, P. W., Buck, K. N., Johnson, K. S., and Saito, M. A. (2017). The integral role of iron in ocean biogeochemistry. *Nature*, 543(7643):51–59.

Tagliabue, A., Salle, J.-B., Bowie, A. R., Lvy, M., Swart, S., and Boyd, P. W. (2014). Surface-water iron supplies in the southern ocean sustained by deep winter mixing. *Nature Geoscience*, 7(4):314–320.

Takahashi, T., Sutherland, S. C., Wanninkhof, R., Sweeney, C., Feely, R. A., Chipman, D. W., Hales, B., Friederich, G., Chavez, F., Sabine, C., Watson, A., Bakker, D. C. E., Schuster, U., Metzl, N., Yoshikawa-Inoue, H., Ishii, M., Midorikawa, T., Nojiri, Y., Krtzinger, A., Steinhoff, T., Hoppema, M., Olafsson, J., Arnarson, T. S., Tilbrook, B., Johannessen, T., Olsen, A., Bellerby, R., Wong, C. S., Delille, B., Bates, N. R., and de Baar, H. J. W. (2009). Climatological mean and decadal change in surface ocean pco2, and net seaair co2 flux over the global oceans. *Deep Sea Research Part II: Topical Studies in Oceanography*, 56(8-10):554–577.

Talley, L. D., Pickard, G. L., Emery, W. J., and Swift, J. H. (2011). *Descriptive Physical Oceanography An Introduction*. Elsevier, Oxford, UK Burlington and San Diego, USA, sixth edition.

Thomalla, S. J., Fauchereau, N., Swart, S., and Monteiro, P. M. S. (2011). Regional scale characteristics of the seasonal cycle of chlorophyll in the southern ocean. *Biogeosciences*, 8(10):2849–2866.

Thompson, A. F. and Youngs, M. K. (2013). Surface exchange between the weddell and scotia seas. *Geophysical Research Letters*, 40(22):5920–5925.

Treml, E. A., Halpin, P. N., Urban, D. L., and Pratson, L. F. (2007). Modeling population connectivity by ocean currents, a graph-theoretic approach for marine conservation. *Landscape Ecology*, 23(S1):19–36.

Tripathy, S. C., Pavithran, S., Sabu, P., Pillai, H. U. K., Dessai, D. R. G., and Anilkumar, N. (2015). Deep chlorophyll maximum and primary productivity in indian ocean sector of the southern ocean: Case study in the subtropical and polar front during austral summer 2011. *Deep Sea Research Part II: Topical Studies in Oceanography*, 118:240–249.

Trusts, T. P. C. (2015). Pew, national geographic applaud creation of pitcairn islands marine reserve.

Tyrrell, T., Merico, A., Waniek, J. J., Wong, C. S., Metzl, N., and Whitney, F. (2005). Effect of seafloor depth on phytoplankton blooms in high-nitrate, low-chlorophyll (hnlc) regions. *Journal of Geophysical Research*, 110(G2).

UNEP (2016). Marine plastic debris and microplastics global lessons and research to inspire action and guide policy change. Report.

van Beek, P., Bourquin, M., Reyss, J. L., Souhaut, M., Charette, M. A., and Jeandel, C. (2008). Radium isotopes to investigate the water mass pathways on the kerguelen plateau (southern ocean). *Deep Sea Research Part II: Topical Studies in Oceanography*, 55(5-7):622–637.

Van Cauwenberghe, L. and Janssen, C. R. (2014). Microplastics in bivalves cultured for human consumption. *Environ Pollut*, 193:65–70.

Van Cauwenberghe, L., Vanreusel, A., Mees, J., and Janssen, C. R. (2013). Microplastic pollution in deep-sea sediments. *Environ Pollut*, 182:495–9.

van der Merwe, P., Bowie, A. R., Qurou, F., Armand, L., Blain, S., Chever, F., Davies, D., Dehairs, F., Planchon, F., Sarthou, G., Townsend, A. T., and Trull, T. W.

(2015). Sourcing the iron in the naturally fertilised bloom around the kerguelen plateau: particulate trace metal dynamics. *Biogeosciences*, 12(3):739–755.

van Gennip, S. J., Popova, E. E., Yool, A., Pecl, G. T., Hobday, A. J., and Sorte, C. J. (2016). Going with the flow: the role of ocean circulation in global marine ecosystems under a changing climate. *Glob Chang Biol*.

van Sebille, E., England, M. H., and Froyland, G. (2012). Origin, dynamics and evolution of ocean garbage patches from observed surface drifters. *Environmental Research Letters*, 7(4):044040.

van Sebille, E., Sprintall, J., Schwarzkopf, F. U., Sen Gupta, A., Santoso, A., England, M. H., Biastoch, A., and Boning, C. W. (2014). Pacific-to-indian ocean connectivity: Tasman leakage, indonesian throughflow, and the role of enso. *Journal of Geophysical Research-Oceans*, 119(2):1365–1382.

van Sebille, E., van Leeuwen, P. J., Biastoch, A., and de Ruijter, W. P. M. (2010). Flux comparison of eulerian and lagrangian estimates of agulhas leakage: A case study using a numerical model. *Deep Sea Research Part I: Oceanographic Research Papers*, 57(3):319–327.

van Sebille, E., Wilcox, C., Lebreton, L., Maximenko, N., Hardesty, B. D., van Franeker, J. A., Eriksen, M., Siegel, D., Galgani, F., and Law, K. L. (2015). A global inventory of small floating plastic debris. *Environmental Research Letters*, 10(12):124006.

Venables, H. and Moore, C. M. (2010). Phytoplankton and light limitation in the southern ocean: Learning from high-nutrient, high-chlorophyll areas. *Journal of Geophysical Research*, 115(C2).

Venables, H. J., Pollard, R. T., and Popova, E. E. (2007). Physical conditions controlling the development of a regular phytoplankton bloom north of the crozet plateau, southern ocean. *Deep Sea Research II*, 54:1949 – 1965.

Wace, N. (1995). *Ocean liter stranded on Australian coast*. Great Barrier Reef Marine Park Authority, Townsville, Queensland.

Wadley, M. R., Jickells, T. D., and Heywood, K. J. (2014). The role of iron sources and transport for southern ocean productivity. *Deep Sea Research Part I: Oceanographic Research Papers*.

Wakata, Y. and Sugimori, Y. (1990). Lagrangian motions and global density distributions of floating matter in the ocean simulated using shipdrift data. *Journal of Physical Oceanography*, 20(1):125–138.

Walsh, J. J. (1991). Importance of continental margins in the marine biogeochemical cycling of carbon and nitrogen. *Nature*, 350(6313):53–55.

Ward, P., Whitehouse, M., Shreeve, R., Thorpe, S., Atkinson, A., Korb, R., Pond, D., and Young, E. (2007). Plankton community structure south and west of south georgia (southern ocean): Links with production and physical forcing. *Deep Sea Research I*, 54:1871–1889.

Watson, R. and Pauly, D. (2001). Systematic distortions in world fisheries catch trends. *Nature*, 414(6863):534–6.

Wernberg, T., Russell, B. D., Moore, P. J., Ling, S. D., Smale, D. A., Campbell, A., Coleman, M. A., Steinberg, P. D., Kendrick, G. A., and Connell, S. D. (2011). Impacts of climate change in a global hotspot for temperate marine biodiversity and ocean warming. *Journal of Experimental Marine Biology and Ecology*, 400(1-2):7–16.

Williams, R. and Follows, M. (2011). *Ocean Dynamics and the Carbon Cycle Principles and Mechanisms*. Cambridge University Press, Cambridge, UK.

Woods, J. D. and Onken, R. (1982). Diurnal-variation and primary production in the ocean - preliminary-results of a lagrangian ensemble model. *Journal of Plankton Research*, 4(3):735–756.

Working Group I, I. (2013). Summary for policymakers. in: Climate change 2013: The physical science basis. contribution of working group i to the fifth assessment report of the intergovernmental panel on climate change. Report.

Wright, S. L., Thompson, R. C., and Galloway, T. S. (2013). The physical impacts of microplastics on marine organisms: a review. *Environ Pollut*, 178:483–92.

Wu, L., Cai, W., Zhang, L., Nakamura, H., Timmermann, A., Joyce, T., McPhaden, M. J., Alexander, M., Qiu, B., Visbeck, M., Chang, P., and Giese, B. (2012). Enhanced warming over the global subtropical western boundary currents. *Nature Climate Change*, 2(3):161–166.

Wyrtki, K. (1973). An equatorial jet in the indian ocean. *Science*, 181:262–264.

Wyrtki, K. (1973b). *Physical oceanography of the Indian Ocean. Vol. 3 of Ecological studies: analysis and synthesis*, volume 3 of *Biology of the Indian Ocean*. Chapman and Hall Ltd, London, UK.

Yang, H., Lohmann, G., Wei, W., Dima, M., Ionita, M., and Liu, J. (2016). Intensification and poleward shift of subtropical western boundary currents in a warming climate. *Journal of Geophysical Research: Oceans*.

Yool, A., Shepherd, J. G., Bryden, H. L., and Oschlies, A. (2009). Low efficiency of nutrient translocation for enhancing oceanic uptake of carbon dioxide. *Journal of Geophysical Research*, 114(C08009).

You, Y., Lutjeharms, J., Boebel, O., and De Ruijter, W. (2003). Quantification of the interocean exchange of intermediate water masses around southern africa. *Deep Sea Research II*, 50:197–228.

Young, E. F., Meredith, M. P., Murphy, E. J., and Carvalho, G. R. (2011). High-resolution modelling of the shelf and open ocean adjacent to south georgia, southern ocean. *Deep Sea Research II*, 58:1540–1552.

Young, E. F., Thorpe, S. E., Banglawala, N., and Murphy, E. J. (2014). Variability in transport pathways on and around the south georgia shelf, southern ocean: Implications for recruitment and retention. *Journal of Geophysical Research*, 119:241–252.

Zhang, Y., Lacan, F., and Jeandel, C. (2008). Dissolved rare earth elements tracing lithogenic inputs over the kerguelen plateau (southern ocean). *Deep Sea Research Part II: Topical Studies in Oceanography*, 55(5-7):638–652.

Zhang, Z. and Chen, Q. (2007). Comparison of the eulerian and lagrangian methods for predicting particle transport in enclosed spaces. *Atmospheric Environment*, 41(25):5236–5248.